IEKP-KA/2017-19

The Rate Dependent Radiation Induced Signal Degradation of Diamond Detectors

Zur Erlangung des akademischen Grades eines
DOKTORS DER NATURWISSENSCHAFTEN
bei der Fakultät für Physik des
KIT – Karlsruher Institut für Technologie

genehmigte

DISSERTATION

von

Dipl.-Phys. Florian Robert Kassel
aus Rastatt

Tag der mündlichen Prüfung: 27.01.2017

Referent: Prof. Dr. Wim de Boer
Korreferent: Prof. Dr. Thomas Müller

"Diamonds are intrinsically worthless, except for the deep psychological need they fill."

Nicky Oppenheimer
former chairman of De Beers

Deutsche Zusammenfassung

Der Large Hadron Collider (LHC) an der Europäischen Organisation für Kernforschung (CERN) in Genf ist der weltweit größte Teilchenbeschleuniger. Der 27 km ringförmige Synchrotonbeschleuniger ermöglichte im Jahr 2012 den Nachweis des Higgs Boson, dem letzten fehlenden Elementarteilchen im Standardmodell [Cha12]. Gegenläufige Protonen werden auf eine Schwerpunktsenergie von $\sqrt{s} = 14\,\text{TeV}$ beschleunigt und zur Kollision gebracht. Die bisher unerreichte Kollisionsenergie ermöglicht die Suche nach neuer Physik jenseits des Standardmodells.

Die Proton Teilchenstrahlen werden an vier Wechselwirkungspunkten frontal zur Kollision gebracht und die entstehenden Zerfallsprodukte mittels Detektoren (ALICE, ATLAS, CMS und LHCb) gemessen. Aus den Messungen der Zerfallsprodukte kann die ursprüngliche Wechselwirkung der Protonen und der an ihr beteiligten Elementarteilchen bestimmt werden. Nachdem der LHC in der ersten Laufzeit zwischen den Jahren $2010 - 2013$ eine maximale Schwerpunktsenergie von 8 TeV erreichte wurde der LHC in einer 2-jährigen Wartung- und Instandhaltungsphase auf die zweite Laufzeit mit erhöhter Schwerpunktsenergie von 14 TeV vorbereitet. Die zweite Laufzeit des LHC, welche am 5. April 2015 startete, ermöglichte die Entdeckung einer neuen Teilchenklasse der Pentaquarks, nachgewiesen durch das LHCb Experiment [Aai15].

Die zwei LHC Teilchenstrahle setzen sich aus bis zu 2808 Protonenpaketen zusammen, wobei jedes Protonenpaket aus ca. 1.1×10^{11} Protonen besteht. Der Teilchenstrahl besitzt bei einer Schwerpunktsenergie von 14 TeV eine Energie von 362 MJ, das ungefähr dem 200-fachen des weltweit zweitgrößtem Hadronbeschleuniger, dem Tevatron am Fermilab in Chicago (USA), entspricht. Schon der Verlust eines Bruchteils des LHC Teilchenstrahl kann schwere Schäden an der umgebenden Infrastruktur, im speziellen an den supraleitenden Magnete die zur Fokussierung und Ablenkung der Teilchenstrahlen verwendet werden, zur Folge haben. Teilchenstrahlverluste geringer Intensität ereignen sich allerdings regelmäßig und müssen daher genau überwacht werden. Diese werden zum Beispiel durch die Wechselwirkung des Teilchenstrahls mit Kollimatoren, mit den Vakuumsystemen oder mit Restgasmoleküle erzeugt. Das LHC Beam Loss System (BLM) ist speziell zur Messung von Teilchenstrahlverlusten entworfen und besteht aus über 4000 installierten Sensoren am LHC welche den Strahlzustand kontinuierlich überprüfen [AG01]. Wird ein Strahlverlust mit erhöhter Intensität gemessen wird das LHC Beam Abort System aktiviert, dass schnellstmöglich ($t_{\text{abort}} \sim 360\,\mu\text{s}$) den Teilchenstrahl entsorgt. Das LHC BLM System überwacht die Teilchenstrahle innerhalb des gesamten Beschleunigerkomplexes, überlässt die Messung der Strahlverluste im Bereich der Kollisionspunkte allerdings den Experimenten.

Für die Messung der Strahlverluste am CMS Experiment wurde hierfür der Beam Condition Monitor (BCML) Detektor, mit maßgeblicher Unterstützung des Institut für Experimentelle Kernphysik (IEKP) des Karlsruher Instituts für Technologie (KIT) [Mue11], entwickelt. Der BCML Detektor ist sehr nahe an dem Strahlrohr montiert ($\text{r} \sim 5\,\text{cm}$) und daher einer sehr hohen Strahlenbelastung ausgesetzt. Als Sensormaterial wurde Diamant gewählt, welches sich durch eine exzellente Strahlenhärte auszeichnet [Ada06]. Die Strahlenschädigung der Diamantsensoren welche während der zweiten Laufzeit des LHCs gemessen wurde war hingegen sehr viel höher als erwartet. Ziel dieser Arbeit ist ein qualitatives und quantitatives

Verständnis dieser Diskrepanz durch die Entwicklung eines Defektmodells, welches die tatsächliche Strahlenschädigung von Diamantsensoren realistisch berechnen kann.

Der Grund für die erhöhte Strahlenschädigung der Diamantsensoren hinsichtlich der Signalerzeugung kann mit der Diamantpolarisation erklärt werden. Die Diamantpolarisation beschreibt die inhomogene Erzeugung von Raumladung, welche das elektrische Feld innerhalb des Diamantsensors stark verformt. Dieses deformierte elektrische Feld erhöht lokal die Ladungsträgerrekombination und führt zu einer reduzierten Ladungssammlungseffizienz und daher zu einem geringeren Sensorsignal. Darüberhinaus konnte gezeigt werden, dass die Diamantpolarisation von der Rate an ionisierenden Teilchen beeinflusst wird. Ein strahlengeschädigter Diamantsensor weist einen reduzierten Signalstrom in einem hochraten Umfeld im Vergleich zu einem niedrigraten Umfeld auf. Die ratenabhängige Diamantpolarisation führt daher zu einem stark, nicht linearem, reduziertem Signalstrom.

Im Rahmen dieser Arbeit wurde die Diamantpolarisation mittels einer Bestrahlungskampagne vermessen. Hierfür wurden neue sCVD Diamantsensoren schrittweise mit Proton oder Neutronen bestrahlt und nach jedem Bestrahlungsschritt mit der Transient Current Technique (TCT) vermessen. Die TCT Technik ermöglicht eine indirekte Messungen des elektrischen Feldes innerhalb der Diamantsensoren und somit die direkte Messung der Diamantpolarisation als Funktion der Strahlenschädigung. Des Weiteren wurde regelmäßig die Ladungssammlungseffizienz der Diamantsensoren als Funktion der Strahlenschädigung vermessen. Basierend auf den experimentellen Messergebnissen wurde ein Defektmodell entwickelt, welches die Strahlenschädigung korrekt berücksichtigt. Basierend auf diesem Defektmodell konnte mittels der Software Silvaco TCAD [SIL16] die Diamantpolarisation und der sich daraus ergebenden Reduktion der Ladungssammlungseffizienz korrekt simuliert werden. Darüberhinaus erklärt dieses Defektmodell die Ratenabhängigkeit der Diamantpolarisation und beschreibt den Verlust der Ladungssammlungseffizienz der BCML Sensoren korrekt. Mittels dieses Defektmodells lässt sich nun die Ladungssammlungseffizienz von Diamantsensoren als Funktion von Strahlenschädigung, Teilchenratenumgebung sowie Elektrischem Feld, bei welchem der Sensor betrieben wird, berechnen.

Contents

Chapter 1

Introduction

The discovery of the Higgs boson in 2012 [Cha12] is unarguably the biggest success in the recent history of particle physics found at the Large Hadron Collider (LHC) [Eva08]. The LHC, located at the European Organization for Nuclear Research (CERN) in Geneva, Switzerland, is the world largest particle accelerator with a circumference of 27 km. The two counter rotating proton beams are accelerated to a center of mass energy of the colliding proton particles of 14 TeV that pushes the limits in terms of energy into new frontier in particle physics and opens up possibilities to find new elementary particles beyond the standard model.

The proton beams are colliding at four different interaction points, at which the four main LHC experiments are located: ALICE, ATLAS, CMS and LHCb. After the first successful LHC Run 1 between the years $2010 - 2013$ where a peak center of mass energy of 8 TeV was reached the LHC entered the phase of the 'Long Shutdown 1'. In this 2-year maintenance period the LHC and its pre-accelerators were upgraded to enable proton-proton collisions at the design center of mass energy of 14 TeV. The upgraded LHC accelerator started the Run 2 on the 5th of April in 2015 and enabled for example the discovery of a new class of particles by the LHCb experiment, know as pentaquarks [Aai15].

The two LHC proton beams consist of up to 2808 bunches separated by 25 ns, where each of the bunches contains up to 1.1×10^{11} protons per bunch at the beginning of a LHC fill. Each LHC beam stores an energy of 362 MJ, which is equivalent to a 400 t heavy train at a velocity of about 150 km/h and hence contains a huge damage potential. If the particle beam would hit solid material it would burn a hole into it. The result of 72 proton bunches with an energy of 450 GeV colliding with copper plates is shown in Fig. 1.1. The first 100 copper plates with a thickness of 2 mm each were shot through.

The loss of the entire particle beam is however unlikely. Nevertheless, even a small fraction of the particle beam could shoot through the vacuum pipe, which are integrated inside the superconducting magnets used to focus and bend the proton particle beams. A loss of vacuum would lead to a quench of the superconducting magnets in a sector, which comprises 1/8 of the 27 km long LHC tunnel. Low intensity beam loss events happen on a regular basis and are typically caused by the interaction of the proton beam with collimators, vacuum chambers or residual gas particles. A dedicated Beam Loss system (BLM) is therefore installed at the LHC accelerator consisting of ~ 4000 monitors that continuously surveys the beam condition [AG01]. In case of a beam loss event above a certain threshold, a trigger is sent to the beam abort system that dumps the LHC beam within 4 turns equal to a duration of $t_{\mathrm{dump}} \sim 360\,\mu\mathrm{s}$. The LHC BLM system covers only the accelerator complex, the beam condition measurements at the interaction points are under the responsibility of the experiments. The Beam Condition Monitor Leakage (BCML) detector, designed as well with major contribution from the Institute of Experimental Nuclear Physics at the Karlsruher Institute of Technology [Mue11, Gut14a], is measuring the beam condition at the CMS experiment. Intense beam loss

Figure 1.1: Beam loss test with 72 proton bunches at 450 GeV colldining with several 2 mm thick copper plates. The first 100 plates are destroyed by the beam loss event. Taken from [LHC16].

events measured with the BCML detector trigger the LHC beam abort system. Diamond was chosen as sensor material because of its excellent radiation hardness [Ada06] and several other unique features like a large band-gap and high charge carrier mobilities that are beneficial for the use as BCML sensor material. However, the observed radiation hardness of the diamond sensors turned out to be far below the expected one. The main objective of this thesis is a study to obtain a qualitative and quantitative understanding of this discrepancy.

The reason for this severe radiation induced signal degradation was found to be caused by the diamond polarization. The diamond polarization originates from the trapping of charge carriers in lattice defects created by radiation damage. These trapped charge carriers, acting as space charge, are strongly modifying the internal electric field in the diamond bulk and lead to a strongly increased charge carrier recombination at locally reduced electric field regions resulting in a reduced charge collection efficiency of the diamond sensor. Furthermore, it was found that the diamond polarization is rate dependent because at a high rate the trapping rate is significant compared with the detrapping rate. The rate dependent polarization leads to a reduced sensor signal in a strongly non-linear way.

The diamond polarization was studied in detail with a dedicated irradiation campaign of high quality single crystalline diamonds. The position dependent internal electric field was measured as function of radiation damage and trapping rate using the Transient Current Technique (TCT). Furthermore, the effects of the diamond polarization to the charge collection efficiency (CCE) of the sensors were regularly measured. The experimental results were used to create an effective deep trap model that takes the number of defects and the amount of space charge into account. Based on this effective defect model the diamond polarization and the accompanied loss of charge collection efficiency could be simulated with the software Silvaco TCAD [SIL16] a commercial program for simulating semiconductors. This effective defect model could predict the rate dependency of the diamond polarization and hence explain the severe signal reduction of diamond sensors operated in high particle rate environment like the BCML sensors.

The diamond based BCML detector will be exposed to a 10× increased radiation damage with the upgrade of the LHC to the 'High Luminosity LHC'. The diamond polarization would lead in such radiation intense environments to a severe signal reduction thus requiring

a frequent replacement of the diamond sensor. New sensor materials are studied in the last chapter 7 that potentially offer an increased radiation hardness compared to the currently used pCVD diamond sensors. The BCML2 sensor mechanics was furthermore upgraded to provide additional functionality and an improved maintainability allowing for an easy replacement of the sensors.

The major contributions within this thesis are:

- The operation of the BCML detector system: The BCML detector was operated the entire Run 2 and enabled a safe operation of the CMS detector. During this time period several beam loss events were measured and studied, which had different origins. One intense beam loss event, caused by an 'Unidentified Falling Object' (UFO) caused the dump of the LHC beam in order to protect the CMS detector.
- Study of the radiation induced signal degradation of diamond detectors with focus on the rate dependent diamond polarization:
  - A dedicated irradiation campaign with high quality single crystal diamond (sCVD) sensors was done. The diamond sensors were stepwise irradiated with proton or neutron particles and the rate dependent electrical field deformation was studied as function of radiation damage. Furthermore, the charge collection efficiency was investigated as function of particle rate environment and radiation damage.
  - The measurement results obtained in the diamond irradiation campaign were used to create a defect model for diamond sensors, which predicts the diamond detector performance with respect to the radiation damage, to the particle rate environment and to the electrical field at which the detector is operated.
- Upgrade studies to improve the radiation hardness of future BCML sensors and the redesign of the BCML2 sensor mechanics.

Chapter 2

The LHC and the CMS Detector

Particle colliders are one of the most important research tools in particle physics to look for new phenomena by accelerating and colliding particles at very high energies. The Large Hadron Collider (LHC) at CERN has pushed the frontiers in terms of instantaneous luminosity and center of mass energy into previously unreachable regions, which finally lead to the discovery of the Higgs Boson [Cha12]. As important as the LHC accelerator itself (see section 2.1) are the experiments located at the 4 interaction points that are measuring the collision products created by the proton proton collisions. The work presented in this thesis was done at the Compact Muon Solenoid (CMS) detector, introduced in more detail in section 2.2, under the BRIL project introduced in section 2.3.

2.1 The LHC and the CERN accelerator complex

The LHC is a synchrotron particle accelerator with a circumference of about 27 km located 45-170 m in the underground[1] in the area of Geneva crossing the border between France and Switzerland [Eva08]. Two proton beams in separated rings are accelerated to a maximum designed center of mass energy of $\sqrt{s} = 14$ TeV and collided at four different interaction points along the machine. At each interaction point (IP) one of the four detectors: CMS, ATLAS, LHCb and ALICE is located. Alternatively to proton beams, lead ions with a energy up to 2.76 TeV per nucleon are accelerated and collided.

2.1.1 The Large Hadron Collider

In contrary to the expectation of a circular accelerator the LHC is not perfectly round. It consists of bent and straight segments; latter ones are cavities for accelerating the protons in high-frequency electric fields. These cavities are cooled down to 4.5 K and work at an electrical field frequency of 400.79 MHz, transferring a energy of 2 MeV to a proton with each passing [Bou99]. The 1232 dipole magnets used to bend the particles on its circular path of radius $r = 2803.98$ m can reach a maximal magnetic field of up to 8.33 T with respect to the particle energy. This strong magnetic field, created by an electrical current of 11850 A, can only be reached in a superconducting state, hence the dipole magnets are cooled down with liquid helium to 1.9 K. A cross section of such a superconducting dipole magnet can be seen in Fig. 2.1.

Beside the cavities on the straight elements, 392 superconducting quadrupole magnets are installed to focus the beam and perform higher order corrections [Ros03]. This is in particular important close to the interaction points where the beams are squeezed to a minimal diameter

[1] The varying depth is caused by the inclination of the layer of rock on which the LHC has been built onto.

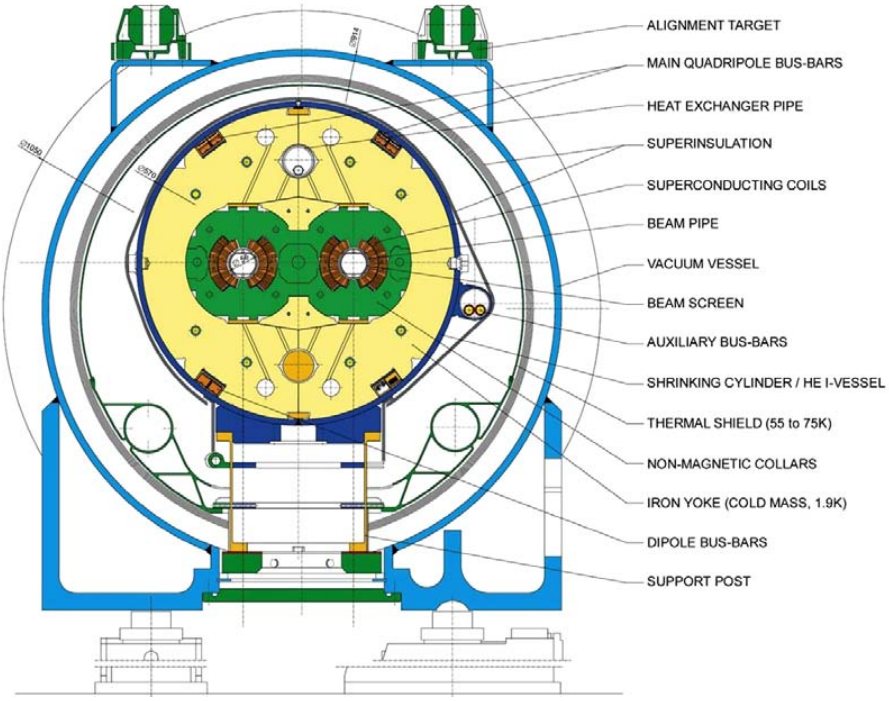

Figure 2.1: Cross section of the LHC dipole magnet [Eva08].

(16 µm) in order to reach maximal instantaneous luminosity. Besides that, further magnets for different purposes are installed in the straight sections: Beam insertion, beam correction and as well beam dumping.

In order to operate the LHC over 8000 superconducting magnets are in use.

2.1.2 Reaching stable beams: The LHC injection chain

The LHC is not capable of accelerating the particles from rest. The protons injected to the LHC ring have already an energy of 450 GeV by passing through a chain of several pre-accelerators. Hence the performance of the pre-accelerators is crucial for the beam properties of the LHC ring, like the bunch intensity or the emittance. The bunch intensity, which significantly determines the maximum LHC luminosity, is for example mostly limited at low energies and hence a challenge for the pre-accelerators.

The entire accelerator complex to reach highest proton energies is shown in Fig. 2.2. In a first the electrons are stripped off from initial hydrogen atoms to create the protons. The protons are then accelerated in the linear LINAC 2 accelerator to an energy of 50 MeV and injected to the Proton Synchroton Booster (PSB). In the PSB a proton energy of 1.4 GeV is reached and followed by the injection into the Proton Synchroton (PS) reaching there a proton energy of 26 GeV. The proton bunches are adopted in the PS to the bunch spacing of the LHC and are injected in the last pre-accelerator called the Super Proton Synchroton (SPS). In the SPS the proton particles are brought to their final injection energy for the LHC of 450 GeV. The pre-accelerator chain is slightly modified for the heavy ion runs, where LINAC2 and the PSB are replaced by the pre-accelerators LINAC3 and LEIR.
The filling time of the LHC ring depends on the amount of bunches injected, hereby a maximum of 2808 bunches is possible. Filling the LHC with $\sim$ 2000 bunches takes about $\sim$ 25 minutes. When all bunches are injected the protons are accelerated to reach the target collision energy, which takes typically up to 10 min. A standard LHC filling scheme consists

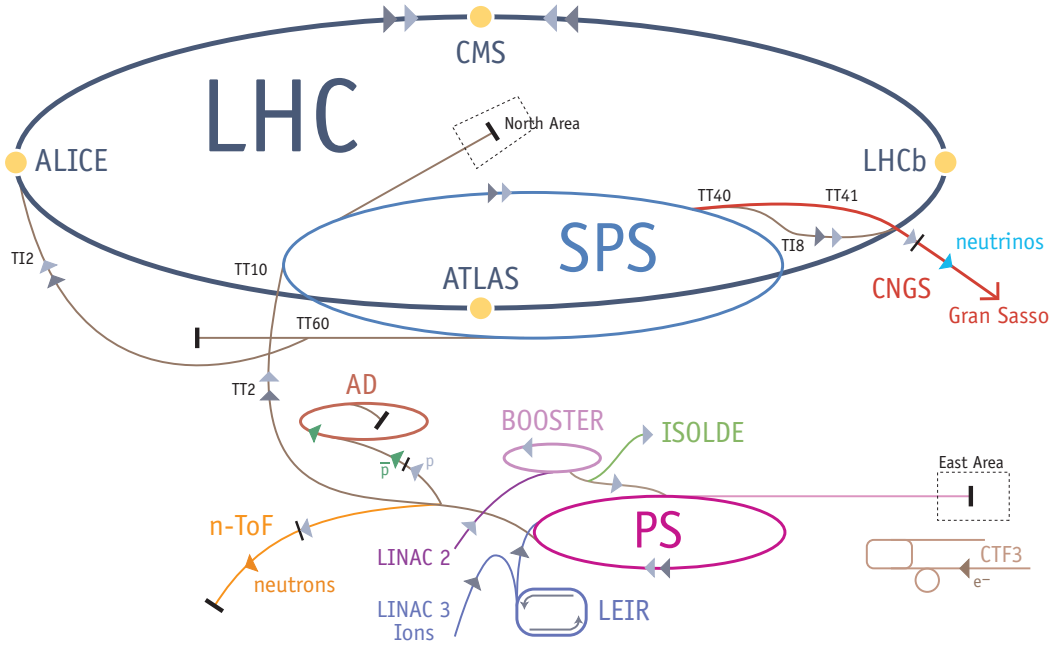

Figure 2.2: The LHC accelerator complex [CDS16].

of some single bunches and mostly bunch trains with a length up to $\sim$ 100 bunches. An animation of the filling schemes used in 2015 and 2016 can be found in [LHC16].

After having reached the maximum beam energy, called 'flat top', the beams are squeezed and adjusted to heads on collision at each interaction point to maximize the instantaneous luminosity. Finally, stable beams are declared and the experiments can take data. Due to the proton collisions, the beam intensity will continuously decrease and after the luminosity has dropped by a factor of $1/e$ the beams are dumped and the LHC is refilled again. A typical LHC fill remains $\approx$ 15 h in the machine if no beam loss event triggered the beam abort.

2.1.3 Layout of the LHC ring

The LHC ring is shaped as an octagon, consisting of eight arcs and eight long straight sections, shown schematically in Fig. 2.3. This subdivision into eight parts is also reflected in the naming of the interaction points (IP), at which the experiments are located. Every LHC octant has a unique task to achieve in order to have a stable and clean particle beam in the LHC ring. The beams are injected in the Octants 2 and 8 and passing after the first interaction point a cleaning section in Octant 3 and 7, which is done by a collimator system. The collimators absorb beam halo particles with a large offset to the central beam position that could otherwise hit the superconducting magnet and cause a quench. The particles are accelerated in Octant 4 where the RF cavities and other beam instrumentation of the LHC are located. When the intensity of the colliding beams has been significantly reduced and the LHC has to be refilled again, the beam are dumped in Octant 6 by guiding the beam into a 7 m long, $\sim$ 900 t heavy steel coated graphite block acting as beam dump system.

The four main experiments sitting at the four IPs are described in short below:

- ATLAS (IP1) is one of the two multi-purpose detectors at the LHC, designed to take a peak luminosity of $\mathcal{L}_{\text{inst.}} = 1\times10^{34}\,\text{cm}^{-2}\text{s}^{-1}$. The ATLAS experiment [ATL08] measures precisely the standard model (SM) and searches as well for new physics.

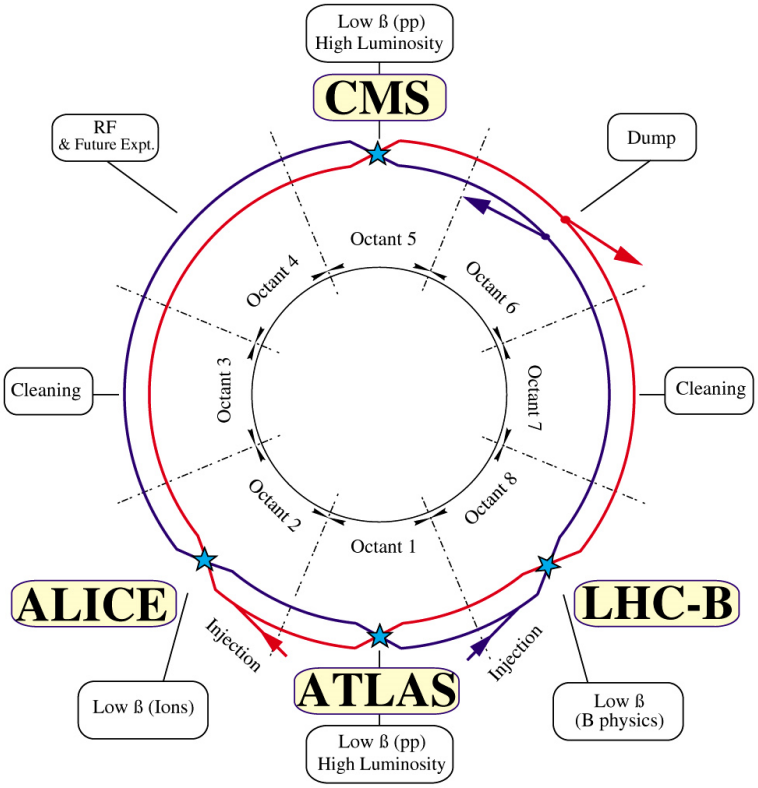

Figure 2.3: Layout of the LHC and location of the four experiments. Beam 1 shown in red is circulating clockwise and Beam 2 in blue in the opposite direction.

- ALICE (IP2) is a dedicated heavy ion experiment, investigating the quark-gluon plasma that was created shortly after the Big Bang [ALI08].
- CMS (IP5) is the second multi-purpose detector at the LHC that discovered together with ATLAS the 125 GeV boson in 2012 [CMS12, ATL12]. Besides measuring precisely the SM, CMS is as well searching for new physics [CMS08] and will be described in more details in section 2.2.
- LHCb (IP8) is specialized in B-physics, investigating CP violation and exotic BSM phenomena [LHC08a].

At the LHC ring are as well smaller experiments with highly specialized research topics located, sometimes in direct neighborhood to the large experiments. The **LHCf** experiment near the ATLAS detector is looking for neutral particles emerging from a pp collision into the very forward region [LHC08b]. The **TOTEM** detector investigates the total pp cross section and studies diffractive and elastic scattering. TOTEM consists of two detector units, whereby one, TOTEM T2, is fully integrated inside the CMS detector [TOT08].

2.1.4 LHC operation between 2010 and 2016

The LHC started regular operation in the year 2010 with a center of mass energy of $\sqrt{s} = 7\,\text{TeV}$, which could be increased in 2012 to $\sqrt{s} = 8\,\text{TeV}$ and reached a preliminary maximum of $\sqrt{s} = 13\,\text{TeV}$ in 2015. During that time period a total integrated luminosity of $\mathcal{L}_{\text{int.}} = 33.6\,\text{fb}^{-1}$ could be collected. Besides increasing the center of mass energy, the instantaneous luminosity was increased to collect collision data at an increased rate. This was reached by e.g. reducing the amplitude function β^* from 350 cm (2010) to 60 cm (2012) and reached

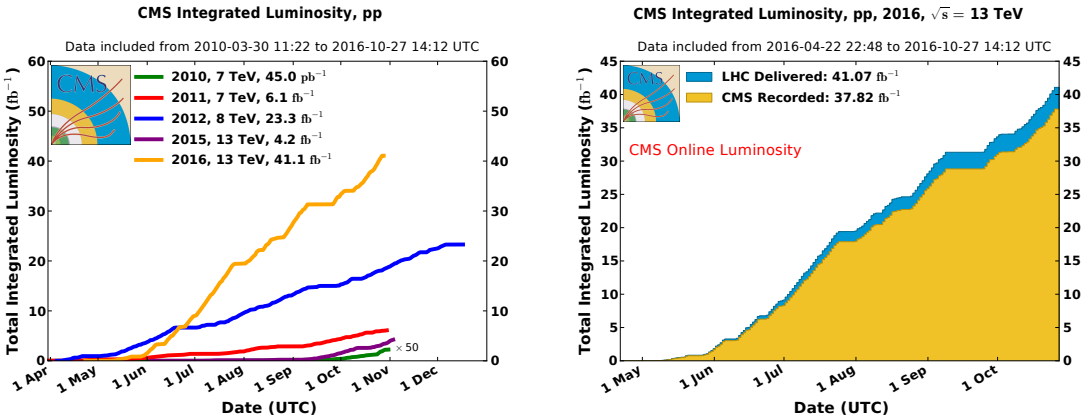

Figure 2.4: Left: The cumulative luminosity delivered to CMS in the years 2010 (green), 2011 (red), 2012 (blue), 2015 (purple) and 2016 (orange) for pp collisions. Right: The delivered (blue) and recorded (orange) total integrated luminosity versus day in 2016, with a mean data taking efficiency of 92.1 %. Plots are taken from [CMS16].

the current minimum of 40 cm in 2016. An increase in the instantaneous luminosity was reached as well by a reduction of the bunch spacing from initially 150 ns (2010) to 25 ns in 2015. This increased the amount of bunches per beam and hence increased the instantaneous luminosity. In 2016 a maximum instantaneous luminosity of $1.53 \times 10^{34}\,\mathrm{cm}^{-2}\mathrm{s}^{-1}$ was reached that is already $\sim 50\%$ above the design value. The yearly data-taking rate can be seen in Fig. 2.4, which shows a steeper slope in integrated luminosity for each year of LHC operation. In 2016 a total integrated luminosity of $\mathcal{L}_{\mathrm{int.}} = 37.8\,\mathrm{fb}^{-1}$ was collected with an data taking efficiency of 92.1%. This value is not at 100%, because of downtime of various detectors, or by a delayed data taking of CMS after the declaration of stable beams from the LHC.

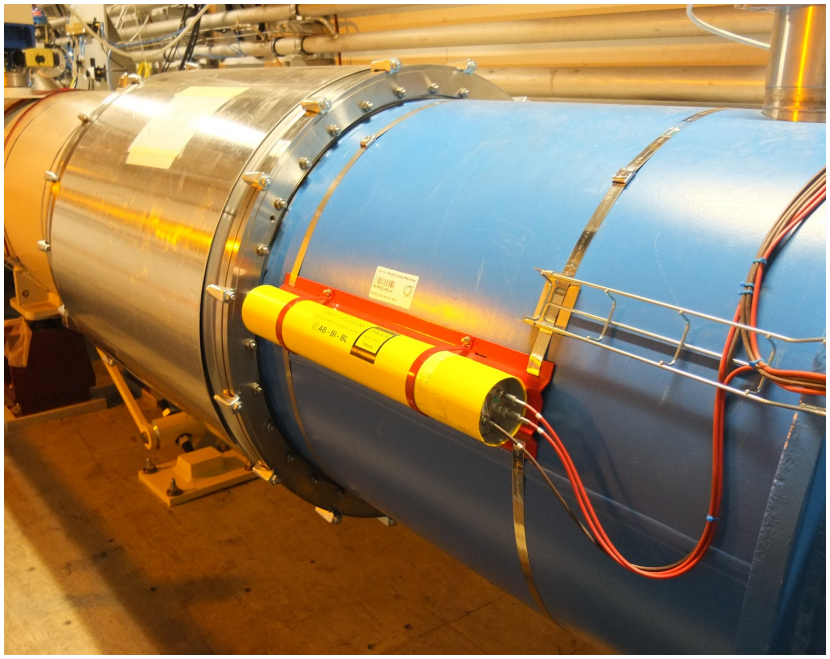

Figure 2.5: A beam loss monitor (yellow) mounted at the LHC pipe (blue) next to a dipole magnet (silver). Picture taken from [Gut14a].

2.1.5 The LHC Beam Loss Monitoring (BLM) system

The BLM system at the LHC consists of $\sim$ 4000 ionization chambers surveying the beam conditions at all quadrupole magnets and as well at several other locations [Deh09]. Ionization chambers have a long history in the detection of ionizing particles, especially for the purpose of radiation dosimetry. The first idea of using ionization chamber was proposed already in 1908 by Paul Villard [Bud98]. Since then the ionization chambers became a principle method of precision measurements and radiation measurements. An ionization chamber consists of a gas-filled volume in which two electrodes apply a high electrical field. An ionizing particle passing through the gas volume is knocking off electrons out of the atomic shell. These free charge carriers created by the ionizing particle are accelerated through the electrical field towards an electrode. This charge carrier drift induces a signal in the electrical read out. Ionization chambers are very reliable and radiation hard detectors and are operated at low electrical fields to prevent charge multiplication through the gas.

The main purpose of the BLM system is to protect the superconducting magnet against quenches or damages caused by beam loss events. This is achieved by dumping the LHC beam when measuring beam losses exceeding predefined thresholds. Such a 1 m long yellow BLM tube can be seen in Fig. 2.5.

At the location of the LHC experiments no BLM tubes are installed, because the responsibility of measuring the beam condition is handed over to the experiment itself. At the CMS experiment, this extension of the LHC BLM system is the CMS BCML system that will be introduces in section 4.

2.2 The Compact Muon Solenoid (CMS) experiment

The entire section describing the Compact Muon Solenoid (CMS) is based on [CMS08, CMS06, CMS07]. The CMS experiment is one of the two general-purpose experiments at the LHC studying the standard model and searching as well for new physics. The experiment in Octant 5 is located 100 m in the underground in Cessy, France.

The CMS experiment has a cylindrical shape that is symmetrical around the interaction point (IP). Disk shaped detectors units, called end-caps, close both ends of the detector. A sketch of CMS can be seen in Fig. 2.6 showing in comparison to the person the huge dimension of the entire detector volume with a barrel diameter of 15.0 m and a length of 28.7 m. The CMS experiment consists of several subdetectors, where each detector has a unique purpose in order to gain an optimal particle identification of the collision products, see Fig. 2.7. In the following sections the most important subdetectors are introduces, starting however with the most important hardware: the superconducting solenoid magnet.

2.2.1 The CMS magnet

The superconducting solenoid is the heart of the CMS experiment, without it particle identification would not be possible. The solenoid shape of the magnet is creating a uniform magnetic field parallel to the beam pipe bending the particles on a helical path inside the magnet. The magnet is embedded in a 12500 t iron return yoke guiding the magnetic field back in the opposite direction. The coil is made of superconducting niobium-titanium with a diameter of 7 m and a length of 13 m and is designed to reach a magnetic field of 4 T, operated however at 3.8 T. To reach such a strong magnetic field a current of $\sim$ 20. 000 A is needed, which is only possible in the superconducting state by cooling down the magnet to 4.5 K. Besides the CMS tracker, the calorimeter is located as well inside the magnet volume to measure the collision products with a high energy resolution, compare Fig. 2.7.

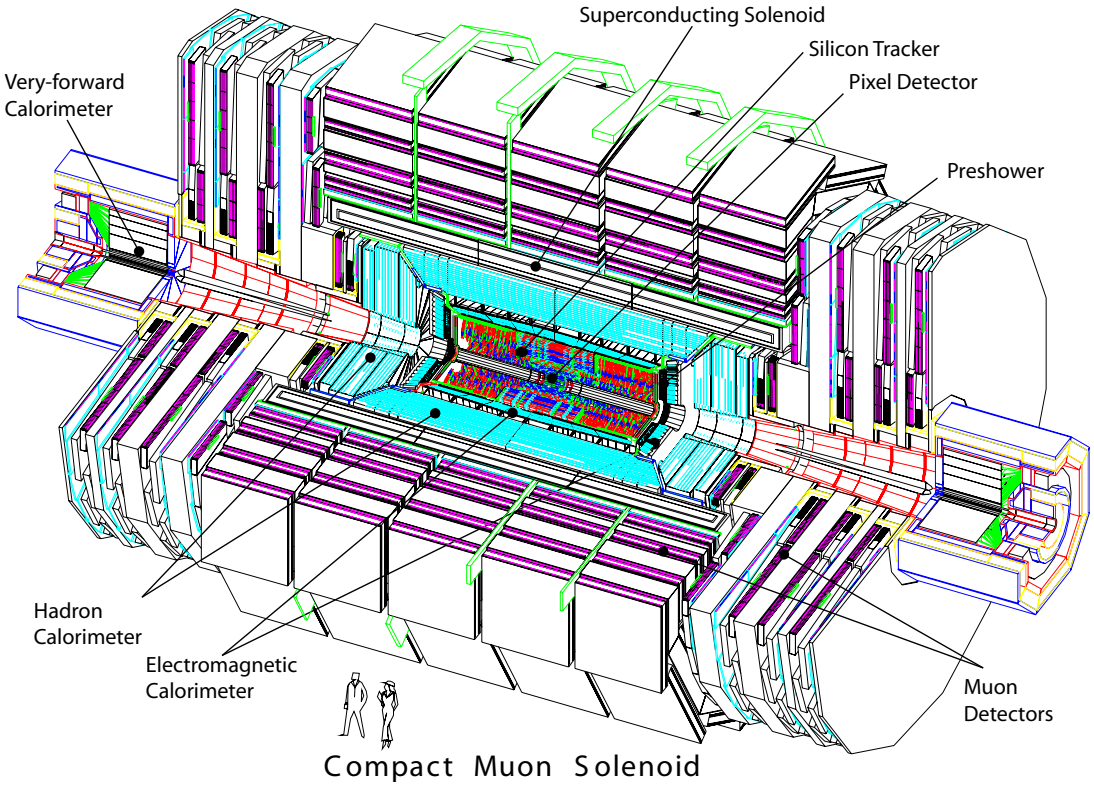

Figure 2.6: A sketch of the CMS experiment, consisting of its subdetectors [CMS08]. Comparing the size of the detector with the two persons gives a feeling of the size of the CMS experiment.

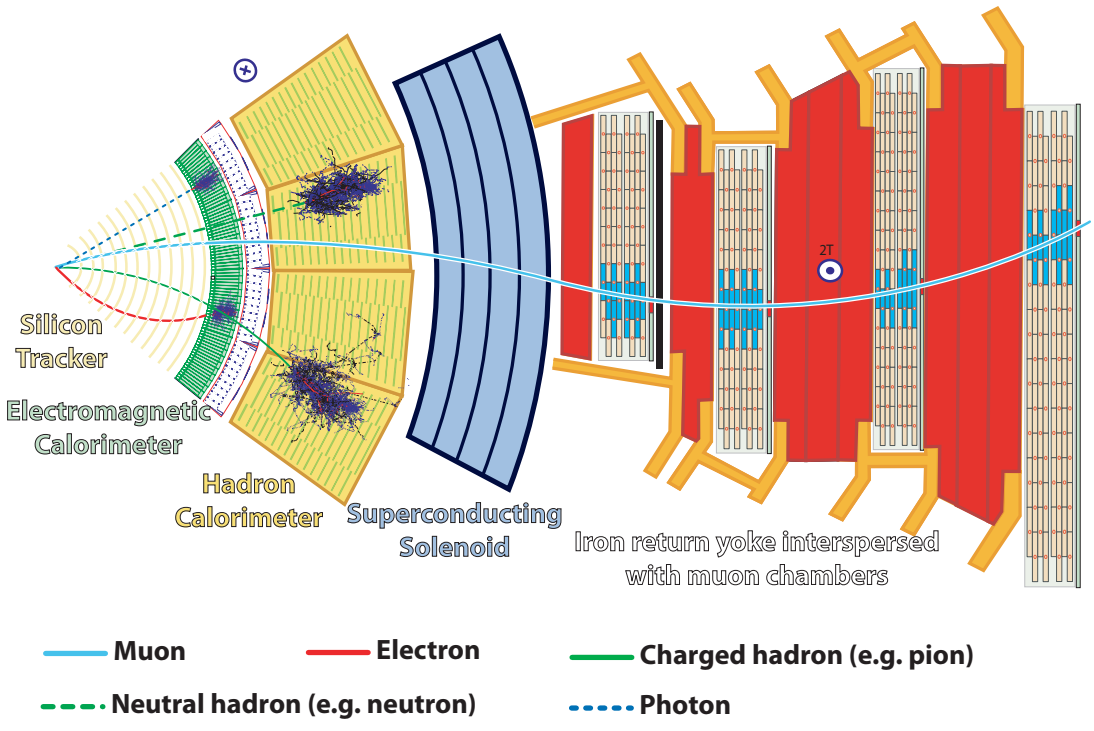

Figure 2.7: Transverse slice of the CMS detector, showing the tracks of different types of particles [Bar11].

2.2.2 Silicon tracker

The CMS tracking system consists of an inner and an outer part. The inner vertex detector, a silicon pixel detector, consists of 3 barrel layers with a minimum radius of 4.4 cm and measures the origin of every charged particle. The pixel tracking system is covering in total a pseudo-rapidity region up to $\eta = 2.4$ with a total amount of 66 million pixels. The pixel have an active surface of typically $100 \times 150\,\mu m^2$ with a thickness of 285 µm. The most inner pixel layer has to withstand severe radiation damage, since it is exposed to large particle fluxes with highly energetic particles.
The outer part of the tracker consists of silicon strip sensors, which further track the bent path of the charged particle in the magnetic field. It consists of 9.6 million sensors with an active area of $\sim 200\,m^2$.

2.2.3 Electromagnetic calorimeter

The next detector unit emerging particle are entering is the electromagnetic calorimeter (ECAL). It consists of 76000 scintillators made of lead tungstate ($PbWO_4$) crystals with a density of $\rho = 8.28\,g/cm^3$ forcing a short radiation length[2] of $X_0 = 0.89\,cm$. The ECAL detector is measuring the energy of electrons and photons with high precision and is covering a pseudo-rapidity of up to $\eta = 3$. An accurate energy measurement of the electron and photons is in particular important to analyze the Higgs boson decay channels: $H \to \gamma\gamma$, $H \to ZZ$ or $H \to WW$.
The ECAL consists of a barrel and an end-cap component with a minimum thickness of 22 cm corresponding to 24.7 radiation lengths, hence stopping almost all electrons or photons.

2.2.4 Hadronic calorimeter

More heavy particles made of quarks, like protons, neutrons or pions, passing through the ECAL are finally stopped and measured in terms of energy in the hadronic calorimeter (HCAL). In contrast to the ECAL where the same material for absorption and scintillation is used, the HCAL is designed as a sampling calorimeter, alternating between absorbing and scintillating material. As absorbing material brass is mainly used that stops as well heavier particles. The HCAL is composed of a barrel and an end-cap detector covering a pseudo-rapidity of up to $\eta = 3$. In addition the very-forward calorimeter (HF) at $Z = \pm 11.15\,m$ is covering a pseudo-rapidity of up to $\eta = 5$.

2.2.5 The Muon system

The muons are the only particle expected to pass all calorimeters without being stopped. This is caused by their large rest mass, 200 times heavier than electrons, leading to an insignificant loss of energy via bremsstrahlung. Besides that, muons interact just minimally with the detector materials ionizing hardly atoms. The muon detectors are therefore located outside of the solenoid magnet and are consisting of 1400 muon chambers: 250 drift tube chambers (DTC), 540 cathode strip chambers (CSCs) and 610 resistive plate chambers (RPCs) [CMS13].

2.2.6 The Trigger system

The nominal LHC bunch spacing of 25 ns translates into a collision rate of 40 MHz. Given the amount of 1 megabyte of raw data for a full read out of CMS, recording of all events is

[2] The length at which the energy of an electron traversing the material has dropped to E_0/e due to radiation.

just not possible by the total data size that would translate to 40 terabytes per second. A two-level trigger system is therefore used initiating a full CMS read-out, if certain criteria are full filled.
The Level-1 trigger (L1T) is the first stage reducing the data rate from 40 MHz to approximately 30 kHz. The L1T decision is based on the input from different subsystem, in particular the calorimeter, the muon detectors or different technical triggers. During the L1T decision for a global CMS readout, which takes $3.2\,\mu s$, the data of the subdetectors is written in a buffer and can be read out in case of a positive L1T decision. A further reduction of the data rate is achieved by the high-level trigger (HLT). The HLT is a software selection of events based on dedicated algorithm using a computer cluster consisting of approximately 1000 CPUs. This leads to a final data rate of about 100 Hz translating in a data rate of about 100 MB/s used for the full physics analysis.

2.3 The Beam Radiation Instrumentation and Luminosity project (BRIL)

The work presented in this thesis was done within the Beam Radiation Instrumentation and Luminosity (BRIL) project at CMS [Gut16]. The responsibility of the BRIL project covers the luminosity measurement, monitoring of machine induced background and as well simulations of the radiation levels at the CMS detector. These different goals are achieved with a variety of detectors, operating independently of the central CMS data acquisition. The work presented in this thesis is focusing on the performance of the BCML detector, measuring the beam condition, hence all BRIL detectors dedicated for the CMS beam monitoring are described in the following. Furthermore, the BRIL detectors measuring the luminosity are briefly introduced, since this key measurement is important for the normalization of the BCML detector signal and for the estimation of the total radiation damage.

2.3.1 Beam background measurements

2.3.1.1 Fast Beam Condition Monitor (BCM1F)

The BCM1F system is a particle counter that uses a fast timing to discriminate machine induced background (MIB) from luminosity products. The BCM1F detector is therefore strategically placed at $Z = \pm 1.8\,m$, a so called 'golden location', where incoming MIB particles and outgoing luminosity products are maximal separated in time by 12.5 ns. The detector is based on 24 single-crystalline diamond detectors, read out by a dedicated fast ASIC in 130 nm technology. The electrical signal is transmitted optically to the back-end electronics using an analog optohybrid. The BCM1F signals are discriminated and histogrammed as function of time with 4 bins per bunch crossing. In addition the BCM1F signals can also be read out with an analog to digital converter to sample and analyze the signal shapes. Details can be found in [Bel10].

2.3.1.2 Beam Halo Monitor (BHM)

The BHM detector provides an online, bunch-by-bunch measurement of machine induced background particles [Orf15]. In order to separate the MIB from the collision products the 20 BHM detectors per side are sitting at an 'golden location' at $Z = \pm 20.65\,m$, on top of the CMS forward shielding. At his location only muon particles are measured, the so called muon halo. The BHM detector is based on the measurement of Cherenkov light created by the particles passing through a quartz bar. The photomultiplier, mounted in an magnetic

shielding, is only sensitive to light emitted in one direction, and hence can assign a beam loss to a certain beam direction.

2.3.1.3 Beam Condition Monitor 'Leakage' (BCML)

The BCML system is an active beam protection device, using $1 \times 1\,\mathrm{cm}^2$, 400 µm thick polycrystalline diamonds. In case of a catastrophic beam loss event the BCML system triggers the LHC beam abort leading to a beam dump within 300 µs in order to prevent further damage to the CMS tracker.
The 32 BCML diamond sensors are located at $Z = \pm 1.8\,\mathrm{m}$ (BCML1) and $Z = \pm 14.4\,\mathrm{m}$ (BCML2) away from the interaction point at a radius of 4.5 cm. The back-end electronic is identical to the LHC Beam Loss Monitoring (BLM) readout system measuring the ionization current of the diamond sensors from beam losses leaking outside the beam pipe, e.g. by scattering on the residual gas or beam collimators. The BCML system is therefore a transparent extension of the LHC BLM system at the CMS detector. This detector system is the base of the data analyzed in chapter 4 and 5 and will therefore be described in more detail later.

2.3.2 Measurement of the Luminosity

The luminosity is a key parameter in collider experiments as it describes the rate of particle collisions per area. Its precise measurement is necessary to determine the cross sections of particle interactions. The luminosity is calculated via:

$$\mathcal{L} = \frac{N_1 N_2 f n_\mathrm{b}}{4\pi\sigma_\mathrm{x}\sigma_\mathrm{y}}, \tag{2.1}$$

for two Gaussian beam profiles colliding head on. N_1 and N_2 are the number of bunches per beam 1 and beam 2, respectively. The number of protons per bunch is given by n_b, the revolution frequency as f and the cross section for each beam with σ_x and σ_y. In real particle colliders the beam shapes are however not perfectly Gaussian shaped, and the cross section of $\sigma_\mathrm{x} \cdot \sigma_\mathrm{y}$ is calculated based on the beam parameters β^* as amplitude function and ϵ_n as emittance of the particle beam, further details can be found in [Her03]. Beside the measurement of the instantaneous luminosity, the dose load to the detector components can be inferred from the integrated luminosity.

BRIL provides the luminosity measurement at the CMS detector based on three luminometers: the Pixel Luminosity Telescope (PLT), the Fast Beam Conditions Monitor (BCM1F) and a dedicated readout of the Hadron Forward (HF) Calorimeter to calculated the luminosity [Dab16].

2.3.2.1 The Pixel Luminosity Telescope (PLT)

The Silicon Pixel Luminosity Telescope (PLT) is a dedicated luminometer monitor for CMS based on 16 tracking telescopes placed at $Z = \pm 1.8\,\mathrm{m}$ from the interaction point with a radius of $r \sim 5\,\mathrm{cm}$. Each telescope consists of 3 planes of silicon pixel detectors bump bonded to the PSI46v2 CMS pixel read- out chip (ROC) [Bar04]. Threefold coincidences of a fast cluster counting (Fast-OR) are used to calculate the luminosity per colliding bunch, further details can be found in [Gut16].

2.3.2.2 BCM1F as luminometer

The BCM1F detector described in the previous section allows to discriminate the beam background and the luminosity products by a fast read out of approximately 6.25 ns per bin. For each bin the measured MIP signals are counted in a real-time histrogramming unit (RHU). Based on the dead-time free RHU measurements the instantaneous luminosity is calculated in real time.

2.3.2.3 HF as luminometer

A secondary readout chain was included in the CMS hadron forward calorimeter (HF) for luminosity measurements. This readout provides a dead-time free readout, independent of the CMS DAQ, and the calculation of the luminosity per colliding bunch.

2.3.3 Beam Position for Timing at the Experiments (BPTX)

The BPTX system is based on the LHC beam position detector, however used to measure the exact timing of the incoming particle bunches. This information is used to calculate the time difference between the two beams, $\Delta T(B1 - B2)$ and the phase between the beams and the CMS clock. Besides that, the BPTX signal is used to compute various technical triggers and is as well an important feedback for the LHC.
The BPTX detectors are located 175 m upstream of the interaction point and are read out by a 5 GS oscilloscope.

Chapter 3

Principles of particle detection using solid state detectors

In the following chapter the theoretical background of solid state detectors with the focus on diamond detectors will be given. The basic interaction processes between different particle types and matter are discussed in section 3.1. In section 3.3 diamond based particle detectors will be introduced.

3.1 Particle Interaction with matter

High energetic particles created by the proton-proton collision at the CMS interaction point are interacting with the matter of the particle detectors in different ways. Photons for example are interacting via various interaction processes with the atomic shells or the nuclei. Charged particles interact almost entirely via ionization with matter and neutron particles only with the nuclei. In the following sections the physics of these processes will be introduced with the focus of ionization, since this is the dominating process creating signals in particle detectors.

3.1.1 Charged particles interaction

Charged particles are loosing their energy when passing through matter via inelastic scattering with the atomic electrons that leads to the ionization of the material. The energy loss is related to the particle energy and charge of the penetrating particle and as well related to the target material itself. The energy loss can be calculated using the Bethe-Bloch equation:

$$-\frac{dE}{dx} = \frac{n_e z^2 e^4}{4\pi\epsilon_0^2 m_e c^2 \beta^2} \cdot \left[\ln\left(\frac{2m_e c^2\beta^2}{\langle E_b\rangle \cdot (1-\beta^2)}\right) - \beta^2\right], \tag{3.1}$$

with n_e as the electron density, z as the charge number of the penetrating particle, e the elementary charge, ϵ_0 the vacuum permittivity, c the speed of light in vacuum, $\langle E_b\rangle$ the mean excitation energy of the target material and $\beta = v/c$, where v is the speed of the penetrating particle.
The ionization energy loss as function of particle energy is shown in Fig. 3.1 for an electron. At non-relativistic energies the ionization energy loss shows a $1/\beta^2$ energy dependence. For increased particle energies in the relativistic regime, the ionization energy loss is growing with respect to the particle energy. Hence at a certain particle energy the ionization energy loss has a local minimum. A particle of that energy is called a 'minimum ionizing particle' (MIP), which is important for the characterization of the detector performance in terms of charge collection efficiency. The MIP energy of an electron for diamond material is $E_{\mathrm{MIP}} = 1.6\,\mathrm{MeV}$

compared to a MIP energy for silicon material of $E_{\mathrm{MIP}} = 1.3\,\mathrm{MeV}$ [Kuz07].
For light particles like electrons, radiative energy losses e.g. due to bremstrahlung are becoming more important with increased particle energies. Above electron energies of 90 MeV radiative energy losses are dominating the energy loss of electrons in matter.

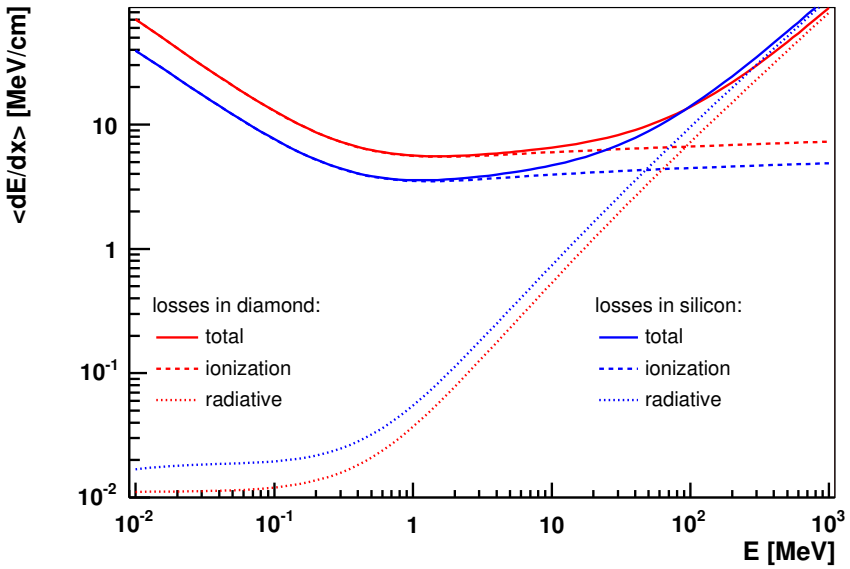

Figure 3.1: Energy loss of electrons in diamond (red) and silicon (blue). Above an electron energy of 90 MeV radiative energy losses are dominating the total energy loss of electrons in matter.

3.1.2 Neutrons interaction

Since the neutron is electrically neutral it dominantly interacts with the nucleus and therefore interacts only weak with matter and can penetrate the material deeply. Theoretically neutrons can also interact via its magnetic dipole moment with electrons, which however is strongly suppressed. Beside the very weak interaction of neutrons with matter, it causes significant radiation damage since the neutron interaction causes nuclear recoils and different other nuclear transmutations. The neutron particles will transverse matter on a straight line till it interacts with a nucleus and induces a nuclear reaction.

3.1.3 Photon interaction

The photon interaction with matter can be differentiated into the following six categories:

- Elastic Scattering: Coherent or Rayleigh scattering describes the interaction of photons with an orbital electron by a momentum transfer. The energy of the photon remains constant.
- Photoelectric Effect: The photon transfers all of its energy to an orbital electron, which is ejected and released from the atom.
- Inelastic Scattering: Is an important ionization process where the photon scatters at an orbital electron and transmits energy. The inelastic scattering (Compton Scattering) is the dominant process for photon interaction with matter at energies between 100 keV and 10 MeV.

- Pair Production: Photons above an energy of 1 MeV can create a electron - positron pair in the close presence of a nucleus. A nucleus is needed for the conservation of the momentum, taking up the momentum of the photon. Pair production is the dominant process for photon energies above 100 MeV.
- Triplet Production: Is a special case of the pair production that includes in addition an orbital electron receiving as well an energy transfer to be ionized. The minimum photon energy for this interaction is 2 MeV.
- Photodisintegration: Describes the uncommon absorption of a photon in a nucleus. The absorbed photon causes the release of a proton and neutron from the nuclei. This interaction is possible for photons above an energy of 10 MeV.

Photons typically depose their energy indirectly by the creation of charged particles, which depose their energy via ionization.

3.2 Selection of Materials used for Solid-State Particle Detectors

Particle detectors, used to detect, track or identify high-energy particles, are typically composed of a sensitive volume and an amplification stage. An ionizing particle crossing the sensitive volumes creates charge carriers that are read out and amplified to a measurable signal in the amplification stage. In solid-state detectors the sensitive volume is characterized by a low intrinsic charge carrier density. In case of a narrow band gap semiconductor like silicon, a PN-junction has to be formed to create a sensitive volume with a low carrier density. Diamond as a wide-band gap semiconductor has intrinsically a low charge carrier density. The sensitive volume is therefore identical to the diamond geometry.

3.2.1 Silicon

Silicon is the standard material for vertex and tracking detectors at high energy particle physics experiments, also because of the rise of the semiconductor industry making the production of high quality silicon material possible. Silicon based particle detectors are diodes with a PN-junction typically reversed biased in order to create a depleted, charge carrier free zone within the detector. With a moderate band gap of 1.12 eV silicon can be as well operated at room temperature, since thermal energy reaches at $T = 300\,\mathrm{K}$ only $k_B T = 1/40\,\mathrm{eV}$. The creation energy of electron-hole pairs is 3.6 eV, which means that a minimum ionizing particle is creating per µm of silicon thickness 80 electron-hole pairs.
Radiation induced defects cause in silicon however a reduction of the depleted volume inside the sensor. Therefore the bias voltage needs to be increased which causes an increase in the dark current. In order to reduce the dark current and create a charge carrier free zone the silicon sensors at the CMS detector are therefore operated at lower temperatures, at $\mathrm{T} = -15\,^{\circ}\mathrm{C}$.

3.2.2 Diamond

Diamond detectors are typically used as beam monitors at location where high radiation damage is expected and silicon sensors are no option. Furthermore, tracking devices based on pixelated diamond sensors where considered to be used at the CMS detector for luminosity measurements [HW11]. A detailed description of diamonds sensors can be found in the next section, see 3.3.

3.2.3 Sapphire

In contrast to the expensive diamond detectors a low cost alternative could be sapphire based sensors. Optical grade single crystal sapphire produced industrially via the Czochralski process are used e.g. for shatter resistant windows or as display windows for smartphones. Hence sapphire is available at high volume, low cost and in any size.
Sapphire, chemically an aluminum oxide Al_2O_3, can be considered, similar to diamond, as a wide band gap semiconductor, with a band gap of 9.9 eV. First measurements indicate a very high tolerance against radiation damage [Sch10], however at a low charge collection efficiency of CCE $\sim 10\,\%$ [Kar15].

3.3 Diamond based Solid-State Particle Detectors

The main focus of this work is the investigation of the radiation induced signal degradation of diamond based particle detectors. Therefore, the intrinsic and physical properties of diamond as material and as particle detector will be explained in detail in this section.

3.3.1 Physical Properties of Diamond

The word *diamond* has its root in the Greek word *adámas* meaning 'proper', 'unalterable' or 'unbreakable', showing already the uniqueness of this material. Diamond combines several extraordinary material properties like its supreme hardness, high thermal conductivity, chemical inertness and singular strength. Hence diamond is not just attractive for jewelry products but as well interesting for scientific and technological interest worldwide. The demand for diamond as a high-end material was further stimulated by the development, in the late 1980s, of the 'Chemical Vapor Deposition' (CVD) technique making the artificial production of high quality diamonds possible [Spe94].
At the end of this section an overview of the physical parameters of diamond compared to silicon and sapphire is given, see Table 3.1.

3.3.1.1 The Carbon Atom

The most common carbon isotope, ${}^{12}_{6}C$, consists of six protons, neutrons and electrons. It has an electron configuration of $1s^2 2s^2 2p^2$ and is therefore bivalent, hence only the outer shell

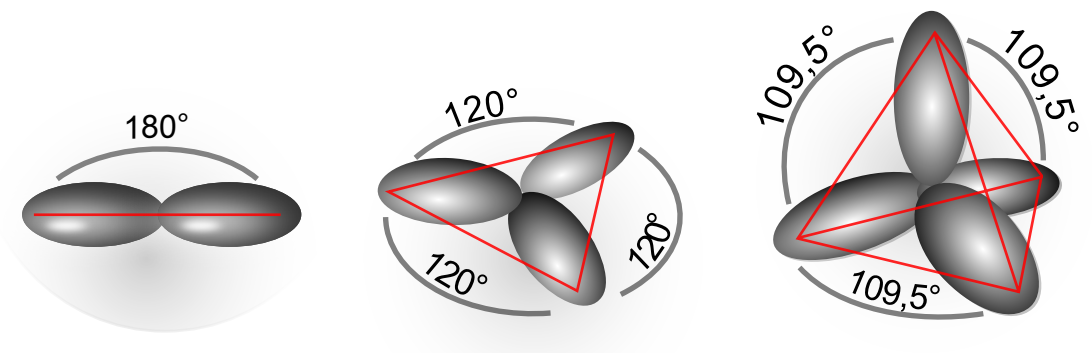

(a) *sp*-hybrid **(b)** sp^2-hybrid **(c)** sp^3-hybrid

Figure 3.2: Schematic representation of the three different hybridizations of the carbon orbitals. Figures taken from [Wikc].

contributes in forming bonds. In the outer L-shell are two electrons in the s-orbital and two electrons in the p-orbital. These orbitals can't form molecular bonds directly, but as a linear combination of the orbitals, called hybridization, molecular bonds are possible. For carbon 3 different configuration of the orbitals are possible, called *sp*-, sp^2- or sp^3-hybridization.

***sp*-hybridization:**
In the most simplest *sp*-configuration only one *p*-orbital is forming a hybridization with one *s*-orbital. This results in two *sp*-orbitals that are opposed to each other with an angle of 180° as shown in Fig. 3.2a. Bonds with this configuration form long chain molecules, e.g. acetylene.

***sp*^{2}-hybridization:**
In the sp^2-configuration two of the three *p*-orbital are hybridizing with the *s*-orbital, leading to three equal *sp*-orbitals that are oriented flat with an angle between each other of 120°. Bonds with this carbon configuration, shown in Fig. 3.2b, are typically graphite lattices, which is the most stable form of carbon under standard conditions.

***sp*^{3}-hybridization:**
The diamond lattice structure is formed in the sp^3-hybridization. Here all three *p*-orbital are hybridizing with the one *s*-orbital leading to four equal sp^3-orbitals. The geometrical form of these sp^3-orbitals, shown in Fig. 3.2c, is tetrahedral with an angle of $109.5°$ between all sp^3-orbitals. This tetrahedral structure of the bonds explains the superb properties of diamonds like its hardness and as well its equal strength in all directions.

The different hybridization of the carbon explains properties like the conductivity or the transparency. In the graphite sp^2-hybridization one electron is not bound into bonds and hence is free to flow and leads to conductivity. The same free electron can absorb photons, hence resulting in the black color of graphite. In the sp^3-hybridization for diamond all electrons from the L-shell are locked into bounds and can't flow, explaining its low electrical conductivity. The missing free electron to interact with photons explains as well the transparency of diamond.

3.3.1.2 Diamond Lattice

The sp^3-hybridization of the carbon in diamond forms a face-centered cubic (FCC) Bravais lattice with a basis of two carbon atoms. The two basis atoms at each lattice point are located at (0,0,0) and $(\frac{1}{4},\frac{1}{4},\frac{1}{4})$. The diamond FCC Bravais lattice, shown in Fig. 3.3, has a side length of the cubic unit cell of $a = 3.567$ Å. Many other semiconductor, like gallium arsenide or indium antimonide, share the same so called *zincblende lattice structure*, however with a nearest neighbor of an other element.

3.3.1.3 Electrical Band Structure

The electronic band structure describes the range of possible and forbidden energy states an electron within the solid can have. With the concept of the electronic band structure four main characteristics of the solid state material can be understood and explained: the electric conductivity, thermal properties like heat capacity and heat conductivity, optical properties like absorption and emission spectra and as well the effective mass of the charge carriers.

By solving Schrödinger's equation, the energy band can be calculated:

$$\left[-\frac{\hbar^2}{2m}\Delta^2 + V(\vec{r})\right]\Phi_k(\vec{r}) = E_k\Phi_k(\vec{r}) \tag{3.2}$$

for a single electron problem. Given a theoretical perfect crystal structure with a lattice periodicity, and therefore with a periodic potential energy $V(\vec{r})$, the Schrödinger equation can be solved using Bloch's theorem. The solution is a basis of wavefunctions, where each wavefunction is an energy eigenstate:

$$\Phi_k(\vec{r}) = e^{i\vec{k}\vec{r}} U_n(\vec{k},\vec{r}) \tag{3.3}$$

where $\vec{r}$ is the position, Φ_k is the Bloch wave, $\vec{k}$ is the crystal wave vector, U_n is the periodic function with the same periodicity as the crystal and with n as index of the band. The electrical band structure of diamond crystal was calculated using the empirical pseudo potential method (EPM) [Phi58, Coh66] by [Sas66] and is shown in Fig. 3.4. At the center of the first Brillouin zone Γ (0,0,0), the valence band has its highest energy, called the valence band maximum (VBM). The lowest energy of the conduction band is localized at (0.77,0,0) called conduction band minimum (CBM). Since the VBM and CBM are not located at the same position, diamond is an indirect semiconductor with a band gap of 5.47 eV at 300 K. This large band gap causes the diamond to be classified as a wide-band gap semiconductor or even an insulator. For comparison silicon as a semiconductor has a band gap of 1.12 eV.

3.3.1.4 Electrical and Thermal Properties of Diamond

Diamond offers unique electrical properties, which are advantageous over alternative materials.

Carrier Mobility and Saturation Velocity

In terms of charge carrier mobility, diamond exhibits the highest electron and hole mobility at room temperature of any wide-band gap semiconductor. In intrinsic single crystalline CVD diamond, mobilities for electrons and holes of about $4500\,\mathrm{cm^2V^{-1}s^{-1}}$ and $3800\,\mathrm{cm^2V^{-1}s^{-1}}$ respectively, have been measured [Isb02]. This high drift velocity of the charge carriers at 300 K offers the possibility to build very fast particle detection devices. At very high electrical field the saturation drift velocity is determined by the generation of optical phonons in the crystal lattice. In diamond the optical phonons reach the highest energy of $E_{\mathrm{opt}} = 0.16\,\mathrm{eV}$ compared to any semiconductor [Wat04], leading to one of the highest saturation drift velocities of $v_{\mathrm{sat}} = 2.7 \times 10^7\,\mathrm{cm/s}$ [Fer75].

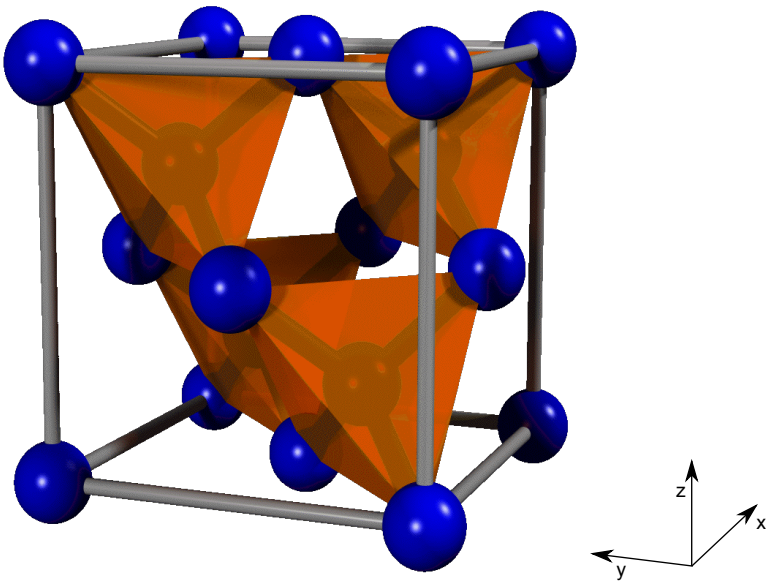

Figure 3.3: The face centered cubic lattice structure of a diamond crystal with a motif of two basis atoms at each lattice point, sitting at (0,0,0) and $(\frac{1}{4},\frac{1}{4},\frac{1}{4})$. The tetrahedral sp^3-hybridization of the carbon are emphasized in orange. Figure is taken from [Wika].

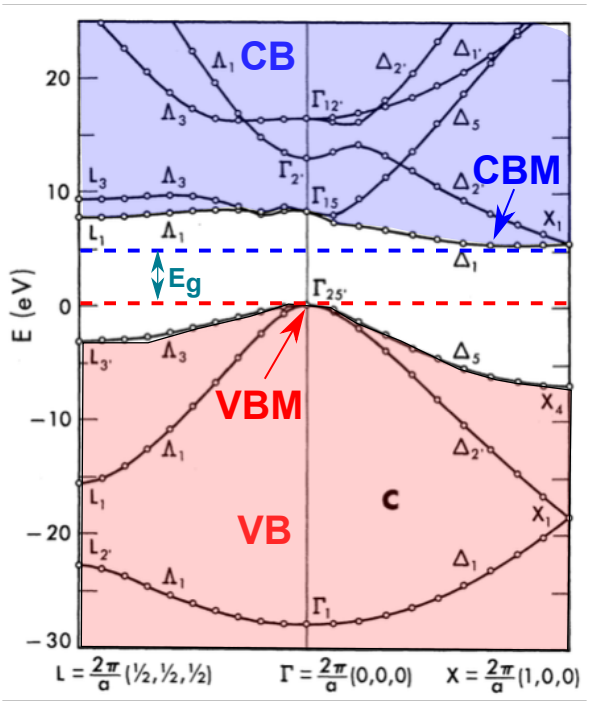

Figure 3.4: The electric band structure of a diamond crystal calculated by [Sas66] at 300 K. The valence band with its VBM is indicated in red, and the conduction band with its CBM is shown in blue. The indirect band gap of diamond is 5.47 eV and the direct band gap at Γ is 7.3 eV.

Carrier lifetime
Another important diamond property is the lifetime of the charge carriers; especially for particle detection devices where the electron-hole pairs created by ionizing particles are measured. A high charge carrier lifetime depends on the recombination possibilities of the charge carriers, and hence is an indicator of the defect concentration and the quality of the material. In single crystalline CVD diamonds carrier lifetimes of more than 2 µs have been reached [Isb02].

Resistivity
In high quality single crystal diamond a resistivity greater than $10^{16}\,\Omega$cm has been measured [Pie93]. This high value is caused by the wide band gap of 5.47 eV but as well by the strength of the electron bonds, which makes it unlikely for an electron to be excited from the valence band to the conduction band. The resistivity is however strongly influenced by the presence of impurities in the diamond. Conductive inclusions of sp^2 bonds (graphite) in form of e.g. grain boundaries or dislocations will strongly decrease the resistivity value.

Thermal Conductivity
The wide band gap of diamond leads to almost no free electrons at room temperature that could transfer the heat; hence the heat is almost exclusively transported via phonons. Since the diamond lattice packs the carbon atoms in a very tight and symmetrical way, high energies are needed to create lattice vibrations. These high phonon frequencies, used to transfer heat, are explaining the very high thermal conductivity of diamond. For high quality single crystalline diamond a thermal conductivity of 25 W/cm K at room temperature has been measured. This is a 6 times higher value compared to the thermal conductivity of copper.

3.3.1.5 Photon Absorption Spectrum of Diamond

The absorption spectrum of high quality single crystalline diamond is shown in Fig. 3.5. The diamond is transparent for photon with energies less than the absorption edge at 225 nm,

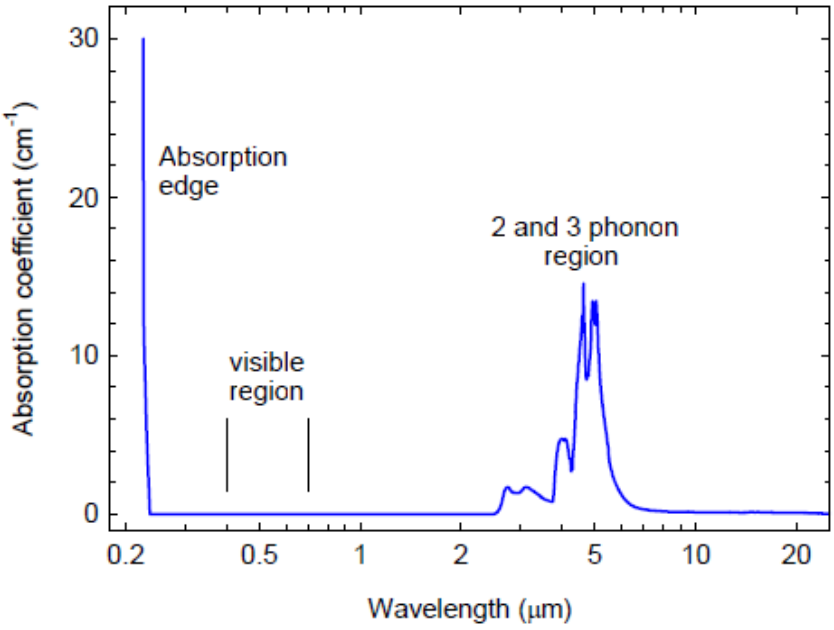

Figure 3.5: Absorption spectrum of intrinsic diamond, taken from [Ben14].

which is corresponding to the energy needed to excite an electron from the VB to the CB indirectly. In the infrared region between 2.5 µm and 6.5 µm the absorption is related to multi phonon excitation [Dor98]. In the optical spectrum intrinsic diamond is transparent for photons, therefore diamond based particle detector have not to be mounted light tight. Radiation damage can however create lattice defects in the middle of the band gap, which can lead to a sensitivity of the diamond sensor to optical photons [Afa14]. Diamond sensors are therefore typically mounted in light tight boxes.

3.3.2 Artificial diamond growth

The first known method to produce artifical diamond was the High Pressure High Temperature (HPHT) method, where the grown diamond was however contaminated with nitrogen. A nitrogen contamination leads to an increased intrinsic charge carrier density and therefore prevents the artificial diamond material to be used for particle detection. The possibility to use artifical diamond as a detector material rose with the development of the Chemical Vapor Deposition (CVD) method in 1949 [Liu95] to synthesize diamond. During the 1970s and 1980s the CVD process was significantly improved by Soviet and Japanese researchers [Spi81, Kam83], which lead to the construction of the first dedicated CVD diamond reactor in 1982 [Mat82]. With improved CVD growing processes and techniques the diamond quality was constantly improved and reached its peak in 2002 with the first 'electronic grade' CVD diamonds with extraordinary charge carrier mobilities and lifetimes [Isb02] that are commercially available [Ele16].

The two techniques in synthesizing artificial diamond, HPHT and CVD growth, are indicated in Fig. 3.6 and follow and contrary approach. While the HPHT synthesis is simulating the natural genesis of diamond, the CVD technique growth the diamonds in a metastable state under low pressure.

Table 3.1: Material properties of diamond compared to silicon and sapphire. Currently little is known about the charge carrier mobility properties of sapphire. The values are taken from the following sources [Agn92, Mol06, Pom08, Ohl09, Pom15, Kar15].

property	parameter	diamond	silicon	sapphire
physical parameter	band gap (eV)	5.48	1.12	9.9
	dielectric strength (V/cm)	10^7	3×10^5	4×10^5
	intrinsic resistivity ($\Omega\,$cm)	$10^{13} - 10^{16}$	2.5×10^5	10^{16}
	breakdown field (V/cm)	10^7	3×10^5	10^6
	density (g/cm^3)	3.52	2.33	3.98
	dielectric constant	5.72	11.9	9.3 - 11.5
	displacement energy (eV)	43	$13 - 20$	24
	thermal conductivity (W/m K)	2000	150	35
charge carrier transport	electron mobility (cm^2/V s)	$1900 - 4500$	1350	600
	hole mobility (cm^2/V s)	$1800 - 3500$	480	-
	electron lifetime (s)	$10^{-10} - 10^{-6}$	$> 10^{-3}$	-
	hole lifetime (s)	$10^{-10} - 10^{-6}$	10^{-3}	-
	electron saturation velocity (cm/s)	2.6×10^7	1×10^7	-
	hole saturation velocity (cm/s)	1.6×10^7	1×10^7	-
particle detector attributes	e/h-pair creation energy (eV)	11.6 - 16	3.62	27
	e/h-pair creation per 100 µm (#)	3602	8892	2200
	radiation length (cm)	12.2	9.36	27.9

3.3.2.1 Basics of the CVD Technique

The following description of the CVD technique is based on [May00]. As the name implies, the chemical vapor deposition technique describes a process, where a gas is chemically reacting with a solid surface, causing the gas constituents to deposit on the substrate. In order to grow CVD diamond, methane gas is heated up in a reactor into the plasma phase where it splits up into free carbon and hydrogen. A reactor is enclosing the plasma and the substrate that is kept at a low pressure, typically at 2.5 - 4 kPa. The plasma can be archived using a hot filament, a plasma arc or as well microwaves, the latter is typically used to create electronic grade CVD diamond. Beside the methane gas the substrate is as well heated up, usually greater than 700 °C, to ensure the formation of diamond rather than amorphous carbon. The deposition takes place, when the substrate is moved into the ball of plasma. Since the plasma is 'floating' and without contact to other material a very low level of impurities in the grown diamond can be reached. The basic concept of the reaction chamber is shown in Fig. 3.7.

The underlying simplified chemical reaction of this process is:

$$CM_4 \Rightarrow C_{\text{diamond}} + 2H_2. \tag{3.4}$$

An additional hydrogen atom is participating the reaction, which is terminating the surface of the substrate. Heating up of the substrate release these hydrogen atoms to form H_2 molecules

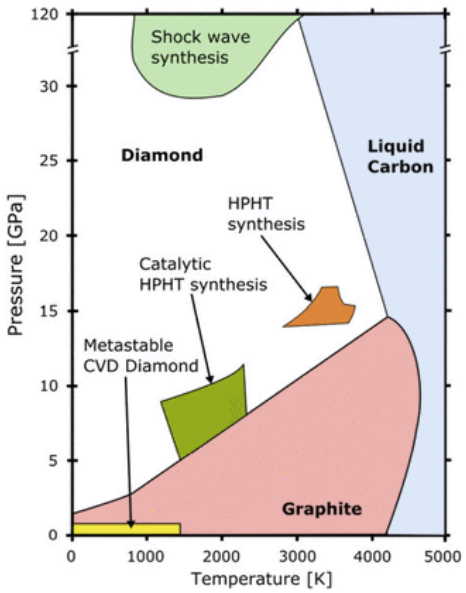

Figure 3.6: Phase diagram of carbon indicates the different synthetical productions of diamond. The graph is taken from [Bur14].

with the free hydrogen atoms originating from the methane. The remaining free carbon atoms can now form bonds with the substrate, which happens to be the sp^3-hybridization, the configuration of diamond (see 3.3.1.1).

3.3.2.2 Homoepitaxial Growth of CVD Diamonds

The homoepitaxial growth of diamond is typically oriented in <1 0 0> and uses diamond as substrate material. Two types of diamonds can be produced: single crystalline diamond (sCVD) or poly crystalline diamond (pCVD). The main difference in the production of sCVD or pCVD diamond is the quality of the diamond substrate. For the production of 'electronic grade sCVD diamond' a perfect single crystalline diamond, typically a HPHT diamond, has to be used as substrate. Even small dislocations in the lattice of the substrate can cause single condensation centers, resulting in many grain boundaries that are characteristic for

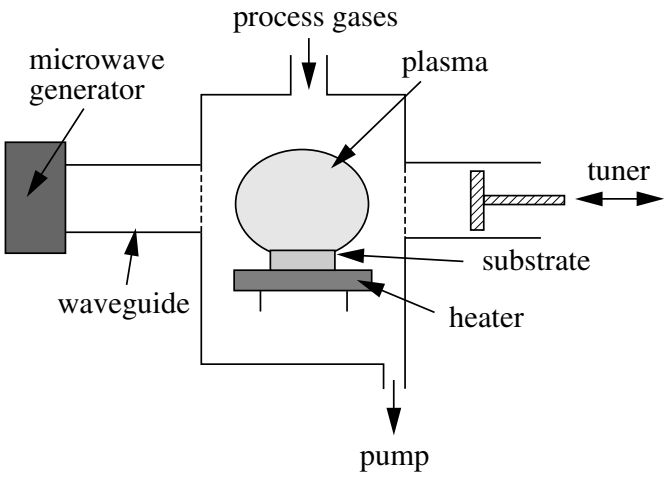

Figure 3.7: Schematic of reactor to grow CVD diamonds [May00]. The process gas pumped through the reactor chamber is locally heated up, in this example with microwaves, to temperatures approaching a few thousand Kelvins, to create the plasma ball at the substrate.

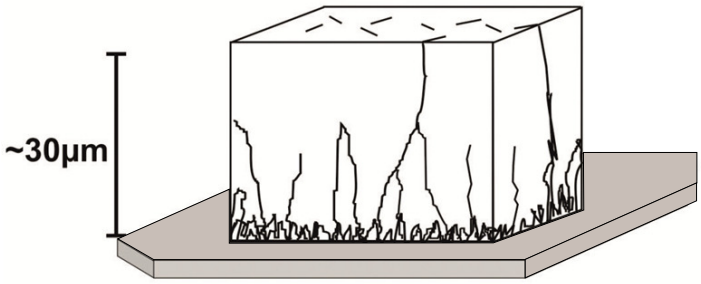

Figure 3.8: Grain boundaries with respect to the thickness of the grown CVD diamond on a substrate [May13].

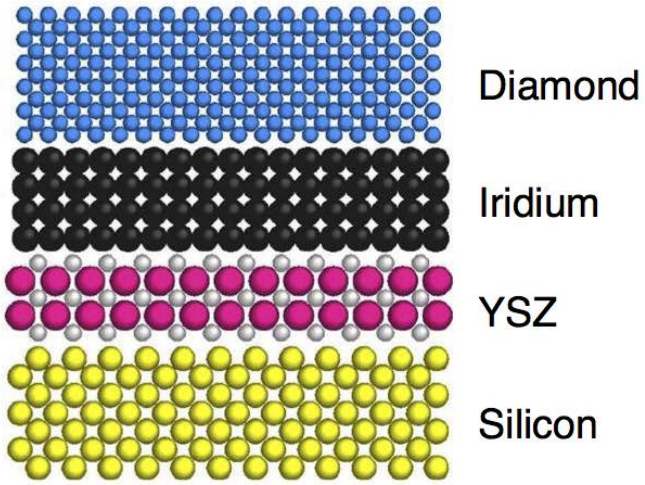

Figure 3.9: Schematic view of the heteroepitaxial multilayer structure to grow single crystalline CVD diamond [May13].

pCVD diamonds. The production in the homoepitaxial growth process of sCVD diamonds is therefore limited to the substrate dimensions, leading to a maximum surface of $5 \times 5\,\mathrm{mm}^2$.

The pCVD diamonds uses diamond powder as substrate and hence can be grown on larger surfaces, typically wafer sizes up to 120 mm in diameter [Ele16a]. This leads to a cheaper product, however with a reduced quality caused by the high amount of grain boundaries.

In order to improve the quality of sCVD and pCVD diamonds and to reduce the lattice defects, the CVD sensors are grown much ticker than needed. With increased CVD diamond thickness the grain size typically grows and some grain boundaries completely disappear, hence the amount of grain boundaries in total decreases with respect to the CVD diamond thickness, see Fig 3.8. Using only the very top part of the grown CVD diamond is therefore used to create high quality CVD diamond material.

3.3.2.3 Heteroepitaxial Growth of CVD Diamonds

A viable alternative to the homoepitaxial growth of CVD diamonds, is the approach of a heteroepitaxial CVD diamond growth, where the substrate differs from diamond. After many years of research iridium as substrate was identified as unique template to grow high quality single crystalline diamond heteroepitaxially, called *diamonds on iridium* (DOI) [Sch99, Sch01, Sch14b]. Iridium however is just the most upper layer in a diamond/Ir/yttria-stabilized zirconia/Si multilayer substrate structure, as shown in Fig. 3.9. In comparison to the traditional sCVD diamond growth the heteroepitaxial substrate is not geometrical limited and makes the growing of single crystal quality diamonds on wafer size possible. The quality

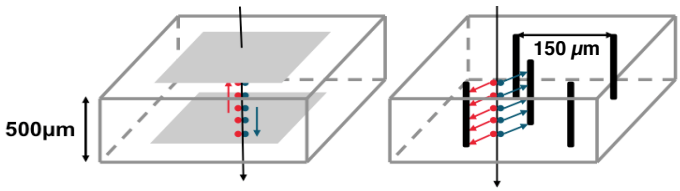

Figure 3.10: Typical layout of planar (left) and 3D (right) diamond detectors. The reduced charge carrier drift path in the 3D geometry is beneficial for the radiation hardness of diamond detectors [Fel16].

of the DOI detectors is continuously improving and reaches almost a quality comparable to sCVD diamonds [Kis15].

3.3.3 Signal Generation in Diamond Detectors

Diamond detectors are typically designed in a parallel plate geometry with two metallized surfaces as electrodes. More recent diamond detectors developments are using a 3D geometry, where the electrodes are located inside the bulk material, see Fig. 3.10. The working principle is however identical: A high voltage is applied to the electrodes to create an electrical field inside the diamond bulk of around 1 V/µm. An ionizing particle passing through the diamond bulk is creating electron-hole pairs via ionization. The average ionization energy for diamond is about 13.2 eV [Can79] that results in the creation of 36 electron-hole pairs per µm of diamond thickness for a minimal ionizing particle (MIP) [Pom08]. The electrical field forces the charge carriers to drift towards the electrodes. This charge carrier drift is inducing directly a current in the read out circuit following Ramos law [Ram39a]. This electrical signal can be used in two ways, either the signal current is measured directly with a sensitive and slow current readout device (BCML detector), or the signal pulse created by a single ionizing particle is quickly amplified, discriminated and counted (BCM1F detector).

An important parameter for the detector characterization is the charge collection efficiency (CCE) defined as:

$$\mathrm{CCE} = \frac{\mathrm{Q_{coll}}}{\mathrm{Q_{ind}}}, \tag{3.5}$$

where Q_{ind} is the amount of charge carriers induced in the diamond bulk by an ionizing particle and Q_{coll} is the charge collected by the readout electronics. High quality sCVD diamond sensors reach a CCE of 100 % at electrical fields above $E = 0.2\,\mathrm{V/\mu m}$. Poly crystal diamond sensors can reach a CCE of $\sim 50\,\%$ [Mue11] at an electrical field of $E = 1\,\mathrm{V/\mu m}$ and DOI sensors currently reach for the same electrical field a CCE of $\sim 75\,\%$ [Kis15]. The reduced CCE can be explained with the trapping of charge carriers at local lattice defects, for poly crystalline diamonds predominantly at grain boundaries. A more detailed explanation of possible lattice defects and recombination centers for charge carriers will be given in the following section 3.3.4.

In the diamond community another parameter, the charge collection distance (CCD) is commonly used. It describes the average drift length of the charge carrier before being trapped in a lattice defect. The CCD is related to the CCE via:

$$\mathrm{CCD} = \mathrm{CCE} \cdot \mathrm{d}, \tag{3.6}$$

with d as diamond thickness. In fact the CCD describes the separation distance of electrons and holes before being trapped in a lattice defect. The parameter is however only valid for CCD values smaller than the diamond thickness, which is true for poly crystalline diamonds.

The CCD can't be used for sensors, like single crystalline diamonds, where CCEs of 100 % are reached and hence a higher CCD then the diamond thickness would be obtained.

A physical more correct description of the average charge carrier drift is the mean free path length λ. The mean free path length describes the average drift length of charge carriers in an infinite thick diamond sensor before they got trapped in a defect. The CCD is related to the mean free path length λ via the following equation [DK08]:

$$\mathrm{CCD} = \sum_{\mathrm{k=e,h}} \lambda_{\mathrm{k}} \left[1 - \frac{\lambda_{\mathrm{k}}}{\mathrm{d}} \left(1 - \mathrm{e}^{-\frac{\mathrm{d}}{\lambda_{\mathrm{k}}}} \right) \right]. \tag{3.7}$$

The CCE and the CCD are depending strongly on the lifetime of the charge carriers before being trapped. The electrical field has therefore to be set into relation to these parameters to get an understanding of the diamond quality. A higher electrical field means a higher charge carrier drift velocity and hence a reduced charge carrier drift time, leading to a reduced charge carrier trapping and an increased CCE and CCD value.

3.3.4 Lattice Defects in Diamond

Like in any other crystal lattice defects are as well present in the diamond lattice. The different types of lattice defects can be categorized by its dimensions: Point like defects (0 D), Line defects (1 D), Planar defects (2 D) and Bulk defects (3 D). All of these lattice defects can be caused in the CVD growth process, whereas radiation damage causes typically point like defects.

3.3.4.1 Point Defects in the Diamond lattice (0 D)

Point like lattice defects are not extended in any direction, typically these are single atoms dislocated in the diamond lattice, see Fig. 3.11. In the following the most important point like defects will be described:

- **Vacancy defects:** A lattice site that is not occupied with a crystal atom. The vacancy can move through the crystal if a neighboring atom overtakes the unoccupied lattice position.
- **Interstitial defects:** An atom sitting in between the normal crystal lattice, hence two or more atoms may share one lattice site.
- **Frenkel defects:** A combination of a vacancy and interstitial defect next to each other. This can be caused by radiation damage, elementary particles with energy above the displacement threshold pushing an lattice atom to a random new lattice position.
- **Impurity defects:** Impurities during the CVD growth cause other atoms (silicon atom in Fig. 3.11) to occupy a carbon lattice side. This defects are called substitutional defects.

One of the most popular point defects in CVD diamonds is the nitrogen-vacancy center (N-V center), consisting of two nearest neighbor pairs of nitrogen atoms, substituting a carbon atom and a lattice vacancy. The electron spin of this N-V center is very stable and can be manipulated at room temperature, hence this defects is very interesting for measurements e.g. of the magnetic field, electrical field or microwaves at highest sensitivities [Sch14a].

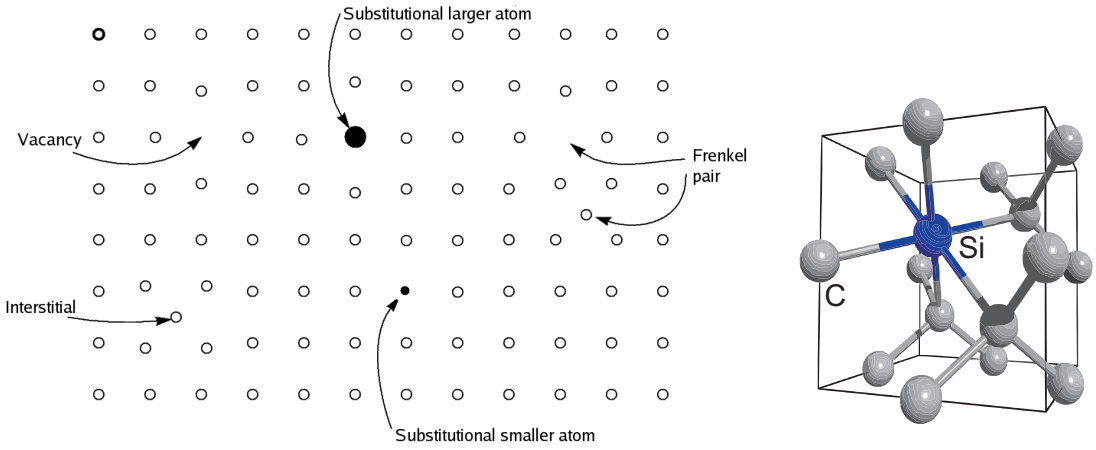

Figure 3.11: On the left side different point like defects in the diamond lattice are shown: Vacancies, Interstitials, Substitutional larger or smaller atoms. On the right side a silicon vacancy center is shown: a silicon atom overtakes the place of a carbon atom. Figures taken from [Wikb, Neu11].

3.3.4.2 Diamond Lattice Defects of Higher Dimension (>0 D)

Diamond lattice defects of higher dimensions are typically caused by strain or stress in the growth process of the CVD diamonds. Typical higher dimension defects are edge or screw dislocations, stacking faults or grain boundaries. The most prominent defects are the grain boundaries, a planar 2 D defect, which is present in all poly crystalline diamonds. The pCVD diamonds are grown on diamond powder as substrate and hence suffer relatively high stress, since individuals grains are grown competitive [Mil13]. Another common defect, the stacking fault, is linked directly to the growth rate of the CVD diamond [Rud15].

All these defects described can have various effects on the electrical, thermal and mechanical properties of the diamond, although they are in some cases may be neutral or even beneficial.

3.3.5 Effects of Lattice Defects to Electrical Diamond Properties

The effects of lattice defects to the electrical properties of diamond, can be understood with the band theory of solids [Pan78]. The energy levels of electrons in a perfect crystal form a series of bands, separated by gaps. A wave function of all states extended over the entire crystal has the same probability amplitude in every unit cell, furthermore periodicity doesn't allow localized states. If there is however a local impurity or defect this periodicity is broken and localized states are allowed. These defects have a dramatic effect on the properties of semiconductors and allow the presence of localized states in the otherwise forbidden energy gap E_g. Furthermore, these defects can exist in various charged states depending on whether the localized states are occupied or not. Shockley [Sho52] introduces a naming convention for the type of defect depending on the charge of the defect: Positively charged impurities are defined as donor traps, and negatively charged impurities are defined as acceptor traps. Uncharged impurities are assigned as neutral traps.

In Fig. 3.12 various lattice defects are shown that are causing three localized states with different energy gaps E_g in the band gap. A defect with an energy depth close to the conduction band and therefore located above the fermi level is in equilibrium in an unoccupied and neutral state. An electron from the conduction band could be trapped in such a defect, causing the neutral trap to become negatively charged. This type of defect is therefore considered to be an acceptor like trap. A defect positioned energetically close to the valence band and therefore below the fermi level is in equilibrium in an occupied and neutral state. The defect

can therefore trap hole carriers to become positively charged, this type of defect is considered as a donor like trap.

Typically recombination processes in diamond sensors are negligible since the band gap is very large. A lattice defect located in the middle of the band gap can trap charge carriers from the conduction or from the valence band. This can result in the annihilation of both charge carriers and therefore strongly increase the charge carrier recombination. The same lattice defect could as well serve as a charge generator. An electron from the defect level could be excited into the conduction band and the unoccupied defect could be filled up with another electron from the valence band. This would effectively generate an additional, free charge carrier. The very same process could be as well described from the perspective of a hole being excited into the valence band and filled up by a hole from the conduction band. This charge generation process can be measured as dark current, which is very low for diamond in the order of 50 pA. Even diamonds with increased radiation damage keep these low levels of dark current, which can be explained by the large band gap that is suppressing these effects.

Increased dark currents are however present in some CVD diamonds sensor, called 'dark erratic currents' [Bru04]. These 'dark erratic currents' appear spontaneous, sometimes immediately after applying bias voltage, sometimes with a time delay of several hours and cause an increase in the dark current level by magnitudes that can even reach currents up to 10 µA. These 'dark erratic currents' can be found predominately at pCVD diamonds, but as well in single crystalline diamonds. The physical process creating these 'dark erratic currents' is not fully understood, but it is evident that these effects are becoming more severe with increased radiation damage. Furthermore, high electrical fields increase the probability to start these charge generating effects. For pCVD diamonds the creation of these 'dark erratic currents' can be entirely suppressed with magnetic field [Mue11]. It is believed that these 'dark erratic currents' are caused by local defects at the diamond surfaces, this topic will be further discussed in section 4.5.2.

Charge trapping in diamond sensors is not desired, since the trapped charges do not contribute to the signal anymore and hence reduce the overall CCE of the diamond sensor. However once a charge is trapped, e.g. an electron in an acceptor trap, this trap is filled and can't trap another electron. Hence the trap can be considered as being passivated. If most of the traps in a diamond sensor are passivated, the average drift length of the charge carriers before

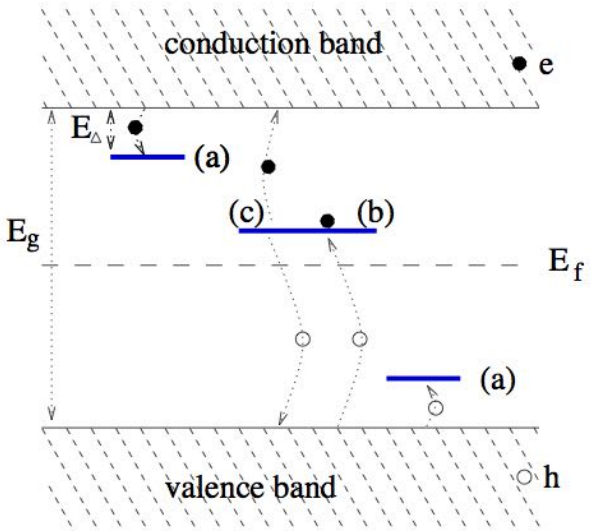

Figure 3.12: Three lattice defects at different energy levels E_Δ inside the band gap E_g. Charge carriers can be trapped (a), recombined (b) or generated (c) at the different lattice defects, with E_f as the fermy energy. Graph taken from [Oh99].

being trapped is increased, resulting in an increased CCE of the diamond sensor [Kra12]. This process is commonly referred to as 'pumping' or 'priming'. If neutral traps are trapping a charge carrier they are becoming positively or negatively charged. Such a localized, fixed charge is called space charge and is affecting the internal electrical field of the diamond sensor. An unhomogeneous build up of space charge can negatively influence the diamond detector performance and result in a reduced charge collection efficiency. This effect is called diamond polarization and will be discussed in detail in chapter 5.5.

3.3.6 Calculation of Radiation Damage in Diamond

Ionizing particles are dominating the signal creation in diamond detectors, however do not have enough energy to damage the diamond lattice and hence are not important in terms of radiation damage. Particles that are scattering elastically with the diamond lattice via non-ionizing energy loss (NIEL) have enough energy to displace atoms and hence cause radiation damage [Vas00]. The total radiation damage with respect to the particle type and energy of the primary particle can be calculated using two different approaches, based on the NIEL or on the Displacements per atom (DPA) model.

Non-Ionizing Energy Loss (NIEL)
The NIEL hypothesis is based on the material specific stopping power $S = dE/dx$ consisting of the ionizing S_i (energy to electrons) and non-ionizing S_n (energy to nuclei) energy transfer [Gut14a]. In order to calculate the fraction of S_n to the total stopping power $S = S_n + S_i$ the Lindhard partition function $\xi(T)$, which depends on the kinetic energy of the primary particle, is used.

$$\xi(T) = \frac{S_n}{S} \tag{3.8}$$

The partition function $\xi(T)$ is calculated in the Lindhard screened potential scattering theory [Lin63] and is based on the Thomas-Fermi model [Vas00].

Displacements Per Atom (DPA)
The DPA model simulates the average fraction of displaced atoms in a lattice. A DPA value of e.g. 10^{-22} means that one out of 10^{22} atoms in a lattice is displaced. The basic idea of the DPA model is that the radiation damages scales with the amount of Frenkel pairs, which can be directly calculated. The calculation of Frenkel pais created by particle interaction, without taking phonon interaction into account, is based on the theory of Norget, Robinson and Torren [Nor75]:

$$N_F = \kappa(T)\frac{\xi(T) \cdot T}{2E_{th}}, \tag{3.9}$$

With N_F the amount of Frenkel pairs, $\kappa(T)$ the displacement efficiency, T the kinetic energy of the primary knocked on atom, $\xi(T)$ the Lindhard partition function and E_{th} the lattice displacement threshold energy.

In the silicon community the NIEL model is usually used to estimate the radiation damage given by any particle. The particle fluence is then converted to a fluence of 1 MeV neutron equivalents for comparison. In the diamond community however most of the experimental irradiation data is available for 24 GeV protons, the radiation damage of a particular particle is therefore normalized to 24 GeV proton equivalents. A comparison of the calculated radiation damage in diamond caused by different particles using the NIEL and DPA model is shown in Fig 3.13 for comparison.

3.3.7 Diamond Surface and Metal Diamond Interface

Producing a high quality diamond based particle detector needs in principle three ingredients: High quality diamond material with little impurities, electrodes on both sides of the diamond

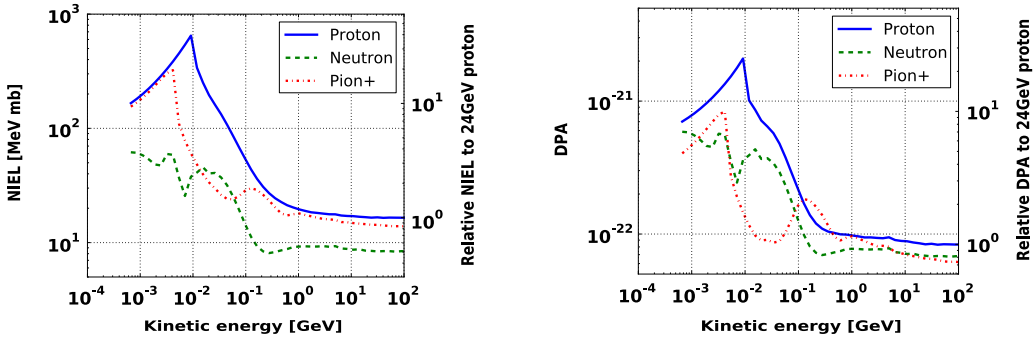

Figure 3.13: Radiation damage calculated for diamond with the NIEL model (left) and the DPA model (right) for different particle types and kinetic energies [Gut14b].

and most important a low ohmic contact between the electrode and the diamond bulk. This section will focus on the challenges in order to create such an interface providing in addition a good mechanical support.

3.3.7.1 Diamond Surface Preparation

Before a metal electrode can be added to the diamond bulk, the surface has to be treated to create an uniform passivization of the dangling bonds of the CVD diamond. The CVD diamond surfaces are therefore processed after the growth process creating a uniform oxygen or hydrogen termination, using typically the reactive ion etching technique [San89].

The Reactive Ion Etching (RIE)
The reactive ion etching process takes away the surface of the diamond ($\approx 1\,\mu m$), before a new metallization layer, acting as electrode, is applied. The RIE uses chemically reactive plasma, generated in vacuum at low pressure by an electromagnetic field, to remove the upper diamond layer. High-energy ions in the plasma are reacting with the surface an breaking up the oxygen or hydrogen termination. With this technique etching rates of 35 nm/min are reached [Pan13].

After the RIE process the diamonds are mechanical polished to create a flat and homogeneous surface for the metallization process.

3.3.7.2 Electrical Interface between Diamond and Electrode

The interface between the diamond and the electrodes has to fulfill two tasks. First, the free charge carriers created by ionizing particles inside the diamond bulk have to be efficiently extracted from the diamond bulk. Second, the interface should prevent free charge carriers from the metal to enter the diamond when a bias voltage is applied. The interface between diamond and electrode can be either an Ohmic or a Schottky contact. The difference between the contacts is based in the question if the transfer of the majority carriers from the diamond to the metal is unimpeded (Ohmic) or not (Schottky). Both types will be discussed in the following. More detailed information to both types of contacts for in particular diamond sensors can be found in [Eva09].

Ohmic contact
A metal-semiconductor contact is defined ohmic when the resistance of the contact is negligible to the resistance of the semiconductor bulk. In this constellation the semiconductor bulk is the limiting charge conductor. The band structure forming an ohmic contact is shown in Fig. 3.14, the conduction band of the semiconductor is lower than the Fermi energy of the

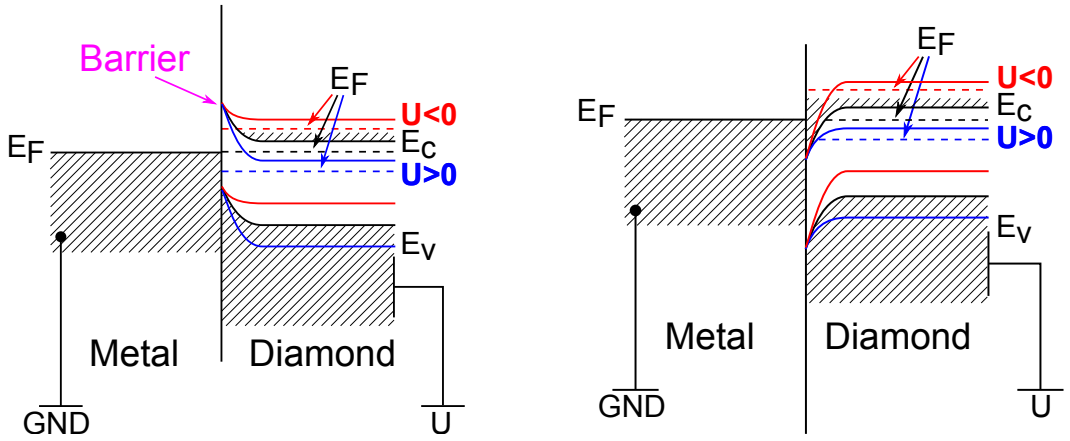

Figure 3.14: Band structure of a Schottky contact (left) and an Ohmic contact (right). At the Schottky contact a barrier is created that is decreased for negative bias voltage and increased for positive bias voltage. The sketch is based on [Bol06].

metal. This leads to an unimpeded transfer of the majority carriers from one material to another, regardless of the direction. Applying a voltage to the semiconductor doesn't change the properties of the ohmic contact. For diamond sensor material, which is inert and has a wide band gap, just a limited amount of metals can provide a good ohmic contact. The metals, e.g. titanium or chromium, can form carbide bindings with the diamond and are typically used to create ohmic contacts.

Schottky contact

A Schottky contact forms a barrier between the metal and the semiconductor. The reason for the barrier is the increased energy level of the semiconductor conduction band with respect to the Fermi energy of the metal. The conduction band of the semiconductor bends away from the Fermi energy of the metal and the semiconductor becomes intrinsic in this region. Hence there are less mobile charge carriers and a depletion width occurs. For Schottky contacts the applied electrical voltage is affecting the barrier height at the metal-semiconductor contact. If a negative voltage on the semiconductor side is applied, the Fermi energy of the semiconductor is increased and therefore the barrier height reduced. The conductivity is increased. For a positive electrical voltage the barrier is vice versa increased and the conductivity reduced.

Chapter 4

The Beam Condition Monitor Leakage (BCML1/2)

In this chapter the 'Beam Condition Monitoring Leakage' detector (BCML) is introduced. The first section 4.1 focuses on the BCML detector hardware, introducing the BCML sensors and explaining the electrical signal read out logic. A highly detailed description of the BCML hardware can be found in [Mue11] and further modification to optimize the BCML detector are described in [Gut14a]. The BCML beam abort thresholds are defined in section 4.2, that are essential for the BCML beam abort functionality. Typical operation of the BCML detector during a LHC fill will be explained in section 4.3. A selection of beam loss events measured by the BCML detector is discussed in section 4.4. The last section 4.5 focuses on the radiation induced signal degradation of the BCML detector during Run 2, which resulted in the adjustment of the beam abort thresholds.

4.1 The BCML Detector Hardware

The BCML detector is a beam-monitoring device that can actively trigger the LHC beam abort in case of catastrophic beam loss events that could damage the CMS detector, in particular the CMS tracker. The BCML system is located at 4 different location inside the CMS detector and is therefore subdivided into the BCML1 detector, located at $Z = \pm 1.8\,\mathrm{m}$, and the BCML2 detector located at $Z = \pm 14.4\,\mathrm{m}$ away from the interaction point. The differences between the BCML1 and BCML2 detector will be discussed in section 4.1.1. In total 16 BCML detector channels are used actively in the beam abort functionality, 4 channels at each BCML detector location. The sensors used by the BCML system, mostly poly crystalline diamond detectors, are introduced in section 4.1.2. The logic of the electrical signal read out and the abort functionality are described in section 4.1.3. BCML hardware problems that occurred during Run 2 are discussed in the last section 4.1.4.

4.1.1 Properties of the BCML1 and the BCML2 Detector

The locations of the BCML1 and the BCML2 detectors at the CMS detector are shown in Fig. 4.1. The BCML1 detectors are located close to the interaction point at $Z = \pm 1.8\,\mathrm{m}$ at a radius of $r = 4.5\,\mathrm{cm}$ resulting in a pseudo rapidity of $\eta = 4.4$. The BCML1 diamond sensors are mounted on PCB[1] boards that are surrounded by two copper boxes acting as a Faraday cages, see Fig. 4.2a. The electrical connection of the diamond sensor to the PCB is established via conductive glue on the backside and a wire bond to the front metallization. The PCB

[1] Printed Circuit Board (PCB)

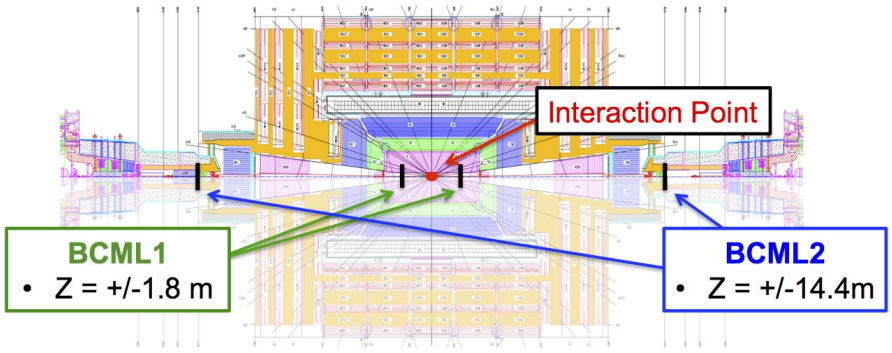

Figure 4.1: Location of BCML1/2 detectors at the CMS detector. The BCML1 detector indicated in green is located inside the CMS tracker volume at $Z = \pm 1.8\,\mathrm{m}$ away from the interaction point. The BCML2 detectors are located further outside at $Z = \pm 14.4\,\mathrm{m}$. Each detector location is equipped with 4 pCVD diamond sensors that are active in the beam abort functionality.

itself is connected via 5 pins to the BCM support C-Shape [Gut16], which provides the bias voltage and the shield connection, see Fig. 4.2. The technical drawing of the BCML1 sensor box can be found in the appendix, see A.1.1.4. Two BCML sensor boxes are mounted on each BCM C-Shape, whereas two BCM C-Shapes are installed at each end of CMS, accumulating up to a total amount of 8 BCML1 sensors. The BCM C-Shape shown in Fig. 4.2b is hosting beside the BCML sensors, the BCM1F detector (see section 2.3.2.2).

The BCML2 detector is located further away from the interaction point at $Z = \pm 14.4\,\mathrm{m}$ (see Fig. 4.1). The BCML2 sensors are mounted at two different radiuses inside a wheel like support structure, shown in Fig. 4.3c. The BCML2 sensors mounted at an inner radius of $r = 5\,\mathrm{cm}$ are exposed to highest particle rates and receive the heighest radiation damage of all BCML sensors at a pseudo rapidity of $\eta = 6.4$. The BCML2 sensors mounted at an outer radius of $r = 28\,\mathrm{cm}$ with a reduced pseudo rapidity of $\eta = 4.6$ are located at a comparable η like the BCML1 sensors, see Fig. 4.3b. The BCML2 sensors are mounted with non-conductive glue on a PCB board inside an aluminum box, see Fig. 4.3a. Two wire bonds are connecting the front and the back metallization of the diamonds sensor with SMA connectors. The bias voltage for the diamonds sensors is provided via the inner cores of the SMA cables connected to the wire bonds, whereas the outer core is connected to the aluminum box as shield. The BCML2 sensor boxes mounted inside the wheel like aluminum support structure can be seen in Fig. 4.3b. Most of the BCML2 sensors have been positioned at the inner radius inside the BCML2 wheel and hence had to be stacked on top of each other because of limited space. The final installation of the BCML2 wheel at the CMS detector can be seen in Fig. 4.3c, where half of the BCML2 wheel is mounted to the support structure of the TOTEM T2 detector [TOT08].

4.1.2 The BCML Sensors

The BCML detector consists in total of 36 sensors, whereas 8 of them belong to the BCML1 detector. Most of the BCML sensors are made of poly crystalline CVD diamond, however as well other sensor material like single crystalline CVD diamond or sapphire is used. Two ionization chamber are installed additionally, one on each side of CMS. The ionization chambers are identical to the Beam Loss Monitor (BLM) system of the LHC. The different BCML sensors are discussed in the following section. A detailed list of all BCML sensors can be found in the append, see A.1.3.1.

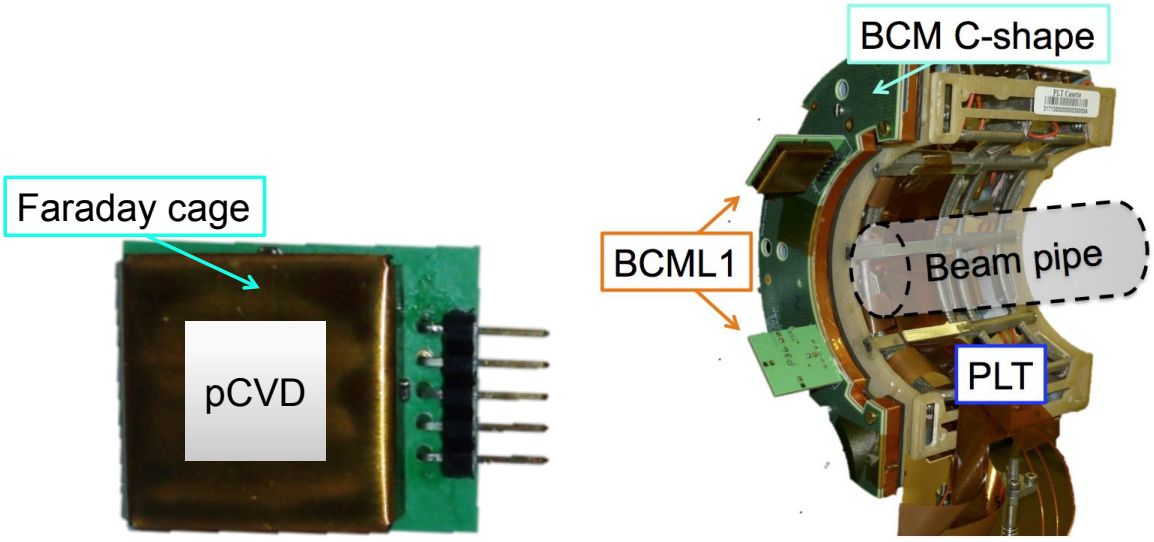

(a) Sensor box. **(b)** BCM assembly.

Figure 4.2: The BCML1 detector. The BCML1 diamond sensors are surrounded by a copper shield acting as Faraday cage, shown in the left figure. The 5 connector pins of the BCML1 sensor box are providing shielding (3 pins), positive and negative bias voltage connection. The BCML1 sensor boxes are mounted on the BCM C-shape that supports as well the BCM1F detector, shown in the right figure. The PLT detector (see 2.3.2.1) is the mechanical support for the BCM C-Shape located around the beam pipe.

4.1.2.1 pCVD Diamond Detectors

The majority of the BCML detector channels (31 of 36) are using pCVD diamond sensors. The pCVD diamond sensors of the BCML1 detector have an average size of $10 \times 10 \times 0.5\,\mathrm{mm}^3$, whereas the pCVD diamonds of the BCML2 detector have an average size of $10 \times 10 \times 0.4\,\mathrm{mm}^3$, see [Mue11]. On the diamond surfaces ohmic titanium/tungsten electrodes were sputtered with a thickness of 100 nm after 1 µm of the surfaces was removed by a chlorine chemistry reactive ion etching, compare section 3.3.7. The metal electrodes with a surface of

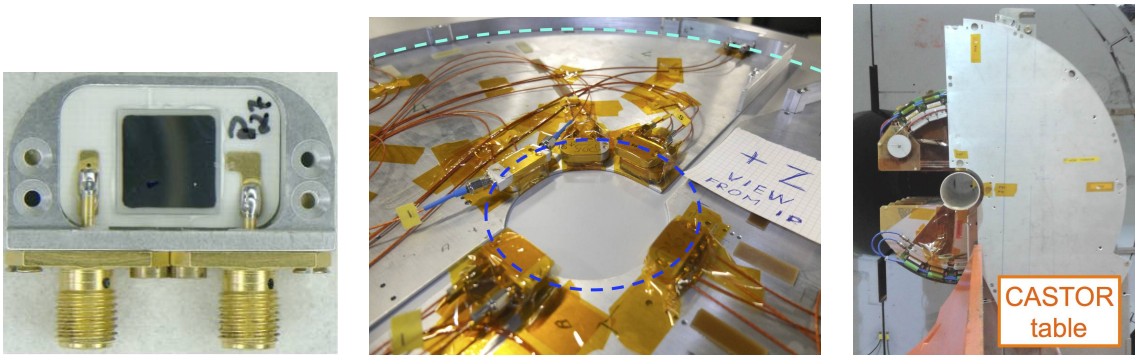

(a) Sensor box. **(b)** View inside the BCML2 wheel. **(c)** BCML2 at CMS.

Figure 4.3: The BCML2 detector. An opened BCML2 sensor box with a $10 \times 10\,\mathrm{mm}^2$ diamond is shown on the left, see (a). The SMA connectors provide positive and negative voltage connection as well as the shield. The BCML2 sensor boxes are mounted inside the BCML2 wheel at a radius of 5 cm indicated in blue and at a radius of 28 cm indicated in cyan, see (b). Due to the limited space at the inner radius, some BCML2 sensors boxes are stacked on top of each other. The BCML2 wheel is mounted in front of the TOTEM T2 detector at CMS, shown in (c). The orange structure is the CASTOR table on which the BLM tubes are mounted. The location of the beam pipe with respect to the BCML2 detector is indicated with a white tube.

$9.25 \times 9.25\,\mathrm{mm}^2$ were annealed in an N_2 environment for 4 min at 400 °C.

Beside new pCVD diamond detectors being installed at the BCML1 detector, most of the pCVD diamonds mounted at the BCML2 detector were already used during Run 1 (between LHC operation 2009 - 2012) and hence experienced irradiation damage resulting in a reduced signal efficiency (SE). The term 'signal efficiency' describes the fraction of signal that an irradiated sensor is creating compared to the signal of an unirradiated sensor. This term should not be confused with the absolute value of the charge collection efficiency. An unirradiated pCVD diamonds sensor has typically a CCE of 50% however a SE of 100%. All BCML pCVD diamonds used during Run 2 can be subdivided into three categories:

- New pCVD diamonds: $\mathrm{SE}_{\text{init. Run 2}} \geq 90\%$.
- Slightly irradiated pCVD diamonds: $\mathrm{SE}_{\text{init. Run 2}} \geq 70\%$.
- Heavily irradiated pCVD diamonds: $\mathrm{SE}_{\text{init. Run 2}} \geq 40\%$.

The signal efficiency is calculated by comparing the extrapolated BCML detector signal for nominal luminosity to a Fluka based estimation of the BCML detector signal, this will be discussed in more detail in section 4.5.1.

4.1.2.2 sCVD Diamond Detector

The BCML2 detector is equipped with a single crystalline CVD (sCVD) sensor at the '+Z inner near' location. This sensor was installed in this high η region to gain further experience of the radiation induced degradation of the signal efficiency of sCVD diamonds in a high particle rate environment. The sCVD diamond called 'sCVD_1' has a size of $5 \times 5 \times 0.491\,\mathrm{mm}^3$ with two $4.25 \times 4.25\,\mathrm{mm}^2$ titanium/tungsten electrodes. The charge collection efficiency of this diamond measured at DESY in Zeuthen reached CCE $\geq$ 97% for a bias voltage of HV $\geq 200\,(\mathrm{V})$.

4.1.2.3 Sapphire Detector

The BCML2 wheel is equipped in addition with a sensor made of sapphire called 'SAP_1'. The sapphire sensor is installed inside the BCML2 wheel at an inner radius in a high η region to gain experience with the radiation induced degradation of the signal efficiency in a high particle rate environment. The sapphire sensor has a size of $10 \times 10 \times 0.525\,\mathrm{mm}^3$ and is metallized from both sides with consecutive layers of Al, Pt and Au of 50 nm, 50 nm and 200 nm thickness, respectively. The electrodes have a square shape of $9 \times 9\,\mathrm{mm}^2$. For a bias voltage of HV = 500 V a charge collection efficiency of CCE $\sim$ 3% is expected [Kar15].

4.1.2.4 BLM Detectors

The BCML detector system is completed by two ionization chambers identical to the LHC BLM tubes discussed in section 2.1.5. The BLM tubes are installed close to the BCML2 detectors on the so called 'CASTOR tables' (see Fig. 4.3c) and are fully integrated into the BCML readout system. The BLM tubes are operated at HV = 1500 V and are expected to be radiation hard and not suffer any radiation induced signal degradation. Hence the BLM monitors can be used as normalization for BCML2 detector to analyze the signal efficiency with respect to the radiation damage.

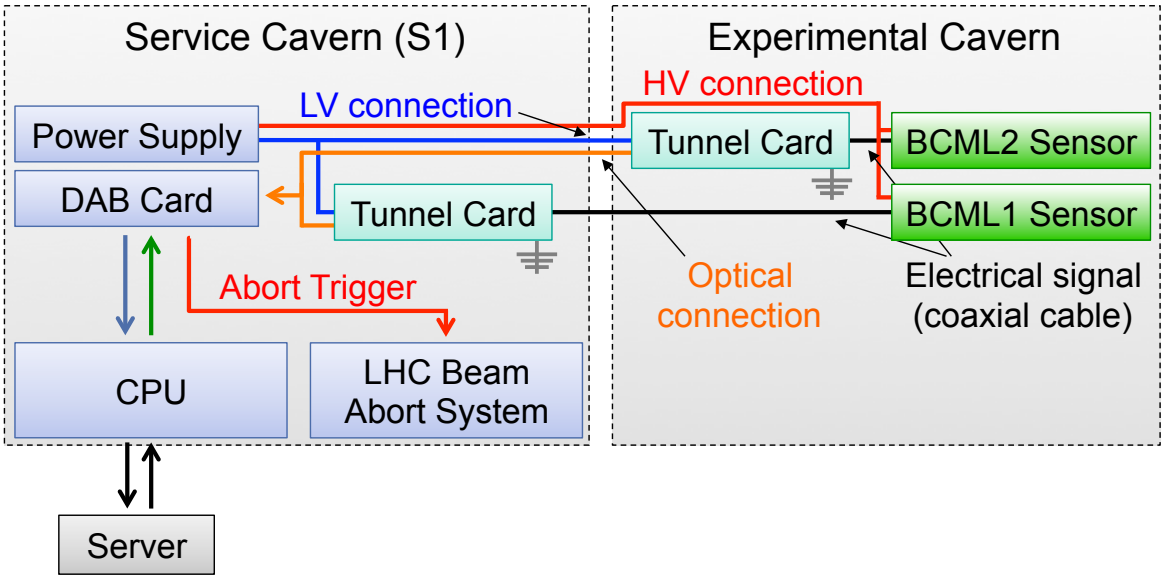

Figure 4.4: Schematic drawing of the electrical connection of the BCML detectors. The signal of the BCML sensors (green) installed at the CMS detector is read out with the tunnel card indicated in cyan (further details in section 4.1.3.2). The tunnel card of the BCML2 detector is located close to the sensors itself inside the experimental cavern via a 7 m long coaxial cable. The tunnel card of the BCML1 detector is however located at the service cavern and the signal is transmitted via a 120 m long coaxial cable. The electrical BCML sensor signal is digitalized in the tunnel card and transmitted optically (orange) to the DAB card, see section 4.1.3.3. In case of a beam abort scenario the DAB card sends the beam abort trigger (red arrow) directly to the LHC Beam Abort System. A local CPU can talk to the DAB card to initialize, read out the signal measurements or to check its healthiness and transmits this information to a server. The high voltage (red) for the BCML sensors and the low voltage (blue) for the tunnel cards are created by a CAEN power supply located in the service cavern, see section 4.1.4.1.

4.1.3 Electrical Signal Read Out System of the BCML detectors

The basic components and connections of the electrical signal read out of the BCML system are shown schematically in Fig. 4.4. The BCML sensors are powered by a power supply located in the service cavern via 120 m long coaxial cables. The sensor signal is read out via the tunnel card (see section 4.1.3.2) that is located directly at the CMS detector for the BCML2 detector and in the service cavern for the BCML1 detector. The BCML2 tunnel card located in the experimental cavern is powered with a power supply located in the service cavern to have the possibility to remotely power cycle the system. The signal measurement of the tunnel card is send optically to the DAB card where it is further processed (further details in section 4.1.3.3). The DAB card contains the logic to decide if a beam abort trigger is send to the LHC beam abort system. The CPU can configure and read out the DAB card and transmits all relevant signal measurement information to a local server. Hence the critical core of the BCML signal read out system consists only of the tunnel card and the DAB card. If a software problem would cause a crash of the CPU unit the only problem would be the loss of the communication to the BCML detector, a safe operation of the CMS detector would however still be guaranteed since the beam abort logic in the DAB card would not be affected.

The BCML system uses during Run 2 in total 34 detector channels, where 8 channels belong to BCML1 and 26 channels to the BCML2 detector. The tunnel card can read out simultaneously up to 8 detector channels, hence one tunnel card is allocated for the BCML1 sensors and 4 tunnel cards are allocated for the BCML2 sensors, increasing the total amount of possible BCML2 channels up to 32. The digital output signal of the tunnel card is fed into

the DAB cards, which can take two tunnel card inputs, respectively 16 detector channels. In total 3 DAB cards are used, where one of them reads out the 8 BCML1 channels and the other two are reading out the 32 BCML2 channels. The core components of the BCML read out system will be introduced in more detail in the following sections separately.

4.1.3.1 Wiring and Grounding

The wiring scheme of an individual BCML channel is schematically shown in Fig. 4.5. A power supply creates a floating high voltage that is applied to a BCML sensor. The tunnel card measures the signal current on the return line to the power supply. Additionally the tunnel card defines the ground of the electrical circuit; hence the BCML1 signal circuit is grounded in the service cavern whereas the BCML2 signal circuit is grounded in the experimental cavern. In the complete BCML signal circuit additional filter elements are located close to the detector and close to the power supply to reduce the noise pick up. The BCML1 signal circuit is discussed in more detail in section 4.1.4.3, the complete BCML2 signal circuit can be found in the Appendix A.1.1.2.

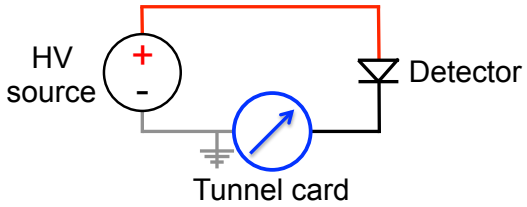

Figure 4.5: Schematic drawing of the electrical connection to a BCML detector channel. The tunnel card measuring the signal current on the return line is defining the ground of the electrical circuit.

4.1.3.2 Tunnel Card

The signal current of the BCML sensors is measured with the so called 'Tunnel Card'. This data acquisition card was developed as radiation hard front-end electronics for the BLM system at the LHC, where the detectors are placed in the LHC tunnel and hence the name 'Tunnel Card' originated. This data acquisition card placed in the LHC tunnel is exposed to magnetic fields and high radiation and was therefore designed to withstand 20 years of operation corresponding to 400 Gy [Eff07]. Test measurements showed a stable operation in a magnetic field of 0.1 T [Eff07]. The tunnel card can measure the signal current of 8 independent channels with a dead time free readout and a high dynamic range reaching from 2.5 pA to 1 mA. The measurement results is digitized and send at a rate of 25 kHz optically to the DAB card that is introduced in the next section 4.1.3.3, compare Fig. 4.4.

The measurement principle of the tunnel card is based on a current to frequency converter (CFC) that has the advantages of no dead time and no loss of charges [Fri02]. In order to increase the dynamic range of the measurement for very low currents, a 12 bit ADC is added that calculates partial CFC counts. The digitized result of the combined CFC and ADC measurement is readout every 40 µs and sent optically to the back-end electronics.

The working principle of the CFC measurement is schematically shown in Fig. 4.6. The detector current discharges a capacitor via an integrator circuit. If the voltage of the capacitor drops below a threshold the capacitor is immediately recharged via an internal current source. The amount of capacitor discharges, so called CFC counts, within 40 µs are accumulated and used to calculate the CFC frequency. A low CFC frequency corresponds to a small current and a high CFC frequency corresponds to a high signal current. The sensitivity and precision of

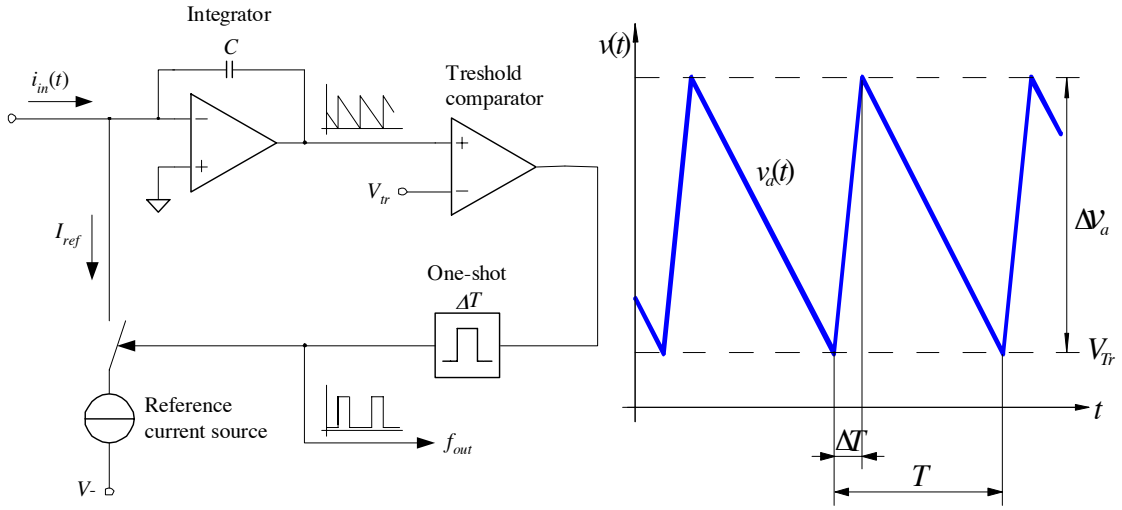

Figure 4.6: Schematic drawing of the CFC based signal measurement in the tunnel cards, figure taken from [Gsc02]. The detector current discharges the capacitor in the top left. If the capacitor voltage drop below a threshold a comparator triggers the recharge of the capacitor and counts it as one CFC count. The amount of CFC counts per 40 µs is used to calculate the CFC frequency on which the detector current calculation is based. The right figure shows the capacitor voltage over time for a constant detector current.

the current measurement is improved by an analog to digital converter (ADC) that measures the voltage of the capacitor every 40 µs. The voltage difference between the current and the previous ADC reading is converted to a signal current equivalent that is added to the current calculated based on the CFC measurement. Thereby the dynamic range of the signal measurement is in particular extended to the measurement of very low signal currents of 2.5 pA.

The tunnel card can only measures positive detector currents. An internal offset current of 10 pA is therefore created to avoid negative currents. Due to production tolerances the absolute capacity of the capacitor in ADC values is unknown, therefore the tunnel card performs every two minutes an internal calibration of the ADC against the full capacitor capacity. These calibrations can sometimes fail and cause so called 'calibration jumps' where the signal measurement is for the duration of 2 minutes slightly in- or decreased. Another source of errors is the combination of the CFC and the ADC measurement. Sometimes mismatches occur during this process resulting in a instant high measurement value in the 40 µs signal measurement. It was found that the frequency of these mismatches, causing spikes in the readout, increases approximately linearly with the measured signal current. Further details to the read out noise of the tunnel cards can be found in [Gut14a].

4.1.3.3 DAB Card: The Real-Time Data Processing Unit

The digital measurement results of the tunnel card are transmitted optically every 40 µs to a FPGA (Field Programmable Gate Array) based real-time processing unit, called 'Digital Acquisition Board' (DAB) [Jon04, Zam06]. The DAB card processes the data by calculating successive running sums (SRS). Besides that, the beam abort conditions and the health of the system are continuously checked. In Fig. 4.7 the highly efficient SRS technique is illustrated, which requires a minimum of memory by a full timing information of a beam loss event.

The basic principle of the SRS technique is the accumulation of the 40 µs signal for different rolling integration windows, so called running sums (RS). In total 12 different RSs are calculated covering integration times between 40 µs and 83 s, see Table 4.1. A RS is a

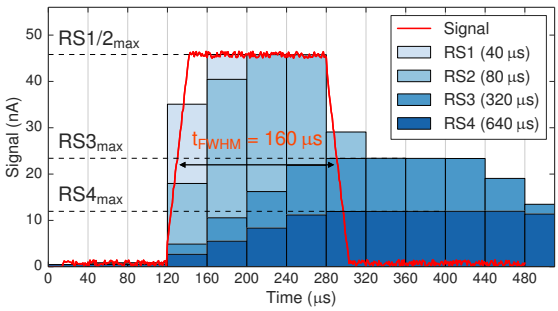

(a) Signal measurement of RS1 and RS2 integration window for a 160 µs long signal.

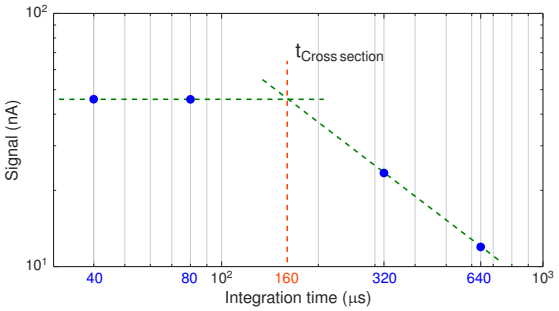

(b) Double logarithmic plot of the maximum RS signal as function of integration time.

Figure 4.7: Signal measurement using different Running Sums (RS). In Fig. (a) an example detector signal is shown in red. The tunnel card sends continuously the total measured charge of the last 40 µs. This charge converted to a signal current is indicated in light blue bars. The DAB card calculates based on the 40 µs readings the accumulated charge for different integration times. The accumulated charge normalized to a mean detector current is shown for RS2 (80 µs), RS3 (320 µs) and RS4 (640 µs) indicated in bright to dark blue. The read out cycle of the DAB card is 1 s (1 Hz) where only the highest value of each RS within the last period are transmitted. The maximum RS values of the RS1-4 can be used to estimate the signal duration shown in Fig. (b). The normalized maximum value of each RS is plotted over the corresponding integration time double logarithmically. By creating linear fits to both legs the cross section indicates the signal duration of 160 µs, see Fig. (b).

moving integration window, hence always according to the particular integration length the appropriate amount of previous 40 µs readings are included in the RS calculation. For the very short integration windows ($\leq$ 640 µs) the RS are recalculated at at frequency of 25 kHz, corresponding to an RS update of every 40 µs. The refresh speed of each RS can be found as well in Table 4.1. A beam abort threshold can be defined for every RS and as soon as one RS measurement exceeds its dedicated abort threshold the beam dump signal is asserted. The beam abort conditions are checked as well at a rate of 25 kHz.

Fig. 4.7a shows an example detector signal (red) and 4 different resulting running sum signals converted to a signal current using equation 4.2. The DAB card is read out at a frequency of 1 Hz where only the maximum values of each RS are recorded. The maximum RS values can be plotted double logarithmically like shown in Fig. 4.7b and be used to extrapolate the duration of a beam loss event. The technique of reading out only the maximum values of each RS overestimates for short RS the noise. For higher integration times ($\leq$ RS8) the readout noise can be neglected and the measured signal currents are realistic. Hence the SRS technique reduced dramatically the amount of data to be stored and still contains the full information of the duration of a beam loss event.

The full data stream of 40 µs readings within one cycle of data acquisition (1 s) is not immediately deleted but written in a buffer containing in total 25000 values:

$$\text{Buffersize}_{\text{PM}} = 1\,\text{s}/40\,\mu\text{s} = 25000. \tag{4.1}$$

The read out of the so called 'post mortem' data is triggered when the system triggers a beam abort signal. The post mortem data can be used to analyze the beam loss event in high detail. During Run 2 of the LHC the BCML system triggered once a beam abort. This triggered the read out of the post mortem data that was used for a detailed analysis of this beam loss event, see section 4.4.1.1.

The running sum values measured by the DAB card are given in ADC counts, corresponding to a total charge Q_{ADC}. The total charge can be converted into a current by the following

Table 4.1: Overview of all 12 running sums calculated in the DAB card [Zam06]. The RS values measured in ADC can be converted into a current in Ampere using Eq. 4.2 and the normalization factor X_{RS}, which is basically the integration time divided by 40 µs.

Name	X_{RS}	Integration time (ms)	Refresh time (ms)
RS1	1	0.04	0.04
RS2	2	0.08	0.04
RS3	8	0.32	0.04
RS4	16	0.64	0.04
RS5	64	2.56	0.08
RS6	256	10.24	0.08
RS7	2048	81.92	2.56
RS8	16384	655.36	2.56
RS9	32768	1310.72	81.92
RS10	131072	5242.88	81.92
RS11	524288	20971.5	1310.72
RS12	2097152	83886.1	1310.72

equation:

$$Q_{\mathrm{RS}}\,(\mathrm{ADC})/\mathrm{X_{RS}}/(204.8\times10^{6}) = \mathrm{I}\,(\mathrm{A}) \tag{4.2}$$

with X_{RS} as normalization factor (see Table 4.1) and 204.8×10^{6} as conversion factor.

4.1.4 BCML Hardware Failures observed during Run 2

The BCML system is a critical for the safety of the CMS detector, therefore failures or hardware incident result typically in the initiation of the LHC beam dump. This feature is intended by design, if the BCML system is not working properly the safety of the CMS detector can't be guaranteed and a LHC beam dump must be triggered. In the following sections all major hardware incidents are listed that triggered a beam dump or prevented injection for a new physical fill. Luckily none of these technical incidents triggered a LHC beam abort during a physical fill.

At the beginning of Run 2 the BCML power supply was repeatedly failing and triggered several times the LHC beam dump, see section 4.1.4.1. A broken CPU in 2016 prevented the injection of a new physical fill, discussed in section 4.1.4.2. And during the first measurement in 2016 a reduced sensitivity of the BCML1 detector for short beam loss events (< 3 ms) was observed. The reason for this inefficiency was found to be a wrongly placed filter element, see section 4.1.4.3.

4.1.4.1 CAEN Power Supply Failures

During the Long Shutdown 1 of the LHC between 2013 and early 2015 the CAEN main power supply of the BCML system was upgraded from the SY1527 model [CAEa] to the model SY4527 [CAEb]. This exchange was needed since the support of the CAEN SY1527

model was discontinued. The new CAEN mainframe was 'burned in' and extensively tested before installation at the CMS detector. After 1.5 month of detector operation the entire CAEN however crashed and went off, this caused the switch off of all BCML HV channels and all BCML2 LV channels and resulted in a beam abort trigger. The very same thing happened again a month later and a third times only another 13 days later and caused each time a beam abort trigger, fortunately a beam was never present. After the second mainframe crash a device (Fluke VR1710 [FLU]) was installed measuring the voltage quality of the grid power. This voltage quality recorder measured a slight increase in the grid voltage at the very same moment when the CAEN mainframe crashed the third time. Such a slight increase of the grid voltage was not recorded before, besides exactly during the crash of the mainframe. This slight voltage increase was perhaps caused by a high frequent signal, injected by another system connected to the same grid, which propagated via the grid into the CAEN mainframe causing there a failure of e.g. the CPU. It is still not clear what finally caused the crash of the mainframe, however in order to guarantee stable operation the CAEN SY1527 (old) replaced the CAEN SY4527 (new). A low pass filter was installed additionally between the power outlet and the mainframe to reject high frequent oscillation. Since these measures the CAEN SY1527 worked reliably.

4.1.4.2 Broken CPU Card Preventing Beam Injection

The CPU unit, which acts as bridge between the BCML DAQ system and the server processing the data, stopped working, compare Fig. 4.4 in section 4.1.3. A broken CPU doesn't immediately result in a beam abort trigger, since the BCML hardware itself still works fine. While trying to recover the CPU and power cycling the particular crate the beam abort was however triggered and the beam injection permit revoked. After a power cycle the CPU initializes the DAB cards. If this operation fails the DAB card sends a beam abort trigger because the defined thresholds are potentially wrong. During the time till the CPU card was replaced (30 min) the BCML system prevented the injection of a new physics beam. After the replacement of the CPU the beam permit was given again.

4.1.4.3 Reduced BCML1 Detector Sensitivity for Short Beam Loss Events

During the splash events, described in section 4.3.2, it became obvious that the BCML1 electrical readout chain is not efficient for short beam loss events (< 3 ms). The entire electrical circuit, shown in detail in Fig. 4.8, consists of two units separated by 120 m long coaxial cables. At each location a passive filter unit (Fig. 4.8: Filter 1) consisting of 4 resistors and 3 capacitors is used to remove high frequent oscillations from the electrical circuit. An additional decoupling filter (Fig. 4.8: Filter 2) is placed close to the detector in order to stabilize the voltage. This decoupling filter provides free charge carriers to prevent a bias voltage drop at the detector when a signal is created. All capacitors in the entire electrical circuit are grounded in the counting room.

In order to verify and understand this reduced efficiency of the BCML1 detector for short beam loss events, the entire electrical circuit used at CMS, including the 120 m long coaxial cable, was set up for tests in the laboratory. Instead of the diamond sensors used at CMS, two silicon diodes were mounted on the BCM C-shape. During setting up the test circuit it turned out that the decoupling filter was mounted on the signal return line instead of the high voltage line, like shown in Fig. 4.9. To confirm that the wrong location of the decoupling filter is causing the inefficiencies of the BCML1 detector for short beam loss events, the silicon diodes mounted on the C-shape were used to inject short signal into the electrical circuit for both decoupling filter configurations. The short silicon sensor signals were created by flashing the silicon sensor with red light created by a LED that was powered with a signal generator, where different pulse lengths could be generated.

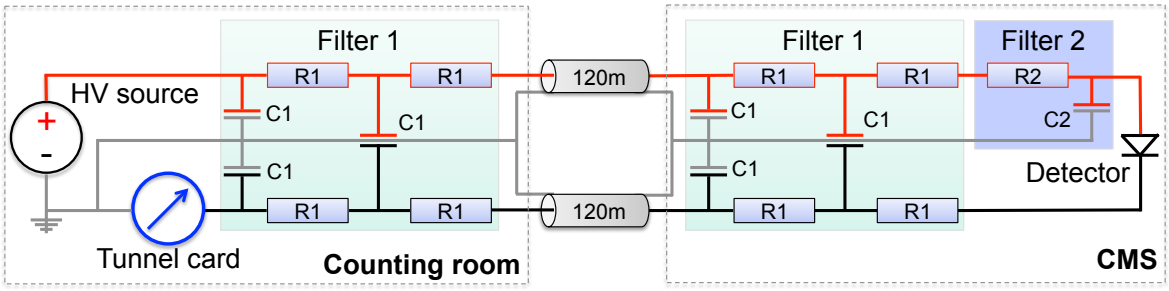

Figure 4.8: Desin of the BCML1 electrical circuit. The electrical detector signal created at CMS is transmitted via a 120 m long coaxial cable to the read out system (tunnel card) located in the counting room. Additional filter units are removing high frequent oscillations and stabilizing the voltage applied to the detector. The values of the passive components are: R1 = 1 Ω, R2 = 1 MΩ, C1 = 1 nF and C2 = 10 nF.

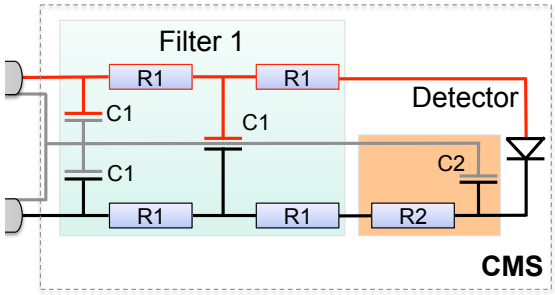

Figure 4.9: Implementation of the BCML1 electrical circuit at CMS. Instead of having the decoupling filter on the high voltage line (red) like shown in Fig. 4.8, the decoupling filter (orange) at the BCML system at CMS is mounted on the signal return line (black).

In Figure 4.10 the running sum spectra[2], measured with the tunnel card, are shown for two different LED pulse lengths. For a LED pulse duration of 10 ms (Fig. 4.10a the signal characteristic of both decoupling filter configuration is equal. For a shorter signal pulse duration of 1 ms the location of the decoupling filter is strongly influencing the signal shape, see Fig. 4.10b. The short signal pulse can be measured as expected with the correct decoupling filter configuration located on the HV line. The measured signal with the decoupling filter on the signal line is however strongly reduced an is only barley visible in higher RS with signal integration times of $I_{\text{int.}} > 3$ ms. For reduced signal integration time no signal is measured. Hence the poor efficiency of the BCML1 detector for short beam loss events (< 3 ms) at the CMS detector can be explained by the wrong positioning of the decoupling filter, see section 4.3.2. This decoupling filter sitting on the signal line can also be understood as a RC filter unit with a time constant of

$$\tau = \text{RC} = 1 \times 10^{6} \cdot 10 \times 10^{-9} = 10\,\text{ms}. \tag{4.3}$$

Therefore, all short beam loss events (<3 ms) were filtered out by the decoupling capacitor. In order to repair the BCML1 electrical circuit at CMS and restore the sensitivity for short beam loss events, the connection of the 120 m long cables to the patch panel in the counting room was swapped like indicated in Fig. 4.11. This changed the position of the decoupling filter to be, like intended, on the HV line. The increased sensitivity of the BCML1 detector after the cable swapping can be seen in Fig. 4.12, where a beam loss event before and after the BCML1 intervention is shown.

To verify a good understanding of the performance of the BCML1 electrical circuit for short signals, the entire electrical read out circuit was simulated with the software LTSpice IV [Lin].

[2]The running sum spectra is explained in detail in section 4.1.3.3.

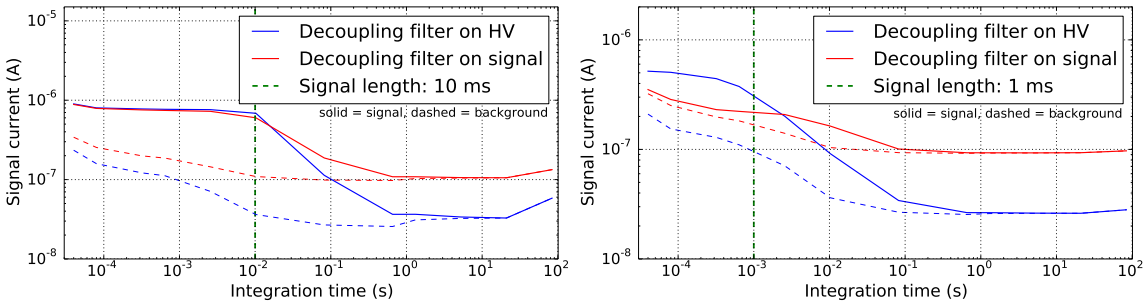

(a) 10 ms LED pulse **(b)** 1 ms LED pulse

Figure 4.10: Running sum spectra measured with tunnel card for a 10 ms and a 1 ms LED pulse. For the longer 10 ms LED signal the running sum spectrum of the two decoupling filter configuration look identical. The shorter LED signal of 1 ms can only be measured with the decoupling filter on the HV line. The configuration with the decoupling filter on the signal line is filtering the signal and is therefore only barely visible.

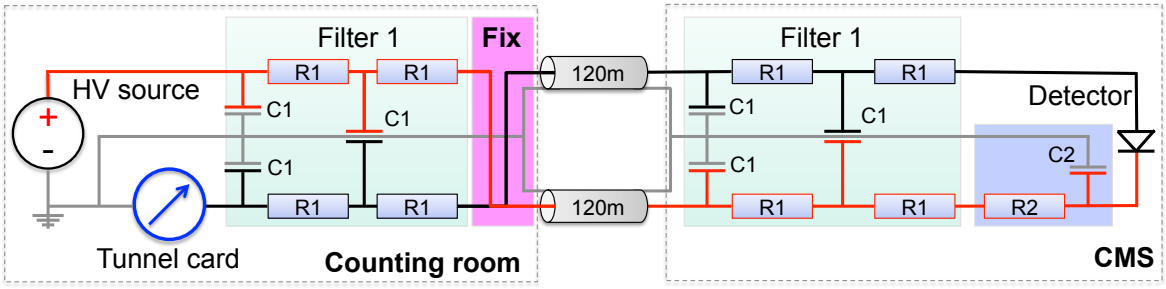

Figure 4.11: The repaired BCML1 electrical circuit at CMS. The HV (red) and the signal (black) cable are swapped in the counting room, indicated in purple. With this fix the decoupling filter is placed back on the HV line, like originally designed. The swapping of the cables changed as well the polarity of the pCVD diamonds, which can be operated in both polarities.

The LTSpice simulation results were compared to measurement results to verify a correct simulation of the BCML1 signal circuit. An increased timing resolution of the silicon diode

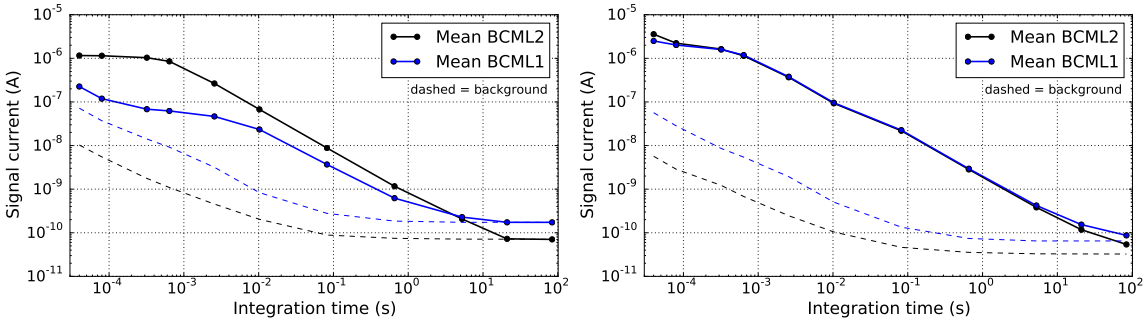

(a) before intervention **(b)** after intervention

Figure 4.12: BCML measurement of beam loss events before and after the BCML1 intervention. A beam loss event measured with the BCML detectors before the BCML1 intervention was done is shown on the left side. The BCML1 signal (blue) is strongly reduced for short integration windows (< 3 ms) with respect to the signal measured by the BCML2 detector (black). A beam loss event measured after the BCML1 intervention is shown in the right figure. The average beam loss signal measured by the BCML1 and BCML2 detector location are identical and demonstrate the full sensitivity of the BCML1 detector as well for very short signals.

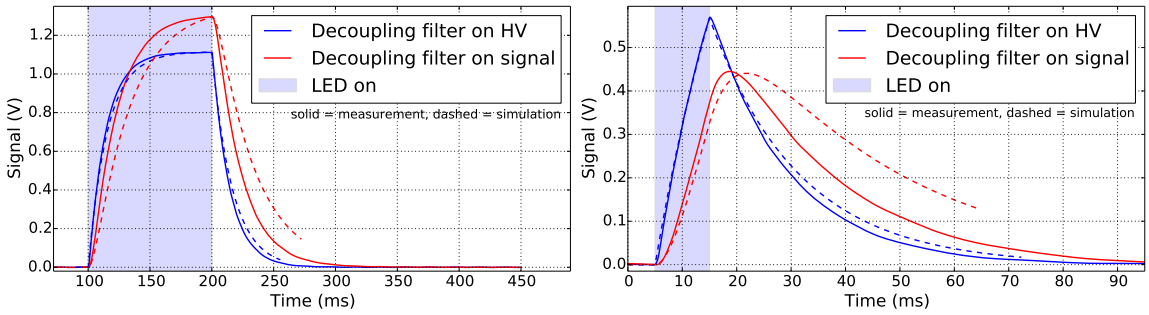

(a) 100 ms LED pulse **(b)** 10 ms LED pulse

Figure 4.13: Timing structure of a 100 ms and a 10 ms LED pulse signal measured with an oscilloscope shown in solid lines for the original and the corrected electrical signal read out circuit. The 100 ms and 10 ms LED signal pulse were simulated with LTSpice for both electrical circuit configurations and are shown in dashed lines.

signal created by the red LED light was gained by replacing the tunnel card measurements with an oscilloscope. Since the signal current was very small, the oscilloscope itself had to be set to a resistance of R = 1 MΩ, leading to a further flattening out of the signal. The measurement results with the oscilloscope for two different pulse length duration is shown in Figure 4.13. For a pulse duration of 100 ms in Fig. 4.13a the signal for both decoupling filter configurations reach saturation. The maximum signal is slightly increased for the configuration with the decoupling filter on the signal line (red), which is caused by a slightly increased exposure of the particular silicon diode to the LED light. For a reduced pulse duration of 10 ms, shown in Fig. 4.13b, the configuration with the decoupling filter on the signal line shows already a strong filter effect resulting in a reduced maximum signal created by the silicon diode. For both pulse duration measurements the simulation results are indicated in dashed lines. The simulation results are in good agreement with the measurements results and confirming a good modeling of the entire electrical BCML1 read out circuit, in particular as well the 120 m long coaxial cable. The LTSpice simulation can therefore be used to optimize the BCML1 electrical read out circuit in terms of reducing high frequent noise oscillations and improving the sensitivity for short beam loss events, see section 7.3.

Further measurements with different LED pulse duration and more detailed information to the LTSpice simulation can be found in the appendix A.1.1.1.

4.2 Definition of the Beam Abort Thresholds

The CMS BCML system is designed to protect the CMS inner detector against intense beam loss events that could potentially cause severe irradiation damage. The beam abort is initiated if the BCML detector is measuring a signal current above predefined abort thresholds. At the beginning of the LHC operations in 2015, two abort thresholds were defined, one for short duration ($\leq 40\,\mu s$) dangerously high beam losses and one for longer-term ($\leq 83\,s$) high beam background conditions that can result in problematic conditions for data taking and in an increased dose to the inner detector region [Kas15]. Due to the reduced BCML1 detector sensitivity for short beam loss events a medium-time scale threshold was temporarily introduced till the inefficiency was understood and repaired [Kas16a, Kas16b], see section 4.1.4.3.

The calculation of the abort threshold definition for the BCML detectors during Run 2 is explained in the following, further details can be found in [Kas15].

Abort threshold for Running Sum 1 (40 µs)
The abort threshold in RS1 is used to protect the CMS tracker before very short and high

intense beam loss events. Damage tolerance studies of the CMS tracker set the maximum limit of particle hitting the detector to $f = 10^9\,\mathrm{MIPs/cm^2}$ per "short beam loss event" ($\leq 40\,\mu\mathrm{s}$) [Mue11]. Adding a safety margin of 1000 results in a maximum particle fluency of $f_{\max} = 10^6\,\mathrm{MIPs/cm^2}$ per short beam loss event. The total charge measured in RS1 for an undamaged pCVD diamond detector based on $f_{\max}$ is then:

$$\begin{aligned} Q_{\max} &= 10^6\,(\mathrm{MIPs/cm^2}) \times 0.925\,(\mathrm{cm^2}) \times 36\,(\mathrm{e/\mu m}) \times\ 210\,(\mu\mathrm{m}) \times \mathrm{q_e} \\ &= 1.12^{-9}\,\mathrm{C} \end{aligned} \tag{4.4}$$

with $0.925\,\mathrm{cm^2}$ active detector surface, 36 as average charge created by a MIP particle per μm of diamond thickness, $210\,\mu$m as average charge collection distance and q_e as elementary charge. This charge deposition $Q_{\max}$ translates in RS1 into a signal current of:

$$I_{\mathrm{RS1\,max}} = Q_{\max}/(40 \times 10^{-6}) = 28\,\mu\mathrm{A}. \tag{4.5}$$

The threshold defined for RS1 was set to an even more conservative value of $I_{\mathrm{RS1\,max}} = 10\,\mu$A equivalent to 2050 ADC. The thresholds defined in RS1 for undamaged pCVD diamond detectors are therefore a factor of 3000× more tight compared to the upper limit of the trackers damage tolerance. This definition of the RS1 abort threshold holds for new pCVD diamond detector with a CCD of $210\,\mu$m. For pCVD diamond detectors with reduced CCDs due to irradiation damage the abort thresholds have to be adjusted accordingly to maintain a minimum safety factor of 1000, see section 4.5.1.

Abort threshold for Running Sum 4 (640 µs)
For the first half of the year 2016 an abort threshold in RS4 was introduces for the BCML1 detector, since very short beam loss events could not be measured, see section 4.1.4.3. The RS4 beam abort threshold was defined identical to the RS1 abort threshold. Based on the charge $Q_{\max}$ (Eq. 4.4) that a very short ($< 40\,\mu$s) and intense beam loss event would induce into a pCVD diamond detector, including the minimum safety factor of 1000×, the average signal current measured in RS4 translates to:

$$I_{\mathrm{RS4\,max}} = Q_{\max}/(640 \times 10^{-6}) = 1.75\,\mu\mathrm{A}. \tag{4.6}$$

The RS4 abort threshold of $I_{\mathrm{RS4\,max}} = 1.75\,\mu$A, corresponding to 5730 ADCs, was removed after the source for the reduced sensitivity of the BCML1 detectors was found and repaired.

Abort threshold for Running Sum 12 (83 s)
The abort threshold for RS12 is calculated based on increased beam background activity compared to the expected particle flux at nominal CMS luminosity. The threshold is defined to be 3× the expected signal based on a data driven extrapolation for nominal instantaneous LHC luminosity of $\mathcal{L}_{\mathrm{inst.}} = 1 \times 10^{34}\,\mathrm{cm^{-2}s^{-1}}$ [Kas15]. The nominal instantaneous luminosity was increased during LHC operations in 2016 to $\mathcal{L}_{\mathrm{inst.}} = 1.4 \times 10^{34}\,\mathrm{cm^{-2}s^{-1}}$ and hence the beam abort thresholds for RS12 were accordingly adjusted [Kas16a, Kas16b].

The abort threshold definition in particular for the RS1 and RS4 are only valid for undamaged pCVD diamond detectors with a average CCD of $210\,\mu$m. The CCD of the diamond detectors was however significantly reduced due to irradiation damage that the abort thresholds had to be adjusted to keep the minimum safety margin of 1000×. The signal efficiency of all BCML channels was tracked closely and resulted three times in a redefinition of the abort thresholds, see [Kas15, Kas16a, Kas16b]. The reduced BCML detector sensitivity due to irradiation damage is discussed in detail in section 4.5.1.

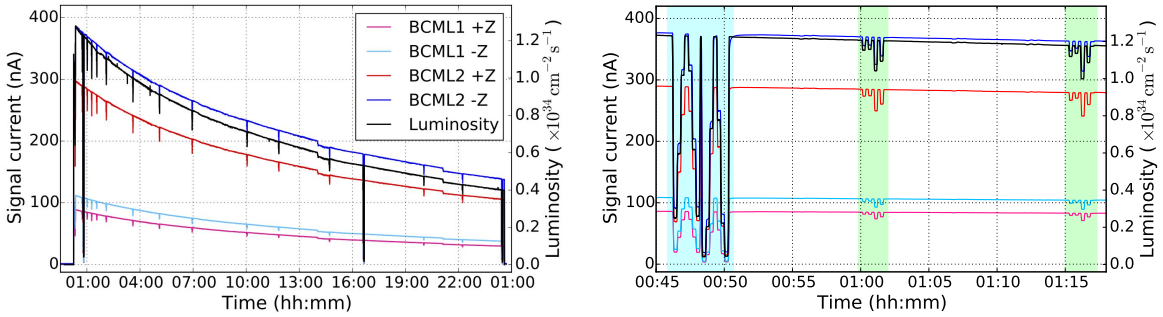

(a) Typical fill of LHC. **(b)** Optimization scans during fill.

Figure 4.14: The BCML detector signal is directly correlated to the luminosity at CMS, shown on the left. During this fill 5277 the luminosity was measured with the PLT detector (see section 2.3.2.1). Throughout the entire LHC fill beam scans or so called 'mini Van Der Meer (VDM)' scans are regularly done in order to optimize the luminosity at CMS. On the right figure a mini VDM (blue) and a short (green) optimization scans are shown.

4.3 BCML detector in operation

4.3.1 Typical measurements during LHC operation

The task of the BCML detector is to monitor the beam conditions continuously without any downtime, regardless if beam is in the machine or not. When a particle beam is inserted in the machine and brought into collision the BCML detectors signal is correlated linearly to the instantaneous luminosity at the CMS detector. The instantaneous luminosity depends on various beam parameters like the beam intensity, β^* or the emittance, further details are discussed in section 2.1.4. At the beginning of a new fill the highest instantaneous luminosity and hence the highest BCML detector signal is measured. With increased fill duration the beam intensity decreases due to beam losses and due to the particle collision at each interaction point. If the luminosity is decreased typically below 35% of it's initial value the beams are dumped and the LHC is refilled. The signals measured with the BCML detectors for the $\pm$ Z location compared to the instantaneous luminosity is shown in Fig. 4.14a. The difference of the signal intensities between the BCML1 and the BCML2 detectors is caused by the different detector locations and hence a different flux of charged particles. Furthermore, the signal intensity for the same detector is varying as well between the +Z and -Z locations dominantly caused by different detector efficiencies due to different radiation damage levels. A detailed analysis of the radiation induced detector damage and the accompanied decreased in signal efficiency is given in chapter 5.

The signal measured by a BCML detector is almost entirely generated by collision products and is therefore proportional to the instantaneous luminosity at CMS. The optimization scans, regularly done during a LHC fill in order to optimize the collision rate at CMS, show this correlation of the BCML signal with the luminosity, see Fig. 4.14b.

4.3.2 First detector check out: Splash events

On Sunday the 5th of April 2015 proton beams were circulating in the LHC for the first time after the Long Shutdown 1, a break of two years. This was followed on Tuesday the 7th of April 2015 by dedicated runs to allow the two experiments CMS and ATLAS to record their first signals coming from particles splashing against collimators. The collimators up- and downstream of the experiments were therefore completely closed, see Fig. 4.15. The proton beam, consisting of one bunch with an intensity of $I \approx 5 \times 10^9$ p/bunch, was colliding with the closed collimator and generating a high MIP particle flux in the entire CMS detector

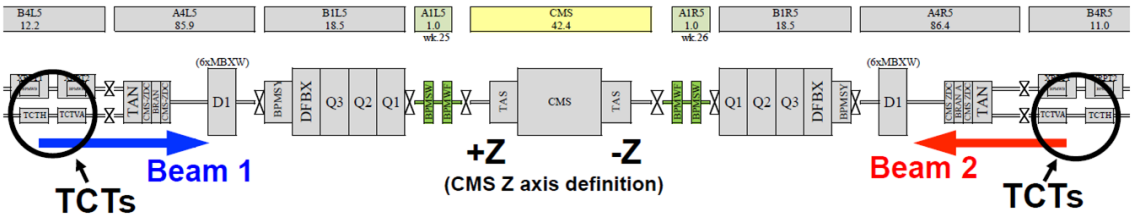

Figure 4.15: Location of the CMS detector with respect to the surrounding infrastructure. The tertiary collimators (TCT), which were closed to create the splash events, are located $d \sim 150\,\text{m}$ upstream and downstream of the CMS detectors. Figure taken from [Gut14a].

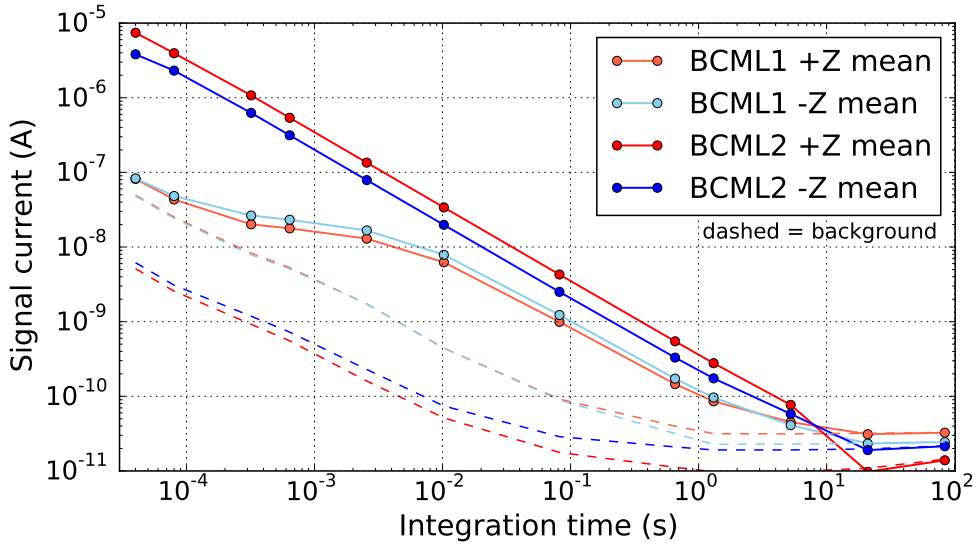

Figure 4.16: BCML measurement of a splash event. The average signal current of the BCML1/2 detectors are plotted double logarithmically over the integration time, see section 4.1.3.3. The expected linear signal decreased for the very short splash events can be seen in the BCML2 measurements for the +/- Z end. During the splash events the BCML1 detectors were not sensitive for short beam loss events and hence show a different pattern. The dashed lines are indicating the mean background.

volume. The splash events were performed for both beam direction. After the 'Year End Technical Stop' (YETS) in 2015/16 these splash events were performed as well, however at higher intensities $I \approx 1 \times 10^{10}$ p/bunch. Such a splash event measured with the BCML detectors is shown in Fig. 4.16 in the typical double logarithmical running sum plot, compare section 4.1.3.3.

A proton particle bunch splashing at the collimators is creating a very intense and short ($< 100\,\text{ns}$) beam loss event. Hence a linear decrease of the signal current with increased integration time, which can be seen for the BCML2 detectors, is expected. The signal shape of the BCML1 detectors however show this linearity only for higher running sums above 3 ms, indicating a strongly reduced efficiency for short signals ($< 3\,\text{ms}$). Based on this measurement the beam abort thresholds discussed in section 4.2 were changed for the BCML1 detector. The reason for the reduced sensitivity of the BCML1 detector for short beam loss events was understood and repaired, and is discussed in detail in section 4.1.4.3.

Beam 2 splashing against the collimators upstream of CMS on the -Z side created the measured splash event shown in Fig. 4.16. This can be seen as well in the measurement of the BCML2 detectors, since the signal measured on the + Z side is about 2 times higher compared to the signal measured on the -Z side. The splash event from Beam 2 arrives first on

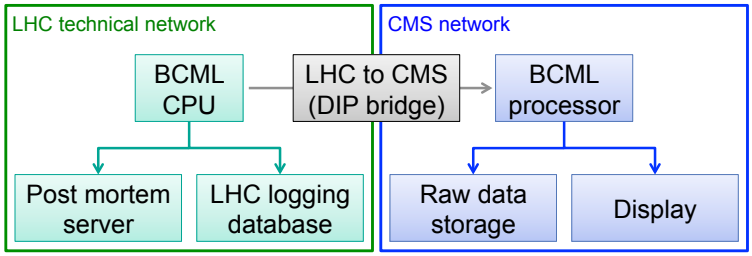

Figure 4.17: Data flow of the BCML detector. The BCML data is sent via the DIP Bridge to the BCML processor. The BCML processor is saving the raw data on a local server and sending selected information to the online displays via a flash list.

the -Z side and is scattering downstream. The particle scattering through the entire CMS volume are creating lots of secondary particles leading to an increased signal on the +Z side.

4.3.3 Feedback of the BCML detector performance by Online Display and Automatic Offline Analysis

The BCML detector is an extension of the LHC BLM system and hence part of the LHC technical network. The BCML data published by the BCML CPU is send to the CMS network via a DIP bridge and picked up by the BCML processor, see Fig. 4.17. The BCML processor is saving the entire raw data on a local server and sending selected data to a flash list used by the online BCML displays.

4.3.3.1 Online Display of the BCML Measurement

The BCML online display shows the BCML signal over the last 24 hours based on the RS9 measurement. In addition the percentage of the beam abort is calculated by the BCML processor and displayed for RS1 and RS12 for the abort channels. The BCML display is based on an elastic search database for two purposes. First, the BCML data can also be queried for a particular time in the past and secondly also very long fills (>24 hours) can be displayed quickly. To prevent long loading times of the data an algorithm is selecting only the maximum data points of a particular window size, reducing the total amounts of data points to be displayed. This online display can be opened with a normal browser and makes quick checks of the BCML detector performance very convenient, a screen short of the display is shown in Fig. A.12 in the Appendix.

4.3.3.2 Automatic Offline Analysis of the BCML Detector Performance

The BCML detector performance is analyzed automatically and the results are summarized in a HTML file for each fill. The BCML fill report includes an individual calculation of the radiation induced detector degradation for each channel. Based on these results the quality of the currently applied abort thresholds is classified and in case of a miss match prominently indicated in the report. The script is looking in addition automatically for beam loss events of any kind. The possible beam loss candidates are plotted in the typical double logarithmical style and are appended to the BCML fill report. The physical hardware parameters of the BCML readout system are analyzed and in case of problems displayed via error messages.

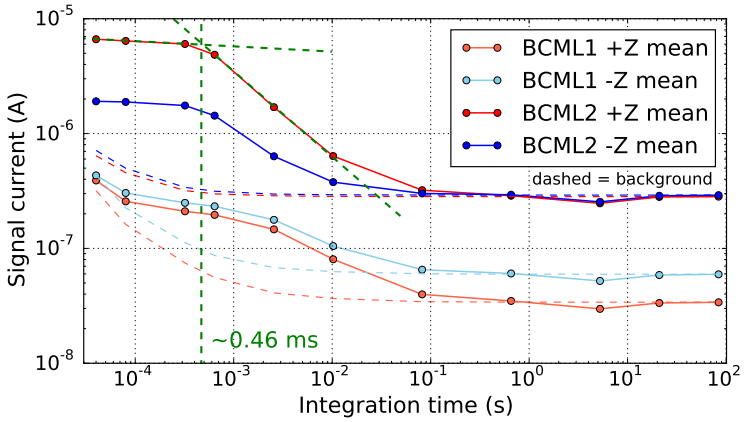

Figure 4.18: BCML running sum spectrum of the beam abort event. The mean running sum values for each BCML detector location are shown. Fitting both legs of the RS spectrum suggests a beam loss duration of 460 µs. During the time of the beam loss event, BCML1 was still inefficient for short beam loss events (<3 ms) explaining the very small signal.

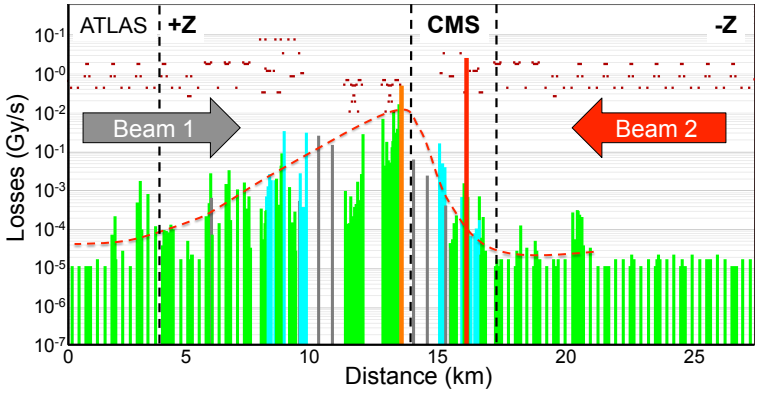

Figure 4.19: Global LHC BLM measurements. The beam loss event triggering the beam abort measured by the global LHC BLM system. A BLM close to CMS measured a beam abort level of 93% (orange) and confirmed the BCML measurement (red). The beam loss event in Beam 2 was scattering further downstream and could even be measured at the ATLAS detector at Point 1.

4.4 Beam Loss Events measured with the BCML Detector

The beam loss events occurring at the LHC can be categorized into short and long beam loss events. Short beam loss events, with a duration of less than 3 milliseconds [Jea96], are typically created by beam interactions with dust particles falling through the proton beam, so called UFO (unknown falling objects) events, see section 4.4.1.2. Longer beam loss events, typically caused by a bad vacuum inside the beam pipe, will be discussed in section 4.4.2. The first subsection 4.4.1.1 however will focus on the first time the BCML system triggered the LHC beam abort in 2016 to prevent severe radiation damage to the CMS tracker.

4.4.1 Short Beam Loss Events

4.4.1.1 Trigger of the Beam Abort during LHC operation in 2016

During the LHC operation in 2015 and 2016 the CMS BCML system triggered once the beam abort of the LHC on the 16th of August in 2016, dumping the LHC beam within the next 300 µs. The beam loss event reached 104 % of the beam abort threshold in the BCML2 +Z

Table 4.2: Average MIP flux estimation for the BCML detectors. Based on the detector degradation induced by radiation damage (see section 4.5.1), the CCEs of BCML1 and BCML2 were estimated to: $\mathrm{CCE_{BCML1}} = 23\%$ and $\mathrm{CCE_{BCML2}} = 17\%$. For the conversion of the BLM signal into a MIP equivalent, the result of a comparison between a BCML2 diamond detector and a BLM detector in a test beam was used, see [Mue11]. For a given particle rate, the BLM signal is correlated to an undamaged BCML2 detector by: $I_{\mathrm{BLM}}(\mathrm{A}) = 1.20 \times I_{\mathrm{BCML2}} - 2.1 \times 10^{-9}$.

Detector location	$I_{40\,\mu\mathrm{s}}$ (μA)	Q (fC)	MIP (#/cm^2/40 μs)
BCML1 +Z	0.39	15.6	0.028×10^6
BCML1 -Z	0.43	17.2	0.030×10^6
BCML2 +Z	6.42	256.8	0.594×10^6
BCML2 -Z	1.89	75.6	0.175×10^6
BLM +Z	4.35	174.0	0.334×10^6
BLM -Z	2.98	119.2	0.229×10^6

inner far channel and was visible in all BCML detector channels on the BCML2 +Z and -Z end. The running sum spectrum shown in Figure 4.18 suggests a duration of this beam loss event of $t \approx 0.46\,\mathrm{ms}$. The BCML1 detectors hardly measured the beam lost event, because the detector was still not sensitive for short beam loss events (<3 ms), see section 4.1.4.3.

This beam loss event created a more than 3 times increased signal on the BCML2 +Z end compared to the BCML2 -Z end. This indicates a beam loss event caused by Beam 2, passing CMS from the -Z side to the +Z side. The primary particles lost due to the beam loss event are scattering mainly at the beam pipe, and causing an increased MIP particle flux further downstream the beam pipe, compare Fig. 4.15. The global structure of this beam loss event is shown in Fig. 4.19 measured by the LHC beam loss monitors. The beam loss caused by Beam 2 upstream of CMS was measurable even at ATLAS (Point 1) on the other side of the LHC ring. A LHC beam loss monitor close to CMS measured a signal of 93% of its abort threshold and hence confirmed the critical beam loss event measured by the BCML detector.

Estimation of the MIP particle flux causing the beam abort

Based on the BCML2 detector signal measurement the MIP particle rate during the UFO event can be calculated. The ADC signal measurement in RS1 is converted into a total amount of charge created in the BCML2 detector within this 40 μs integration window using Eq. 4.2:

$$Q_{\mathrm{RS1}}\,(\mathrm{C}) = \mathrm{Q_{RS1}}\,(\mathrm{ADC})/204.8 \times 10^6 \times 40\,\mu\mathrm{s} \tag{4.7}$$

with Q_{RS1} as total measured charge. The amount of MIP particle is given by:

$$\mathrm{MIPs}\,(\#/\mathrm{cm}^2) = \frac{Q_{\mathrm{RS1}}}{q_{\mathrm{e}} \times Q_{\mathrm{MIP}} \times l \times \mathrm{CCE} \times S} \tag{4.8}$$

with $q_e = 1.602 \times 10^{-19}\,\mathrm{C}$ as elementary charge, $Q_{\mathrm{MIP}} \approx 36\,\frac{\mathrm{e/h-pairs}}{\mu\mathrm{m}}$ as MIP ionization yield for diamond [Pom08], $l = 500\,\mu\mathrm{m}$ as thickness of the sensors, CCE = 17% the mean detector charge collection efficiency and the mean active surface of the BCML2 detector of $S = 0.925 \times 0.925 = 0.855\,\mathrm{cm}^2$, see section 4.1.2.1. The calculation of the mean CCE of the BCML2 detector is based on the continuous tracking of the signal degradation during the LHC Run 2 in 2015 and 2016, discussed in detail in section 4.5.1. Hence the MIP particle amount per cm^2 causing the beam abort can be calculated using equations 4.7 in equation 4.8. The BCML2 detector triggering the beam dump measured an average MIP particle flux

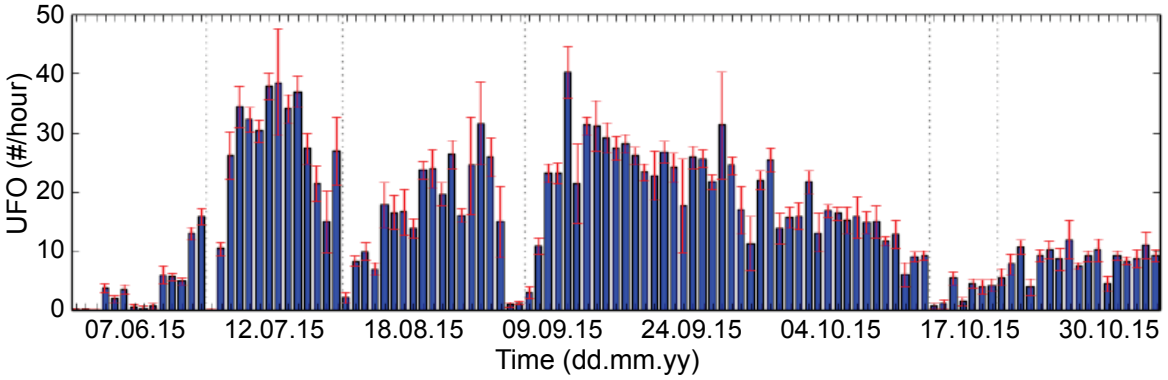

Figure 4.20: UFO events measured by the LHC BLM system. Rate of measured UFO events per hour at the LHC during physics operation in 2015. Graph taken from [Pap16].

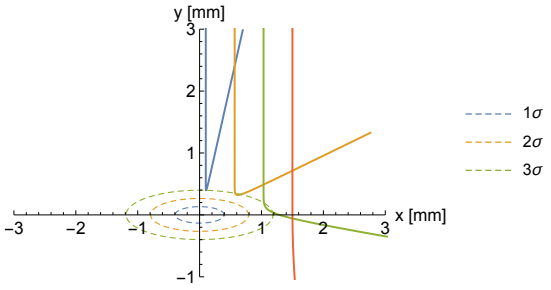

(a) Numerical simulation of a falling marcoparticle for different flight paths. The proton beam is indicated in dashed lines.

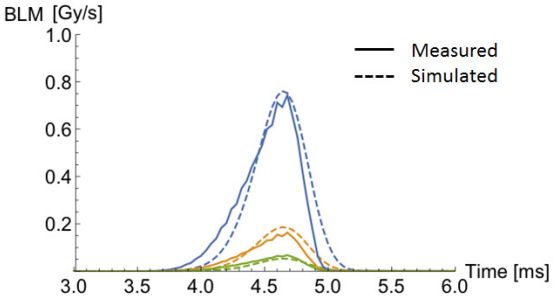

(b) Comparison between the simulated (dashed) and the measured (solid) signal of a BLM monitor for a UFO event for different flight paths indicates a Gaussian signal shape.

Figure 4.21: Figures are taken from [Row15].

during this beam loss event of:

$$\mathrm{MIP}_{\mathrm{BCML2\ +Z\ inner\ far}} = 0.972 \times 10^6\,\mathrm{MIPs/cm^2/40\,\mu s}$$

for a total measured charge in the 40 µs integration window of $Q_{\mathrm{RS1}} = 2132\,\mathrm{ADC}$ equivalent to a signal current of $I_{\mathrm{RS1}} = 10.5\,\mu\mathrm{A}$. Hence this beam loss event reached $< 1‰$ of the trackers damage threshold, defined to $10^9\,\mathrm{MIP/cm^2}$ per 'short beam loss event' [Dab11] maintaining the minimum safety margin of 1000, see section 4.2. The mean results for the BCML1 ±Z, the BCML2 ±Z detector locations and as well the results of the BLM tubes ±Z are listed in table 4.2. The BLM tubes ±Z confirm the measurement of the BCML2 ±Z detectors, the BCML1 detector however was still not sensitive for short beam loss events and measured almost no signal, see section 4.1.4.3.

This beam abort event demonstrates the importance of the BCML detector system protecting the CMS tracker before potentially damaging beam losses locally at the CMS detector.

4.4.1.2 Beam Losses caused by Unidentified Falling Objects (UFOs)

Short beam loss events are typically caused by Unidentified Falling Objects, so called UFO events. This well understood phenomena describes the resulting beam loss event when macro particles (dust particles) are falling down from the inside wall of the beam pipe on to the proton beam, further details can be found in [Bae11, Bae12]. During physics operation in 2015 with a beam energy of 6.5 TeV an UFO rate of 30-40 events per hour was observed at

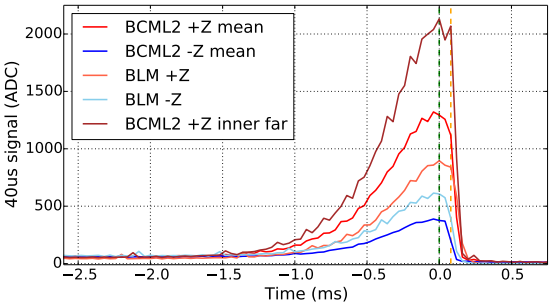

(a) The BCML2 detectors compared to the BLM detectors installed at CMS.

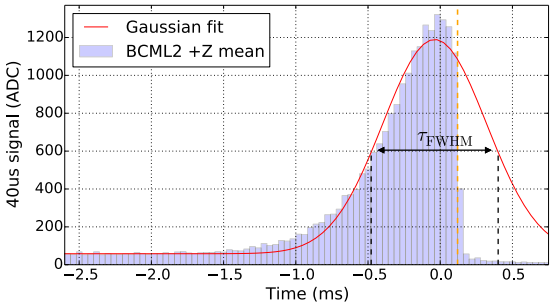

(b) Gaussian fit to the post mortem data measured by the BCML2 +Z detectors.

Figure 4.22: Timing structure of the beam loss event causing the beam dump. At 0 ms the beam dump was triggered (green line) and after 120 µs (orange line) the LHC beam was dumped. On the right side the post mortem data of the BCML2 +Z detectors was fitted with a Gaussian shape typical for UFO events. A beam loss duration of $t_{\mathrm{FWHM}} = 879\,\mu\mathrm{s}$ can be calculated based on the Gaussian fit.

the LHC, shown in Fig. 4.20. These macro particles and proton beam interactions produce particle showers that could lead to a significant energy deposition in the beam pipe periphery, threatening the superconducting magnets of the LHC that could ultimately lead to quenches or as well threatening the CMS tracker. UFO events were therefore studied in details in order to effectively protect the LHC hardware against these kind of beam loss events. The UFO signal, measured with a BLM detector, was numerical simulated for different flight-paths, see Fig. 4.21. The simulation results show that a Gaussian shaped signal is expected independent from the actual flight path, further details can be found in [Row15]. Three key characteristics were found describing the UFO events:

- Is a localized beam loss event
- Signal has a Gaussian shape
- Duration is typically around 640 µs

Based on these results the LHC BLM system was optimized in order to minimize the number of quenches, while keeping the number of avoidable beam dumps due to the BLM system to a minimum [Auc14]. The beam abort event measured by the BCML2 detector showed a UFO like timing structure with a duration of $\approx 460\,\mu\mathrm{s}$. Since the beam abort was triggered the post mortem data was read out as well. The full timing structure of all BCML detectors for this short beam loss event is therefore available. In Figure 4.22a the mean BCML2 detector response for ±Z is compared to the BLM monitors mounted at the same location. The beam abort is triggered at 0.0 ms and was executed 120 µs later indicated in the orange dashed line. The typical Gaussian signal shape of an UFO event can be seen in Fig. 4.22b for the mean signal of the BCML2 +Z detectors. The total duration of the beam loss event without the trigger of the beam abort system cab ve estimated by the applying a Gaussian fit to the data, resulting in a loss duration of $t_{\mathrm{FWHM}} = 879\,\mu\mathrm{s}$, which is in agreement with the expectations for a UFO beam loss event.

Overview of UFO events measured with the BCML detector during Run 2

The most intense UFO measured during the LHC operation in 2015/16 was the beam loss event discussed in the section before, leading to the LHC beam abort. Besides that, around 20 other UFO events were measured in Run 2, however with reduced intensities and as well with different timing characteristics. The shortest UFO events measured took only $t = 219\,\mu\mathrm{s}$, whereas the longest UFO event had a duration of $t = 1368\,\mu\mathrm{s}$. The running sum spectra of these two events are shown in Fig. 4.23. The intensities of the UFO beam loss events were

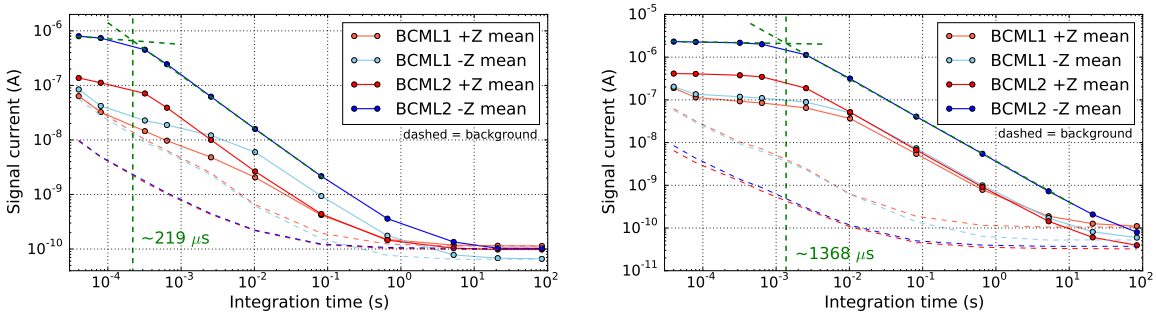

Figure 4.23: The running sum spectra of two UFO events measured with the BCML detectors. On the left side a very short UFO event with a duration of only t = 219 µs and on the right side a UFO event with a longer duration of t = 1368 µs are shown. During these measurements the BCML1 detector was still not repaired to be sensitive for short beam loss events (see section 4.1.4.3), however the UFO event with the long duration of 1368 µs could be seen as well.

increased for the LHC operations in 2016 compared to 2015. This can be explained by the increased beam intensities in 2016 with an instantaneous luminosity of $\mathcal{L}_{\text{inst.}} = 12.6\,\text{Hz/nb}$ compared to 2015 of $\mathcal{L}_{\text{inst.}} = 5.1\,\text{Hz/nb}$.

4.4.2 Long Beam Loss events caused by Machine Induced Beam Background

A beam loss is being defined as 'long' or 'slow' when it lasts longer than 2200 beam turns that are equivalent to $\approx 0.2\,\text{s}$ [Jea96]. Typically such slow beam loss events are building up slowly and hence can be plotted as function of time. The most important contribution of long beam loss events are caused by machine induced backgrounds. In Fig. 4.24 the BCML detector signals for a typical LHC fill is plotted logarithmically. Before the beams are brought into collision and the BCML detector signal is almost entirely dominated by collision products, a small increase in the detector signal can be observed. This slightly increased signal, indicated in blue, is caused by the machine induced background. The machine induced background is created via three different types of beam loss events:

1. **Inelastic and elastic beam gas scattering.** Interactions of beam particles with nuclei of the residual gas inside the beam pipe can cause particle showers approaching the CMS detector, see section 4.4.2.1.

2. **Beam halo particles that are caused by an inefficient betatron cleaning.** Beam halo particles are characterized by having a high transverse momentum and are typically caught by the betatron cleaning with its collimations system. The beam halo particles that are not caught by the collimators can collide with the TCTs at IP5 and cause particle showers inside the CMS detector, see sections 4.4.2.2 and 4.4.2.3.

3. **Collisions products from neighboring IPs.** A fraction of collision products of a neighboring IP may reach the IP at CMS and cause an increased beam background.

These three sources of machine induced background are as well correlated to the intensity and energy of the beams itself. An increased beam energy or beam intensity raises the possibility to create one of the above mentioned beam loss events and hence increases the measured machine induced background [Tal06a], see Fig. 4.25a. The direct correlation between the machine induced background measurement of a BCML detector with the beam intensity and the beam energy is shown in Fig. 4.25b. Further details to machine induced background can be found in [Cor06, Bru13].

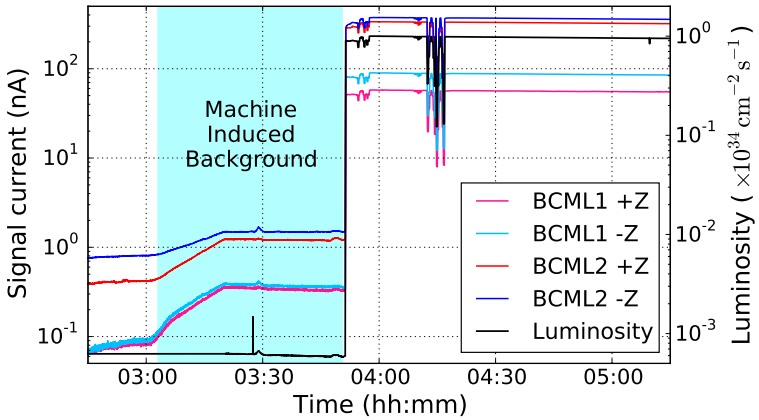

Figure 4.24: The machine induced background (MIB) indicated in blue can be measured with the BCML detectors before the beam goes into collisions of fill 5068. During particle collision the BCML signal is increased by some orders of magnitude and dominated by collision products. The luminosity measurement remains unaffected to the increased machine induced beam background.

In the following subsections dedicated studies were done to analyze separately the impact of the different machine induced beam background sources to the BCML detector signal.

4.4.2.1 Beam Loss events caused by Beam Gas

The vacuum pressure inside the beam pipe is one of the most important contributions to the measured beam background. An increased vacuum pressure causes an increased number of collisions of beam particles with residual gas. Secondary particles created in these collisions hit the beam pipe or surrounding material that leads to intense particle showers inside the CMS detector. The duration of such beam background events depend directly on the time, the vacuum system need to recover nominal operation conditions. Such increased background measurements caused by an increased vacuum pressure was measured several times during the LHC operation in 2010 and 2011 at the CMS detector. It was found that the electrical interconnection between two parts of the beam pipe close to the CMS detector was damaged and causing the increased vacuum pressure. The interconnection was repaired at the beginning of 2012 and the nominal vacuum pressure was again restored. Further details of this

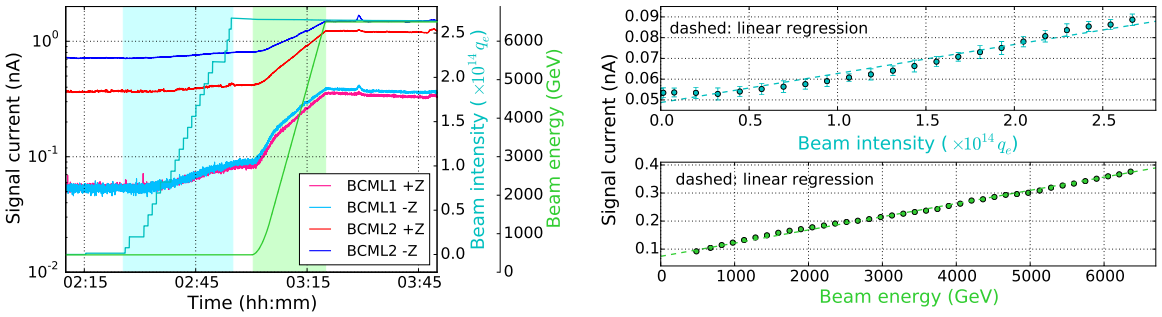

(a) Machine induced background measured with the BCML detectors.

(b) Mean BCML1 -Z detector signal as function of beam intensity and beam energy.

Figure 4.25: The machine induced background is directly correlated to the beam energy and the beam intensity. An increase of either of these parameters is directly linked to an increased machine induced background measurement, shown on the left plot. The right plot shows the linear correlation of the mean BCML1 -Z signal with respect to the beam intensity (turquoise) and the beam energy (green).

incident can be found in [Gut14a].

In order to study the effect of an increased vacuum pressure in more detail, a dedicated beam gas study was done. The vacuum pressure inside the beam pipe was therefore locally increased. This was achieved by activating NEG cartridges[3] that were installed during LS1 at several locations around IP5. The NEG cartridges are heated via an electrical current causing a release of hydrogen trapped at the surface. The trapped hydrogen at these locations was previously pumped out of the beam pipe to create a high vacuum. Further details to the NEG cartridges can be found in [Bag14]. With this technique a locally increased vacuum pressure can be artificially created. The beam gas study was done during the fill 4905 with 301 colliding bunches and an instantaneous luminosity of $\mathcal{L}_{\text{inst.}} = 1 \times 10^{33}\,\text{Hz/cm}^2$. The vacuum inside the beam pipe located $Z = \pm 148\,\text{m}$ upstream of CMS, was increased and hence affected Beam 1 and Beam 2. In Figure 4.26 the BCML detector signal based on running sum 9 normalized to the instantaneous luminosity is plotted over time. In addition the vacuum pressures inside the beam pipe at $Z \pm 148\,\text{m}$ is plotted. For an increased vacuum on the CMS +Z end an increased beam background measurement downstream of CMS, on the BCML detectors located on -Z, is expected due to the creation of intense particle shower inside the CMS volume and vice versa. Hence the vacuum pressure of the +Z end should be correlated with the BCML detectors on the -Z end, and the vacuum pressure of the -Z end should be correlated with the BCML detectors on the +Z end. This correlation can be seen for both BCML detector locations, however is more pronounced for the BCML2 detectors, since these are located further downstream of CMS at $Z \pm 14.4\,\text{m}$ and measure a strongly increased and different particle shower compared to the BCML1 detectors located at Z±1.8 m. The direct correlations between the vacuum pressures and the normalized signals for the BCML1 and BCML2 detector locations are shown in Fig. 4.27. The normalized BCML1 and BCML2 detector signals from the -Z end are plotted over the vacuum pressure of the +Z end and vice versa. The correlation between an increase in vacuum pressure and an increase in the measurement of the machine induced background signal can be seen for both BCML detector locations. The effect is as expected more pronounced for the BCML2 detector location, since they're further separated from each other.

4.4.2.2 Beam loss events caused by beam particles splashing against the Tertiary Collimator during a collimator scan

Before high intensity beams are allowed to be injected into the LHC, aperture measurements are regularly carried out [AP11]. These measurements are used to verify the LHC collimator settings with respect to the particle beam. The LHC collimator system [Ass06] is essential for a safe beam operation and protection of the LHC machine, consisting of in total 3 different collimation devices. The primary (TCP) and secondary (TCS) collimators are installed at the beam insertion region and the tertiary collimators (TCT) are sitting close to the interaction points to protect the superconducting triplet magnet and to reduce the machine induced background at the experiments [Her16].

During the scan of the TCTs, located at $Z \pm 147.5\,\text{m}$ away from IP5, the collimators are stepwise moved closer to the particle beam. When the collimators are scratching the beams, high beam losses downstream of the TCT are created and the relative position of the collimator is known. These beam losses can last several seconds depending on the beam intensity. Beam losses produced at the TCTs are creating strong particle showers inside CMS and pose the biggest threat to the detector.

[3]Non evaporable getters (NEG) are placed inside a vacuum system to complete and maintain the vacuum. Gas molecules striking the getter material combine with it chemically or by absorption and hence improve the vacuum. The NEGs installed close to the CMS detector operate at high temperatures and are also based on the principle of surface sorption of gas molecules.

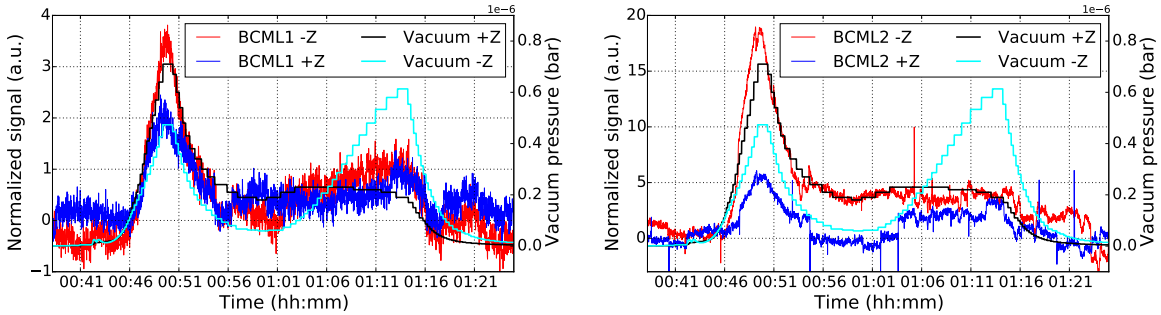

Figure 4.26: The mean BCML1 (left) and the mean BCML2 (right) detector signal for the +Z and -Z location as function of time. Additionally the vacuum pressures inside the beam pipe Z ± 148 m upstream of CMS are shown. The peaks in the BCML2 signals are caused by calibration jumps in the tunnel card, see section 4.1.3.2.

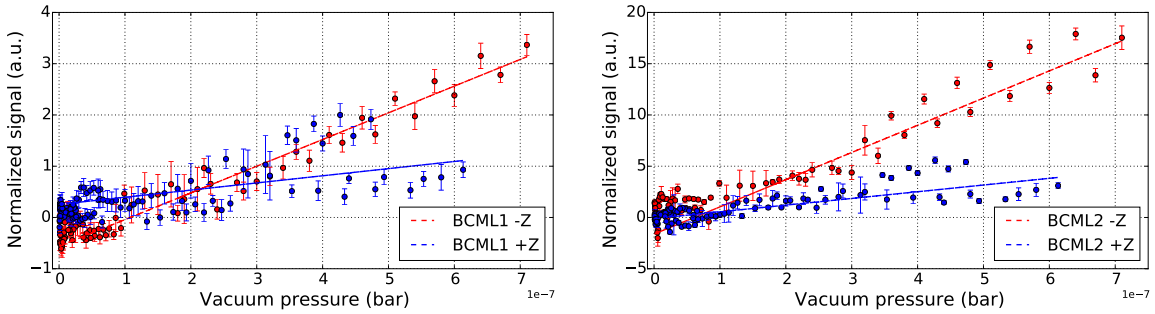

Figure 4.27: Correlation of the mean BCML1 (left) and the mean BCML2 (right) normalized detector signal with respect to the vacuum pressures measured on the opposite location of CMS. The BCML1 -Z signal is for example plotted over the vacuum pressure on the +Z side.

Figure 4.28 shows the detector response from BCML2 and BCM1F during a collimator scan in 2015. The TCT collimator, which has been scanned, is located upstream of CMS on the +Z side, and hence affecting Beam 1, compare Fig. 4.15. The scan started at a TCT opening of 2.7 cm, where no beam loss events were measured. A stepwise decrease of the TCT opening to finally 2.25 cm caused lots of beam loss events that could be measured with the BCML2 -Z detector, which is located on the opponent side of CMS with respect to the TCT position where the beam loss originated. The BCML2 +Z detector located more closely to the TCT did not measure beam loss events caused by the TCT scan. This behavior is expected, since the upstream part of the beam pipe geometry is not creating strong particle shower, like the beam pipe geometry inside the CMS detector. Hence an increased signal due to an increased particle shower is expected downstream of CMS to be measured with the BCML2 -Z detector. This behavior is expected based on Fluka simulations of machine induced background [Mue11]. The signal measured with the BCML2 -Z detector matches the measurements of the dedicated CMS background monitor (BCM1F) of Beam 1. The timing structure of such a beam loss event is shown in Fig. 4.29 for the BCML2 ±Z detectors. The signal duration is in the order of $t_{loss} \approx 0.01 - 3$ s.

4.4.2.3 Beam loss events caused by artificially created beam halo particles splashing against the Tertiary Collimator

Another way to regular qualify the LHC collimator settings in order to proof their protection and cleaning functionality is via so called Beam Loss Maps. During this procedure the beam is artificially excited to increase the transverse amplitude of the particle beam. This provokes

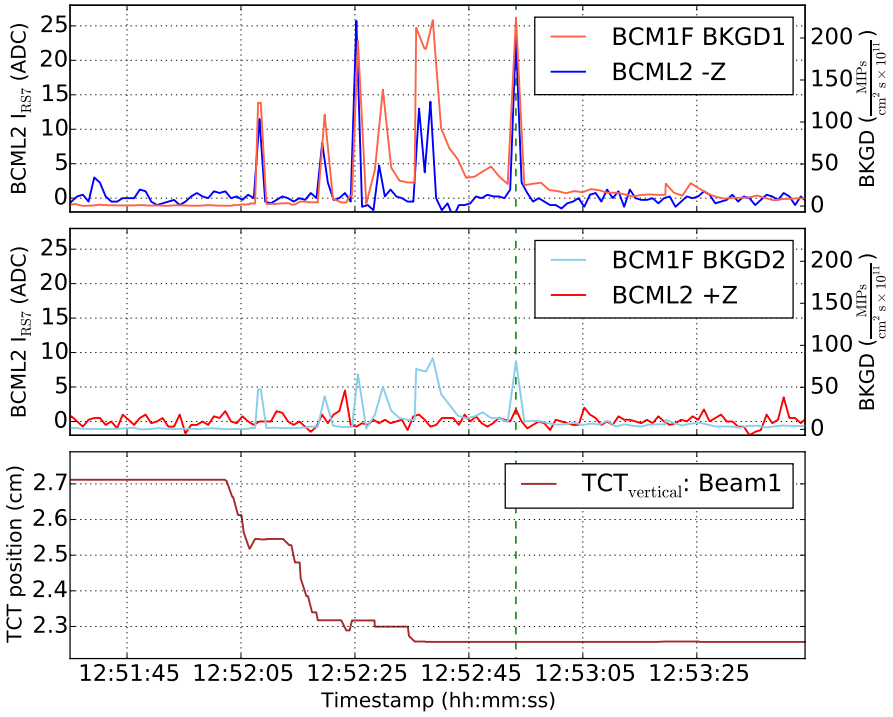

Figure 4.28: During the collimator scan the TCT opening was closed (lower plot) till beam loss events were created. The upper plots show the mean signals of the BCML2 ±Z and the BCM1F detectors. The TCT, located on the CMS +Z upstream side, caused beam loss events in Beam 1 that could be measured downstream of CMS with the BCML2 -Z detector. These measurements are in agreement with the dedicated beam background measurements of Beam 1 with the BCM1F detector. The most intense beam loss event indicated with the dashed green line is plotted double logarithmically, shown in Fig. 4.29.

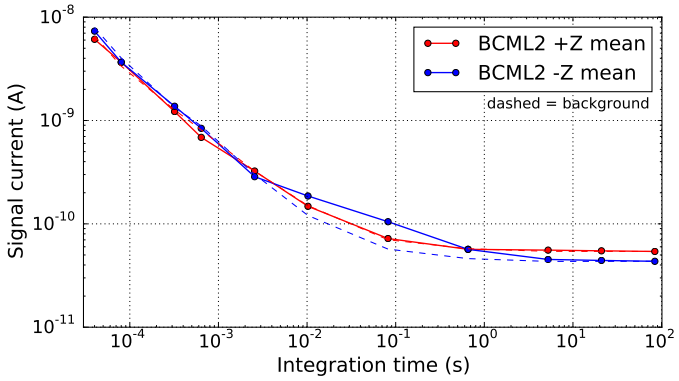

Figure 4.29: Running sum spectra of the BCML2 ±Z detectors for a beam loss event during the collimator scan. The beam loss event is only visible for the BCML -Z detector (blue), where a slight increase over the background (blue - dashed) can be seen. The duration of this 'slow' beam loss event can be estimated to: $t_{loss} \approx 0.01 - 3\,s$. The measurement signal of the BCML2 +Z detector remains unaffected.

beam loss events at the collimators and verifies their correct positioning and functionality. There are various methods to artificially excite the particle beam, in this section the focus is on the beam loss maps created by a Momentum Offset (MO). Increasing or decreasing the RF frequency in the cavities creates the MO beam loss maps. This changes the beam energy and hence the orbit of the beam, resulting in the loss of the beam at the primary collimators in the cleaning sections in octant 3 and 7, compare Fig. 2.3. Further details to the creation

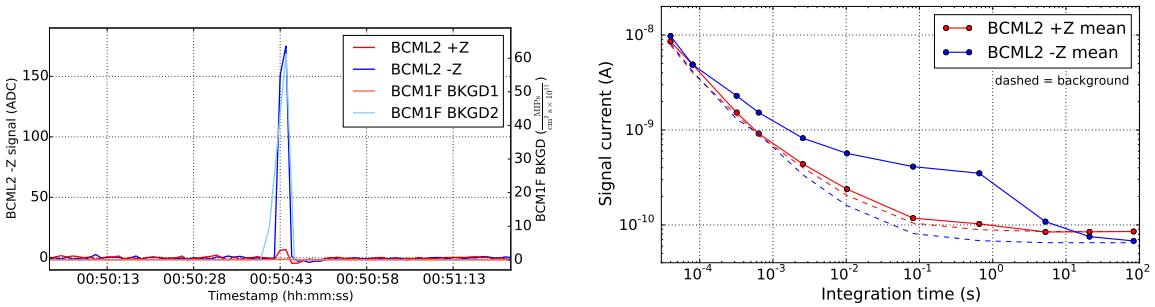

Figure 4.30: Beam Loss Maps caused by a beam momentum offset of the RF cavities by +500 Hz measured with the BCML2 and BCM1F detectors. The beam losses created by the artificially excited Beam 2 colliding at the primary collimators, could be measured with the BCML2 -Z detector (blue). The dedicated BCM1F background measurement for Beam 2 losses (light blue) is in agreement with the BCML2 measurement. The double logarithmic running sum spectrum shown on the right, suggests a beam loss duration of up to $\tau_{\text{loss}} \approx 3\,\text{s}$.

of beam loss maps can be found in [Moe13].

During the machine development on 4th of July 2015 such MO beam loss maps were created by adding 500 Hz to the nominal RF cavity oscillations of 400 MHz resulting in beam loss events at the primary collimators in octant 3 and 7 resulting in a beam dump. The artificially excited Beam 2 colliding at the primary collimators in Octant 7[4] caused very intense beam loss events further downstream, which could be measured at CMS with the BCML2 -Z detector and the BCM1F detector, shown in Fig. 4.30. The running sum spectra, measured with the BCML2 detectors, show a rather long beam loss event of up to $t_{\text{loss}} \approx 3\,\text{s}$. The beam loss event is hardly measurable on the BCML2 +Z side, the opposite side of which the beam loss originated. The beam loss signal measured with the BCML2 -Z was therefore created by very low energetic particles that where stopped inside the CMS detector and didn't reach the BCML2 +Z detector further downstream. The global LHC loss map measured by the BLM system is shown in Fig. A.11 in the Appendix.

4.5 Radiation induced BCML detector degradation

The performance of the BCML diamond sensors decreased during Run 2 due to radiation damage. The radiation damage caused a severe signal reduction that forced a redefinition of the abort thresholds in order to keep a minimum safety margin, see section 4.5.1. Furthermore, the high voltage stability of a quarter of all BCML diamond sensors had to be reduced to prevent the creation of 'erratic currents' [Mue11], discussed in the section 4.5.2.

4.5.1 Modification of the BCML Abort Thresholds to guarantee a safe CMS operation

The BCML detector signal efficiency was individually calculated continuously during Run 2 in order to ensure the desired protection of the abort thresholds defined in section 4.2, see Fig. 4.31. The absolute detector efficiency was calculated based on the assumption of having a signal efficiency of 100% for undamaged diamond sensors. The signal efficiency refers to the measured signal output relative to the initial value of an undamaged pCVD diamond detector, which has typically an average CCE of 40% - 50% for pCVD diamonds. The signal measured by an undamaged diamond sensor in the year 2010 is extrapolated to nominal instantaneous luminosity of $10^{34}\,\text{cm}^{-2}\text{s}^{-1}$ and used as reference. This extrapolation includes

[4] Octant 7 is located upstream on the CMS -Z side, compare Fig. 2.3

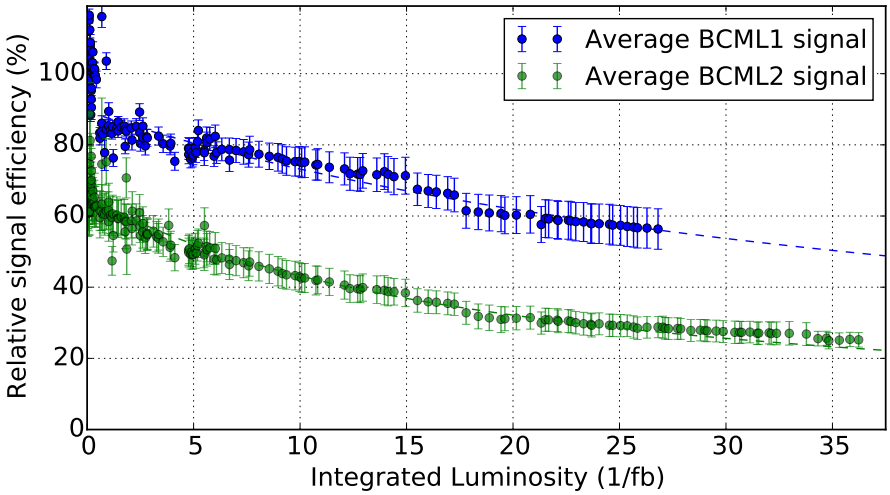

Figure 4.31: The BCML radiation induced detector degradation. The BCML signal efficiency is calculated by interpolating the detector signal to nominal luminosity of $\mathcal{L}_{\text{inst.}} = 10^{34}\,\text{cm}^{-2}\text{s}^{-1}$ (see section 5.3.1) and comparing this to the nominal detector signal of an undamaged pCVD diamond detector. The mean relative signal efficiencies of the BCML1 and BCML2 detectors are plotted over the integrated luminosity. The increased signal efficiency of the BCML1 detector until the first $1\,\text{fb}^{-1}$ is caused by an increased bias voltage of HV = 500 V. The BCML1/2 abort channels were apart from that operated at a bias voltage of HV = 200 V.

an additional factor, calculated with Fluka, which takes the increased beam energy from 3.5 TeV to 6.5 TeV into account. The extrapolated signal currents at nominal instantaneous luminosity of $10^{34}\,\text{cm}^{-2}\text{s}^{-1}$ for undamaged BCML detectors at the increased beam energy of 6.5 TeV are:

- BCML1: $100\,\text{nA} \times 1.19 = 119\,\text{nA}$
- BCML2: $750\,\text{nA} \times 1.42 = 1064\,\text{nA}$

Here 100 nA (750 nA) for BCML1 (BCML2) is the undamaged signal current measured in 2010 extrapolated to nominal luminosity. The factor 1.19 (1.42) for BCML1 (BCML2) are the Fluka based factors, which take the increased beam energy into account.

To compensate for the signal reduction, the BCML abort thresholds were modified during Run 2 three times and are documented in [Kas15, Kas16a, Kas16b]. The abort threshold in running sum 1 is set per definition to an absolute value resulting for an undamaged diamond detector in a safety factor of 3000, whereas a minimum safety factor of 1000 is required. A signal reduction of 66% can therefore be tolerated, since the minimum requirements are still satisfied. The BCML2 detector efficiency however dropped below an efficiency of 33% after $30\,\text{fb}^{-1}$, shown in Fig. 4.31, making an adjustment of the abort thresholds in RS1 necessary [Kas16b]. The abort thresholds in running sum 12 are defined relative to the detector performance and hence have to be adjusted regularly [Kas15, Kas16a, Kas16b]. A table of the all abort threshold set during Run 2 can be found in the Appendix A.1.2. The irradiation induced severe signal degradation of the BCML detectors are studied in detail in the next chapter 5.

4.5.2 Reduced High Voltage Stability of Diamond Detectors with increased Radiation Damage

All BCML diamond detectors were set initially in 2015 to bias voltage settings where a stable operation was possible. With increased radiation damage 25% of the diamond detectors had

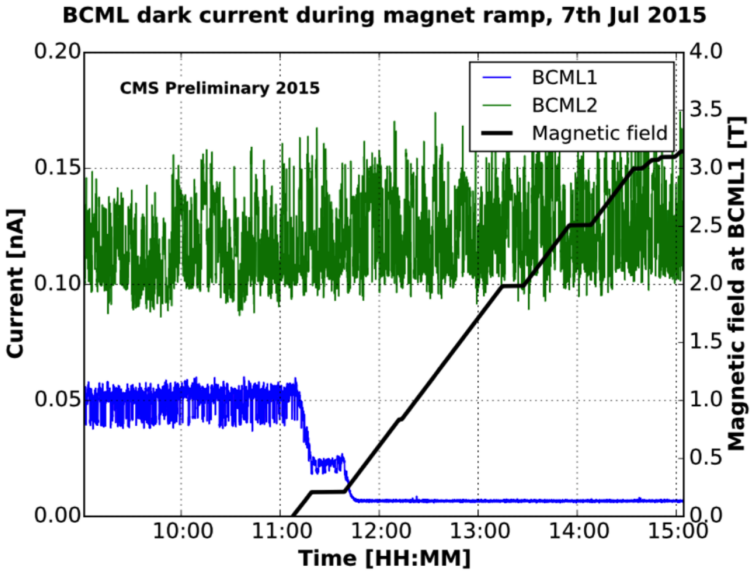

Figure 4.32: Erratic Currents of the BCML diamond detectors. An increase in the magnetic field affects immediately the signal stability of the diamond sensors located within the magnetic field, like BCML1 in blue. The BCML2 diamonds sensors are located outside of the magnetic field and are not affected.

to be operated at a lower bias voltage in order to maintain a stable signals and to avoid the so called 'erratic currents', compare section 3.3.5. The erratic currents affected the pCVD as well as the one sCVD diamond detector installed at the BCML2 location. The erratic current behavior can however be suppressed by the presence of a magnetic field, see Fig. 4.32. The BCML1 pCVD diamond sensors are located inside the CMS tracker and therefore inside the magnetic field of the CMS detector. The signal current of an erratic BCML1 diamond detector stabilizes as soon as the magnetic field reaches 0.5 Tesla. The magnetic field at the BCML2 detector location was too low to affect the erratic current behavior of these diamond sensors. The magnetic field is beneficial for the signal stability of the diamond sensors if the electrical and the magnetic field are perpendicular to each other. The current understanding of this phenomenon is that the Lorentz force pushes the charge carriers against grain boundaries and hence prevents an erratic free charge carrier flow inside the diamond. Further information to the phenomena of erratic currents in the presence of magnetic field can be found in [Bru04, Edw05, Mue11].

Chapter 5

Radiation induced signal Degradation of the BCML detector

The radiation induced signal degradation of the BCML detectors during Run 2 will be discussed in this chapter. The signal reduction was much stronger than expected from low particle rate laboratory measurements [Ada06, Cri10], similar results were obtained for the BCML detector operation in Run 1 [Gut13, Gut14a, Gut15]. In the first section 5.1, the widely acknowledged standard radiation damage model assuming homogeneous trapping probability will be introduced. In order to quantify the radiation induced signal degradation, the particle composition causing the radiation damage is simulated with Fluka [Fer05, Böh14] for each BCML detector location, see section 5.2. The radiation induced signal degradation of the BCML detector is discussed and quantified in section 5.3. In section 5.4 the rate dependency of the BCML signal efficiency is discussed for diamond detector operated in different particle rate environments and for diamond sensors operated at different electric fields. The diamond polarization effect that is believed to be responsible for the severe signal degradation and as well for the rate dependency of the signal efficiency is qualitatively discussed in section 5.5. The chapter is concluded with a discussion about the problems and limitation of the standard radiation model for diamond detectors, see section 5.6.

5.1 Diamond Radiation Damage

The performance of diamond detectors with respect to the radiation damage has been studied extensively by the 'CVD Diamond Radiation Detector Development' group, called RD42 collaboration [Ada96]. This collaboration, found in 1995, studies the development of detectors based on polycrystalline CVD (pCVD) diamond. The RD42 collaboration performed several irradiation studies to analyze the radiation induced degradation of the charge collection distance (CCD) of the diamond sensors [Ada06, Tri08, Kag09, Cri10, Tsu12]. Based on the results of these irradiation studies a model was created describing the reduction of the CCD of the diamond sensors with respect to the radiation damage that will be outlined in the following and is based on [Bor94].

The charge collection efficiency of a diamond detector is determined by the mean free path length λ of the charge carriers. A diamond detector with a mean free path length higher than the detector thickness d has a full charge collection efficiency of 100%, whereas a detector with $\lambda < d$ has a reduced CCE. The mean free path length of the charge carriers is determined by their lifetime τ that is determined by the amount of defects in the material that possibly trap charge carriers and hence reduce their lifetime. The standard radiation model is based on the assumption that the number of defects N increases linearly with the irradiation damage:

$$N(\Phi) = N_0 + k_N \times \Phi, \tag{5.1}$$

where Φ is the particle fluence causing radiation damage, k_N as a damage constant defining the linearity between defects created per unit of fluence and with N_0 as initial number of defects for the un-irradiated diamond sensor material. The lifetime of the charge carrier τ is inverse proportional to the number of defects N in the diamond lattice:

$$\tau_{e,h} \sim N^{-1}. \tag{5.2}$$

The charge carrier lifetime in diamond is different for electron and hole carriers. In order to simplify this model the next steps are however calculated using only one common charge carrier lifetime for electron and hole carriers: $\tau_{e,h} = \tau$. This can be done, since the standard radiation model will finally be expressed in term of CCD, where electron and hole carriers are not distinguished any more. Combining the equations 5.1 and 5.2 leads to:

$$\frac{1}{\tau(\Phi)} = \frac{1}{\tau_0} + k_\tau \times \Phi, \tag{5.3}$$

where the constant k_τ keeps the linearity to k_N in Eq. 5.1 and τ_0 is the initial lifetime of the charge carriers for an un-irradiated diamond sensor. The mean free path length λ can be expressed as a function of the lifetime τ and the drift velocity $\mathrm{v_{drift}}$ of the charge carriers:

$$\lambda = \mathrm{v_{drift}} \times \tau. \tag{5.4}$$

By replacing the charge carrier lifetime τ in Eq. 5.3 with the relation in Eq. 5.4 for the mean free path length the following equation is obtained:

$$\frac{1}{\lambda(\Phi)} = \frac{1}{\tau_0 \times \mathrm{v_{drift}}} + \frac{k_\tau}{\mathrm{v_{drift}}} \times \Phi. \tag{5.5}$$

The term $\tau_0 \times \mathrm{v_{drift}}$ can be expressed as λ_0, the initial free path length for an un-irradiated diamond sensor and the k_τ and $\mathrm{v_{drift}}$ can be combined to a final radiation damage constant k resulting in:

$$\frac{1}{\lambda(\Phi)} = \frac{1}{\lambda_0} + k \times \Phi. \tag{5.6}$$

The Eq. 5.6 is the commonly used parameterization describing the radiation damage in diamond. Since the mean free path length can't be measured directly, Eq. 5.6 is typically converted into an equivalent in CCD using Eq. 3.7:

$$\frac{1}{\mathrm{CCD}(\Phi)} = \frac{1}{\mathrm{CCD_0}} + k \times \Phi. \tag{5.7}$$

The CCD of a diamond detector with respect to the radiation damage is fully characterized by the radiation constant k, which is determined by the particle type and energy causing the radiation damage. Irradiation studies done by the RD42 collaboration determined a radiation constant of $k = 6.5 \times 10^{-19}\,\mathrm{cm^2 \mu m^{-1}}$ [Cri10] for an irradiation with 24 GeV protons. In these irradiation studies, the CCD of poly crystal CVD diamond sensors has been measured regularly after several irradiation steps. The 24 GeV protons are therefore the 'golden standard' to which any irradiation damage has to be converted in order to make predictions of the pCVD diamond detector performance. Furthermore, it was found that the standard radiation model describes as well the radiation induced CCD reduction of sCVD diamond with the same k factor. The difference between pCVD diamonds and sCVD diamonds is only the initial CCD value $\mathrm{CCD_0}$, which is strongly increased for sCVD diamond sensors. The diamond sensors used in this irradiation study were operated at a bias voltage of HV = 500 V, resulting in an electric field of $E = 1\,V/\mu\mathrm{m}$.

Based on this k factor the charge collection distance can be extrapolated for the three BCML detector locations for the lifetime of the LHC, see Fig. 5.1. During the LHC operation in Run 2 a total integrated luminosity of $100\,\mathrm{fb^{-1}}$ and in Run 3 a total integrated

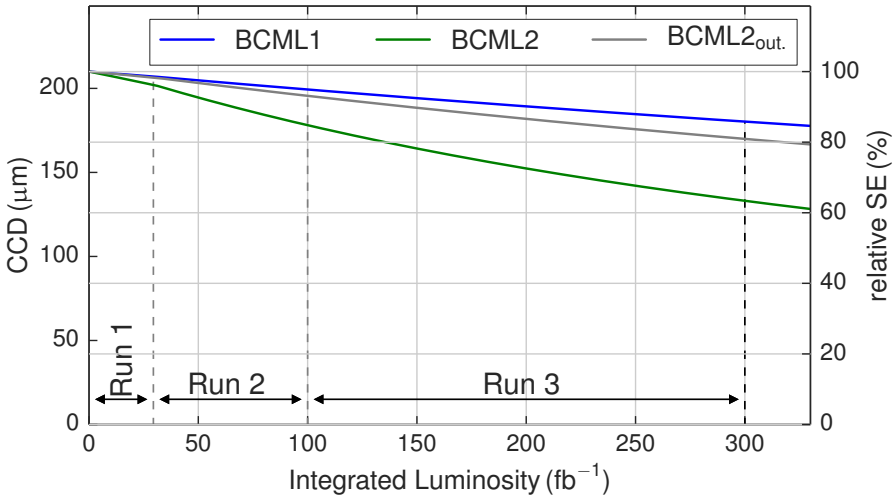

Figure 5.1: Based on the radiation constant $k = 6.5 \times 10^{-19}\,\mathrm{cm^2 \mu m^{-1}}$ the radiation induced CCD degradation of the BCML detectors is extrapolated for the entire lifetime of the LHC.

luminosity of $300\,\mathrm{fb}^{-1}$ is expected. Based on Fluka estimation, discussed in section 5.2.1, a total fluence of 0.9×10^{15} 24 GeV proton equivalents is expected for the BCML1 location. The BCML2 ($\mathrm{BCML2_{out.}}$) location would be exposed to an increased total fluence of 4.3×10^{15} (1.7×10^{15}) 24 GeV proton equivalents. Based on the radiation constant found by the RD42 collaboration all BCML diamond detectors would resist the radiation damage experienced during the entire lifetime of the LHC. Unfortunately, the radiation induced signal degradation of the BCML pCVD diamonds was much stronger than expected, resulting in the replacement of all 16 abort detectors at the BCML1 and BCML2 detector location.

5.2 Simulation of the Particle Composition at the BCML Detector Locations

An important key to understand the radiation induced signal degradation of the BCML detectors is the simulation of the particle composition that is penetrating the diamond sensors during nominal proton-proton collisions at the CMS detector. The particle spectrum can be simulated using the publicly available software Fluka [Fer05, Böh14]. Based on the Fluka simulation the radiation damage (section 5.2.1) and the detector signal (section 5.2.2) can be calculated.

5.2.1 Radiation Damage at the BCML Detector Locations

Test beam irradiations to study radiation damage are typically done with mono-energetic beams. The BCML diamond detectors are however exposed to a plutonia of different particle types with different energies. Furthermore, the particle composition is different for each BCML detector location. To calculate the diamond radiation damage for each BCML detector locations, the entire particle environment was simulated for each BCML detector location using Fluka.
The Fluka simulated particle spectra of protons, neutrons and pions at the BCML1 detector locations is shown in Fig. 5.2. Based on these results the radiation damage in 24 GeV proton equivalents was calculated. The radiation damage was calculated based on the DPA model, see section 3.3.6.

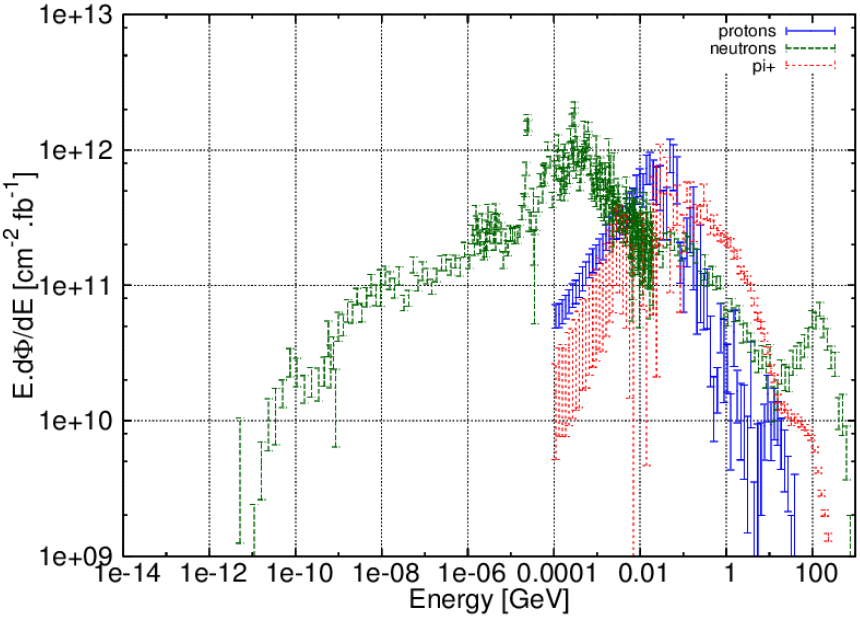

Figure 5.2: Simulated particle spectra at the BCML1 detector location for a beam energy of 7 TeV. The Fluka simulated particle flux is normalized to an integrated luminosity of $\mathcal{L}_{\text{integ.}} = 1\,\text{fb}^{-1}$.

Table 5.1: Overview of the Fluka based simulation results of the BCML radiation damage for the three detector locations. The radiation damage was simulated using the DPA model and the results are converted into 24 GeV proton equivalents per $1\,\text{fb}^{-1}$ of integrated luminosity. The error represents the statistical uncertainty of the simulation result. The results for the beam energy of 3 TeV and 4 TeV are taken from [Gut14a].

Detector	24 GeV $p_{eq.}$ ($\text{cm}^{-2}/\text{fb}^{-1}$)		
	3 TeV	4 TeV	7 TeV
BCML1	$(0.34 \pm 0.04) \times 10^{13}$	$(0.36 \pm 0.03) \times 10^{13}$	$(0.41 \pm 0.09) \times 10^{13}$
BCML2	$(0.90 \pm 0.06) \times 10^{13}$	$(1.00 \pm 0.05) \times 10^{13}$	$(1.46 \pm 0.12) \times 10^{13}$
$\text{BCML2}_{\text{out.}}$	$(0.38 \pm 0.02) \times 10^{13}$	$(0.45 \pm 0.01) \times 10^{13}$	$(0.59 \pm 0.04) \times 10^{13}$

The Fluka simulation results are normalized to one proton-proton collision. To make use of the Fluka simulation, the results have to be multiplied by the actual proton-proton collision rate at CMS. The collision rate R can be calculated, using:

$$R = \mathcal{L} \times \sigma_{\text{inelastic}} \tag{5.8}$$

with $\sigma_{\text{inelastic}} = 80\,\text{mb}$ as cross section of inelastic collisions and $\mathcal{L}$ as integrated or instantaneous luminosity. The $\sigma_{\text{inelastic}}$ is simulated by various Monte Carlo event generators, predicting a cross section between $75\,\text{mb} \leq \sigma_{\text{inelastic}} \leq 90\,\text{mb}$ [Bel13]. A Monte Carlo event generator optimized for the LHC results predicts a cross section of $\sigma_{\text{inelastic}} = 80\,\text{mb}$, which is used in this work [Pie15].

The Fluka calculated irradiation damage of the BCML diamond detectors in units of 'displacement per atom' (DPA) can be normalized to an equivalent fluence of 24 GeV protons, using:

$$\Phi_{24\,\text{GeV}} = \frac{\text{DPA}_{\text{sim.}}}{\text{DPA}_{24\,\text{GeV}}} \times R(\mathcal{L}_{\text{integrated.}}) \tag{5.9}$$

Table 5.2: Simulation based calculation of the signal currents for the three different BCML detector locations. The CCE values of the BCML sensors are based on CCE measurements before the diamond detectors were installed, see section 5.3.1.

Detector	Q_{ind} (MeV)	$V_{\text{eff.}}$ (cm^3)	CCE_{init} (%)	I_{Fluka} (nA)	f_{BCML}	$I_{\text{corr.}}$ (nA)
BCML1	0.44 ± 0.02	0.045	37%	71 ± 4	2.04	147 ± 8
BCML2	2.40 ± 0.10	0.036	46%	394 ± 16	3.41	1342 ± 56
$\text{BCML2}_{\text{out.}}$	0.04 ± 0.01	0.036	46%	6 ± 1	2.23	14 ± 1

with $\text{DPA}_{24\,\text{GeV}} = 8.924 \times 10^{23}$ ($24\,\text{GeV proton}_{\text{eq.}}/\text{cm}^2$) the radiation damage created by one 24 GeV proton in diamond [Gut14a].

The simulation results are summarized in table 5.1 and are given in 24 GeV proton equivalents per $1\,\text{fb}^{-1}$ of integrated luminosity. In addition, the Fluka simulation results for the reduced beam energy during Run 1 are listed. The increase in beam energy leads to an on average $\sim 38\%$ increased radiation damage for all BCML detector locations.

5.2.2 Simulation based calculation of the BCML Detector Signal

Besides simulating the radiation damage of the BCML diamond detectors, the total energy deposition Q_{ind} in the diamond sensors can be simulated with Fluka. Based on the total energy deposition per proton-proton collision the signal current of the diamond sensor for nominal instantaneous luminosity $\mathcal{L}_{\text{inst.}}$ can be calculated via:

$$I_{\text{Signal}}(A) = \frac{Q_{\text{ind}}}{E_{\text{Ion.}}} \times q_{\text{e}} \times V_{\text{eff.}} \times \text{CCE} \times \text{R}(\mathcal{L}_{\text{inst.}}) \tag{5.10}$$

with $E_{\text{Ion.}} = 13\,\text{eV}$ as average ionization energy to create an electron hole pair, q_{e} as elementary charge, $V_{\text{eff.}}$ as active diamond detector volume, CCE as charge collection efficiency and using Eq. 5.8 with an instantaneous luminosity of $\mathcal{L}_{\text{inst.}} = 1 \times 10^{34}\,\text{cm}^{-2}\text{s}^{-1}$. The simulated signal currents are calculated based on the initial CCE of the diamond sensors at the beginning of Run 2 and are listed in Table 5.2 for all BCML detector locations.

During Run 1 Fluka was used as well to simulate the signal currents for the three BCML detector locations. The Fluka based signal prediction was however reduced compared to the real signal currents measured with the undamaged diamond sensors at the CMS experiment. The reasons for this discrepancy are not fully understood, however most likely related to energy cuts in the simulation that results in an underestimation of low energetic particles. The discrepancy between measurement and Fluka simulation results for Run 1 is represented in the factor f_{BCML}, listed as well in Table 5.2. The discrepancy factor can be used to calculate a realistic BCML detector signal $I_{\text{corr.}}$ for Run 2. Further details to the discrepancy between Fluka simulation and measurement can be found in [Gut14a].

5.3 Signal Degradation of the BCML Detectors caused by Irradiation Damage

During the first years of LHC operations in Run 1 no significant diamond detector degradation was expected, compare Fig. 5.1. During the BCML detector operation in Run 1 a severe radiation induced signal reduction was however observed. The signal efficiency of the BCML diamond detectors was reduced by more than 40% compared to an expected signal reduction

of 6%[1]. At the most radiation exposed locations, the signal efficiency was reduced even by 80% (expected 9%[1]) [Gut14a]. Due to the hyperbolic signal degradation as function of radiation damage, the radiation damage was therefore a factor $\sim 100\times$ stronger than expected. Furthermore, a rate dependency of the diamond detector signal was found [Gut14a]. This section will focus on the diamond signal degradation due to irradiation damage observed during Run 2.

5.3.1 Normalization of the Detector Signal to the Nominal Instantaneous Luminosity

In order to analyze the BCML detector performance during Run 2, the BCML detector signal has to be normalized. The BCML detector signal is almost entirely created by collision products, compare Fig. 4.24 in section 4.4.2. Other contributions, like e.g. the machine induced background, are two orders of magnitudes lower and hence can be neglected. The BCML detector signal is therefore, to the first order, proportional to the instantaneous luminosity. The instantaneous luminosity and therefore the BCML detector signal is however not constant over time. The instantaneous luminosity depends strongly on the beam intensity, which is slightly different for each fill. Furthermore, the instantaneous luminosity and therefore the BCML detector signal varies within one fill, since the beam intensity is reduced by the proton-proton collisions itself and by beam losses, see Fig. 4.14a in section 4.3. The BCML detector signal is therefore plotted for each fill over the instantaneous luminosity, which is measured by the PLT, the HF or the BCM1F detector. A linear fit is applied to the data and the BCML detector signal for nominal luminosity of $\mathcal{L}_{\text{inst.}} = 1 \times 10^{34}\,\text{cm}^{-2}\text{s}^{-1}$ is calculated, see Fig. 5.3. The data analysis presented in this chapter is based on a selection of LHC fills that satisfied the following restriction in order to minimize the systematic error caused by the linear fit:

- The LHC fill has to be in stable collisions for at least 1 hour.
- Minimum instantaneous luminosity required: $\mathcal{L}_{\text{inst.}} \geq 1 \times 10^{33}\,\text{cm}^{-2}\text{s}^{-1}$.
- Instantaneous luminosity has to be decreased by: $\Delta_{\mathcal{L}_{\text{inst.}}} \geq 0.2 \times 10^{33}\,\text{cm}^{-2}\text{s}^{-1}$.

In the following sections the normalized detector response is used for the data analysis, which was calculated individually for each BCML detector channel.

5.3.2 Calculation of the effective charge collection distance for the BCML detectors

Besides, new pCVD diamond detectors being used at the BCML1 detector, most of the pCVD diamonds mounted at the BCML2 detector were already used during Run 1. These 'old' diamond detectors experienced different irradiation damage related to the locations at which they were installed during Run 1. In order to quantify and compare the detector efficiencies of the BCML diamond detectors, the charge collection distance (CCD) is the preferred unit since it is independent of the detector thickness. The CCD can however only be measured with a dedicated setup, where MIP particles create a known amount of charge carriers. Therefore, the effective charge collection distance $\text{CCD}_{\text{eff.}}$ is introduced. The $\text{CCD}_{\text{eff.}}$

[1]The expected signal degradation was calculated using the radiation constant found by the RD42 collaboration of $k = 6.5 \times 10^{-19}\,\text{cm}^2\mu\text{m}^{-1}$ and by simulation the particle spectrum during proton-proton collisions at the CMS detector, see section 5.2.1. As limiting factor however, the radiation constant was determined for diamond detectors operated at an electric field of $E = 1\,\text{V}/\mu\text{m}$, whereas the BCML diamonds were operated at an electric field of $E = 0.5\,\text{V}/\mu\text{m}$ during Run 1.

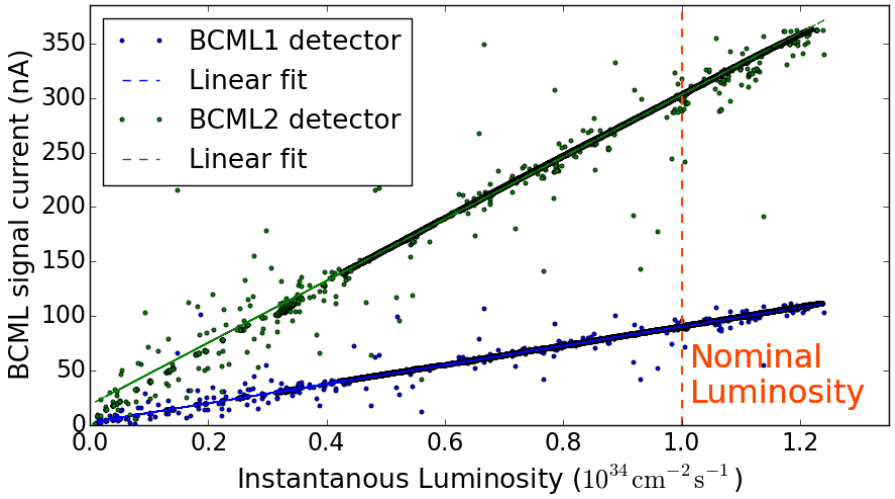

Figure 5.3: Interpolation of the BCML detector signal with respect to the instantaneous luminosity.

is calculated based on the signal current measurements of the BCML detectors at the CMS detector. The definition and calculation of the $CCD_{eff.}$ will be discussed in the following for the BCML1 and the two BCML2 detector locations separately.

5.3.2.1 Calculation of the effective charge collection efficiency for BCML1

The BCML1 diamond detectors were characterized before installation at the CCE measurement setup in DESY - Zeuthen, see section 6.1.2. Beside measurements of the leakage current and the signal stability at high electrical fields, the charge collection distance (CCD) was measured. The measurement results were used to select the best diamond sensors for the BCML1 detector. A typical CCD measurement of a pCVD diamond sensor (CMS15) is shown in Fig. 5.4. At a bias voltage of HV = 500 V a charge collection distance of $CCD_{500\,V} = 188\,\mu m$ was measured. All CCD measurement results of the BCML1 diamond sensors are summarized in Table 5.3 for a bias voltage of HV = 500 V, at which the BCML1 detector is preferably operated. The average charge collection distance of the un-irradiated BCML1 diamond sensors is $CCD_{init.} = 181 \pm 10\,\mu m$ at a bias voltage of HV = 500 V.

The normalized signal current $I_{norm.}$, defined in section 5.3.1 is used as reference to calculate

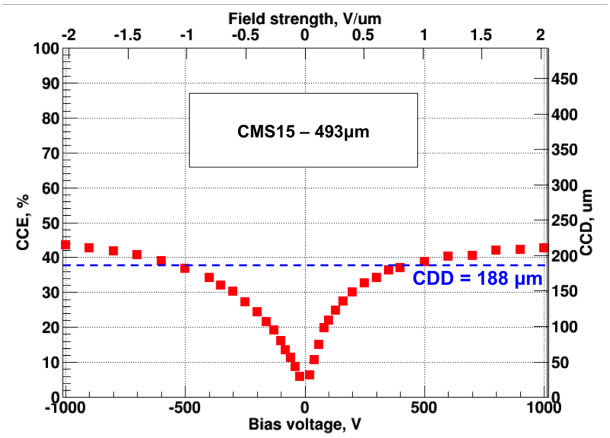

Figure 5.4: A typical CCD measurement of a pCVD diamond used in the BCML1 detector. The CCD measurement was done at the CCE setup at DESY in Zeuthen. The blue dashed line indicates the measured CCD = 188 µm for a bias voltage of HV = 500 V.

Table 5.3: The CCD of the BCML1 sensors. The charge collection distance of all BCML1 sensors was measured before installation at the CCE setup at DESY in Zeuthen. The BCML1 sensors[1] CMS15 and P37 were not working properly and were excluded from this calculation. Details to the CCE setup can be found in section 6.1.2.

Name	Thickness (µm)	CCD (µm)
CMS05	509	185
CMS06	512	194
CMS07	500	180
CMS10	520	187
CMS12	483	169
CMS15[1]	493	188
P36	419	168
P37[1]	424	170
average	491 ± 37	181 ± 10

an effective charge collection distance $\mathrm{CCD}_{\mathrm{eff.}}$. At the beginning of Run 2 the un-irradiated BCML1 detectors created a normalized signal current of $I_{\mathrm{BCML1,\,init.}} = 130\,\mathrm{nA}$ at a bias voltage of $\mathrm{HV} = 500\,\mathrm{V}$. Hence, the signal current of $I_{\mathrm{BCML1,\,init.}} = 130\,\mathrm{nA}$ corresponds to the measured $\mathrm{CCD}_{\mathrm{BCML1,\,init.}} = 181 \pm 10\,\mu\mathrm{m}$ of the BCML1 detectors. The effective charge collection distance of the BCML1 detectors can therefore be calculated based on the interpolated signal current $I_{\mathrm{norm.}}$ for nominal luminosity via:

$$\mathrm{CCD}_{\mathrm{eff.}} = \frac{I_{\mathrm{norm.}}}{I_{\mathrm{BCML1,\,init.}}} \times \mathrm{BCML1,CCD}_{\mathrm{init.}} \tag{5.11}$$

with $I_{\mathrm{BCML1,\,init.}} = 130\,\mathrm{nA}$ as initial normalized signal current for an initial charge collection distance of $\mathrm{CCD}_{\mathrm{BCML1,\,init.}} = 181 \pm 10\,\mu\mathrm{m}$.

5.3.2.2 Calculation of the effective charge collection efficiency for BCML2

The BCML2 diamond sensors used during Run 2 were 'old' diamonds sensors installed during Run 1 and therefore experienced already irradiation damage during Run 1. Absolute CCD measurements of these diamond sensors were only done before the first installation in 2008. After Run 1 no additional CCD measurements were done. The nominal signal current for an undamaged diamond sensor is therefore based on the Fluka simulations discussed in section 5.2.2. The nominal signal current for the BCML2 sensors operated at a bias voltage of $\mathrm{HV} = 200\,\mathrm{V}$ are therefore:

$$\begin{aligned} I_{\mathrm{BCML2,\,init.}} &= f_{\mathrm{BCML2}} \times I_{\mathrm{BCML2,\,Fluka}}, \\ &= 1342\,\mathrm{nA}, \end{aligned} \tag{5.12}$$

$$\begin{aligned} I_{\mathrm{BCML2_{out.},\,init.}} &= f_{\mathrm{BCML2_{out.}}} \times I_{\mathrm{BCML2_{out.},\,Fluka}}, \\ &= 13.7\,\mathrm{nA}. \end{aligned} \tag{5.13}$$

The average CCD measured in 2008 for the BCML2 detectors is $\mathrm{CCD}_{\mathrm{BCML2,\,init.}} = 184 \pm 15\,\mu\mathrm{m}$ at a bias voltage of $\mathrm{HV} = 200\,\mathrm{V}$. A detailed list with all CCD measurement results can be

found in [Mue11]. The effective charge collection distance of both BCML2 detector locations can therefore be calculated as well based on the normalized signal current $I_{\text{norm.}}$ via:

$$\text{CCD}_{\text{eff.}} = \frac{I_{\text{norm.}}}{I_{\text{BCML2, init.}}} \times \text{CCD}_{\text{BCML2, init.}}, \tag{5.14}$$

$$\text{CCD}_{\text{eff.}} = \frac{I_{\text{norm.}}}{I_{\text{BCML2}_{\text{out.}}\text{, init.}}} \times \text{CCD}_{\text{BCML2, init.}} \tag{5.15}$$

with $I_{\text{BCML2, init.}} = 1342\,\text{nA}$ and $I_{\text{BCML2}_{\text{out.}}\text{, init.}} = 13.7\,\text{nA}$ as initial normalized signal currents for an initial charge collection distance of $\text{CCD}_{\text{BCML2, init.}} = 184 \pm 15\,\mu\text{m}$.

5.3.2.3 Parameterization of the Radiation Constant using the $\text{CCD}_{\text{eff.}}$

The radiation induced signal degradation of the BCML detectors discussed in the next sections will be parameterized using the standard radiation model described in Eq. 5.7. The standard diamond radiation damage model is based on absolute CCD measurements. The effective charge collection distance $\text{CCD}_{\text{eff.}}$ is based on the normalized signal current that is linear proportional to the absolute CCD. Eq. 5.7 can therefore be written as:

$$\frac{1}{\text{CCD}_{\text{eff.}}(\Phi)} = \frac{1}{\text{CCD}_{\text{eff.,0}}} + k_{\text{prime}} \times \Phi, \tag{5.16}$$

with k_{prime} as radiation constant.

5.3.3 Radiation induced signal degradation of the BCML detectors

In total 34 BCML sensors are used to measure the beam condition at the CMS detector. Those diamond sensors are mounted at three different locations, the BCML1, BCML2 inner and the BCML2 outer position for the $\pm Z$ end of the CMS detector. Furthermore, the BCML sensors at each location are distributed uniformly around the beam pipe. Given the Φ and the $\pm Z$ symmetry of the CMS detector, the BCML detector signals for these three BCML detector location are averaged and discussed in this section. Some BCML2 sensors are operated at an increased bias voltage or experienced increased radiation damage, these BCML2 sensors will be assigned into separate groups, discussed in section 5.3.3.2. All BCML detectors are summarized in Table A.3 and Table A.4 in the appendix, listing the electrical field at which they are operated and the BCML detector group they are allocated to.

For each LHC fill, the detector response of each BCML detector group was analyzed. The signal current of each sensor within its particular BCML detector group was therefore extrapolated to nominal luminosity of $\mathcal{L}_{\text{inst.}} = 1 \times 10^{34}\,\text{cm}^{-2}\text{s}^{-1}$, as described in section 5.3.1. The normalized signal current of each BCML detector was used to calculate the average signal current for each BCML detector group. Finally, the normalized signal current of each BCML detector group was used to calculate the effective charge collection distance ($\text{CCD}_{\text{eff.}}$), as discussed in the previous section 5.3.2. The effective CCD is plotted over the total integrated luminosity, which was calculated by integrating the luminosity of all previous LHC fills during Run 2.

5.3.3.1 Signal degradation of the BCML abort channels in Run 2

The radiation induced signal degradation of the BCML1 detector is shown in Fig. 5.5. The BCML1 detector was operated at the beginning of Run 2 at a bias voltage of $\text{HV} = 500\,\text{V}$, which is equivalent to an electric field of $E \sim 1\,\text{V}/\mu\text{m}$ for the pCVD diamond sensors with an

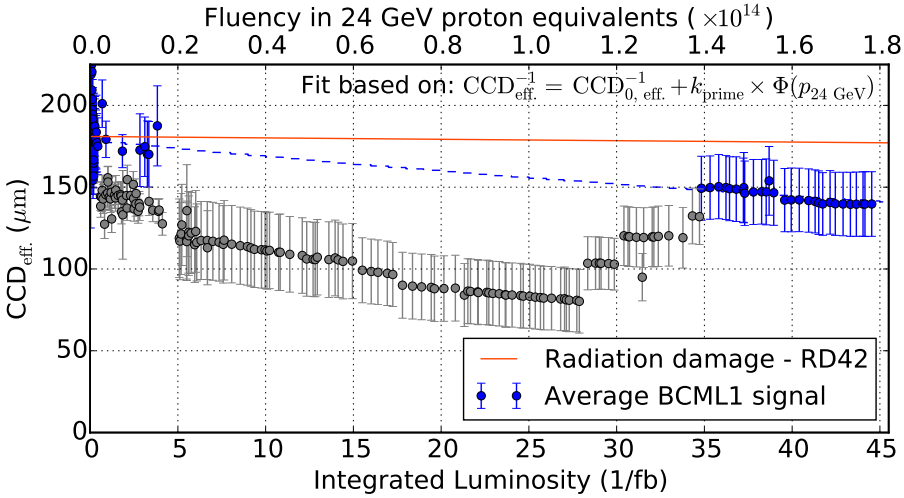

Figure 5.5: The average BCML1 detector signal normalized to nominal luminosity as function of total integrated luminosity. The BCML1 detector signal, converted into an effective charge collection efficiency, was used to calculate the radiation constant k_{prime} for the time where the BCML1 detector was operated at an electric field of $E = 1\,\text{V}/\mu\text{m}$ indicated in blue. Due to problems with the CMS magnet affecting as well the signal stability of the BCML1 detector, the bias voltage was reduced for an extended period of time indicated in grey.

average thickness of $d \sim 500\mu\text{m}$. After the first 3 month of LHC operation in 2015, cooling problems forced a temporary ramp down of the CMS magnet several times. During these periods of down time the bias voltage of the BCML1 detector was lowered to HV = 200 V to enable a stable detector operation. With the absence of the magnetic field and a bias voltage of HV = 500 V erratic currents would have been created that could result in an unjustified trigger of the LHC beam dump, see section 4.5.2. The average BCML1 detector signal at a bias voltage of HV = 500 V is shown in Fig. 5.5 in blue, whereas the BCML1 detector signal at reduced bias voltages is shown in grey. The BCML1 sensors installed at the beginning of Run 2 were undamaged and therefore showed initially a full signal efficiency, equivalent to a $\text{CCD}_{\text{init.}} = 181\,\mu\text{m}$. After an integrated luminosity of $\mathcal{L}_{\text{integr.}} = 45\,\text{fb}^{-1}$ the $\text{CCD}_{\text{eff.}}$ of the BCML1 detectors dropped to $\text{CCD}_{\text{eff.},\,45\,\text{fb}^{-1}} = 140\,\mu\text{m}$, a reduction of 22.6%. Based on the radiation constant $k = 6.5 \times 10^{-19}\,\text{cm}^2\mu\text{m}^{-1}$ [Tsu12] measured by the RD42 collaboration and indicated in red, a signal reduction of 2% is expected for the BCML1 location after an integrated luminosity of $\mathcal{L}_{\text{integr.}} = 45\,\text{fb}^{-1}$. The average BCML1 detector signal as function of radiation damage was fitted to Eq. 5.16 in order to determine the radiation constant k_{prime}. The radiation damage was converted into 24 GeV proton equivalents using the Fluka simulated conversion factors, see 5.2.1. For the radiation induced signal degradation of the BCML1 diamond detectors operated at an electric field of $E = 1\,\text{V}/\mu\text{m}$ a radiation constant of $k_{\text{prime}} = 0.56 \times 10^{-17}\,\text{cm}^2\mu\text{m}^{-1}$ was found.

In Fig. 5.6 the radiation induced signal degradation of the BCML2 detector is shown. In the BCML2 detector group all BCML2 abort channels are included, which are mounted at the inner location of the BCML2 wheel see Table A.4 in the appendix. The BCML2 detectors with an average thickness of $d \sim 400\mu\text{m}$ were operated at a bias voltage of HV = 200 V, equivalent to an electric field of $E = 0.5\,\text{V}/\mu\text{m}$. The BCML2 diamond sensors experienced already radiation damage during Run 1 and therefore had a reduced effective CCD at the beginning of Run 2 of $\text{CCD}_{\text{eff.}} = 95\,\mu\text{m}$. After an integrated luminosity of $\mathcal{L}_{\text{integr.}} = 45\,\text{fb}^{-1}$ the detector efficiency dropped by 64% to a $\text{CCD}_{\text{eff.}} = 34\,\mu\text{m}$. The expected signal degradation based on the radiation damage constant found by the RD42 collaboration is indicated in Fig. 5.6 in red. In comparison to the expected signal degradation to a $\text{CCD}_{\text{eff.,\,RD42}} = 91\,\mu\text{m}$, the BCML2 signal degradation was $\sim$ 15 times more severe than expected. An explanation for

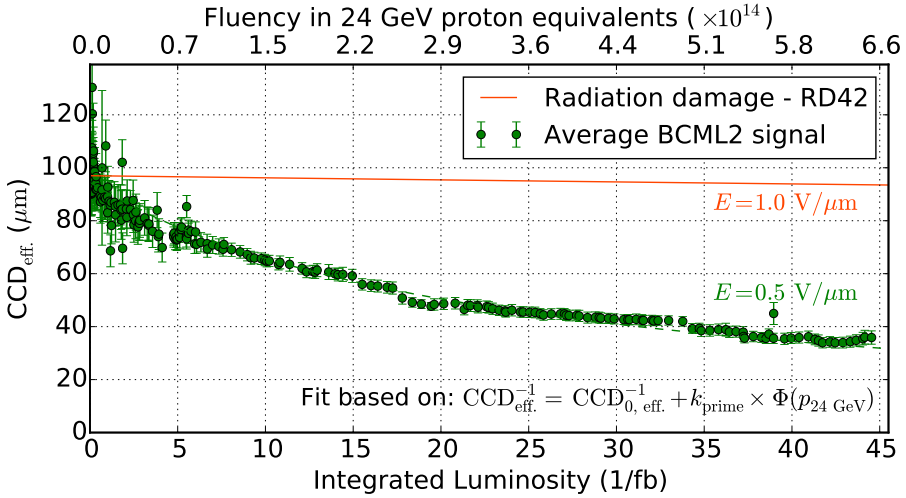

Figure 5.6: The BCML2 detector signal converted into an effective CCD value is shown as function of integrated luminosity for the entire detector operation in 2015 and 2016. The radiation induced signal degradation of the BCML2 detector (green) is compared to the predicted signal degradation based on the radiation constant $k_{\mathrm{RD42}} = 6.5 \times 10^{-19}\,\mathrm{cm^2 \mu m^{-1}}$.

the strong discrepancy is the difference in the electrical field at which the diamond sensors were operated. Based on the signal degradation during Run 2 a radiation constant of $k_{\mathrm{prime}} = 3.16 \times 10^{-17}\,\mathrm{cm^2 \mu m^{-1}}$ is calculated.

Using the standard radiation model the BCML1 and BCML2 signal degradation is extrapolated for the lifetime of the LHC, shown in Fig. 5.7. For a safe BCML detector operation, well above the read out noise, the lowest limit of the abort threshold are 1000 bits, equivalent to a signal current of $\sim 4.9\,\mu\mathrm{A}$ in RS1. The equivalent minimum required charge collection distance is calculated using Eq. 4.4 defined in section 4.2 via:

$$\begin{aligned} \mathrm{CCD_{min.}} &= \frac{4.9\,(\mu\mathrm{A}) \times 40\,(\mu\mathrm{s})}{10^6\,(\mathrm{MIPs/cm^2}) \times 0.925\,(\mathrm{cm^2}) \times 36\,(\mathrm{e/\mu m}) \times \mathrm{q_e}} \\ &= 36\,\mu\mathrm{m}. \end{aligned} \tag{5.17}$$

The absolute minimum of charge collection distance required for a save operation of the BCML detector was set to a slightly more conservative value of $\mathrm{CCD_{min.}} = 40\,\mu\mathrm{m}$, indicated in orange in Fig. 5.6. Based on this restriction the BCML2 diamond sensors already passed the minimum charge collection distance defined for a safe detector operation and will therefore be replaced at the 'Year End Technical Stop' in 2016/17 to guarantee a safe operation within the entire year 2017 and beyond. The BCML1 detector operated at an increased electrical field of $E = 1\,\mathrm{V/\mu m}$ could be operated the entire LHC lifetime without the need of another replacement. Nevertheless, Fig. 5.7 demonstrates the strongly increased radiation damage of the BCML1 detectors compared to the expected signal decrease.

5.3.3.2 Signal degradation of the BCML2 outer diamond detectors

Beside the BCML abort channels discussed in the previous section, the BCML2 diamond detectors located at the BCML2 outer locations are studied in this section. The BCML2 outer detectors, in total 11 pCVD diamond sensors, are located at an increased radius to the beam pipe of 28 cm. These diamond sensors were operated during Run 1 and experienced different radiation damage, depending on the location at which they were installed. The BCML2 outer sensors were separated into three groups, with similar irradiation damages. These three BCML2 outer detector groups were furthermore operated at three different bias

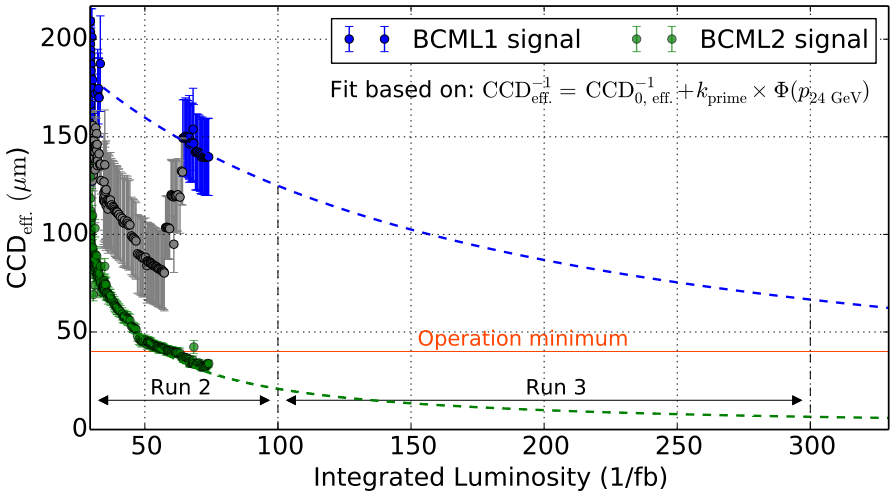

Figure 5.7: Based on the radiation induced signal degradation measured during Run 2 the $CCD_{eff.}$ is extrapolated for the entire lifetime of the LHC. The orange line indicates the operation minimum that is already passed by the BCML2 detector and therefore forces a complete replacement of all BCML2 diamond sensors. Based on this extrapolation the BCML1 detector could be operated till the end of the life time of the LHC.

voltages, leading to the three BCML2 outer detector groups: $BCML2_{out.\,200V}$, $BCML2_{out.\,350V}$ and $BCML2_{out.\,500V}$.

The radiation induced degradation of the effective charge collection efficiency was calculated for each BCML2 outer detector group separately and is shown in the Figs. A.8, A.9 and A.10 in the appendix. Since the BCML2 outer detector groups experienced different amounts of radiation damage, the effective CCD can't be compared directly. However, the same normalization in the calculation of the effective CCD is used for all BCML2 outer detector groups. Therefore, k_{prime} can be used to compare the radiation induced signal degradation of the BCML2 outer diamond detectors, since it is independent of the absolute $CCD_{eff.}$. Based on the individual calculated radiation constants k_{prime} for each BCML2 outer detector group the radiation induced signal degradation is normalized to an initial $CCD_{init,\,eff.} = 184\,\mu m$ and compared in Fig. 5.8. The expected signal degradation based on the RD42 radiation constant is plotted in red for comparison. An increased electric field leads directly to reduced signal degradation, however even at the highest electric field of $E = 1.25\,V/\mu m$ the measured signal reduction is increased compared to the RD42 prediction.

In Table 5.4 all radiation constants k_{prime} calculated for each detector locations are summarized. The comparison of the k_{prime} found for each detector location are consistent with respect to the bias voltage at which the detectors are operated. The strongest signal degradation is observed for the BCML2 detectors operated at the lowest electrical field of $E = 0.5\,V/\mu m$. For both detector locations BCML2 inner and BCML2 outer a radiation constant of $k_{prime} \sim 3.1 \times 10^{17}\,cm^2\mu m^{-1}$ is extrapolated, which is almost ~ 50 times higher than the radiation constant found by the RD42 collaboration of $k = 6.5 \times 10^{19}\,cm^2\mu m^{-1}$ measured at an electrical field of $E = 1.0\,V/\mu m$. The radiation constant measured for the BCML2 outer detector operated at an increased electric field of $E = 0.88\,V/\mu m$ is reduced to $k_{prime} \sim 1.85 \times 10^{17}\,cm^2\mu m^{-1}$. The lowest radiation induced signal degradation is measured for the two BCML detectors operated at a bias voltage of $HV = 500\,V$ with a radiation constant of $k_{prime} \sim 0.5 \times 10^{17}\,cm^2\mu m^{-1}$. This radiation constant is however still ~ 8 times increased compared to k_{RD42}, where the diamonds were operated at the same electrical field. Hence, the severe radiation damage observed during Run 1 [Gut14a] cannot only be explained by the reduced bias voltage, at which the BCML detectors were operated. A possible explanation for the severe radiation induced signal degradation is the polarization of the diamond

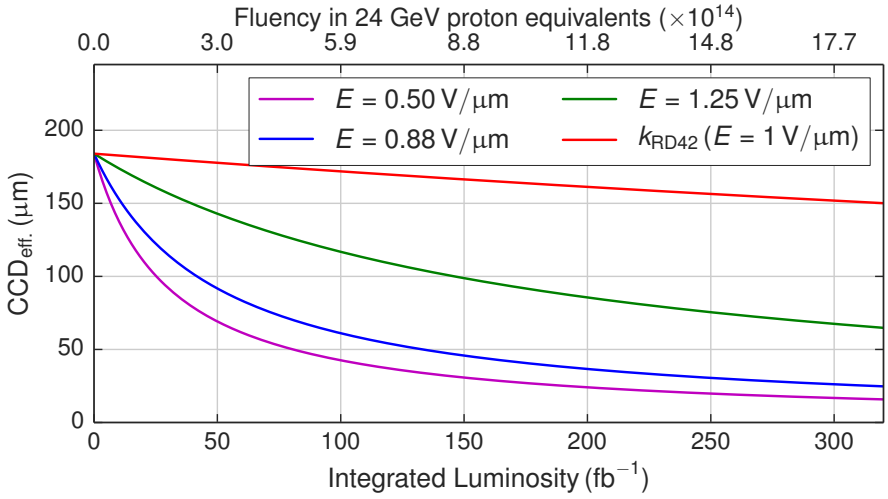

Figure 5.8: The BCML2 outer diamond sensors were operated at three different bias voltages: HV = 200 V (purple), HV = 350 V (blue) and HV = 500 V (green). The signal degradation based on the RD42 radiation constant for an electric field of $E = 1.0\,\mathrm{V/\mu m}$ is indicated in red.

Table 5.4: Overview of the calculated BCML radiation damage constants k_{prime}.

Detector group	HV (V)	E (V/µm)	$\mathrm{CCD}_{\mathrm{eff.,init.}}$ (µm)	k_{prime} ($\mathrm{cm^2\mu m^{-1}}$)
BCML1	500	1.00	180.7 ± 1.3	$(0.56 \pm 0.04) \times 10^{-17}$
BCML2	200	0.50	94.5 ± 0.6	$(3.16 \pm 0.08) \times 10^{-17}$
$\mathrm{BCML2_{out.\,200V}}$	200	0.50	114.3 ± 0.7	$(3.06 \pm 0.07) \times 10^{-17}$
$\mathrm{BCML2_{out.\,350V}}$	350	0.88	149.6 ± 1.1	$(1.85 \pm 0.07) \times 10^{-17}$
$\mathrm{BCML2_{out.\,500V}}$	500	1.25	178.5 ± 0.9	$(0.53 \pm 0.02) \times 10^{-17}$

sensors, see section 5.5.

5.4 Rate dependency of the BCML signal efficiency

The signal degradation of the BCML diamond detectors discussed in the previous section was observed as well during Run 1 [Gut13, Gut14a, Gut15]. Furthermore, the measurement results suggest that the signal efficiency of the diamond sensor is sensitive to the particle rate environment. That means pCVD diamond sensors operated at the same electrical field showed increased signal degradation at locations with an increased particle flux. In section 5.4.1 the signal efficiency will be studied with respect to the ionizing particle rate. In section 5.4.2 the rate dependency of the signal efficiency will be studied with respect to the electrical field at which the sensors are operated.

5.4.1 Rate dependency of the Signal Efficiency within one LHC fill

For a protection device like the BCML detector, the linearity of the sensor signal to the exposed particle rate is essential. Based on this signal linearity a beam abort threshold can be extrapolated and defined. If this signal linearity is not given the abort threshold could be defined wrong and therefore not effectively protect against catastrophic beam loss events.

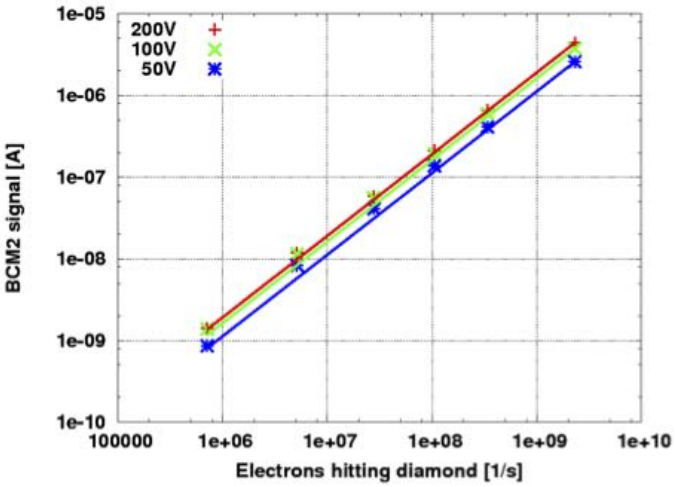

Figure 5.9: Signal linearity of an un-irradiated BCML2 diamond sensor as function of the exposed particle rate. At an operating bias voltage of HV = 50 V a saturation for high particle rate is visible. For increased operating bias voltages the diamond signal is linear to the particle rate [Mue11].

The signal linearity of the BCML diamond signal with respect to the exposed particle rate was therefore studied in several test beams [Mue11]. For un-irradiated diamond sensors a linear signal response was found up to particle rates corresponding to the BCML beam abort thresholds, see Fig. 5.9.

During a typical LHC fill the BCML sensors are exposed as well to different particle rates, see section 4.3.1. At the beginning of the LHC fill, the proton beams have the highest intensities and therefore the highest instantaneous luminosity is measured. With increased LHC fill duration the proton beam intensity and respectively the instantaneous luminosity is reduced, due to the proton-proton collision itself and beam losses. Based on the signal current of the BCML detectors the particle flux in MIP equivalents can be estimated. For nominal luminosity of $\mathcal{L}_{\text{inst.}} = 1{\times}10^{34}\,\text{cm}^{-2}\text{s}^{-1}$ the BCML1 (BCML2) locations is exposed to a particle rate of $\sim 50\,\text{MHz}$ ($\sim 500\,\text{MHz}$) in MIP equivalents. The signal linearity of the BCML1 and BCML2 detectors during the Fill 5199 is shown in Fig. 5.10. The normalized BCML detector

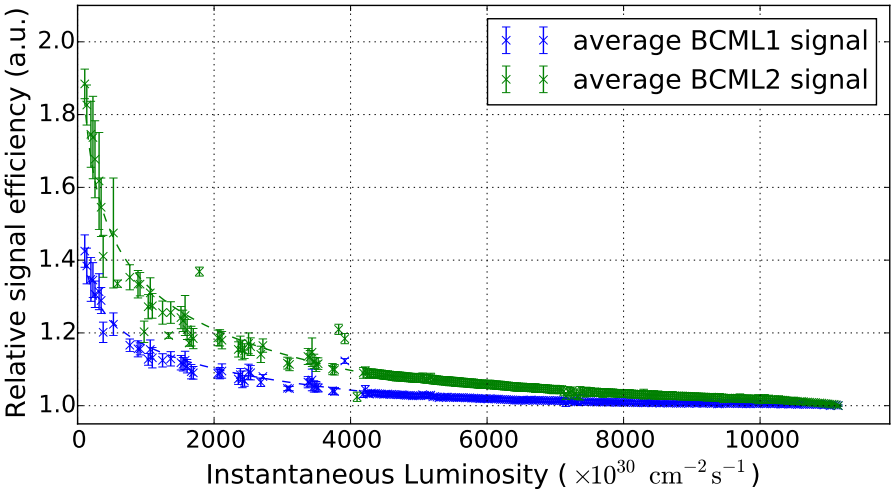

Figure 5.10: The normalized BCML signal efficiencies plotted as function of instantaneous luminosity. The BCML signal is normalized to the maximum instantaneous luminosity during Fill 5199 of $\mathcal{L}_{\text{inst.}} = 1.12 \times 10^{34}\,\text{cm}^{-2}\text{s}^{-1}$. Both detectors were operated during that fill at a bias voltage of HV = 200 V.

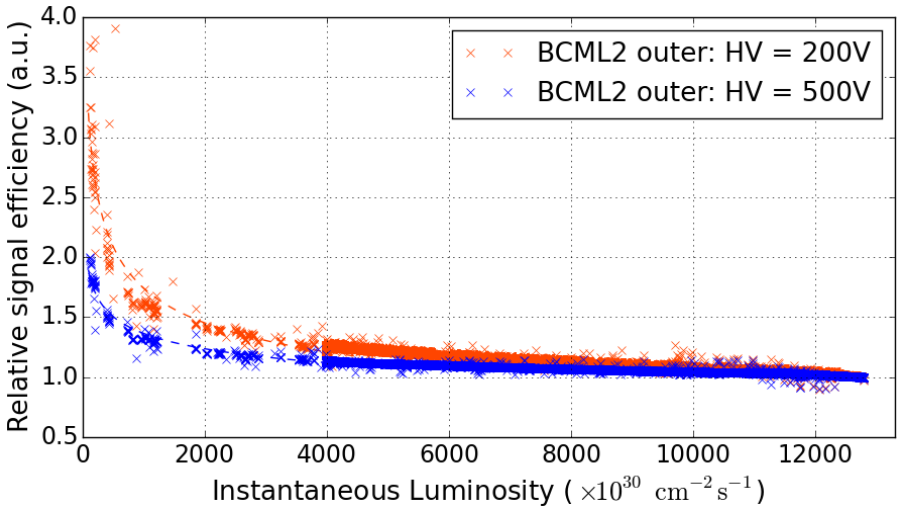

Figure 5.11: Comparison of the rate dependent signal efficiency of two BCML2 outer diamond detectors operated at different bias voltages. The BCML2 detector signal is normalized to the maximum instantaneous luminosity and plotted over the instantaneous luminosity. The rate dependency of the signal efficiency of the BCML2 detector operated at a reduced bias voltage of HV = 200 V is increased compared to the BCML2 detector operated at an increased bias voltage of HV = 500 V.

signal to the maximum instantaneous luminosity of $\mathcal{L}_{\text{inst.}} = 1.12 \times 10^{34}\,\text{cm}^{-2}\text{s}^{-1}$ is plotted as function of the instantaneous luminosity, measured by the HF detector. The relative signal efficiency of the BCML detector shows an increased signal efficiency for lower rates, indicating a reduced detector efficiency for high particle rates. The rate dependency for the BCML2 detector is increased compared to the BCML1 detector, this could be either related to the increased radiation damage of the BCML2 detector or to the increased particle rate at the BCML2 detector locations. Both BCML detectors were operated during this fill at the same bias voltage of HV = 200 V.

5.4.2 Signal Rate Dependency with respect to the Operating Bias Voltage

The rate dependency of the signal efficiency with respect to the bias voltage, at which the BCML diamond sensors are operated, is shown in Fig. 5.11. At the BCML2 outer location, diamond sensor with comparable radiation damage are operated at bias voltages of HV = 200 V and HV = 500 V. The diamond sensors operated at the reduced bias voltage of HV = 200 V shows an increased rate dependency of the signal efficiency, compared to the diamond sensors operated at an increased bias voltage. Hence, the electric field is crucial in understanding the effects causing the particle rate dependency of the diamond signal.

5.5 Rate Dependent Diamond Polarization

The unexpected severe radiation induced signal degradation of the BCML detectors, operated as well at an electric field of $E = 1\,\text{V}/\mu\text{m}$, and the rate dependency of the BCML detector efficiency can be explained by the polarization of the diamond sensor. The basic idea of the diamond polarization is a highly dynamic build-up of space charge in the sensor bulk with respect to the particle rate environment. This space charge manipulates the internal electric field resulting in a severe signal reduction at high particle rates.

The diamond polarization is schematically shown in Fig. 5.12 and explained in detail in the following. The diamond sensors installed at CMS are exposed to high rates of ionizing

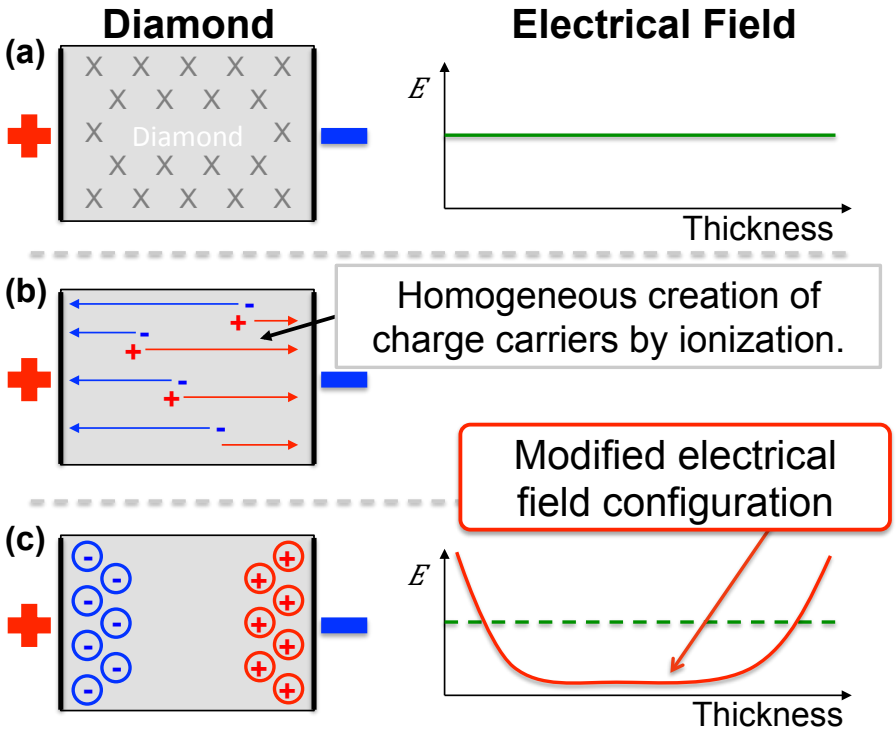

Figure 5.12: Diamond polarization: Radiation damage leads to a homogeneous distribution of lattice defects in the diamond bulk (a). The external electrical field leads to an asymmetrical distribution of the charge carrier density, since the flux and therefore the trapping probability of positive (negative) charge carriers is proportional to the thickness of the collecting region, as shown in (b). This results in an asymmetrical build-up of space charge (c) and hence in a locally reduced electric field that causes an increase in charge carrier recombination and results therefore in a reduced charge collection efficiency.

particles ($\sim 500\,\mathrm{MHz}$) that are creating lots of electron hole pairs in the diamond bulk. With an external electrical field applied the electrons are drifting to the anode and the holes are drifting to the cathode, see Fig. 5.12b. These charge carriers can be trapped at defects in the diamond bulk that are created by irradiation damage. The lattice defects are homogeneously distributed in the diamond bulk, see Fig. 5.12a. The probability of a charge carrier being trapped in a defect is linearly proportional to the charge carrier density. Due to the external electrical field the electron density is increased close to the anode and the hole density is increased close to the cathode. Hence, the probability for electron (hole) trapping is increased at the anode (cathode). This inhomogeneous charge trapping probability causes the creation of space charge predominantly towards the edges of the sensor. The electric field, formed by the space charge counteracts the external applied electrical field and leads to a local minimum in the central region, see Fig. 5.12c. Since the externally applied voltage is kept constant, the integral over the entire electric field is conserved as well. Increased electrical fields towards the sensor edges compensate the local minimum in the electrical field. In the low electric field region the recombination rate is increased and hence the overall charge collection efficiency of the sensor reduced. An increased particle rate or an increased amount of bulk defects result both in an higher charge carrier trapping rate and hence in an increased build-up of space charge that finally leads to a further reduction of the CCE. Since lattice defects in diamond sensors are not only created by irradiation damage but are also created during the diamond growth process, the diamond polarization is always present as well for un-irradiated sensors.

The simulation and prediction of the diamond detector performance with respect to the radiation damage and the particle rate environment is the core component of this work. Therefore, a quantitative understanding of the diamond polarization is essential. This was

gained by a dedicated diamond irradiation campaign that was used to create an effective defect model describing the irradiation damage and the accompanying diamond polarization, discussed in chapter 6.

5.5.1 Detector Efficiency with respect to the Bias Voltage

If the polarization of the diamond bulk is the reason for the severe signal degradation, an increased bias voltage should overcome the polarization and should restore the CCE. The build-up of space charge and hence the modification of the internal electric field is determined by the amount of bulk defects and by the particle rate environment. An increase in the bias voltage should therefore reduce the impact of the electric field created by the space charge. With a theoretically infinite high bias voltage any polarization field could be compensated entirely.

The BCML1 signal degradation during Run 2 with respect to the total integrated luminosity is shown in Fig. 5.13 for different bias voltage settings. The BCML1 detector was operated during Run 2 most of the time at a bias voltage of 200 V. At an integrated luminosity of $\mathcal{L}_{\text{integr.}} = 27.5\,\text{fb}^{-1}$ the normalized BCML1 signal dropped to 65 nA. Increasing the bias voltage step wise up to 500 V, which corresponds to an electric field of $E = 1\,\text{V}/\mu\text{m}$, increased the normalized BCML1 signal to 114 nA. In terms of effective charge collection distance, the initial value of $\text{CCD}_{\text{eff.}} = 181\,\mu\text{m}$ dropped after an integrated luminosity of $\mathcal{L}_{\text{integr.}} = 27.5\,\text{fb}^{-1}$ at a bias voltage of $\text{HV} = 200\,\text{V}$ to $\text{CCD}_{\text{eff.}} = 90\,\mu\text{m}$, a reduction of 50%. Increasing the bias voltage back to $\text{HV} = 500\,\text{V}$ resulted in a $\text{CCD}_{\text{eff.}} = 160\,\mu\text{m}$, and hence could restore to 88% of the initial $\text{CCD}_{\text{eff.}} = 181\,\mu\text{m}$ value.

In order to minimize the impact of the polarization the sensors should always be operated at the maximum stable bias voltage.

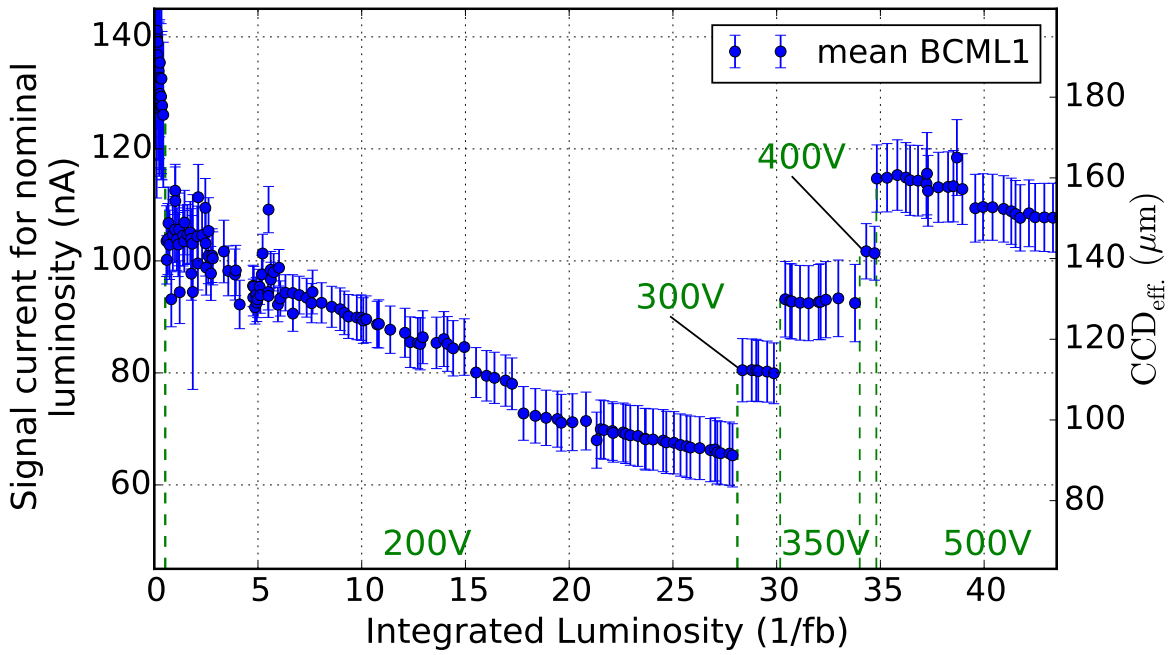

Figure 5.13: BCML1 signal degradation during Run 2 with respect to different bias voltages. During the first $0.5\,\text{fb}^{-1}$ in Run 2 the BCML1 detector was operated at 500 V. However, due to problems with the CMS magnet, the BCML1 bias voltage was reduced to 200 V, see 4.5.2. At 200 V the signal efficiency dropped to 50% and could be increased to 88% by increasing the bias voltage back up to 500 V.

5.6 Limitation of the Trapping Model describing the Radiation Damage in Diamond Detectors

The most important weakness of the standard diamond radiation model is the assumption of having a constant charge carrier drift, see Eq. 5.4. This equation is however only true for a constant electric field inside the diamond detector. If we consider highly dynamic effects like the diamond polarization, discussed in the previous section 5.5, the internal electric field of the diamond sensor is modified and hence the charge carrier drift velocity directly affected. The standard diamond irradiation model has therefore to fail at such high particle rates environment, since the modified electric field is not taken into account. The charge carrier drift is linear proportional to the electric field:

$$\mathrm{v_{drift,e/h}} = \mu_{\mathrm{e/h}}\mathrm{E} \tag{5.18}$$

with $\mu_{e/h}$ the mobility for electron or holes. The non constant charge carrier drift velocity is affecting directly the mean free path length and hence determines the overall charge collection distance of the diamond sensors.

In order to create a new diamond radiation model that also takes dynamic effects like the diamond polarization into account, a dedicated diamond irradiation study was done with single crystalline diamonds. The measurement results of the irradiation campaign were used to create an effective diamond defect model that takes as well highly dynamic effects, like the diamond polarization, into account. This new effective diamond defect model and the irradiation campaign on which it is based are discussed in the next chapter 6.

Chapter 6

Simulation of the Radiation Induced Signal Degradation of Diamond Sensors using an effective defect model

The severe radiation induced signal loss of the BCML detectors discussed in the previous chapter is believed to be caused by the diamond polarization. In order to quantitatively study the rate dependent electrical field deformation with respect to the radiation damage, a diamond irradiation campaign was started. Beside electrical field measurements via the Transient Current Technique (TCT), the CCE was measured. The experimental results were used to create an effective deep trap model that takes the radiation damage into account. Using this trap model the rate dependent electrical field deformation and the charge collection efficiency could be simulated with the software Silvaco TCAD [SIL16]. The simulation, tuned to the rate dependent measurements from a strong radioactive source, was able to predict the non-linear decrease of the CCE in the harsh environment of the LHC, where the particle rate is a factor ~ 100 higher.

Four high quality single crystalline diamonds, produced by *Element6* [Ele16], were bought for the diamond irradiation campaign and were stepwise irradiated either with neutron or proton particles. After each irradiation step the rate dependent electrical field deformation of the diamond sensors was studied using different measurement techniques introduced in section 6.1. The irradiation facilities providing the proton or neutron particles are introduced in section 6.2. The measurement results of the diamond irradiation campaign are discussed in section 6.3. In the last section 6.4, the effective defect model describing quantitatively the diamond polarization as function of radiation damage will be introduced.

6.1 Techniques to measure the Electrical Properties of the Diamond Sensors

This section will focus on different measurement techniques used to characterize the diamond sensors after each irradiation step. The most important measurement is the Transient Current Technique (TCT) that allows an indirect measurement of the electrical field inside the diamond sensor, see section 6.1.1. The performance of the diamonds as particle detectors is measured with the charge collection efficiency (CCE) method introduced in section 6.1.2. Cross polarized pictures can be used as a visible comparison of the diamond quality, introduced in section 6.1.3.

6.1.1 The Transient Current Technique (TCT) measurement Setup

The electrical field can be measured indirectly using the Transient Current Technique (TCT), by inducing electron-hole pairs on one side of the diamond via α particles. The external applied electrical field causes the charge carries created by the α particle, to drift in opposite direction through the diamond bulk. Since α particles have a small penetration depth of $d \leq 15\,\mu m$ (see section 6.4.3.3) one type of charge carrier reaches immediately the electrode. The other type of charge carrier is drifting through the entire diamond bulk. The charge carrier drift is linear proportional to the local electrical field. Based on Ramo's theorem [Ram39b] drifting charge is inducing instantaneously a current in the electrical circuit. This current as function of time is proportional to the charge carrier drift velocity as function of distance, which is equivalent to the electrical field as function of distance. The measurement of the signal current as function of time is therefore an indirect measurement of the electrical field as function of sensor thickness. The electrical field can be estimated based on the shape of the TCT pulse, see Fig. 6.1a. For a constant electrical field a square TCT signal is expected. The TCT measurement contains furthermore information of the intrinsic charge carrier properties like: drift velocity, mobility or the effective mass, see Fig. 6.1b. Creating the electron-hole pairs on the cathode or anode side allows measuring the electron or the hole drift, respectively.

The TCT setup shown in Fig. 6.2 consists of a Picosecond 5531 bias tee, a Particulars wide band current amplifier (53 dB, 0.01-2 GHz) [Par16], a Tektronix TDS 5104B oscilloscope (5 GSPS, 1 GHz) and a Keithley 2410 as bias voltage source. The limiting component in terms of bandwidth is the oscilloscope with 1 GHz. A 3.56 kBq ^{241}Am source is used to create α particles. In addition β particles from a 32. 2 MBq ^{90}Sr source are used to create a constant ionization rate, creating electron-hole pairs homogeneously in the entire diamond bulk. The α particle is stopped inside the material; therefore an internal trigger has to be used. The read-out by the digital storage scope is triggered internally with a threshold of 10 mV. The TCT pulses from the scope are read out with a frequency of 2.5 Hz. The post processing of the data consists of baseline subtraction, realignment and averaging.

TCT setup extension to measure the electrical field at alternating bias voltage

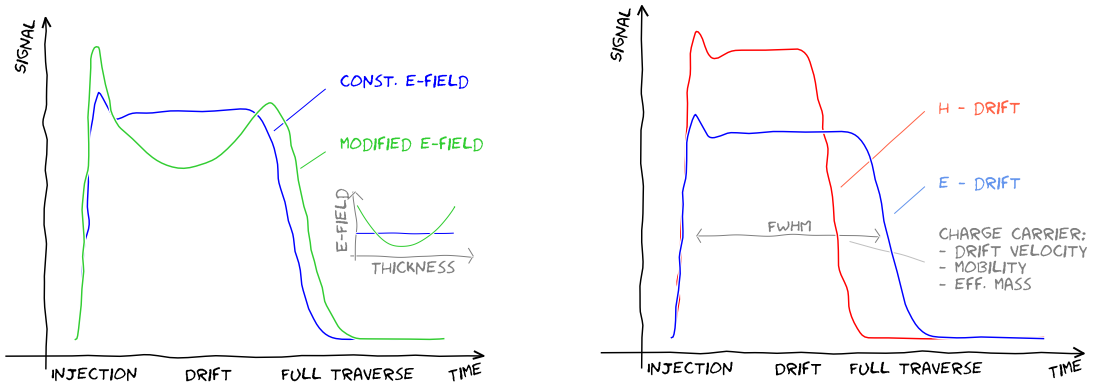

(a) TCT pulse for a constant (blue) and modified (green) electrical field.

(b) TCT pulse for electron (blue) and hole (red) charge carrier in diamond.

Figure 6.1: The TCT measurement can be used to estimate the electrical field with respect to the thickness inside the diamond bulk, see left figure. In the right figure the TCT pulses for electron (blue) and hole (red) charge carrier are compared to each other for the same electrical field. At an electrical field of $E = 1\,V/\mu m$ the hole mobility is increased compared to the electron mobility, resulting in a shorter and higher TCT pulse for the hole charge carriers.

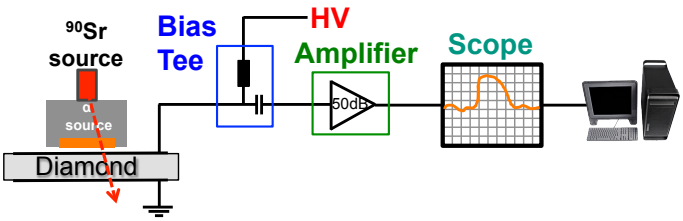

Figure 6.2: Schematically drawing of the TCT setup. The TCT setup consists of a bias tee, a signal amplifier and an oscilloscope. The TCT signal created by the α particles is decoupled from the high voltage circuit into the signal circuit via the bias tee. The high frequent TCT signal is amplified and read out with a digital storage scope with a bandwidth of 1 GHz.

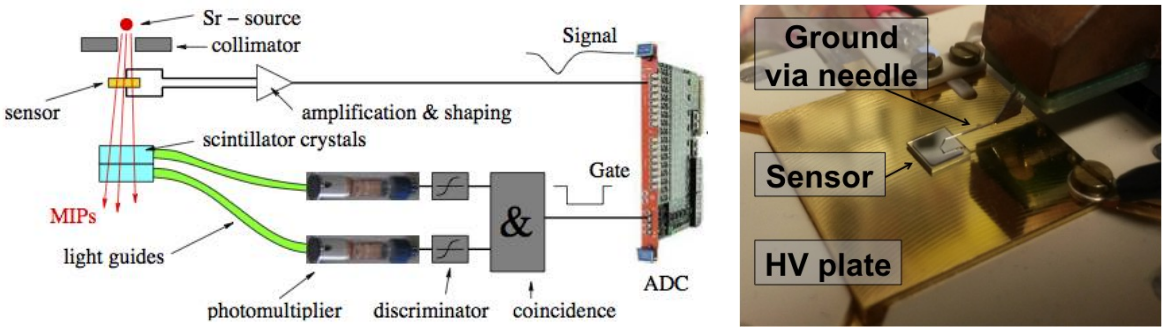

(a) Schematic of the CCE setup, taken from [Ohl09]. **(b)** sCVD diamond at CCE setup.

Figure 6.3: The MIP particles used to create a defined amount of charge carriers in the sensor volume are passing through two scintillators located on the opposite side of the sensor. The scintillators are used to trigger the signal read out of the sensor. The right picture shows a diamond sensor at the CCE setup in DESY Zeuthen. The bias voltage is applied via the bottom plate and the MIP signal is read out via the ground line through the needle on top of the diamond sensor.

The TCT setup was extended to enable the measurement of the rate dependent diamond polarization for alternating electrical fields. The power supply was therefore replaced by a signal generator in combination with a voltage amplifier. The voltage amplifier Trek Model 2220 [Tre16] has a slew rate of 100 V/µs with a DC voltage gain of 200. A rectangular bias voltages of HV = ±500 V was therefore created by a signal generator input of HV = ±2. 5 V to the voltage amplifier. The read-out software of the digital storage scope was adjusted to pick up the polarity of the signal generator in order to set the trigger polarity accordingly.

6.1.2 Charge Collection Efficiency (CCE) measurements

The charge collection efficiency (CCE) or the charge collection distance (CCD) is one of the key measurements in order to characterize particle detectors. The CCE measurements presented in this work were done at the measurement setup at DESY Zeuthen, Germany. In this section a brief introduction of the particular CCE setup and its working principle is given, a more detailed description of this measurement setup can be found in [Ohl09] and [Ste15].

The basic working principle of the CCE measurement is the creation of a well-defined amount of charge carriers inside the semiconductor, and comparing this to the measured amount of charge carriers of this particular event. This fraction is defined as charge collection efficiency (CCE) that can be used as well to calculate the charge collection distance (CCD). The CCE setup at DESY is shown schematically in Fig. 6.3a. A well-defined amount of charge carriers can be induced into the diamond sensor by using minimum ionizing particles (MIP). A MIP

event ionizes 36 electron-hole pairs per µm of diamond thickness. The total amount of induced charge carriers can therefore be calculated by:

$$Q_{\text{induced}} = 36\,(\frac{\text{e,h pairs}}{\mu\text{m}}) \times d_{\text{Diamond}}\,(\mu\text{m}), \tag{6.1}$$

with d_{Diamond} as diamond thickness. The MIP particles, created by a β particle source, passing through the diamond detector can be detected on the opposite side by two scintillators, compare Fig. 6.3a. If both scintillators detect the MIP the coincidence unit triggers the signal read out of the diamond sensors. The external trigger based signal read out reduces the systematic error of the CCE measurement. The diamond signal is amplified and shaped before being digitized with an analog-to-digital converter (ADC). The measured particle spectrum is histogrammed and fitted with a Landau distribution convoluted with a Gaussian distribution in order to calculate the most probable value (MPV). Furthermore, the noise pedestal is measured and subtracted from the MPV value in order to calculate the total amount of measured charge Q_{meas}. The CCE measurement setup is calibrated by injecting a well-defined amount of charge from a capacitor. The measured charge is therefore calculated via:

$$Q_{\text{meas}} = (MPV - Ped) \cdot Calib. \tag{6.2}$$

Hence the charge collection efficiency (CCE) and the charge collection distance (CCD) of the diamond detector are calculated via:

$$\text{CCE} = \frac{Q_{\text{meas}}}{Q_{\text{induced}}}, \tag{6.3}$$

$$\text{CCD} = \text{CCE} \cdot \text{d}_{\text{Diamond}}. \tag{6.4}$$

The MIP particles are created by a 33.4 MBq ^{90}Sr source, which creates simultaneously a constant ionization rate.

(a) Setup to take cross-polarized pictures.

(b) Cross polarized picture of diamond sample (#27135476).

Figure 6.4: Two linear polarized filters below and above the diamond sensor are aligned perpendicular to each other, see figure on the left. The linear polarized light created by the first filter can only pass the second filter, if its polarization is changed. On the right side a cross polarized picture of a high quality sCVD diamond sensor is shown. One point like tension indicated in red and increased tensions close to the corners are visible, most probably caused by the cutting of the diamond sensor.

6.1.3 Cross Polarized Pictures

A method to compare optically the quality of diamond sensors is the usage of cross-polarized pictures [Tan74, Mar04, Tal06b]. Lattice defects in the diamond sensor can cause tensions or

stress it the material. These tensions or stress in the diamond material can lead to birefringence that changes the polarization of light. In Fig. 6.4a the setup to take cross-polarized pictures is shown. Two linear polarized filters, aligned perpendicular to each other, prevent any light passing through both filters, except its polarization was modified. A resulting cross-polarized picture of a high quality single crystalline diamond is shown in the picture 6.4b.

6.2 Irradiation Facilities for Proton and Neutron Irradiation

The sCVD diamond sensors were irradiated either with reactor neutrons at the Jozef Stefan Institute of Ljubljana or with protons from a compact cyclotron at the KIT. The diamond irradiation at these facilities was enabled by the 'Advanced European Infrastructures for Detectors at Accelerators' project (AIDA-2020), which provides free transnational access to different irradiation facilities [AID16]. Both irradiation facilities will be shortly introduced in the following.

6.2.0.1 Neutron Irradiation

An experimental nuclear reactor at the Jozef Stefan Institute of Ljubljana in Slovenia is used to create a neutron particle flux reaching energies of up to 10 MeV, see neutrons spectrum in Fig. 6.5a. The radiation damage caused by these fast neutrons (neutrons of energy greater than 100 keV) was calculated based on the non-ionizing energy loss (NIEL - see section 3.3.6) of neutrons in the range of $100\,\mathrm{keV} - 30\,\mathrm{MeV}$. The damage factor, normalized to 1 MeV neutron equivalents was found to be 1.2 [Lag15].

6.2.0.2 Proton Irradiation

The compact cyclotron at the KIT [Ins16] is accelerating H^- molecules to an energy of $E_{H^-} \sim 25\,\mathrm{MeV}$. The negatively charged hydrogen is scattered at a foil, where both electrons are removed. The proton irradiating the diamond sample has an energy of $E_{\mathrm{proton}} = 22.9\,\mathrm{MeV}$ [Die10]. This value is based on simulation with SRIM [Zie16] shown in Fig. 6.5b. The radiation damage factor of these proton particles translates to 2.8, by normalizing to 1 MeV neutron equivalent, based on the NIEL model for diamond [Gut14b].

6.3 Measurement Results of the Diamond Irradiation Study

The measurement results of the diamond irradiation campaign, obtained with the different techniques discussed in the previous section 6.1, will be presented in the following. Before the high quality single crystalline diamonds were metallized, cross polarized pictures were taken to compare their quality, see section 6.3.2. The metallized diamond sensors were irradiated stepwise with proton or neutron particle, see section 6.3.3. In the sections 6.3.4 and 6.3.5 the CCE and TCT measurement results are discussed as function of radiation damage. In the last section 6.3.7 the charge carrier drift velocity is analyzed as well as function of irradiation damage.

6.3.1 High quality Diamond Samples used in the Diamond Irradiation Study

Four new single crystalline diamonds of highest quality 'electronic grade' corresponding to $[N] < 5\,\mathrm{ppB}$ and $[B] < 1\,\mathrm{ppB}$ produced by *Element6* [Ele16] were used to investigate the

rate dependent diamond polarization with respect to the irradiation damage. In addition an unused BCM1F diamond sensor '#24990289' from the same production batch was included in the irradiation study. After the cross-polarized pictures were taken, see section 6.3.2, the diamond samples were metallized at the Princeton University. On the 5×5 mm diamond surfaces ohmic titanium/tungsten electrodes were sputtered with a thickness of 100 nm after 1 μm of the surfaces was removed by a chlorine chemistry reactive ion etching. The metal electrodes with a surface of 4×4 mm were annealed in an N_2 environment for 4 min at 400 °C. The geometrical dimension of the metallized diamond sensors was measured by a high accuracy microscope. The diamond thicknesses are of special interest to calculate the electrical field at which the diamond sensors are operated, see Table 6.1.

Table 6.1: Overview of the geometrical dimensions of the diamond sensors used in Irradiation Study.

Name	Thickness (µm)	Electrical field (V/µm)			
		0.18	0.36	0.73	1.09
27135473	549	100 V	200 V	400 V	600 V
27135474	549	100 V	200 V	400 V	600 V
27135475	526	96 V	192 V	383 V	575 V
27135476	538	98 V	196 V	392 V	588 V
24990289	542	99 V	197 V	395 V	592 V

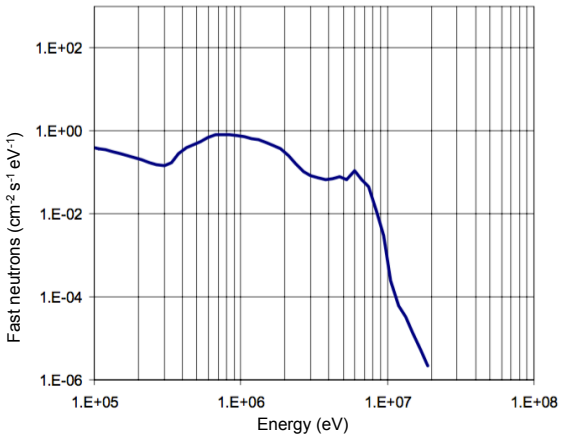

(a) The neutron spectrum created by the experimental nuclear reactor at the Jozef Stefan Institute. The spectrum was measured by irradiating well-understood materials and measuring their gamma ray spectra. Based on these results the neutron spectrum was calculated. The figure is taken from [Kri03], where further details can be found.

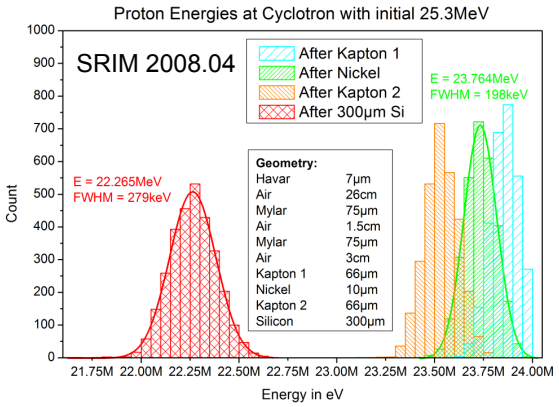

(b) The energy of the protons created by the compact cyclotron at the KIT was simulated using SRIM [Zie16]. The mean simulated energy of the protons approaching the sample is $E_{\text{proton}} = 23.8$ MeV (green) and after passing through 300 µm of Si is reduced to an energy of $E_{\text{proton}} = 22.3$ MeV. Hence the average proton energy in the middle of the sensor is $E_{\text{proton}} = 22.9$ MeV. Figure and simulation results taken from [Die10].

Figure 6.5: Proton and neutron spectrum used to irradiate the diamond sensors.

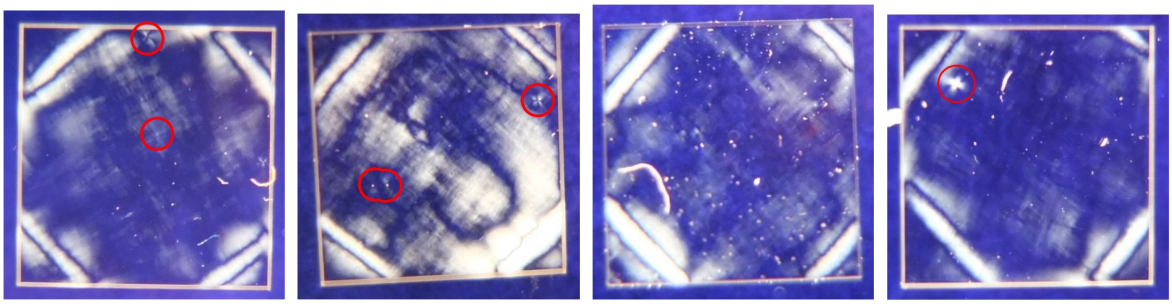

(a) #27135473 **(b)** #27135474 **(c)** #27135475 **(d)** #27135476

Figure 6.6: Cross polarized pictures of the 4 new sCVD diamonds from Element6. All diamonds show elongated tensions close to the sensor corners. The few visible localized tensions in the diamond bulk are indicated in red.

Table 6.2: Overview of the diamond irradiation steps. The diamond samples were irradiated up to 7 times to a total irradiation damage of $3.0 \times 10^{14}\, n_{1\,\mathrm{MeV}}$. The CCE of the diamond sensors was measured before irradiation and after the irradiation steps indicated in blue. The CCD measurement results with the diamonds irradiated with neutron particles indicated a underestimation of the radiation damage by a factor of 3.05. The corrected radiation damage is therefore given in brackets.

Name	Particle type	Total irradiation damage in 1 MeV neutron equivalents ($\times 10^{13}$)						
		1^{st}	2^{nd}	3^{rd}	4^{rd}	5^{rd}	6^{rd}	7^{rd}
27135473	$p_{23\,\mathrm{MeV}}$	0.3	**0.6**	0.9	1.5	4.5	**15.1**	-
27135474	$p_{23\,\mathrm{MeV}}$	0.3	0.6	**0.9**	1.2	1.8	4.8	**30.1**
27135476	$n_{\leq 10\,\mathrm{MeV}}$	0.1 (0.3)	**0.2 (0.6)**	0.3 (0.9)	0.6 (1.83)	**1.8 (5.5)**	-	-
24990289	$n_{\leq 10\,\mathrm{MeV}}$	0.1 (0.3)	**0.2 (0.6)**	0.3 (0.9)	0.6 (1.83)	**1.8 (5.5)**	-	-

6.3.2 Cross Polarized Pictures of the Diamond Samples

With the cross polarized pictures technique lattice defects in the diamond bulk can be made visible, see section 6.1.3. The cross polarized pictures of the 4 sCVD diamond sensors are shown in Fig. 6.6. A general pattern that can be observed for all diamond sensors, are elongated tensions close to the sensor corners. Only a few localized defects are visible that appear in the shape of a star, indicating a very high diamond quality with a small amount of lattice defects.

6.3.3 Stepwise Irradiation of the Diamond Sensors

Two of the four single crystalline diamond sensors have been irradiated stepwise with the 10 MeV neutron particle spectrum at the JSF experimental nuclear reactor. The other two sCVD diamonds have been irradiated at the proton irradiation facility in Karlsruhe. In Table 6.2 an overview of the irradiation steps of the 4 sCVD diamond sensors is given in 1 MeV neutron equivalents. The sCVD diamond sensors were irradiated up to $3.0 \times 10^{14}\, n_{1\,\mathrm{MeV}}$, equivalent to a particle fluence of $1.0 \times 10^{15}\, p_{24\,\mathrm{GeV}}$ or equivalent to a total integrated luminosity of $82.5\,\mathrm{fb}^{-1}$ at the BCML2 location using the NIEL model. The irradiation steps in equivalents of 24 GeV protons or as integrated luminosity for the BCML2 locations can

be found in the appendix in the Tables A.5 and A.6. The charge collection efficiency of the sCVD diamonds has been measured three times. The first CCE measurement of the sCVD diamonds was done with the un-irradiated samples, the second and third CCE measurement was done after different irradiation steps that are indicated in blue in Table 6.2.

6.3.4 Charge Collection Efficiency with respect to the Radiation Damage

The charge collection efficiency of the diamond sensors used in the irradiation campaign was measured regularly at the CCE setup at DESY in Zeuthen, introduced in section 6.1.2. Two different CCE measurement procedures were done to characterize the CCE of the sCVD diamond sensors. The standard CCE measurement procedure is the measurement of the CCE as function of bias voltage, see section 6.3.4.1. In the second type of CCE measurement the charge collection efficiency was measured as function of time at a constant electrical field, which is discussed in section 6.3.4.2. The BCM1F diamonds sensor #24990289 is metallized on both surfaces with a split pad metallization. With increased irradiation damage the CCE measurements done with this particular diamond showed charge sharing effects. This means, a part of the charge carriers are induced in the not connected and therefore floating pad that leads to a strongly reduced charge collection on the pad used for the signal read out. Hence this diamond sensor is excluded from the data analysis, however will be discussed separately in section 6.3.4.3.

6.3.4.1 CCE as function of Radiation Damage and Bias Voltage

The CCE measurement as function of bias voltage is a very common measurement to characterize the quality of diamond detectors. In order to keep the CCE measurement reproducible and consistent the following measurement procedure was used:

- The diamond sensor is exposed to the ^{90}Sr source of the CCE setup for 1 hour without having any bias voltage applied.
- The bias voltage is ramped up quickly to the target voltage and the CCE measurement is started.
- 20.000 MIP events are measured that are used to calculate the CCE value. The 20.000 events are measured within $t_{\text{meas.}} \sim 85\,\text{s}$.
- The bias voltage is ramped down quickly to HV = 0 V after the CCE has been measured for a particular electrical field.
- The diamond sensor is exposed to the ^{90}Sr source at HV = 0 V as well for a duration of $t_{\text{meas.}} \sim 85\,\text{s}$ in order to remove any build up of space charge created during the previous CCE measurement.
- The diamond is quickly ramped up to the next bias voltage for the next CCE measurement.

Very high quality diamond sensors reach full charge collection efficiency already at very low electrical fields of $E \leq 0.2\,\text{V}/\mu\text{m}$. The blue curves in Figs. 6.7a, 6.7b and 6.7c show the measured charge collection efficiencies of the unirradiated diamond sensors used in the irradiation campaign. All sensors reach full charge collection efficiency at electrical fields below $E \leq 0.2\,\text{V}/\mu\text{m}$ and hence confirm their excellent quality. At an increased radiation damage of up to $0.9 \times 10^{13}\, n_{1\,\text{MeV eq.}}/\text{cm}^2$ shown in green, a full charge collection efficiency is only reached for increased electrical fields. At the highest irradiation damages between $5.5-$

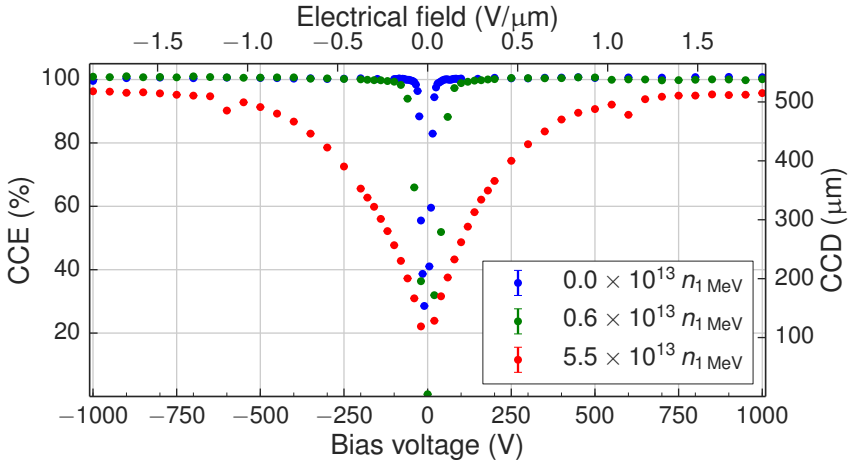

(a) #27135476

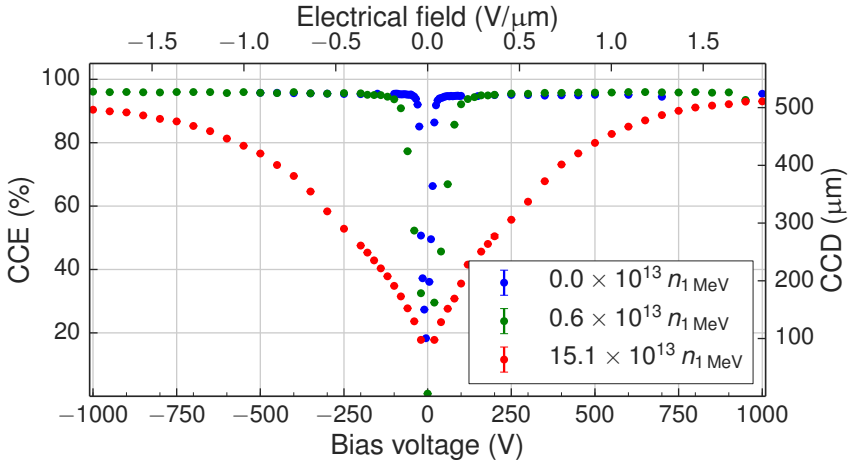

(b) #27135473

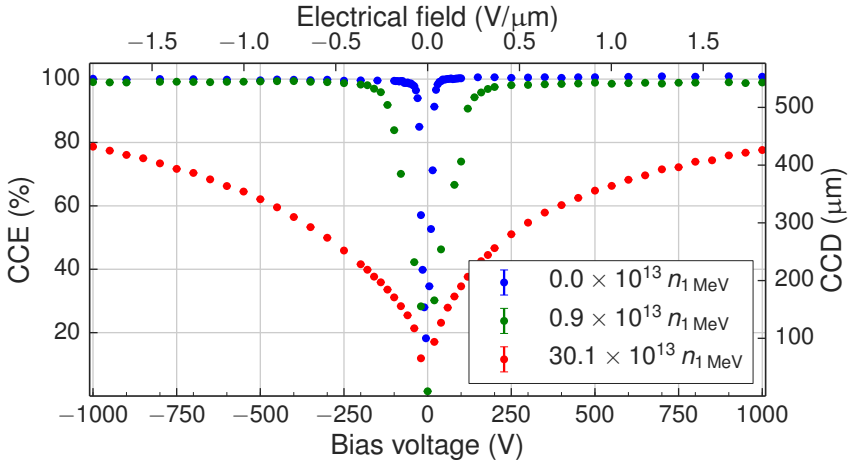

(c) #27135474

Figure 6.7: The CCE measurement of the diamond sensors as function of bias voltage and with respect to different irradiation damages. The diamond samples are ordered from the lowest to the highest irradiation damage from top to down. The CCE measurements for the unirradiated diamond sensors are indicated in blue and show a full charge collection efficiency for all diamond detectors at very low bias voltages ($HV \leq 100\,\mathrm{V}$). After an increased radiation damage up to $0.9 \times 10^{13}\,n_{1\,\mathrm{MeV\,eq.}}/\mathrm{cm}^2$ indicated in blue an increased electrical field is needed in order to measure a full CCE of the sensors. At the highest irradiation damage of $5.5 - 30.1 \times 10^{13}\,n_{1\,\mathrm{MeV\,eq.}}/\mathrm{cm}^2$ none of the diamond sensors reaches a full charge collection efficiency at the highest electrical field of $E = 1.85\,\mathrm{V}/\mu\mathrm{m}$.

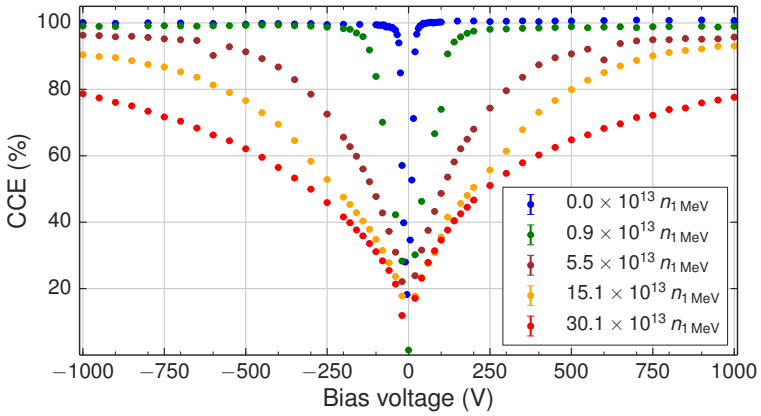

Figure 6.8: The CCE as function of bias voltages with respect to the irradiation damage. This plot combines the CCE measurement results of different irradiation damages measured with different diamond samples, compare Fig. 6.7.

$30.1 \times 10^{13}\, n_{1\,\mathrm{MeV\,eq.}}/\mathrm{cm}^2$ the CCE of all diamond sensors doesn't saturate and therefore is not reaching a full charge collection efficiency, see red curves in Fig. 6.7. In Fig. 6.8 the different irradiation damages of all sensors are combined into one plot. At a total radiation damage of $5.5 \times 10^{13}\, n_{1\,\mathrm{MeV\,eq.}}/\mathrm{cm}^2$ the diamonds reaches almost full charge collection efficiency at bias voltage above HV $\geq \pm 750\,\mathrm{V}$, indicated in brown. A further increase in the total irradiation damage, indicated in orange and red, results in a reduced charge collection efficiency, even for the highest bias voltages of HV $= \pm 1000\,\mathrm{V}$.

In Fig. 6.9a the measured CCD of the proton irradiated diamond sensors is plotted over the radiation damage in units of 24GeV $\mathrm{p_{eq.}}$. The same plot is shown in Fig. 6.9b for the neutron irradiated diamond sensors. Based on these CCD measurement results as function of radiation damage the radiation constant k is calculated and listed in Table 6.3 for 4 different electrical fields of $E \geq 0.75\,\mathrm{V/\mu m}$. At reduced electrical fields the diamond polarization is dominant and the standard parameterization fails. The calculated radiation constants k for the proton irradiated diamond sensors match the radiation constant measured by the RD42 collaboration of $k_{\mathrm{RD42}} = 6.5 \times 10^{-19}\,\mathrm{cm^2 \mu m^{-1}}$ at electrical fields of $E \geq 1.0\,\mathrm{V/\mu m}$. The same calculation of the radiation constant for the neutron irradiated diamond sensors however indicates a strong underestimation of the radiation damage caused by the neutron

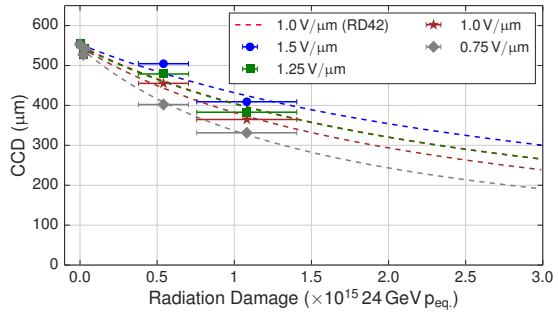

(a) #27135473 and #27135474 irradiated with 23 MeV proton.

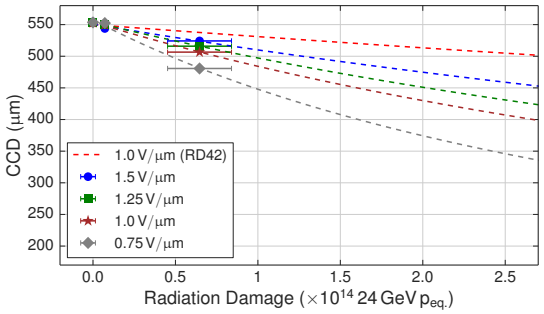

(b) #27135476 irradiated with a spectrum of neutrons up to 10 MeV.

Figure 6.9: The CCE as function of radiation damage for different electrical fields. The measurement results are fitted to the standard radiation model for each electrical field configuration (dashed lines) to calculate the corresponding radiation constant k. The radiation induced signal degradation, based on $k_{\mathrm{RD42}} = 6.5 \times 10^{-19}\,\mathrm{cm^2 \mu m^{-1}}$ is indicated in red for comparison. The measured CCD as function of radiation damage for an electrical field of $E = 1.25\,\mathrm{V/\mu m}$ lies on top of the RD42 result for the proton irradiation.

Table 6.3: Calculation of the radiation constant k. The radiation constant calculated by the RD42 collaboration of $k_{\mathrm{RD42}} = 6.5 \times 10^{-19}\,\mathrm{cm^2 \mu m^{-1}}$ was obtained for diamond sensor operated at an electrical field of $E = 1\,\mathrm{V/\mu m}$. The CCD measurements with the proton irradiated diamond sensors operated an electrical fields of $E \geq 1\,\mathrm{V/\mu m}$ confirm this result. The neutron irradiated diamond sensors show however a strongly increased radiation damage constant that is caused by an underestimation of the radiation damage caused by the neutron particles. At a reduced electrical field of $E = 0.75\,\mathrm{V/\mu m}$ the signal reduction is increased by $\sim 70\%$.

Electrical field	Radiation constant k ($\times 10^{-19}\,\mathrm{cm^2 \mu m^{-1}}$)		Ratio
(V/µm)	23 MeV protons	10 MeV neutrons	$k_{10\,MeV,n}/k_{23\,MeV,p}$
0.75	11.4 ± 0.73	43.87 ± 4.90	3.85
1.00	7.88 ± 0.76	26.03 ± 1.36	3.30
1.25	6.49 ± 0.92	20.63 ± 0.55	3.18
1.50	5.08 ± 0.85	14.55 ± 3.61	2.67

particles. The radiation constant based on the neutron irradiated sample is on average a factor of $k_{10\,MeV,n}/k_{23\,MeV,p} = 3.05$ increased compared to the proton irradiated diamond samples. The radiation hardness factor of 1.2 calculated by [Lag15] using NIEL scaling will therefore be replaced by a damage factor of 3.66 based on the CCD measurement results. The absolute radiation damage of the neutron irradiated diamond sensors is recalculated for each radiation step in Table 6.2 and listed additionally in brackets.

Space charge affecting the CCE measurement results

The importance of the CCE measurement routine introduced at the beginning of this section will be demonstrated in the following. To study the possible influence of the build up of space charge, namely the diamond polarization, to the CCE measurement results, the CCE measurement routine was changed. In order to force the creation of space charge, the CCE of the diamond was measured in reverse order of applied bias voltages. The CCE measurement was started at a bias voltage of $\pm 1000\,V$ and followed by the next lower bias voltage, without a ramp down in between two CCE measurement steps. The difference of both measurement routines is shown for the diamond sensor #27135474 in Fig. 6.10. For high bias voltages,

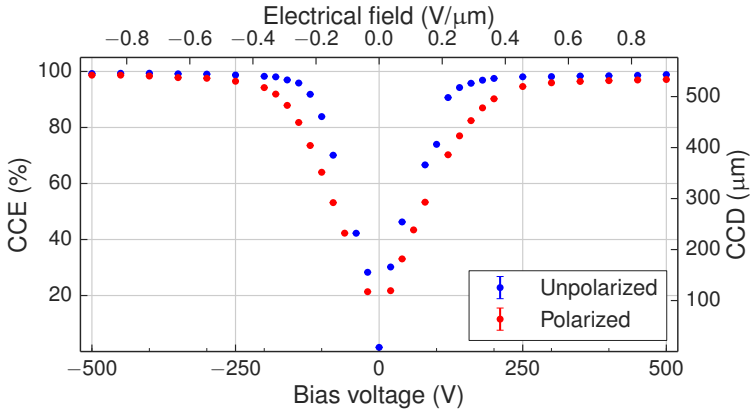

Figure 6.10: The CCE as function of bias voltage was measured with two different measurement procedures, explained in detail in the text. The CCE measurement results of the irradiated diamond sensor #27135474 are increased for the standard measurement procedure, indicated in blue. With the modified CCE measurement procedure reduced CCE values are measured.

at full charge collection efficiency, no difference between the polarized and the unpolarized diamond is visible. At reduced bias voltages however, the measured CCE for the polarized diamond is strongly decreased compared to the unpolarized diamond measurement. This results demonstrates the strong influence of the diamond polarization reducing the absolute charge collection efficiency of the diamond detector.

In order to study the build up of space charge in more detail, the CCE was measured as function of measurement time, shown in the next section 6.3.4.2.

6.3.4.2 CCE measurement over Time

The CCE measurements discussed in the last section indicated already a build up of space charge in the diamond sample, which results in a decreased charge collection efficiency measurement. The CCE measured as function of total measurement time is therefore discussed in this section. The ^{90}Sr source creating MIP signals, which are used to calculate the CCE of the diamond sensors, is at the same time causing a constant ionizing current in the diamond sensors. This constant ionization current can also result in the build up of space charge and hence modify the electrical field and lead to a reduced CCE measurement due to the diamond polarization. In order to increase the measurement frequency the amount of MIP events per CCE measurement was reduced to 5.000 MIP events for this type of measurement. This leads to a 4× reduced measurement time of $t_{\text{meas.}} \sim 23\,\text{s}$ and hence increases the CCE measurement frequency. The shortfall in precision due to the decreased MIP amount is balanced out by the increased CCE measurement rate.

In Fig. 6.11 the CCE measurement over time is shown for the undamaged diamond sensor #27135474. At bias voltages above HV $\geq 50\,\text{V}$, equivalent to an electrical field above $E \geq 91\,\text{mV}/\mu\text{m}$, no reduction of the measured CCE with increased measurement time is visible. At a low bias voltage of HV $= 20\,\text{V}$, equivalent to an electrical field of $E = 36\,\text{mV}/\mu\text{m}$, a reduction of the measured CCE as function of measurement time is observed. The initial measured CCE is reduced from $\text{CCE}_{\text{init.}} = 94.4\%$ to $\text{CCE}_{\text{fin.}} = 89.2\%$. Hence the diamond polarization is as well present in un-irradiated high quality single crystalline diamonds, even only measurable for low electrical fields.

In order to parameterize and compare the time constants of the diamond polarization for different radiation damages and different electrical fields, the CCE as function of measurement

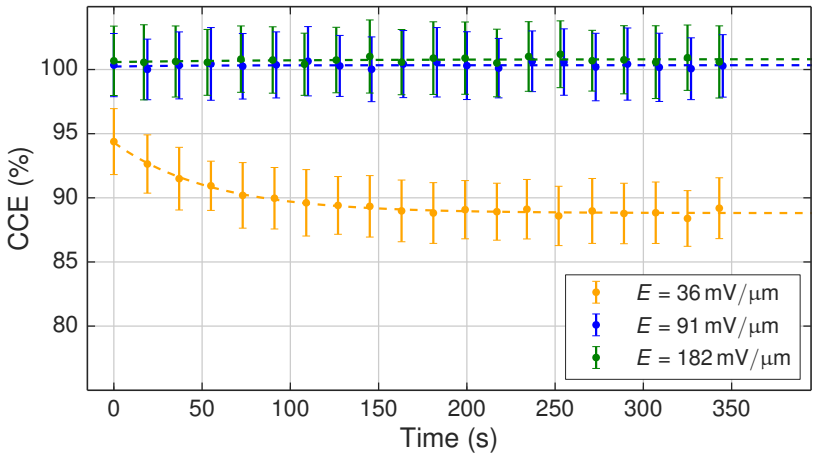

Figure 6.11: The CCE measured as function of time for an un-irradiated sCVD diamond sensor #27135474. At electrical fields above $E \geq 91\,\text{mV}/\mu\text{m}$ no change in the measured CCE with increased measurement time is visible, indicated in green and blue. For an electrical field of $E = 36\,\text{mV}/\mu\text{m}$ indicated in orange, a reduction of the CCE is measured for an increased exposure time of the diamond sensor to the ^{90}Sr source.

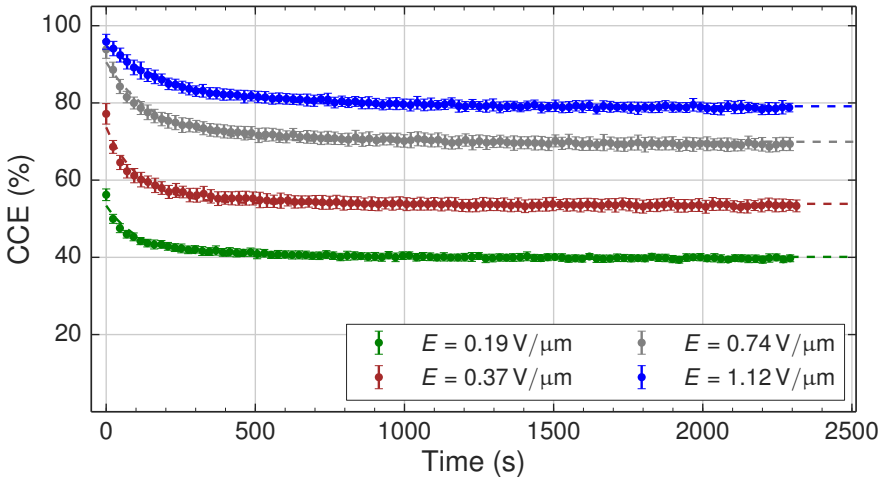

(a) #27135476 with a total radiation damage of $5.5 \times 10^{13}\, n_{1\,\mathrm{MeV\,eq.}}/\mathrm{cm}^2$

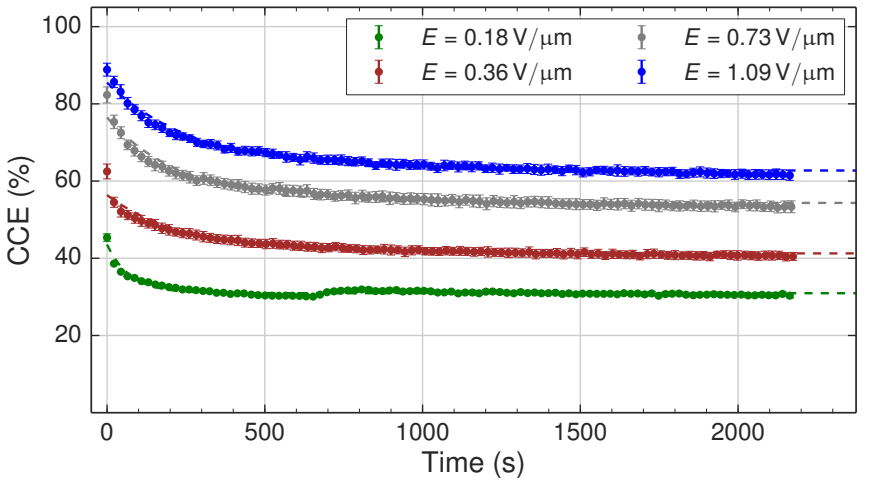

(b) #27135473 with a total radiation damage of $15 \times 10^{13}\, n_{1\,\mathrm{MeV\,eq.}}/\mathrm{cm}^2$

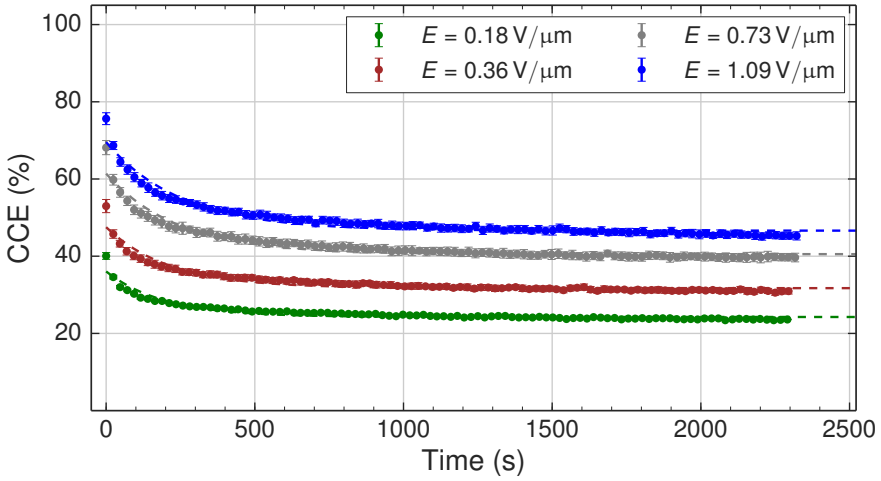

(c) #27135474 with a total radiation damage of $30 \times 10^{13}\, n_{1\,\mathrm{MeV\,eq.}}/\mathrm{cm}^2$

Figure 6.12: CCE measurements as function of time for different irradiation damages. The diamond samples are order from the lowest to the highest irradiation damage from top to down. The CCE measurements of all irradiated diamond samples are reduced with increased duration of the measurement, and hence with increased time of being exposed to the ^{90}Sr source creating a constant ionizing particle rate in the diamond sensors. The reduction of the CCE measurement as function of time is fitted with an exponential decay with the form of: $\mathrm{CCE}\,(\mathrm{t}) = \mathrm{CCE}_{\mathrm{pol.}} \cdot \mathrm{e}^{-\mathrm{t}/\tau} + \mathrm{CCE}_{\mathrm{fin.}}$ that is indicated with dashed lines.

time can be fitted to an exponential decay function of:

$$\mathrm{CCE}\,(\mathrm{t}) = \mathrm{CCE}_{\mathrm{pol.}} \cdot \mathrm{e}^{-\mathrm{t}/\tau} + \mathrm{CCE}_{\mathrm{fin.}} \tag{6.5}$$

with CCE (t) as charge collection efficiency as function of time, $\mathrm{CCE}_{\mathrm{pol.}}$ the amplitude of the decay, τ the decay time and $\mathrm{CCE}_{\mathrm{fin.}}$ as final charge collection efficiency for the fully polarized diamond sensor. Fitting Eq. 6.5 to the CCE measurement results of the un-irradiated diamond sensor, results for the lowest bias voltage in a time constant of $\tau = 55.2\,\mathrm{s}$.

In Fig. 6.12 the CCE measurements as function of measurement time are shown for different irradiation damages of $5.5 \times 10^{13}\,n_{1\,\mathrm{MeV\,eq.}}/\mathrm{cm}^2$, $15 \times 10^{13}\,n_{1\,\mathrm{MeV\,eq.}}/\mathrm{cm}^2$ and $30 \times 10^{13}\,n_{1\,\mathrm{MeV\,eq.}}/\mathrm{cm}^2$ and for different electrical fields at which the diamond sensors are operated. The CCE as function of total measurement time is reduced for all three diamond sensors. Even at the highest electrical fields of $E \sim 1.1\,\mathrm{V/\mu m}$ the CCE is reduced by $\geq -15\%$ from its initial value. Hence the build up of space charge, the diamond polarization, is strongly influencing the charge collection efficiency of the diamond sensors, even at high electrical fields above $E > 1\,\mathrm{V/\mu m}$. All measurement results shown in Fig. 6.12 are fitted with Eq. 6.5 and the calculated parameters are listed in Table 6.4. The fit results obtained for all CCE over time measurements show in Fig. 6.12 indicates a correlation between the electrical field at which the diamond is operated and the polarization time constant: $E \sim \tau$.

The reduction of the CCE with increased exposure time to the ^{90}Sr particle source can be understood in the picture of the diamond polarization as the following. Initially the diamond sensor is 'primed' or 'pumped' meaning that all traps are homogeneously filled and the highest CCE is measured. A constant electrical field in the diamond bulk is present. With increased measurement time a polarization field is building up, due to an inhomogeneous trapping of the charge carriers created via ionization, compare section 5.5. This polarization field leads to a modified electrical field distribution resulting in an increased charge carrier recombination and therefore in a decreased charge collection efficiency. The duration to build up the space charge is mainly driven by the particle rate of the ^{90}Sr source, which is identical for all measurements shown in Fig. 6.12. At, however, a reduced applied bias voltage the total amount of trapped charge carriers needed to create a polarization field strong enough to manipulate the overall measured charge collection efficiency is lower compared to an increased bias voltage. The time constant depends therefore strongly on the electrical field at which the diamond sensor is operated: $\tau_{0.2\,\mathrm{V/\mu m}} < \tau_{1.1\,\mathrm{V/\mu m}}$.

In Fig. 6.13 all CCE measurements over time for different irradiation damages but the same electrical field are combined into one particular plot. At the lowest electrical field of $E \sim 0.18\,\mathrm{V/\mu m}$ already the lowest radiation damage of $0.2 \times 10^{13}\,n_{1\,\mathrm{MeV\,eq.}}/\mathrm{cm}^2$ leads to the build up of space charge and therefore to a reduced CCE with increased measurement time. At an electrical field of $E \sim 0.73\,\mathrm{V/\mu m}$ an increased radiation damage of $1 > \times 10^{13}\,n_{1\,\mathrm{MeV\,eq.}}/\mathrm{cm}^2$ is necessary to affect the CCE measurement.

6.3.4.3 CCE measurements of a Split Pad Diamond

The diamond sensor #24990892 included in the irradiation campaign had a split pad metallization on both surfaces with a gap of 5 µm. The 'split pad' metallization was done instead of the normal 'single pad' metallization to increase the granularity of the BCM1F detector, for which purpose the diamond sensor was originally produced. The gap between the two pads of 5 µm was chosen that narrow in order to avoid any negative electrical field effects. The CCE measurements of the un-irradiated diamond sensor showed a full charge collection efficiency and no negative influences caused by the split pad metallization were found. With increased radiation damage of these split pad diamonds an increased reduction of the charge

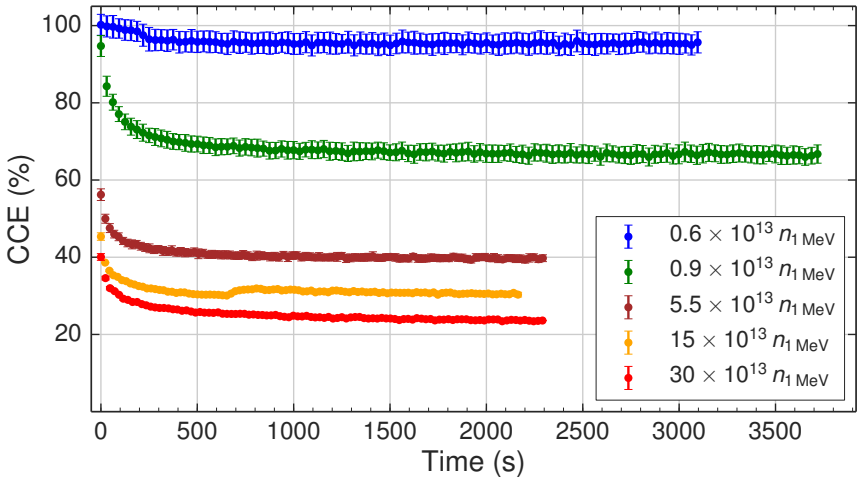

(a) Diamond sensors operated at an electrical field of $E \sim 0.18\,\mathrm{V/\mu m}$.

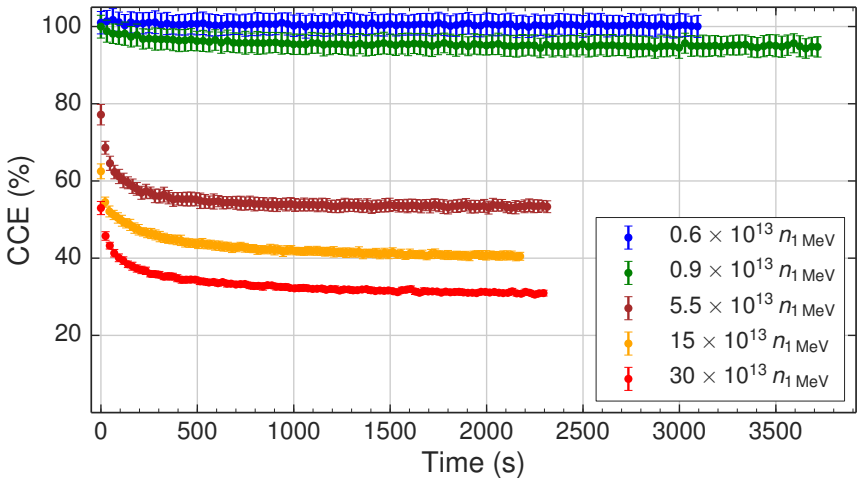

(b) Diamond sensors operated at an electrical field of $E \sim 0.36\,\mathrm{V/\mu m}$.

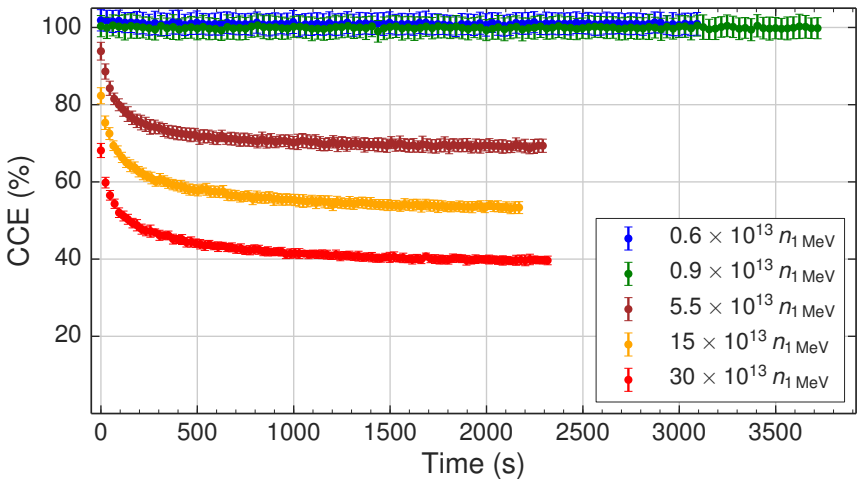

(c) Diamond sensors operated at an electrical field of $E \sim 0.73\,\mathrm{V/\mu m}$.

Figure 6.13: The three figures show the CCE measurement as function of total measurement time for three different electrical fields ($E \sim 0.18\,\mathrm{V/\mu m}$ - top, $E \sim 0.36\,\mathrm{V/\mu m}$ - middle, $E \sim 0.73\,\mathrm{V/\mu m}$ - bottom) at which the diamond sensors are operated. Furthermore, the CCE over time was measured for different irradiation damages from low (green) to very high (red).

Table 6.4: Overview of the parameterization of the CCE degradation as function of measurement time. The time constant τ of the CCE degradation is increased for higher electrical fields, since more charge carrier have to be trapped to effect the internal electrical field and lead to a reduced CCE measurement.

Name	Radiation Damage ($\times 10^{13}\, n_{1\mathrm{MeV,\,eq.}}/\mathrm{cm}^2$)	E (V/µm)	$\mathrm{CCE}_{\mathrm{pol.}}$ (%)	τ (s)	$\mathrm{CCE}_{\mathrm{fin.}}$ (%)
27135476	5.5×10^{13}	0.2	13.3	116.2	40.1
		0.4	19.8	110.2	53.9
		0.7	20.6	163.7	69.9
		1.1	15.6	246.2	79.1
27135473	15×10^{13}	0.2	12.6	73.5	31.0
		0.4	15.1	245.8	41.3
		0.7	22.1	237.1	54.3
		1.1	22.8	282.6	62.7
27135474	30×10^{13}	0.2	11.8	194.6	24.3
		0.4	15.8	214.3	31.7
		0.7	20.9	240.2	40.5
		1.1	22.9	252.4	46.6

collection efficiency was observed. It was found that charge sharing between the two pads amplified the radiation induced signal degradation. Drifting charge carriers created close to the gap in the metallization are effectively inducing a signal in both pads, however not just for the 5 µm region, but as well for an increased region of ±200 µm around the gap in the metallization. Simulations based on the Weighting potential could reproduce this behavior, further details can be found in [Hem14].

The resulting CCE measurement of the irradiated diamond sensor (#24990892) is shown in Fig. 6.14. For a MIP signal a Landau distribution is expect, like shown in Fig. 6.14a. The histogram of the signal intensity of MIP events measured with the irradiated diamond sensor (#24990892) shown in Fig. 6.14b shows however a different structure. Due to the charge sharing a second peak at reduced signal intensity is visible and therefore an accurate fitting of the main peak without a contribution of the charge sharing is impossible. The diamond sensor was therefore excluded from the diamond irradiation campaign.

6.3.5 Development of TCT pulse shapes with increased Radiation Damage

The TCT measurement technique is used to indirectly measure the electrical field of the diamond sensors. An α particle source is inducing charge carriers close to the diamond surface, which drift through the entire diamond bulk. The charge carrier drift inducing a signal current, is proportional the electrical field. Hence, the signal current as function of time is proportional to the electrical field as function of diamond thickness. The TCT measurement setup is described in detail in section 6.1.1. In order to maintain consistency in the TCT measurements the following procedure was used:

1. The diamond is exposed during the entire measurement to a ^{90}Sr source that is creating a constant ionizing particle rate. The electron-hole pairs created by ionization in the entire diamond bulk are filling up the traps. In the steady state the trapping and detrapping are in equilibrium. According to the simulations discussed below, about 55 % of the effective deep traps are filled.

2. In order to remove any residual field and set the diamond into an unpolarized state, the sensor is exposed to the ^{90}Sr source for a duration of 20 minutes without bias voltage applied. A homogeneous trap filling in the diamond bulk, and hence an unpolarized diamond state, is reached.

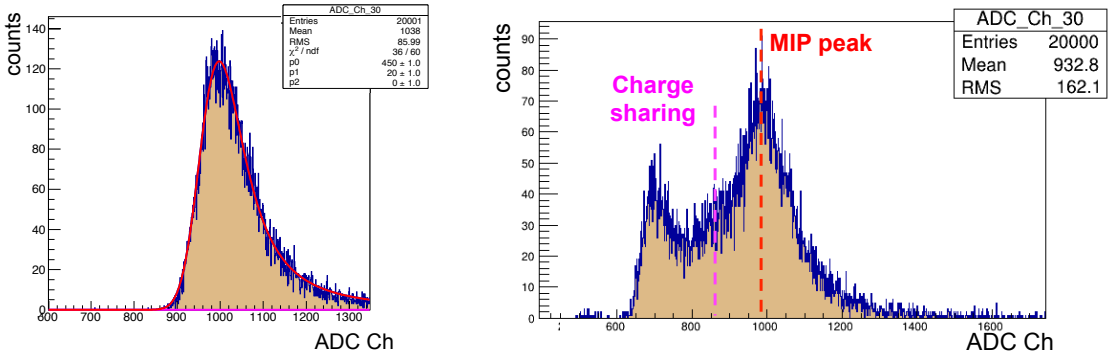

(a) #27135476 single pad. **(b)** #24990892 split pad.

Figure 6.14: Histogram of 20000 MIP events measured with the CCE setup at DESY. On the left side the expected Landau distribution can be seen. The right side shows the resulting histogram for the diamond sensor #24990892 with a split pad metallization. Beside the main MIP peak a second peak at a reduced energy can be seen. This second peak is caused by charge sharing to the second pad that is not connected to the read out.

3. The bias voltage is ramped up fast ($t_{\text{ramp}} \leq 10\,\text{s}$) and the measurement is started immediately ($t = 0\,\text{s}$).

4. With bias voltage applied the diamond starts to polarize. The measurement is performed over an extended period of time ($t > 3000\,\text{s}$) until the diamond is fully polarized and the measurement results are stable.

The charge carrier drift was measured separately for electron and hole charge carriers by exposing the diamond sensor either on the cathode or anode to the alpha particle source, compare section 6.1.1. Furthermore, the charge carrier drift of a particular type was measured for both diamond orientations. During the irradiation campaign the build up of space charge and hence the diamond polarization was measured for the electrical fields of: $E = 0.18\,\text{V}/\mu\text{m}$, $E = 0.36\,\text{V}/\mu\text{m}$ and $E = 0.73\,\text{V}/\mu\text{m}$. The diamond polarization for the high irradiated diamonds ($10 > \times 10^{13}\,n_{1\,\text{MeV eq.}}/\text{cm}^2$) were additionally measured at an electrical field of $E = 1.09\,\text{V}/\mu\text{m}$. All TCT measurement results are shown in the Appendix in section A.2.2. In the following the most important results of the TCT measurements will be discussed.

For an un-irradiated diamond sensor with a small amount of initial defects no build up of space charge due to the exposure to a MIP particle source is expected. This should lead to a constant electrical field distribution and result in a rectangular TCT pulse shape. The TCT measurement results of the un-irradiated diamond sensor (#27135475) at an electrical field of $E = 0.18\,\text{V}/\mu\text{m}$ are shown in Fig. 6.15a for the hole carrier drift and in Fig. 6.15d for the electrons carrier drift. Both TCT measurements show the expected rectangular pulse shape, indicating a constant electrical field. The TCT pulse shapes remain furthermore constant over the entire measurement time of up to ($t \sim 3000\,\text{s}$) demonstrating the absence of diamond polarization. The same TCT measurements after a total irradiation damage of $\Phi_1 = 0.6 \times 10^{13}\,n_{1\,\text{MeV eq.}}\text{cm}^{-2}$ are shown in Figs. 6.15b and 6.15e measured with the diamond sensors

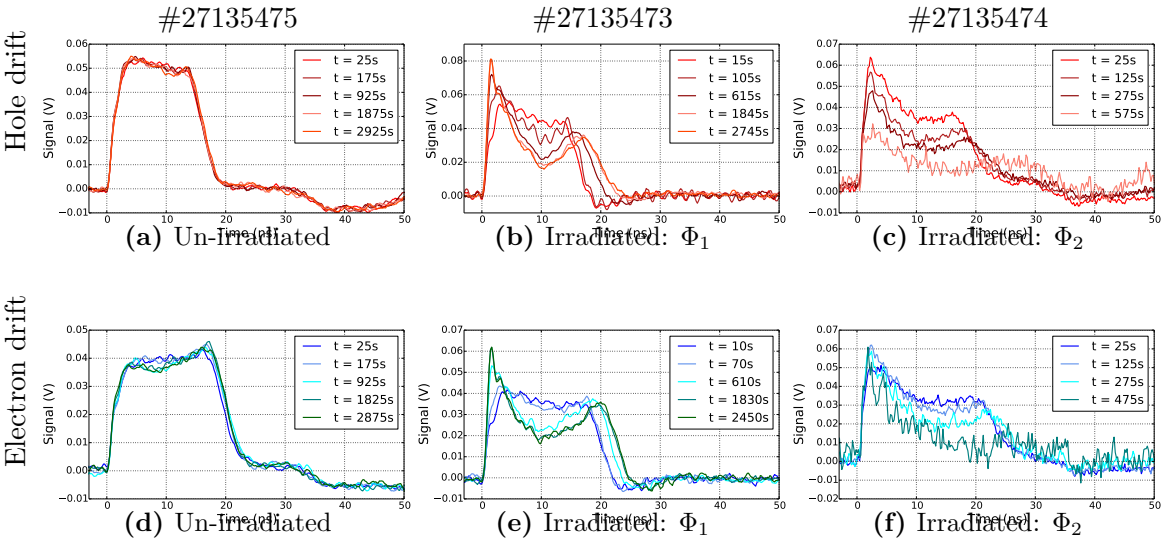

(a) Un-irradiated **(b)** Irradiated: Φ_1 **(c)** Irradiated: Φ_2

(d) Un-irradiated **(e)** Irradiated: Φ_1 **(f)** Irradiated: Φ_2

Figure 6.15: Comparison of the TCT measurement results for different radiation damages (from left to right) at an electrical field of $E = 0.18\,\text{V}/\mu\text{m}$ for holes (top row) and electrons (bottom row). The diamond sensors (#27135473 and #27135474) were irradiated with a total particle fluence of $\Phi_1 = 0.6 \times 10^{13}\,n_{1\,\text{MeV eq.}}\text{cm}^{-2}$ and $\Phi_2 = 1.8 \times 10^{13}\,n_{1\,\text{MeV eq.}}\text{cm}^{-2}$, compare section 6.3.3. The TCT pulses and hence the electrical field is constant over time for the undamaged sensor. Increased radiation damage of Φ_1 leads to the diamond polarization and hence to a modified TCT shape corresponding to a modified electrical field configuration. With increased radiation damage the effect of the diamond polarization is more significant resulting in a stronger modification of the final TCT pulse shape. The shape of the hole and electron drift is comparable and indicating a symmetrical charge up of the diamond bulk.

#27135473. The initial measured TCT pulses after a short exposure time to the ^{90}Sr source of $t \sim 10\,\mathrm{s}$ show the expected rectangular TCT pulse shapes, resulting from a constant electrical field distribution in the diamond bulk. With increased exposure time to the β particle source ($t > 300\,\mathrm{s}$) the TCT pulse shapes are strongly modified. A new stable TCT pulse shape and therefore a new stable electrical field configuration is reached after an exposure time of $t \sim 650\,\mathrm{s}$. This two-peak structure of the final TCT pulse configuration can be explained by the diamond polarization, leading to the creation of space charge predominately towards the edges. The resulting electrical field has a local minimum in the central region of the diamond bulk and an increased electrical field towards the diamond metallizations. Such an electrical field configuration is first accelerating the induced charge carriers and causing the first peak of the TCT pulse. The reduced electrical field in the central diamond bulk region is slowing down the drift velocity of the charge carriers, leading to a reduced induced signal current and hence resulting in the central dip in the TCT pulse shape. The second peak in the TCT pulse shape is caused by the re-acceleration of the charge carriers, due to the increased electrical field towards the second electrode. In Figs. 6.15c and 6.15f the TCT measurement of the diamond sensor (#27135474) is shown after an irradiation of $\Phi_2 = 1.8 \times 10^{13}\, n_{1\,\mathrm{MeV\,eq.}}\mathrm{cm}^{-2}$. The initial TCT pulse ($t = 25\,\mathrm{s}$) measured immediately after the pumping of the diamond sensors has still a rectangular shape. However, the build up of space charge leads to a very strong diamond polarization, resulting in the loss of the trigger after $t = 575\,s$. The diamond polarization is creating such strong modified electrical fields in the diamond bulk that only the first peak in the TCT pulse can be measured. Beside the strong TCT pulse shape modification due to the build up of space charge, the comparison between the hole and electron drift shows a similar behavior, indicating a symmetrical build up of space charge in the diamond bulk.

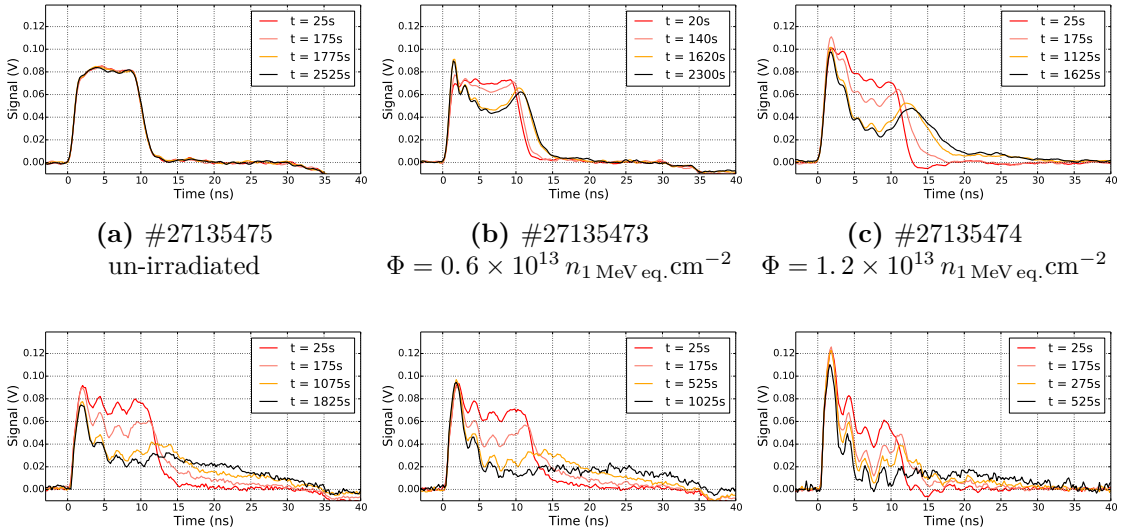

(a) #27135475 un-irradiated

(b) #27135473 $\Phi = 0.6 \times 10^{13}\, n_{1\,\mathrm{MeV\,eq.}}\mathrm{cm}^{-2}$

(c) #27135474 $\Phi = 1.2 \times 10^{13}\, n_{1\,\mathrm{MeV\,eq.}}\mathrm{cm}^{-2}$

(d) #27135474 $\Phi = 1.8 \times 10^{13}\, n_{1\,\mathrm{MeV\,eq.}}\mathrm{cm}^{-2}$

(e) #27135474 $\Phi = 4.8 \times 10^{13}\, n_{1\,\mathrm{MeV\,eq.}}\mathrm{cm}^{-2}$

(f) #27135473 $\Phi = 15.1 \times 10^{13}\, n_{1\,\mathrm{MeV\,eq.}}\mathrm{cm}^{-2}$

Figure 6.16: TCT measurements of the hole charge carriers at an electrical field of $E = 0.36\,\mathrm{V/\mu m}$ for different irradiation damages. The rectangular TCT pulse shape for the un-irradiated diamond sensors, shown in Fig. 6.16a, is visible as initial pulse shape measured directly after the start of the TCT measurement at $t = 25\,\mathrm{s}$ independent of the total amount of irradiation damage. The increased radiation damage causes an increased build up of space charge as function of exposure time to the ^{90}Sr source. This results primarily in a stronger modification of the TCT pulse shape, secondarily however as well in a faster transition to the final TCT pulse and hence electrical field configuration. After a total irradiation damage of $\Phi = 15.1 \times 10^{13}\, n_{1\,\mathrm{MeV\,eq.}}\mathrm{cm}^{-2}$ and fully polarized ($\mathrm{t} = 525\,\mathrm{s}$) only the primary peak in the TCT pulse is visible.

The TCT measurement results at an increased bias voltage of HV = 200 V equivalent to an electrical field of $E = 0.36\,\mathrm{V/\mu m}$ are shown in Fig.6.16 for the hole carrier drift and in Fig. 6.17 for the electron drift. The TCT measurement results are comparable to the TCT results measured at a reduced electrical field of $E = 0.18\,\mathrm{V/\mu m}$. The expected rectangular TCT pulse shape is measured for the un-irradiated diamond sensor that furthermore remains stable as function of exposure time to the ^{90}Sr source. This rectangular TCT pulse shape is measured as well for all irradiated diamond samples immediately after the bias voltage has been applied and the TCT measurement has been started ($t = 25\,\mathrm{s}$). In this initial moment the diamond is in a pumped state and the defects are homogeneously ionized. With increased radiation damage of the diamond sensors, the TCT pulse shapes are not stable anymore as function of exposure time to the β particle source, identical to the measurements obtained at an electrical field of $E = 0.18\,\mathrm{V/\mu m}$. The increased bias voltage however reduces the impact of the space charge caused by the diamond polarization. Hence, the TCT pulses are measurable as well for the highest radiation damages of $\Phi = 15 \times 10^{13}\,n_{1\,\mathrm{MeV\,eq.}}\mathrm{cm}^{-2}$, see Fig. 6.16f. The TCT measurement results for the electron charge carrier drift, shown in Fig. 6.17, show a identical modification of the TCT pulse shapes with increased radiation damage. This confirms the TCT measurement results for an electrical field of $E = 0.18\,\mathrm{V/\mu m}$, which indicated a symmetrical creation of space charge in the diamond bulk.

TCT pulse modification of an irradiated diamond sensor as function of the electrical field

In Fig. 6.18 the effect of an increased bias voltage and hence an increased electrical field to the diamond polarization is shown. The hole charge carrier drift of the diamond sensor #27135474 irradiated with $\Phi = 1.8 \times 10^{13}\,n_{1\,\mathrm{MeV\,eq.}}\mathrm{cm}^{-2}$ was measured at four different electrical fields. At the lowest electrical field of $E = 0.18\,\mathrm{V/\mu m}$, shown in Fig. 6.18a, the diamond polarization leads to a strongly modified TCT pulse shape caused by a strongly deformed internal electrical field. This strong deformation of the electrical field results in the loss of the alpha particle signal after an exposure time to the ^{90}Sr particle source of about $t \sim 600\,\mathrm{s}$. At an increased bias voltage of $E = 0.36\,\mathrm{V/\mu m}$ the impact of the space charge

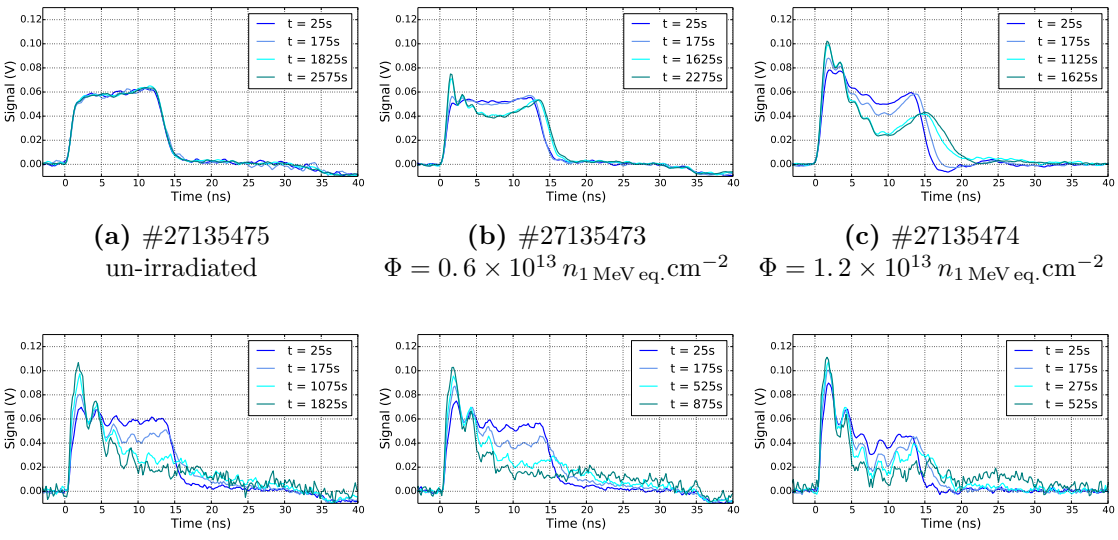

(a) #27135475 un-irradiated

(b) #27135473 $\Phi = 0.6 \times 10^{13}\,n_{1\,\mathrm{MeV\,eq.}}\mathrm{cm}^{-2}$

(c) #27135474 $\Phi = 1.2 \times 10^{13}\,n_{1\,\mathrm{MeV\,eq.}}\mathrm{cm}^{-2}$

(d) #27135474 $\Phi = 1.8 \times 10^{13}\,n_{1\,\mathrm{MeV\,eq.}}\mathrm{cm}^{-2}$

(e) #27135474 $\Phi = 4.8 \times 10^{13}\,n_{1\,\mathrm{MeV\,eq.}}\mathrm{cm}^{-2}$

(f) #27135473 $\Phi = 15.1 \times 10^{13}\,n_{1\,\mathrm{MeV\,eq.}}\mathrm{cm}^{-2}$

Figure 6.17: TCT measurements of the electron charge carriers at an electrical field of $E = 0.36\,\mathrm{V/\mu m}$ for different irradiation damages. The TCT pulse modification due to the increased radiation damage of up to $\Phi = 15.1 \times 10^{13}\,n_{1\,\mathrm{MeV\,eq.}}\mathrm{cm}^{-2}$ behave similar to the results obtained for the hole carrier drift shown in Fig. 6.16. The similar pulse shape of electron and hole charge carriers indicates a symmetric build up of space charge in the diamond bulk.

created by the diamond polarization to the TCT pulse is reduced, see Fig. 6.18b. The measured TCT pulses are stabilizing after an exposure time of $t \sim 1000\,\mathrm{s}$, indicating however still a strongly deformed electrical field. The diamond polarization is further suppressed with the operation of the diamond sensors at higher bias voltage, and is in Fig. 6.18d at an electrical field of $E = 1.09\,\mathrm{V/\mu m}$ almost not visible.

6.3.6 TCT pulse shapes of an irradiated Diamond Sample as function of Radiation Damage for Alternating Bias Voltage

Another possibility to verify the theory of the diamond polarization is the usage of alternating bias voltage. The use of alternating bias voltage should avoid any preferred trapping locations of the charge carriers in the diamond bulk and result in a homogeneous trap ionization in the diamond bulk. A comparison of CCD measurements of irradiated diamond sensors with alternating and constant bias voltage showed a significantly higher CCD for the diamond sensor operated with alternating bias voltage [Gut14a]. To verify this result, the TCT setup in Karlsruhe was extended with a signal generator and a voltage amplifier in order to measure the resulting charge carrier drift using alternating bias voltage, see section 6.1.1.

In Fig. 6.19 the TCT measurement results using alternating voltage are shown for different irradiation damages. The diamond sensors were operated at an alternating bias voltage of $\mathrm{HV} = \pm 200\,\mathrm{V}$ with a frequency of $0.5\,\mathrm{Hz}$. The TCT measurements of the undamaged diamond detector, see Fig. 6.19a, show the expected rectangular shape for a constant electrical field. The TCT pulses remain unaffected to the exposure to the ^{90}Sr particle source. At an increased radiation damage of $\Phi = 4.8 \times 10^{13}\,n_{1\,\mathrm{MeV\,eq.}}\mathrm{cm}^{-2}$ the measured TCT pulses using alternating voltage are still rectangular and remain unaffected to the exposure of the β particle source, see Fig. 6.19b. The TCT measurement result of the very same diamond

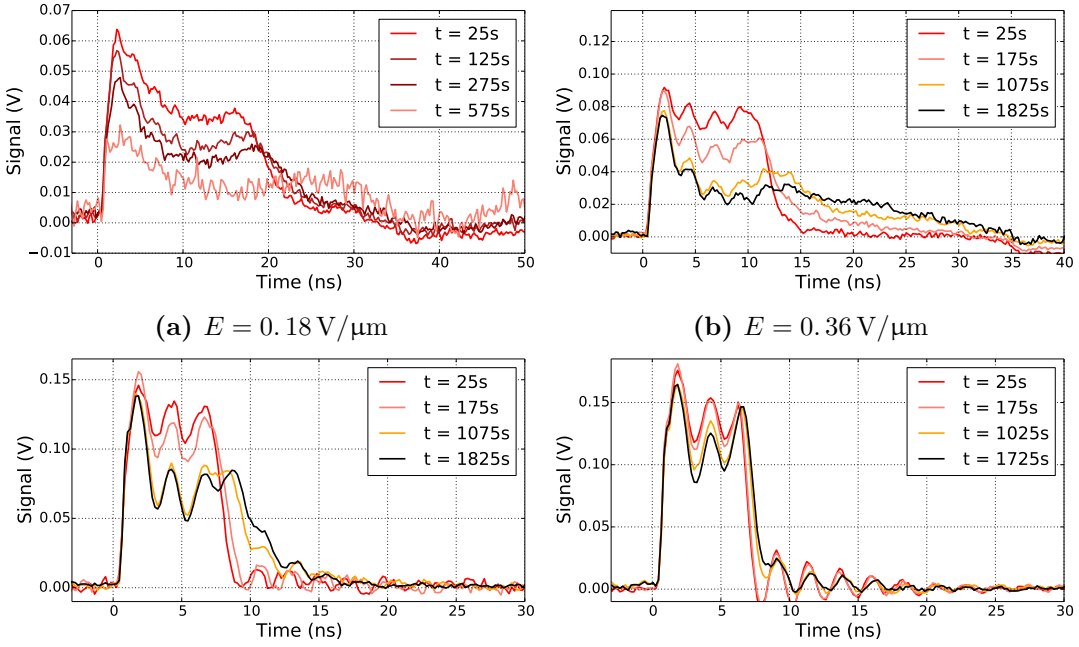

(a) $E = 0.18\,\mathrm{V/\mu m}$ **(b)** $E = 0.36\,\mathrm{V/\mu m}$

(c) $E = 0.73\,\mathrm{V/\mu m}$ **(d)** $E = 1.09\,\mathrm{V/\mu m}$

Figure 6.18: TCT measurements of hole charge carriers with the diamond sensor #27135474 at a total radiation damage of $\Phi = 1.8 \times 10^{13}\,n_{1\,\mathrm{MeV\,eq.}}\mathrm{cm}^{-2}$. The TCT measurements were done at for 4 different electrical fields between $E = 0.18\,\mathrm{V/\mu m}$ in Fig. 6.18a and $E = 1.09\,\mathrm{V/\mu m}$ in Fig. 6.18d. An increased electrical field leads to a reduced impact of the polarization field and hence to a more stable TCT pulse as function of exposure time to the ^{90}Sr particle source.

with the same irradiation damage using constant bias voltage is shown in Fig. 6.19e. Using a constant bias voltage, results in a strong diamond polarization that is not visible using alternating bias voltage. This measurement is a direct proof of the diamond polarization effect, which is affecting the diamond bulk. At the highest irradiation damage of $\Phi = 15.1 \times 10^{13}\, n_{1\,\mathrm{MeV\,eq.}}\mathrm{cm}^{-2}$ the TCT pulses measured using alternating bias voltage remains still stable as function of ^{90}Sr exposure time. The shape of the TCT pulses is slightly changed to a more triangular shape that can be caused by a slight mismatch in the trapping probabilities of both charge carriers.

The TCT measurements using alternating voltage demonstrate that the diamond polarization is caused by the build up of space charge in the diamond bulk and can be avoided by frequently changing the polarity of the bias voltage. The alternating electrical field causes a homogeneous creation of space charge in the diamond bulk and hence preservers a constant electrical field. Using alternating voltage is a valuable possibility to improve the signal stability of the diamond sensors with respect to the radiation damage.

6.3.7 Charge Carrier Drift Velocity as function of Irradiation Damage

In this section the charge carrier drift velocity as function of radiation damage is studied. The basic question is, if an increased amount of lattice defects in the diamond bulk affects the charge carrier drift velocity. The drift velocity is linear proportional to the electrical field, linked together with the mobility $\mu_{e,h}$:

$$v_{e,h} = \mu_{e,h} \cdot E. \tag{6.6}$$

The charge carrier drift velocity $v_{e,h}$ can be measured using the TCT technique. The drift velocity of the charge carriers can be calculated via:

$$v_{e,h} = d/\tau_{FWHM}, \tag{6.7}$$

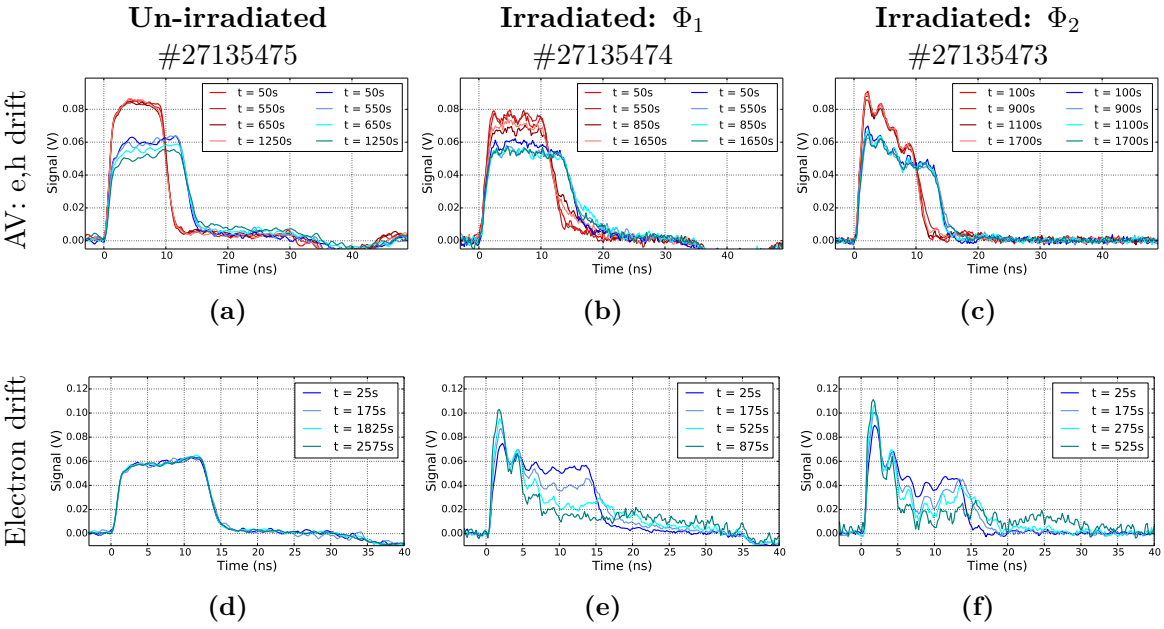

Figure 6.19: Comparison of the TCT measurement results for alternating bias voltage (top row) and constant bias voltage (bottom row). The TCT measurements are compared for an undamaged (left column), irradiated diamond ($\Phi_1 = 4.8 \times 10^{13}\, n_{1\,\mathrm{MeV\,eq.}}\mathrm{cm}^{-2}$ - middle column) and for a highly irradiated diamond sensor ($\Phi_2 = 15 \times 10^{13}\, n_{1\,\mathrm{MeV\,eq.}}\mathrm{cm}^{-2}$ - right column). The TCT measurement results for the alternating bias voltage of $\pm 200\,\mathrm{V}$ at $0.5\,\mathrm{Hz}$ show the results of the electron (blue) and the hole (red) charge carrier drift. For comparison the electron charge carrier drift measured at constant bias voltage of $\mathrm{HV} = 200\,\mathrm{V}$ is shown.

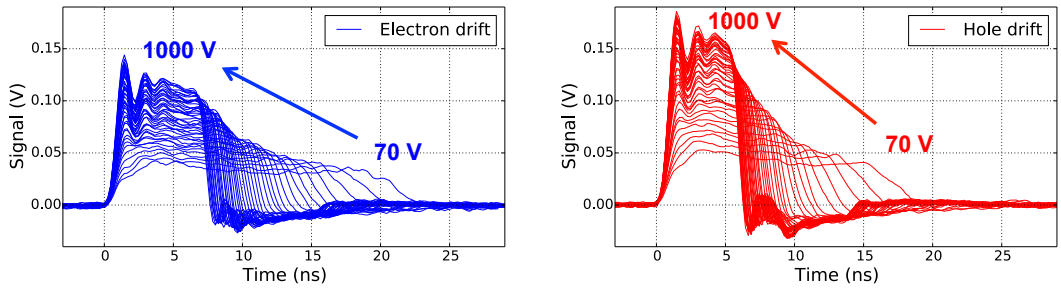

(a) Electron drift. **(b)** Hole drift.

Figure 6.20: TCT measurements of the electron (blue) and hole (red) charge carrier drift as function of bias voltages between HV = 70 − 1000 V.

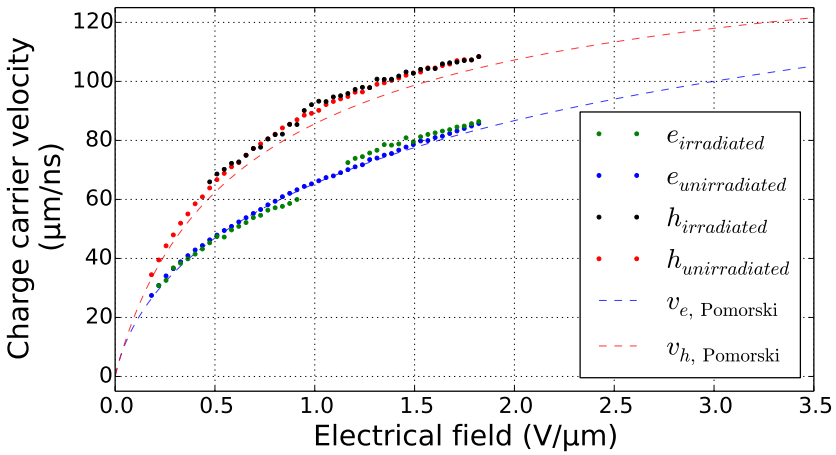

Figure 6.21: The measured charge carrier velocity of the hole and electrons as function of electrical field. The charge carrier velocity of the un-irradiated diamond sensors (red and blue) is identical to the charge carrier velocities of the irradiated diamond sensors (black and green). The diamond sensor was irradiated with $\Phi = 30.1 \times 10^{13}\, n_{1\,\mathrm{MeV\,eq.}}\mathrm{cm}^{-2}$. The dashed lines indicate the charge carrier velocities found by M. Pomorski [Pom15].

with d as thickness of the diamond and τ_{FWHM} as TCT pulse duration at full with half maximum (FWHM). Since the drift velocity is linear proportional to the electrical field a polarized diamond sensor with a non-constant electrical field would manipulate the measurement result. In order to prevent a diamond polarization, the ^{90}Sr source was only used for pumping of the diamond sensor and was removed when the TCT measurement was started. In Fig 6.20 the measured TCT curves for the electron and hole charge carriers are shown, at bias voltages between HV = 70 − 1000 V. The measured TCT pulse duration τ_{FWHM} is used to calculate the drift velocity, using Eq. 6.7. In Fig. 6.21 the measured drift velocities $v_{e,h}$ for an un-irradiated and an irradiated diamond sensor (#27135474) are plotted as function of applied electrical field. The measured drift velocities $v_{e,h}$ of the diamond sensor irradiated with $\Phi = 30.1 \times 10^{13}\, n_{1\,\mathrm{MeV\,eq.}}\mathrm{cm}^{-2}$ are identical to the measurement results obtained for the same diamond without irradiation damage. Hence a radiation damage of up to $\Phi = 30.1 \times 10^{13}\, n_{1\,\mathrm{MeV\,eq.}}\mathrm{cm}^{-2}$ is not affecting the charge carrier transport properties.

6.4 Simulation of the Radiation Induced Signal Degradation of Diamond Detectors

In order to gain a quantitative understanding of the radiation induced signal degradation, a diamond sensor was modeled with the software Silvaco TCAD [SIL16]. Besides the electrical

properties, like e.g. band gap or mobility parameters, radiation induced lattice defects can be taken into account by introducing effective deep traps acting as recombination centers. These effective recombination centers were found by optimizing the simulation of TCT and MIP pulses to match the experimental data. The simulated MIP pulses were used to calculate the charge collection efficiency of the diamond sensor.

The first subsection 6.4.1 will outline the theoretical framework used to simulate the intrinsic electrical properties of the diamond sensor. The parameterization of the lattice defects acting as charge carrier traps is introduced in section 6.4.2. The limitation and specification of the TCT and CCE measurement setups are taken into account, by adjusting several input parameters of the simulation, see section 6.4.3. The TCT and CCE simulation optimized to match the experimental measurement results and the resulting effective trap model are discussed in section 6.4.4. In the last section 6.4.5, the optimized effective trap model is used to simulate the diamond detector performance with respect to the radiation damage, the electrical field at which the sensor is operated and with respect to the particle rate environment in which the sensor is operated.

6.4.1 Theoretical model of the Semiconductor Device Simulation

The theoretical model that is used for the calculation of the electric properties of a semiconductor device will be introduced in this section. The theoretical model is based on a set of fundamental equations, which link together the electrostatic potential and the charge carrier densities. These equations originate from the Maxwell's laws and result in the Poission's Equation 6.11, the continuity equations (Eq. 6.16 and Eq. 6.17) and the charge carrier transport equations (Eq. 6.19 and Eq. 6.20). The Poisson's Equation describes the electrostatic potential with respect to variation in the charge carrier density, e.g. calculates the modified electrical field caused by space charge. The continuity and the transport equations describe the charge carrier densities inside the semiconductor as a result from charge carrier transport, generation and recombination processes. Beside this short introduction, further details of the simulation framework can be found in [SIL10].

The Poission's Equation is received from the fist Maxwell's law 6.10. The electromagnetic field $\vec{E}$ is a conservative field and hence can be expressed as a gradient of the electrostatic potential $\vec{\Phi}$:

$$\vec{E}\,(\vec{\mathrm{r}}) = -\nabla\vec{\Phi}\,(\vec{\mathrm{r}}). \tag{6.8}$$

Applying to Eq. 6.8 the divergence operator results in:

$$\nabla \cdot \vec{E}\,(\vec{\mathrm{r}}) = -\triangle\,\vec{\Phi}\,(\vec{\mathrm{r}}). \tag{6.9}$$

Comparing Eq. 6.9 to the first Maxwell's law of:

$$\nabla \cdot \vec{E} = \frac{\rho}{\epsilon_0}, \tag{6.10}$$

leads to Poisson's Equation of:

$$\triangle\,\vec{\Phi}\,(\vec{\mathrm{r}}) = -\frac{\rho\,(\vec{\mathrm{r}})}{\epsilon_0}, \tag{6.11}$$

with $\rho\,(\vec{\mathrm{r}})$ as charge density and ϵ_0 as permittivity. The electrostatic potential is defined in the Silvaco simulation framework as the intrinsic Fermi potential. The space charge density $\rho\,(\vec{\mathrm{r}})$ determining the electrostatic potential via Eq. 6.11 is calculated as sum of all charge carrier contribution from mobile or fixed electron and hole charge carriers or as well ionized impurities. Hence the electrical field can be calculated based on the electrostatic potential via Eq. 6.8.

The continuity equations are expressing the charge conservation that can be derived from the second and the fourth Maxwell's equations. Since the divergence of the curl of a vector field is zero, the divergence to the second Maxwell's law is zero as well:

$$\nabla \cdot (\nabla \cdot \vec{B}) = 0. \tag{6.12}$$

Applying the divergence to the fourth Maxwell's law (Ampere's law) leads to:

$$\nabla \cdot (\mu_0 \vec{J} + \mu_0 \epsilon_0 \frac{\partial \vec{E}}{\partial t}) = \nabla \cdot (\nabla \cdot \vec{B}) = 0, \tag{6.13}$$

$$-\nabla \cdot \vec{J} = \epsilon_0 \frac{\partial (\nabla \cdot \vec{E})}{\partial t}. \tag{6.14}$$

Applying the first Maxwell's law Eq. 6.10 results in:

$$\nabla \cdot \vec{J} = -\frac{\partial \rho}{\partial t}. \tag{6.15}$$

The continuity equations can be extend by the charge generation G and the recombination R processes and are defined for both charge carriers separately:

$$\frac{\partial n}{\partial t} = \frac{1}{q} \cdot \nabla \vec{J_n} + G_n - R_n, \tag{6.16}$$

$$\frac{\partial p}{\partial t} = \frac{1}{q} \cdot \nabla \vec{J_p} + G_p - R_p, \tag{6.17}$$

with n and p as electron and hole concentration, $\vec{J_n}$ and $\vec{J_p}$ the electron and hole current densities, G_n and G_p as generation rates for electrons and holes, R_n and R_p as recombination rates for electrons and holes, and q as elementary charge of an electron.

With the equations 6.11, 6.16 and 6.17 the foundation of the simulation framework is already covered. Further secondary equations are however needed in order to calculate the physical quantities of: $\vec{J_n}$, $\vec{J_p}$, G_n, G_p, R_n and R_p. These physical quantities can be calculated based on different physical models, which can be chosen based on the physical problem that is studied. In the following section the physical models are introduced, which were used in order to calculate the mentioned physical quantities.

6.4.1.1 The Drift-Diffusion Transport Model calculating the Current Densities $\vec{J_n}$ and $\vec{J_p}$

The calculation of the current densities in the semiconductor is based on a simplified approximation of the Boltzmann Transport Equation. One simplification is the drift-diffusion model [Sel12] that is used in the context of this work.

The current density $\vec{J}$ of charged particles is basically the product of the particle concentration times the charge of a single particle multiplied by the average drift velocity of the particles:

$$\vec{J_n} = q\, n\, \vec{v_n} \quad \text{and} \quad \vec{J_p} = q\, p\, \vec{v_p}, \tag{6.18}$$

with $\vec{v_n}$ and $\vec{v_p}$ as electron and hole drift velocity, and with n and p as concentration of electron and hole charge carriers. With this simplified model, all forces acting on the charge carriers are reduced to the sum of the Lorentz force and the diffusion force. The current densities for the electron $\vec{J_n}$ and for the hole $\vec{J_p}$ charge carrier can therefore be written as:

$$\vec{J_n} = q\, n\, \mu_n \vec{E} + q\, D_n\, \nabla n, \tag{6.19}$$

$$\vec{J_p} = q\, p\, \mu_p \vec{E} + q\, D_p\, \nabla p. \tag{6.20}$$

The left term in both equation is the component caused by the Lorentz force using $\vec{v} = \mu\vec{E}$, which is true with the absence of induction caused by a magnetic field. The second term on the right side of the equation represents the charge carrier diffusion towards the gradient of the carrier concentration assuming that the Einstein relationships holds [Iba10]:

$$D_n = \frac{k\,T_\mathrm{L}}{q}\,\mu_n \quad \text{and} \quad D_p = \frac{k\,T_\mathrm{L}}{q}\,\mu_p, \tag{6.21}$$

with k as Boltzmann's constant and T as absolute temperature of the lattice.

6.4.1.2 Electric Field-Dependent Mobility - Saturation Velocity Model

Charge carriers that are accelerated in the electrical field can reach a material dependent saturation velocity. The saturation of the charge carrier drift velocity for high electrical fields can be accounted by an effective reduction of the charge carrier mobility, since the drift velocity is the product of mobility and electrical field. The field-dependent mobility is implemented in the simulation via the empirical formula found by Caughey and Thomas [Cau67]:

$$\mu_n(E) = \mu_{n,0}\left[\frac{1}{1+(\frac{\mu_{n,0}\cdot E}{v_\mathrm{sat,n}})^{\beta_n}}\right]^{\frac{1}{\beta_n}} \tag{6.22}$$

$$\mu_p(E) = \mu_{p,0}\left[\frac{1}{1+(\frac{\mu_{p,0}\cdot E}{v_\mathrm{sat,p}})^{\beta_p}}\right]^{\frac{1}{\beta_p}} \tag{6.23}$$

with E as parallel electrical field, $\mu_{n,0}$ and $\mu_{p,0}$ as low-field electron and hole mobilities, $v_\mathrm{sat,n}$ and $v_\mathrm{sat,p}$ as saturation velocities of electron and holes, and with the $\beta_{n,p}$ as unit less fit parameters of the Caughey and Thomas mobility model. The three parameters μ_0, v_sat and β describing the field-dependent mobility were measured with high quality single crystalline, see section 6.4.3.4.

6.4.2 Implementation of Traps and Defects

Lattice defects or traps in a semiconductor can have a significant influence to the electrical characteristics of the device. Lattice defects can trap charge carriers and therefore are influencing directly the charge collection distance, the density of space charge in the semiconductor bulk and as well charge carrier recombination processes. These lattice defects can be caused e.g. by impurities during the growth process or caused by irradiation damage. More details on the different types and characteristics of lattice defects can be found in section 3.3.4. In order to implement lattice defects in the semiconductor simulation, the defects have to be characterized, which is explained in the following.

The lattice defects can be describes as electron or hole traps that are however no distinct physical entities. That means a particular lattice defect can act as electron and as hole trap, as it is only determined by its state of occupancy. An empty trap can receive an electron and therefore operates as an electron trap. This charged trap is now ready to trap a hole, hence acting as a hole trap.

The traps can be characterized as donor- or acceptor-like traps. The type of trap is defined by the polarity of the space charge it can cause. A donor-type trap can be either neutral or positively charged; an acceptor-type trap can be either neutral or negatively charged. The definition of the trap type is based on the assumption that in equilibrium all traps are neutral

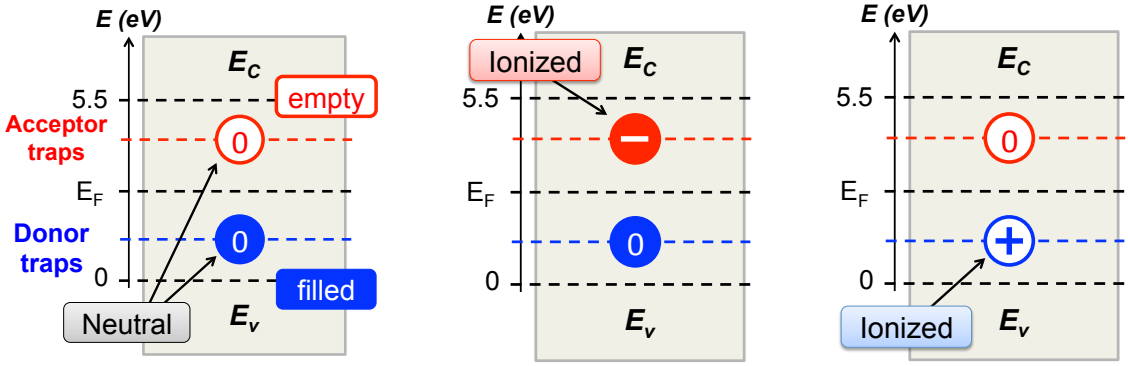

(a) Thermal equilibrium. **(b)** Acceptor ionized. **(c)** Donor ionized.

Figure 6.22: In thermal equilibrium all traps inside the semiconductor are neutral. Traps above the Fermi level E_{rmF} are empty and traps below E_{rmF} are filled. The empty and neutral trap above the Fermi level can trap an electron charge carrier and become ionized. Hence traps located close to the conduction band E_{C} are acceptor-like traps indicated in red. The neutral filled donor like trap close to the valence band E_{V} indicated in blue can be ionized by loosing an electron charge carrier and therefore becomes positively charged.

and the traps above the Fermi level are empty, whereas the traps below the Fermi level are filled, see Fig. 6.22a. The empty trap above the Fermi level is considered to be an acceptor-like trap, since when capturing an electron it is charged negatively, see Fig. 6.22b. By releasing the electron the acceptor like trap becomes empty and neutral. The filled and neutral trap below the Fermi level is considered as a donor-like trap. It can release an electron, equivalent to capturing a hole, and become positively charged, see Fig. 6.22c. Further detailed information can be found in [Sim71].

Another important parameter of the donor- and acceptor-like traps is the energy level at which the traps are located. The energy level for acceptor like traps E_t is defined with respect to the conduction band, whereas the energy level of the donor like traps is defined with respect to the valence band. The probability of charge carrier being trapped in donor- and acceptor-like traps is defined via cross sections, separately defined for trapping a hole σ_p or an electron σ_n charge carrier. It should be noted that the charge trapping is only determined by the particular capture cross-section and not by its state of charging. Therefore, a charged and a neutral electron trap with the same cross section will capture electrons at the same rate [Sim71].

6.4.2.1 Formalism to calculate Space Charge caused by Ionized Traps

The Poisson's Equation 6.11 can also be written as an integral over the entire boundary surface:

$$\oint_S \vec{E} \cdot \mathrm{dA} = \frac{\mathrm{Q}}{\epsilon_0}, \tag{6.24}$$

The space charge that is caused by ionized traps inside the semiconductor bulk is subtracted directly from the right hand side of the Poisson's Equation, resulting in:

$$\oint_S \vec{E} \cdot \mathrm{dA} = \frac{1}{\epsilon_0} \cdot (\mathrm{Q} - \mathrm{Q_T}), \tag{6.25}$$

with:

$$Q_T = q(N_{tD}^{+} - N_{tA}^{-}) \tag{6.26}$$

where N_{tD}^{+} and N_{tA}^{-} are the densities of the ionized donor- and acceptor-like traps. The density of an ionized state of e.g. the donor-like trap depends on the trap density ρ_{tD} and as

well on the probability of its ionization F_{tD} leading to:

$$N_{tD}^{+} = \rho_{tD} \cdot F_{tD} \quad \text{and} \quad N_{tA}^{-} = \rho_{tA} \cdot F_{tA} \tag{6.27}$$

For multiple traps the total trap density is calculated as sum over all single trap densities. The probability of a trap ionization is based on [Sim71] and assumes that the capture cross section is constant for all energies inside the band. The probability of an ionized acceptor-like trap is:

$$F_{tA} = \frac{v_n \cdot cs_n \cdot n + e_{pA}}{v_n \cdot cs_n \cdot n + v_p \cdot cs_p \cdot p + e_{nA} + e_{pA}} \tag{6.28}$$

with cs_n and cs_p as capture cross sections for electron and holes, with e_{nA} and e_{pA} as emission rates for electron and holes, and with v_n and v_p as thermal velocities for electron and holes. This equation calculates the fraction between the processes ionizing the trap, either by capturing an electron ($v_n \cdot cs_n \cdot n$) or by releasing an hole (e_{pA}), to all possible capture and emission processes. The emission rate of a particular charge carrier can be calculated via:

$$e_{nA} = \delta v_n cs_n n_i \cdot exp\frac{E_t - E_i}{kT_{\mathrm{L}}}, \tag{6.29}$$

$$e_{pA} = \frac{1}{\delta} v_p cs_p n_i \cdot exp\frac{E_i - E_t}{kT_{\mathrm{L}}}, \tag{6.30}$$

with E_i as intrinsic Fermi level, E_t as trap energy level and with δ as degeneracy factor of the trap center. The calculation of the donor-like trap ionization probability is equivalent to 6.28 with exchanged indices n instead of p.

6.4.2.2 Calculation of the charge carrier Recombination

The charge carrier recombination in a semiconductor can happen via three different recombination processes. The simplest, for indirect semiconductor however the most unlikely, recombination process is a direct 'band-to-band' recombination process, where an electron transitions directly from its state in the conduction band to an empty state in the valence band associated with a hole. In an Auger recombination a charge carrier e.g. an electron from the conduction band is as well 'band-to-band' recombining with an hole from the valence band, additionally a third charge carrier is involved that is receiving the resulting energy. Since the Auger recombination is a three particle process the recombination rate is affected and therefore has to be treated separately compared to the two particle band to band recombination process. The most important recombination process for indirect semiconductor like diamond is the trap-assisted recombination where an electron falls first into a trap located inside the band gap. In a second step the electron is than falling into an empty state in the valence band and hence recombining with a hole state. The theory for this trap-assisted recombination was first derived by Shockley and Read [Sho52] and then by Hall [Hal52] and is therefore often considered as Shockley-Read-Hall (SRH) recombination. The SRH recombination for a donor-like trap can be calculated by:

$$R_{Da} = \frac{pn - n_{ie}^2}{\tau_n \left[p + \delta\, n_{ie} exp(\frac{E_i - E_t}{kT_{\mathrm{L}}})\right] + \tau_p \left[n + \frac{1}{\delta}\, n_{ie} exp(\frac{E_t - E_i}{kT_{\mathrm{L}}})\right]} \tag{6.31}$$

where the electron τ_n and hole τ_p lifetimes are related to the capture cross sections via:

$$\tau_n = \frac{1}{cs_n\, v_n\, \rho_D} \quad \text{and} \quad \tau_p = \frac{1}{cs_p\, v_p\, \rho_D} \tag{6.32}$$

The SRH recombination for an acceptor-like trap is defined equivalent with exchanged indices n instead of p.

6.4.3 Adjusting and Optimizing of the Silvaco TCAD Device Simulation

6.4.3.1 Modeling of the Diamond Sensors with the Device Simulation

One of the many challenges in the diamond sensor device simulation is the correct description of the ionizing particles. A MIP passing through the diamond bulk is creating along its way electron hole pairs that will start drifting and diffusing under the influence of an electrical field and the carrier concentration gradient. These kind of problems are typically solved in a three dimensional geometry. However a full three dimensional simulation needs a lot more computing power since an increased amount of grid points has to be solved. The simulated diamond device in a full 3D simulation has to solve $\times 40$ more grid points compared to a 2D simulation that approximately translates directly into a $40\times$ increased simulation time. In a two dimensional simulation (see Fig. 6.23a) all physical quantities are extruded into the third dimension, leading to either a correct description of the charge carrier density or a correct description of the total amount of charge carries, not both. Different approaches have been done to improve the scaling schemes in order to adjust e.g. the charge carrier recombination, however at the price of an underestimation of the charge density [Fu85]. A possibility to overcome the limitation of the simulation in the two-dimensional space is a quasi-3D simulations based on cylindrical symmetry and coordinate transformations, see Fig. 6.23b. The simulation of the detector device is still done in a two dimensional space and the amount of grid points to be solved is therefore identical to a 2D simulation. The physical quantities are however calculated for a three dimensional cylindrical symmetric space, allowing a correct description of the charge carrier density and the total amount of charge carriers at the same time. Further information to quasi-3D simulations can be found in [Dod96].

6.4.3.2 Optimization of the Simulation Grid

The definition of a good grid is crucial for a correct and efficient device simulation. The decision of the grid settings is typically a trade-off between the required accuracy of the simulation and the numerical efficiency. The grid defined for the diamond device simulations was therefore optimized to the requirements for the simulation of TCT and MIP signals.

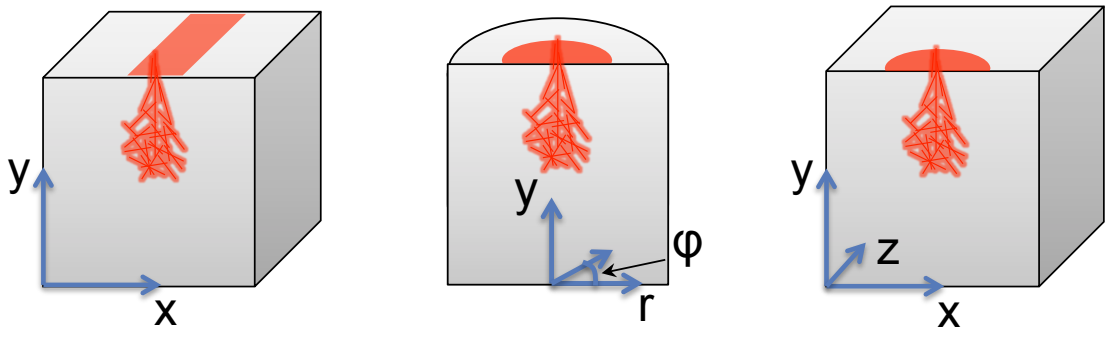

(a) Two Dimensional
Correct charge density
or
Correct total charge
Incorrect geometry

(b) Quasi three Dimensional
Correct charge density
Correct total charge
Incorrect geometry

(c) Three Dimensional
Correct charge density
Correct total charge
Correct geometry
Computing intense

Figure 6.23: Comparison of the device simulation in two dimensions, quasi three dimension and in three dimension. The quasi-three dimension combines a correct description of all physical quantities with a very computing efficient simulations, can however only be used for cylindrical symmetric problems.

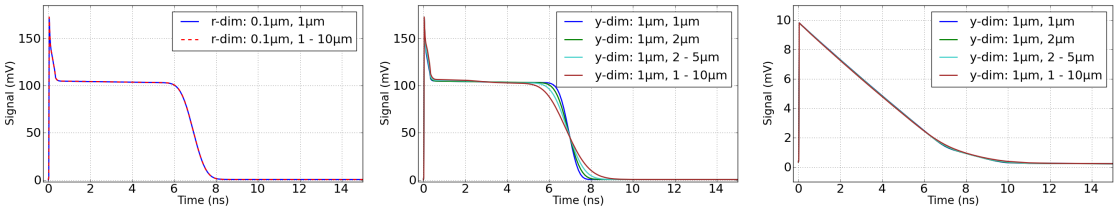

(a) Grid variation in r. **(b)** Grid variation in y. **(c)** Grid variation in r.

Figure 6.25: Grid optimization in the r- and y-dimension of the quasi-3D diamond detector simulation. The grid of the simulation was optimized to an accurate and time efficient simulation of the charge carrier drift caused by an α particle (a) and (b), and by an electron in (c).

The alpha particles are injected from the top or bottom side of the diamond sensors and are penetrating the diamond till a maximum thickness of 15 µm. The MIP events are homogeneously creating charge carriers inside the entire diamond bulk along the y-axis. The grid can therefore be divided into 2 regions, like indicated in Fig. 6.24. In region I where the α particles are injected a very fine grid is needed. In the middle of the diamond bulk, indicated as region II, the MIP events are creating a descent amount of charge carrier (36 e-h pairs per µm), or the cloud of charge carriers injected in region I is drifting through the diamond sensor. The charge carrier drift is determined by drift and diffusing forces under the influence of the electrical field. The grid in this region can potentially be reduced to improve the simulation efficiency. The α and the β particles are injected along the y-axis at a radius of $r = 0\,\mu m$. Hence the finest grid in the r dimension has to be close to $r = 0\,\mu m$, for an increased radius the grid gap can be increased. Two regions are therefore defined for the r-dimension, $r_I < 1\,\mu m$ and $1\,\mu m < r_{II} < 100\,\mu m$. In order to find an optimal solution several different grid definition have been simulated and are compared to the finest grid configuration with a grid gap in the y-dimension of $y_{I,II} = 1\,\mu m$ and in the r-dimension of $r_I = 0.1\,\mu m$ and $r_{II} = 1\,\mu m$. In Fig. 6.25a the simulation results of an α particle hit is shown for two different configuration of the grid in the r-dimension. The grid with the reduced resolution, increasing the steps in the r_{II} region up to 10 µm steps, shows the identical simulation results compared to the finest grid configuration. In Fig. 6.25b the α particle event is simulated for different configuration of the grid in the y_{II} region. Increasing the gaps in the y_{II} grid up to 10 µm steps results in a smearing out of the TCT pulse, hence a different grid configuration closer to the finest grid results should be chosen. In Fig. 6.25c a MIP event is simulated for different y grid configuration, however without any modification to the simulation result. Based on these results shown in Fig. 6.25 the grid with the best performance in terms of accuracy and numerical efficiency indicated in blue in Table 6.5 was used for the simulation of the diamond sensor device.

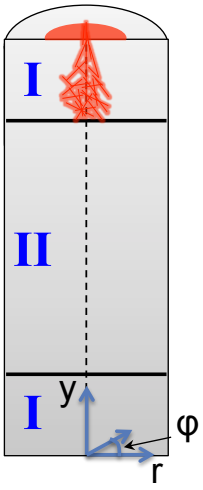

Figure 6.24: Optimization of the grid for the quasi-3D diamond simulation

6.4.3.3 Customizing Diamond Simulation to adapt to the real TCT and CCE measurement setup

In this section different input quantities used in the simulations are discussed. Furthermore, experimental limitations of the measurement setup were taken into account in the interpretation of the simulation result.

Table 6.5: Grid optimization in the r and y dimension for an optimal simulation of the charge carrier drifts caused by α and β particles with respect to a high accuracy and numerical efficiency.

Region	r-steps		y-steps			
r_I	0.1	**0.1**	0.1	**0.1**	0.1	0.1
r_{II}	1	**1-10**	1-10	**1-10**	1-10	1-10
y_I	1	**1**	1	**1**	1	1
y_{II}	2	**2**	1	**2**	2-5	1-10
Calculation time (h)	6	**3.2**	6.1	**3.2**	1.9	1.4

The energy deposition of the α and β particles in the diamond sensors are strongly related to the geometrical setup of the TCT and CCE measurements. An α particle with an energy of $E_\alpha = 5.486\,\text{MeV}$ looses for example $0.762 \pm 0.04\,\text{MeV}$ in 5 mm of air [Pom08]. Both measurement setups were therefore accurately simulated using Fluka and the energy deposition in the diamond sensors calculated for the α and β particles. In Fig. 6.26 the simulated energy deposition of both particle types for both measurement setup is shown. The energy deposition of the α particle, shown in Fig. 6.26a, shows the Bragg peak that causes the creation of charge carriers up to a thickness of $d = 15\,\mu\text{m}$ inside the diamond bulk. In Fig. 6.26b the charge carrier creation rate caused by the β particle sources are shown as function of diamond thickness. ^{90}Sr decays in lots of low energetic β particles ($E < 0.546\,\text{MeV}$) and in ^{90}Yr which decay creates the MIP particles with an energy of $E = 1.6\,\text{MeV}$. The low energetic β particles are responsible for the increased charge carrier creation within the first 100 µm of thickness of the diamond bulk. An increased energy deposition is simulated for the CCE setup in Zeuthen, where a slightly more radioactive β particle source with an activity of $A = 33.4\,\text{MBq}$ (TCT: $A = 32.2\,\text{MBq}$) is used.

Besides the geometrical properties of the measurement setup, the hardware limitation of the scope and the amplifier are taken into account. The raw TCT signal calculated by the simulation is therefore subjected to a bandwidth filter (shown in Fig. 6.27) to simulate the limited bandwidth of the scope with 1 GHz used in the TCT setup, see section 6.1.1. The unfiltered simulation result shows a narrow peak at the beginning of the TCT pulse, which is caused by the drift of both charge carriers in opposite directions immediately after the alpha particle hit. The small penetration depth $d_{\text{alpha}} \leq 15\,\mu\text{m}$ (see Fig. 6.26a) explains the short

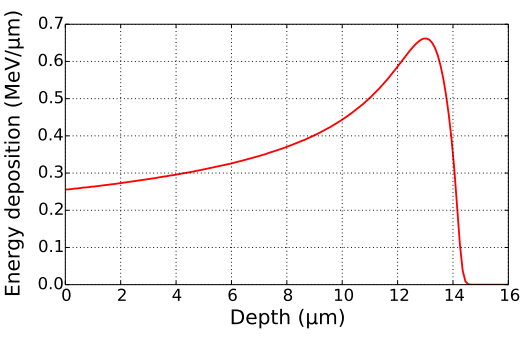

(a) Simulation of an α particle with an energy of $E_\alpha = 5.486$.

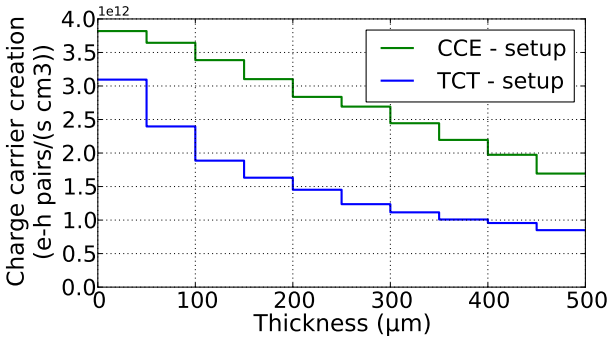

(b) Charge carrier creation rate caused by the β particle sources for the CCE and TCT setup.

Figure 6.26: Fluka based simulation of the energy deposition for α and β particles.

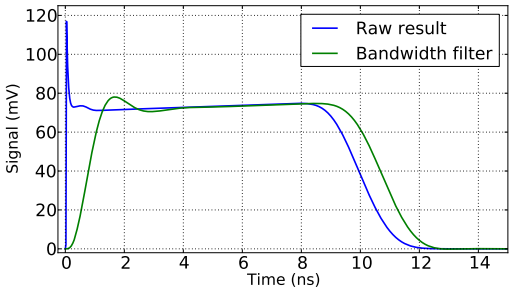

Figure 6.27: The raw TCT signal calculated by the simulation (blue) is manipulated with a bandwidth filter to simulate the limited bandwidth of the TCT hardware. The narrow peak at the beginning of the unfiltered TCT pulse is caused by the drift of both charge carriers in opposite direction immediately after the alpha particle hit [Kas16c].

duration of this peak ($t < 0.2\,\text{ns}$).

6.4.3.4 Measurement of the Charge Carrier Mobility

The mobility and drift parameters of the charge carriers inside the diamond are crucial for a correct TCT pulse simulation. The drift velocity of the charge carriers can be calculated dividing the diamond thickness by the average TCT pulse duration, see section 6.3.7. The measured drift velocities of all 5 un-irradiated sCVD diamond sensors as function of the electrical field between $E = 0.13\,\text{V/µm}$ and $E = 1.82\,\text{V/µm}$ are shown in Fig. 6.28 and are in agreement with the drift velocities measured by [Pom15].

The charge carrier drift as function of the electrical field can be parameterized by the empirical formula by [Cau67], see section 6.4.1.2:

$$v_{\text{drift}} = v_{\text{sat}} \frac{E/E_c}{(1 + (E/E_c)^{\beta})^{1/\beta}}, \tag{6.33}$$

with

$$E = v_{\text{drift}}/\mu_0. \tag{6.34}$$

By fitting the function in Eq. 6.33 to the measured drift velocities the parameters μ_0, β and E_c are obtained. The parameter μ_0 can be understood as the low field mobility, β as a unit less fit parameters and E_c as critical electrical field. Based on the measurement of the drift

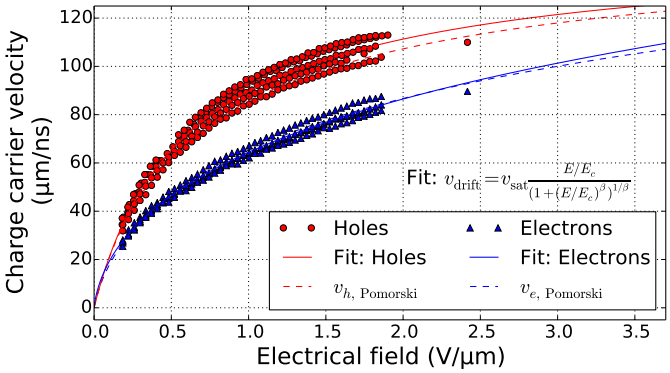

Figure 6.28: The measured drift velocities of both charge carriers, indicated in red dots and blue triangulars, as function of applied electrical field. The measurement results obtained with all un-irradiated diamond samples are in agreement with the drift velocities measured in [Pom15]. The charge carrier velocity as function of the electrical field is fitted to the empirical formula found by Caughey and Thomas [Cau67] noted in the plot.

Table 6.6: Overview of the mobility parameters calculated based on the measurements of all 5 un-irradiated diamond samples in comparison to literature values based on [Pom15]. The parameters indicated in blue were used in the diamond sensors simulation.

Parameters	E_c (kV/cm)	μ_0 (cm^2/Vs)	β
e_{exp}	4.325 ± 0.731	14948 ± 8303	0.26 ± 0.06
h_{exp}	5.836 ± 0.251	2615 ± 148	0.90 ± 0.09
e_{lit}	5.779 ± 0.772	4551 ± 500	0.42 ± 0.01
h_{lit}	5.697 ± 0.529	2750 ± 70	0.81 ± 0.01

velocity as function of the electrical field for all 5 un-irradiated diamond samples, the fit parameters are calculated and listed in Table 6.6. In comparison to the fit parameters found by [Pom15], the parameterization for the electron drift fails even if the measured values are on top of the literature values in Fig. 6.28. The parameterization of the curve is strongly influenced by drift velocity measurements for high electrical fields. The TCT setup was however limited to a maximum high voltage of HV = 1000 V that already the drift velocity measured at an electrical field of $E = 2.4\,\mathrm{V/\mu m}$ equivalent to a bias voltage of HV = 1300 V was very critical.

The mobility parameters used in the diamond detector simulation were the experimental determined parameters for the hole drift and the literature parameters for the electron drift, indicated in blue in Table 6.6.

6.4.4 Simulation of the TCT and CCE measurement based on an Effective Trap Model

The irradiation creates a plutoria of defects, which can trap charges (electrons or holes) or stay in an ionized state. Since the energy levels of the defects are poorly known, four effective deep traps acting as recombination centers are introduced to approximate the many different defects in reality. The energy levels and cross sections of such a simple model are obtained by fitting the evolution of the TCT pulse shapes as function of exposure time T_{exp} to the ^{90}Sr particle source. Simulating a MIP particle used to calculate the charge collection efficiency and fitting to the measurement results further refined the effective trap model.

The Silvaco diamond simulation follows the experimental measurement procedure and simulates the same time duration of the experimental measurement, in total 3600 s. The diamond sample is exposed during the entire simulation to the Fluka simulated ^{90}Sr source, see section 6.4.3.3.

In a first step the diamond is exposed to the ^{90}Sr source over a time duration of 20 minutes with no bias voltage applied in order to fill the diamond traps homogeneously. Depending on the simulation of a TCT measurement or a CCE measurement the appropriate ^{90}Sr source is simulated. In a next simulation step the bias voltage is quickly ramped up (< 1 s), and followed by α particle hits simulated on both surfaces successively to simulate the TCT pulse of the electron and the hole drift. In the CCE simulation a MIP signal is simulated that is used to calculate the CCE. The simulation of the two α or the one MIP signal is repeatedly simulated for different exposure times of $T_{exp} = 0$ s, 300 s, 600 s, 1200 s, 1800 s, 2400 s, 3000 s and 3600 s in order calculate the TCT pulse modification or the CCE as function of exposure

Table 6.7: Physical parameters of the effective recombination centers. Both effective recombination centers $eRC1/2$ are present as acceptor- and donor-like traps.

Trap name	$eRC1$	$eRC2$
Energy level E_t (eV)	1.8	0.83
Density ρ ($\times 10^{12}\,\mathrm{cm}^{-3}$)	1.0	0.8
Cross section σ_e ($\times 10^{-14}\,\mathrm{cm}^2$)	0.7	2.0
Cross section σ_h ($\times 10^{-14}\,\mathrm{cm}^2$)	0.7	1.0

time to the ^{90}Sr source. At these measurement steps additional diamond information like electrical field and recombination rates are probed as well.

Based on the optimization of the TCT and CCE simulation results to the experimental data an effective trap model was determined for each irradiation step for every diamond sensors. In the next section 6.4.4.1 the simulation of the TCT and CCE measurement for one example irradiation step are discussed in detail. Based on the individual optimized trap configurations for each irradiation step an effective defect model as function of radiation damage was found, which is introduced in section 6.4.4.4.

6.4.4.1 Effective Trap Model optimization to TCT and CCE measurements

In Fig. 6.29 the simulation of the TCT pulses as function of exposure time to the ^{90}Sr particle source are compared to the measurement results. The modification of the TCT pulse is caused by the build up of space charge, which is directly related to the trap configuration as predicted by the diamond polarization discussed in section 5.5. An automated routine changed the trap configuration in order to fit the simulated TCT pulse shapes to the measurement results by optimizing with the least square method:

$$S = \sum_{T_{exp}=0\,\mathrm{s}}^{3600\,\mathrm{s}} \sum_{t=0\,\mathrm{ns}}^{50\,\mathrm{ns}} \left(S_{\mathrm{sim.,T_{exp}}}(\mathrm{t}) - \mathrm{S_{meas.,T_{exp}}}(\mathrm{t})\right)^2 \tag{6.35}$$

The optimized trap configuration, listed in Table 6.7, results in a correct description of the TCT pulses for the hole and electron drift as function of T_{exp}. The fit optimization of the electron drift leads to a mean discrepancy of 3.15 mV ($T_{exp} = 0\,\mathrm{s}$) between simulation and measurement, 4.34 mV and 2.78 mV for $T_{exp} = 285\,\mathrm{s}$ and $T_{exp} = 2385\,\mathrm{s}$, respectively. The build up of space charge and hence the modification of the TCT pulses as function of exposure time is primarily determined by the trap density of the effective recombination center $eRC1$. The trap density of the second effective recombination center $eRC2$ is an important parameter by the optimization of the simulated MIP signal used to calculate the charge collection efficiency of the diamond sensor. The MIP particle creates homogeneously 36 electron hole pairs per µm along its path through the diamond sensor. The simulated MIP signal, shown in Fig. 6.30a, has therefore the expected triangular shape for the fully primed diamond sensors at $T_{exp} = 0\,\mathrm{s}$. The signal duration of the MIP event is $t_{\mathrm{MIP}} \sim 20\,\mathrm{ns}$ for an electrical field of $E = 0.18\,\mathrm{V/\mu m}$. The total charge Q_{induced} used to calculate the charge collection efficiency with Eq. 6.3 (see section 6.1.2) was obtained by integrating the signal current created by the MIP particle. The build up of space charge affects the shape of the MIP signal and results in a reduced simulated CCE value that is in agreement with the measurement, see Fig. 6.30b. The final simulated charge collection efficiency of CCE = 72.92% at an exposure time of $T_{exp} = 3000\,\mathrm{s}$ is increased by about $\sim 6\%$ compared to the measured charge collection efficiency of $\mathrm{CCE_{meas.}} = 66.72 \pm 2.4\%$.

6.4.4.2 Consistency Check at an increased Electrical Field of $E = 0.36\,\mathrm{V/\mu m}$

In order to check the consistency of the simulation results, the same trap model was used to simulate the TCT and CCE measurement for an increased electrical field of $E = 0.36\,\mathrm{V/\mu m}$. The simulated TCT pulses for the electron charge carrier drift is in agreement with the measurement results at the increased electrical field, see Fig. 6.31a. The simulated CCE as function of exposure time, shown in Fig. 6.31b, matches as well the measurement results. The defect model optimized at an electrical field of $E = 0.18\,\mathrm{V/\mu m}$ to the TCT and CCE modifications as function of exposure time describes as well the measurement results at different electrical fields and hence indicates a good description of the real processes happening in the diamond sensors.

6.4.4.3 Quantitative Analysis of the Diamond Polarization

The diamond polarization at the electrical field of $E = 0.18\,\mathrm{V/\mu m}$ is analyzed in more detail using the results obtained by the Silvaco TCAD simulation. The electrical field causing the strong modification of the TCT pulse shapes is shown in Fig. 6.32a. The electrical

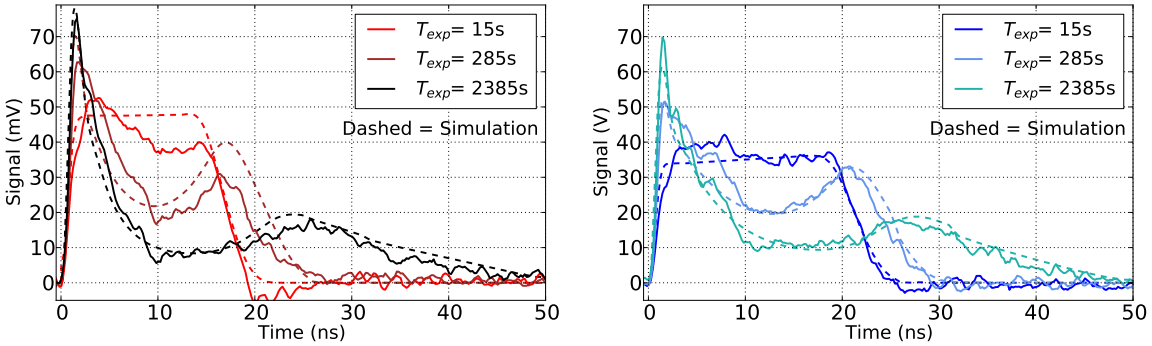

(a) Simulation of TCT pulse - Hole drift. **(b)** Simulation of TCT pulse - Electron drift.

Figure 6.29: Comparison of the TCT pulse deformation for the hole (left) and the electron (right) drift as function of exposure time to the ^{90}Sr source. The simulation (dashed) and measurement (solid) are in agreement. The measured and simulated diamond sensor (#27135474) was irradiated with a fluence of $\Phi = 0.9 \times 10^{13}\,n_{1\,\mathrm{MeV\,eq.}}\mathrm{cm}^{-2}$ and operated at a bias voltage of $\mathrm{HV} = 100\,\mathrm{V}$ equivalent to an electrical field of $E = 0.18\,\mathrm{V/\mu m}$.

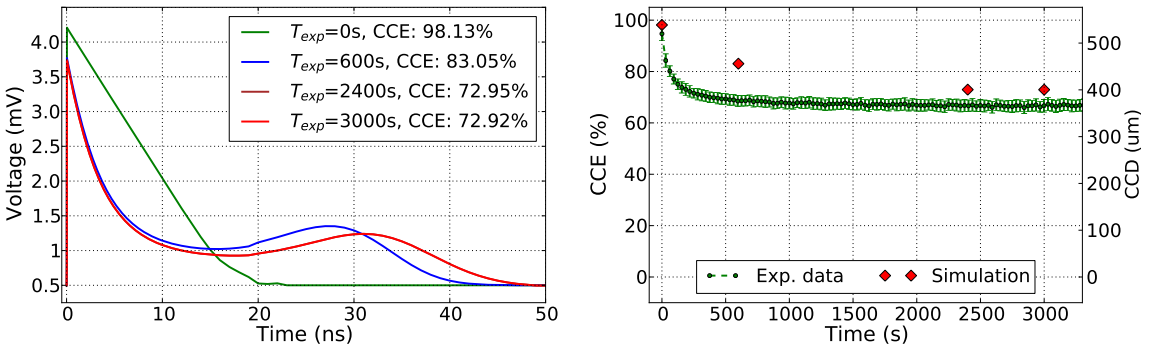

(a) Simulation of MIP pulse. **(b)** CCE as function of T_{exp}.

Figure 6.30: The left plot shows the simulated MIP signal for the diamond sensor #27135474 that was irradiated with a fluence of $\Phi = 0.9 \times 10^{13}\,n_{1\,\mathrm{MeV\,eq.}}\mathrm{cm}^{-2}$ and was operated at an electrical field of $E = 0.18\,\mathrm{V/\mu m}$. The CCE as function of T_{exp} (red), calculated based on the simulated MIP signal, is in agreement with the measured CCE (green) shown in the right figure.

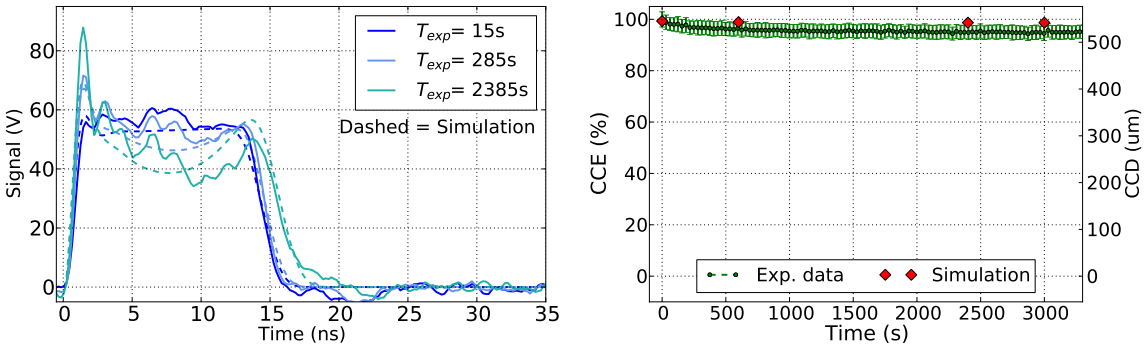

(a) Electron drift at $E = 0.36\,\mathrm{V/\mu m}$. **(b)** CCE as function of T_{exp}.

Figure 6.31: The trap model optimized to the measurement results obtained at an electrical field of $E = 0.18\,\mathrm{V/\mu m}$ is used to simulate the TCT (left) and the CCE (right) measurements at an increased electrical field of $E = 0.36\,\mathrm{V/\mu m}$. The simulated TCT and CCE results as function of exposure time to the ^{90}Sr particle source are both in agreement with the measurement results.

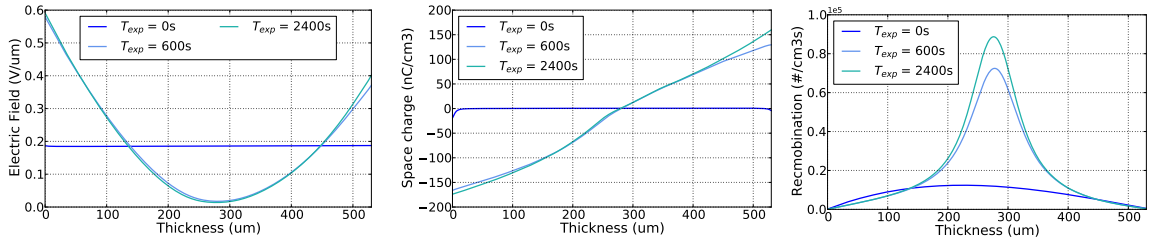

(a) Electrical field **(b)** Space charge **(c)** SRH recombination

Figure 6.32: Quantitative analysis of the diamond polarization: Electrical field, Space charge and Recombination as function of T_{exp}

field is simulated for the same time steps at which the TCT pulses in Fig. 6.29 have been simulated. For the unpolarized diamond sensors at $T_{exp} = 0\,\mathrm{s}$ the electrical field is constant as expected. With increased exposure time to the ionizing particle flux ($T_{exp} > 0\,\mathrm{s}$) the diamond polarization causes a strong modification of the electrical field, leading to a local minimum in the middle of the diamond bulk that is $\sim 6\times$ reduced compared to the electrical field for the unpolarized diamond state. This local minimum in the middle of the diamond bulk is compensated by increased electrical field towards the edges. The trapped charge carriers causing the electrical field modification are shown in Fig. 6.32b. At the edges of the diamond sensors a total amount of space charge of $Q_{\mathrm{SC}} = \pm 150\,\mathrm{fC}$ is trapped. The electrical polarization field caused by the space charge can be calculated by assuming a parallel-plate capacitor, where the electrical field is calculated by:

$$E_{\mathrm{pol}} = \frac{Q_{\mathrm{SC}}}{\epsilon_0 \epsilon_r A} = 0.169\,\mathrm{V/\mu m} \tag{6.36}$$

with the vacuum permittivity of $\epsilon_0 = 8.854 \times 10^{12}\,\mathrm{F/m}$, the relative permittivity for diamond of $\epsilon_r = 10$ and the surface of the parallel-plate capacitor A. Hence the electrical field caused by the polarization E_{pol} is almost identical to the applied external electrical field of $E = 0.18\,\mathrm{V/\mu m}$. The locally reduced electrical field in the middle of the diamond bulk is increasing the recombination rate of the charge carriers by a factor of ~ 9, see Fig. 6.32c, thus explaining the drop from 93 % to 65 % in CCE.

6.4.4.4 Dynamic Trap Model

The four diamond sensors used in the irradiation campaign were irradiated stepwise with proton or neutron particles up to a fluency of $\Phi = 30.1 \times 10^{13}\,n_{1\,\mathrm{MeV\,eq.}}\mathrm{cm}^{-2}$. The diamond

sensors were irradiated with slightly different fluencies (see Table 6.2) resulting in 12 different absolute irradiation damaged diamond measurements. The behavior of the electrical field was measured after each irradiation step with the TCT technique and the charge collection efficiency was measured in total 3 times for each diamond sensor. The TCT and CCE simulation, discussed in the previous section 6.4.4.1, were fitted to each TCT and CCE measurement and a uniquely optimized trap configuration was found with respect to the particular irradiation damage. The traps were optimized to each measurement by adjusting the quantity of the trap density, since the trap properties like energy level or cross section should not be affected by the irradiation damage. The Figure 6.33 shows the simulated TCT pulses of the hole charge carrier drift for the optimized trap configurations at different radiation damages. At low radiation damages below a fluence of $\Phi < 1 \times 10^{13}\, n_{1\,\mathrm{MeV\,eq.}}\mathrm{cm}^{-2}$ the TCT pulses were optimized for measurements at an electrical field of $E = 0.18\,\mathrm{V/\mu m}$. At increased radiation damages of $1 \times 10^{13} < \Phi < 3 \times 10^{13}\, n_{1\,\mathrm{MeV\,eq.}}\mathrm{cm}^{-2}$ the simulated TCT pulses were optimized to the measurement results for an increased electrical field of $E = 0.36\,\mathrm{V/\mu m}$, since the strongly modified TCT pulses for reduced electrical fields couldn't be measured with high precision. At the highest irradiation damages of $\Phi > 3 \times 10^{13}\, n_{1\,\mathrm{MeV\,eq.}}\mathrm{cm}^{-2}$ the simulated TCT pulses were fitted to even higher electrical fields.

In Fig. 6.34a - 6.34c the simulated MIP signal as function of T_{exp} is shown for three different irradiation damages. At the lowest radiation damage of $\Phi = 0.9 \times 10^{13}\, n_{1\,\mathrm{MeV\,eq.}}\mathrm{cm}^{-2}$ in Fig. 6.34a the MIP signal is simulated for an electrical field of $E = 0.18\,\mathrm{V/\mu m}$ resulting in a signal duration of $t_{\mathrm{MIP}} \sim 20\,\mathrm{ns}$ for the primed diamond sensors at $T_{exp} = 0\,\mathrm{s}$. In Fig. 6.34b and 6.34c the MIP signal is simulated at an increased electrical field of $E = 0.72\,\mathrm{V/\mu m}$ that reduces the duration of the MIP signal to $t_{\mathrm{MIP}} \sim 10\,\mathrm{ns}$. The CCE signal simulated for the primed diamond sensors at $T_{exp} = 0\,\mathrm{s}$ is always CCE = 100% independent of the total radiation damage, since all defects are passivated and no space charge is build up. The initial

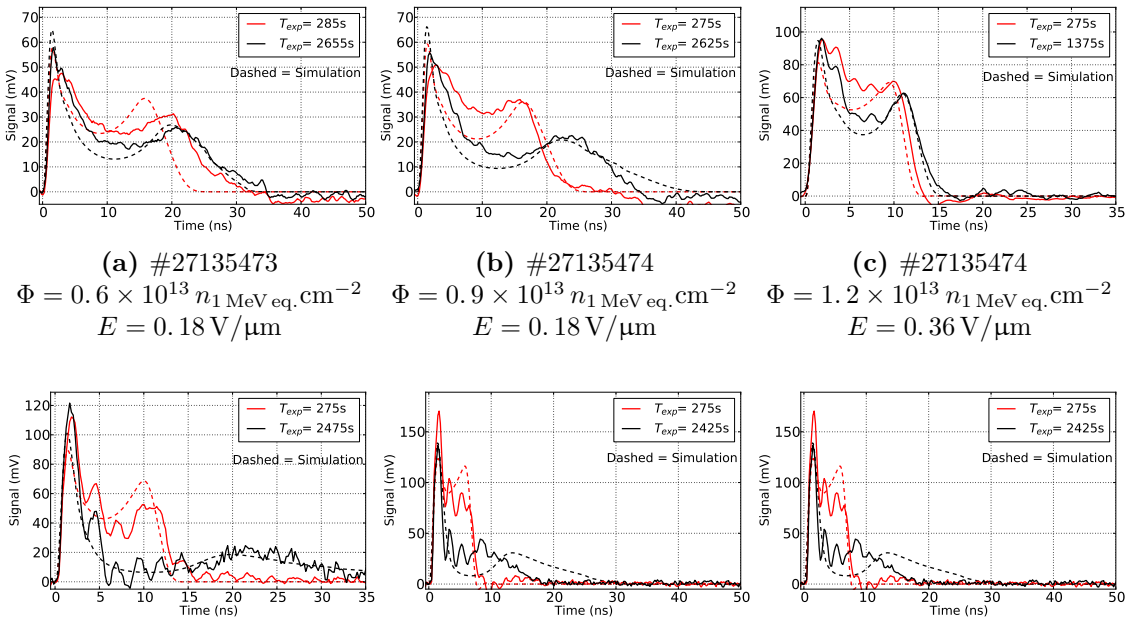

(a) #27135473
$\Phi = 0.6 \times 10^{13}\, n_{1\,\mathrm{MeV\,eq.}}\mathrm{cm}^{-2}$
$E = 0.18\,\mathrm{V/\mu m}$

(b) #27135474
$\Phi = 0.9 \times 10^{13}\, n_{1\,\mathrm{MeV\,eq.}}\mathrm{cm}^{-2}$
$E = 0.18\,\mathrm{V/\mu m}$

(c) #27135474
$\Phi = 1.2 \times 10^{13}\, n_{1\,\mathrm{MeV\,eq.}}\mathrm{cm}^{-2}$
$E = 0.36\,\mathrm{V/\mu m}$

(d) #27135476
$\Phi = 5.5 \times 10^{13}\, n_{1\,\mathrm{MeV\,eq.}}\mathrm{cm}^{-2}$
$E = 0.36\,\mathrm{V/\mu m}$

(e) #27135474
$\Phi = 4.8 \times 10^{13}\, n_{1\,\mathrm{MeV\,eq.}}\mathrm{cm}^{-2}$
$E = 0.73\,\mathrm{V/\mu m}$

(f) #27135474
$\Phi = 30.1 \times 10^{13}\, n_{1\,\mathrm{MeV\,eq.}}\mathrm{cm}^{-2}$
$E = 1.09\,\mathrm{V/\mu m}$

Figure 6.33: Comparison between the TCT simulation and measurement for the hole charge carrier drift at different irradiation damages. The optimized TCT simulation for the lowest radiation damage of $\Phi = 0.6 \times 10^{13}\, n_{1\,\mathrm{MeV\,eq.}}\mathrm{cm}^{-2}$ is shown in (a) up to the highest irradiation damage of $\Phi = 30.1 \times 10^{13}\, n_{1\,\mathrm{MeV\,eq.}}\mathrm{cm}^{-2}$ shown in (f). For each radiation damage a unique defect model was optimized to match the measurement results.

experimental measured CCE will never reach this value, since the measurements will always take non-zero amount of measurement time in which the diamond polarization will build up space charge and modify the measurement results. Based on the simulated MIP signals, the calculated charge collection efficiency is plotted in the Figs. 6.34d-6.34f as function of exposure time T_{exp} and compared to the experimental measured CCE values.

The measurement and simulation results shown in Fig. 6.33 and 6.34 are representatives for the in total 12 optimized trap configurations for different irradiation damages, fitted to the measurement results of the diamond sensors irradiated with proton and neutron particles. In Fig. 6.35 the optimized trap densities for both effective recombination centers $eRC1$ and $eRC2$ are plotted as function of the radiation damage Φ. The error to the absolute radiation damage in the x-dimension is due to the limited accuracy of the irradiation facilities. The accuracy of the proton irradiation is $\pm 20\%$ and the accuracy of the neutron irradiation is $\pm 30\%$. The linear regression of the trap densities with respect to the total radiation damage gives:

$$\rho_{eRC1}\,(\mathrm{cm}^{-3}) = \Phi \cdot (2.52 \pm 0.13) \times 10^{-2} + (9.40 \pm 1.11) \times 10^{11} \tag{6.37}$$

$$\rho_{eRC2}\,(\mathrm{cm}^{-3}) = \Phi \cdot (2.15 \pm 0.04) \times 10^{-2} + (6.67 \pm 0.38) \times 10^{11} \tag{6.38}$$

with the radiation damage caused by a particle fluency of Φ in $n_{1\,\mathrm{MeV\,eq.}}\mathrm{cm}^{-2}$.

A possibility to verify this effective trap model is the simulation and calculation of the radiation constant for an electrical field of $E = 1\,\mathrm{V/\mu m}$. This simulated radiation constant will be compared to the radiation constant found by the RD42 collaborations. This direct comparison can be done, since the radiation constant is independent of the diamond material (sCVD or pCVD) used to measure the radiation induced signal degradation [Cri10]. The different diamond material is only reflected in a different initial charge collection distance value, compare sec. 5.1. The CCE of the diamond sensor is simulated for a typical particle rate environment created by a ^{90}Sr, comparable to the laboratory measurements done by the

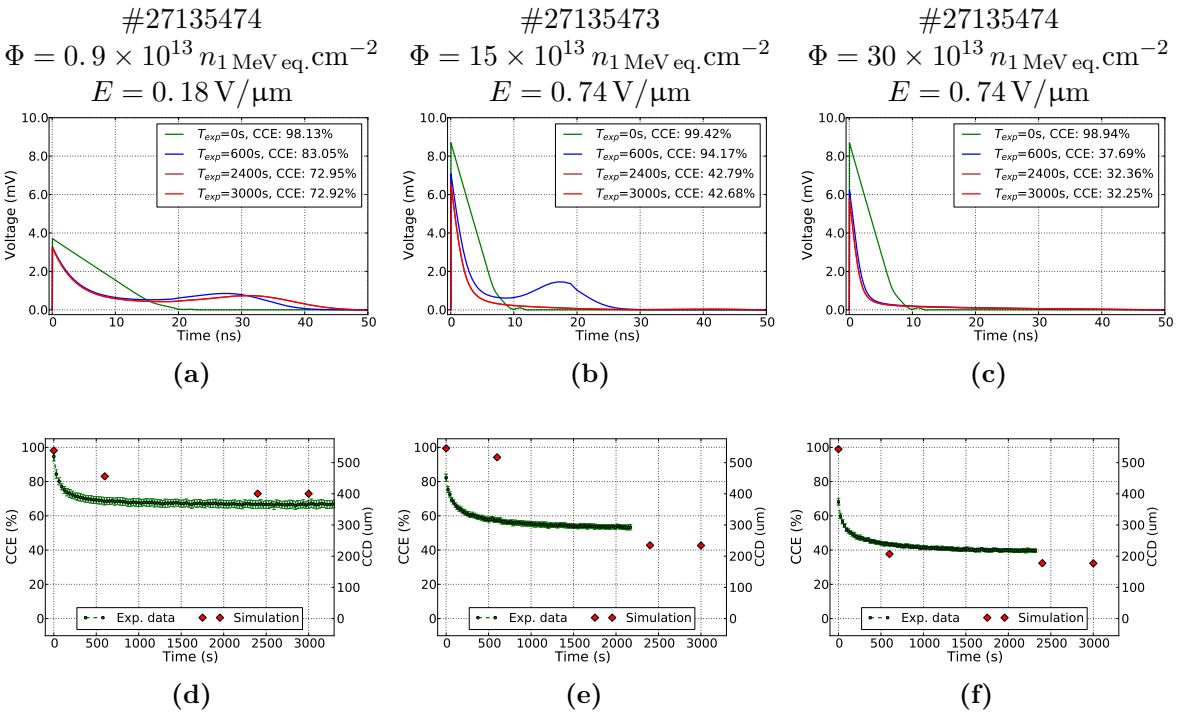

Figure 6.34: Simulation of CCE as function of radiation damage. The top row shows the simulated MIP signal as function of polarization for different radiation damage. The calculated CCE based on the integrated MIP signal is shown in the lower row.

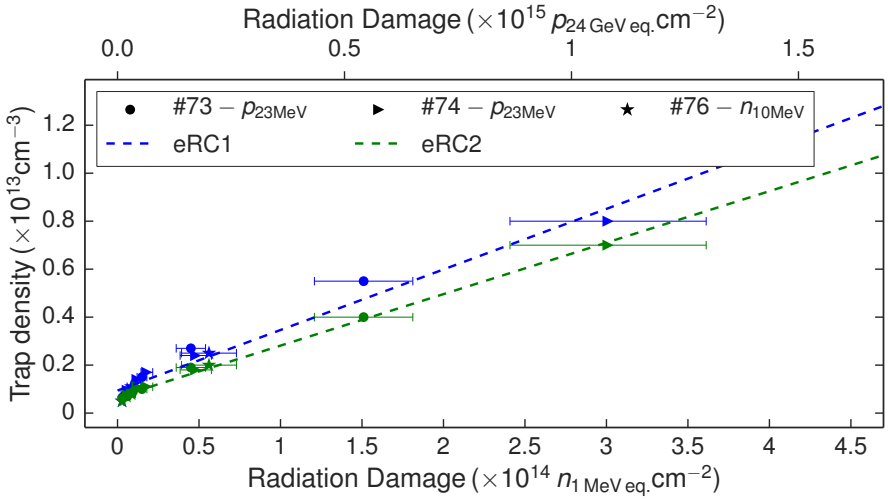

Figure 6.35: The optimized trap configuration of $eRC1$ (blue) and $eRC2$ (green) for the different irradiation damages of the proton (circle and triangle) and neutron (star) irradiated diamond sensors. The trap densities of both effective recombination centers increased linearly with the irradiation damage. The trap densities as function of radiation damage are calculated with a linear regression, see Eq. 6.38.

RD42 collaboration. In Fig. 6.36 the effective defect model is compared directly to the standard radiation model based on the RD42 measurement results. At radiation damages below an equivalent fluence of $\Phi < 2 \times 10^{15}\, p_{24\mathrm{GeV}}/\mathrm{cm}^2$ the simulated CCD is only slight reduced by $\sim 5\%$ to a charge collection distance of CCE $= 526\,\mu\mathrm{m}$. The electrical field modification, caused by the radiation damage and the diamond polarization, is for these radiation damages not strong enough to strongly influence the recombination rate, see Fig. 6.37. The recombination rate is strongly increased if the internal electrical field is reduced to $E < 0.02\,\mathrm{V}/\mu\mathrm{m}$, compare Figs 6.37b and 6.37c. For radiation damages of $\Phi < 2 \times 10^{15}\, p_{24\mathrm{GeV}}/\mathrm{cm}^2$ such a severe electrical field modification are not created and hence explain the high CCD. In real diamond sensor with a plutonia of different diamond defects such a sharp barrier for increased charge carrier recombination is not present and the effective trap model is underestimating the real recombination rate. The effective trap model represents better increased radiation damage that lead to stronger electrical field modification where the charge recombination is described correctly.

Beside the two simulation results indicated in red, the simulated charge collection distances are matiching the measurement results found by the RD42 collaboration and demonstrates the quality of the effective trap model. Based on the simulation results indicated in blue a radiation constant of $k_{eDM} = (8.9 \pm 1.1) \times 10^{-19}$ is calculated for a diamond sensors operated at an electrical field of $E = 1\,\mathrm{V}/\mu\mathrm{m}$. This radiation constant is slightly increased compared to the radiation constant of $k_{\mathrm{RD42}} = 6.5 \times 10^{-19}\,\mathrm{cm}^2\mu\mathrm{m}^{-1}$ found by the RD42 collaboration [Cri10] however is in agreement with the CCE measurement results from the irradiation campaign, compare section 6.3.4.1.

6.4.5 Simulation of the Radiation Damage of Diamond Sensors with the Dynamic Defect Model

The effective defect model describes correctly the signal degradation of diamond sensors operated at an electrical field of $E = 1\,\mathrm{V}/\mu\mathrm{m}$, see previous section. The effective defect model can now be used to calculate the signal degradation as function of radiation damage for different electrical field at which the diamond sensors are operated, see section 6.4.5.1. Furthermore, the influence of a modified particle rate environment is studied in section 6.4.5.2.

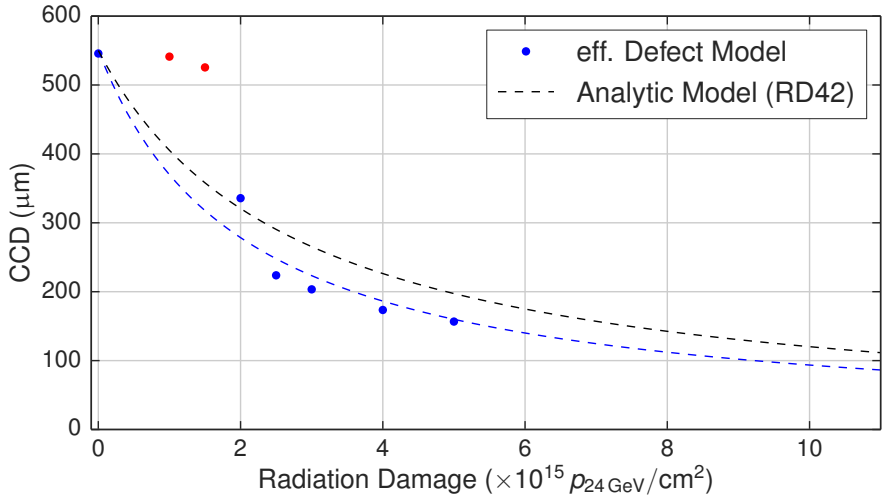

Figure 6.36: Simulated charge collection distance as function of radiation damage for a diamond sensor operated at an electrical field of $E = 1\,\mathrm{V/\mu m}$. The CCD simulation results based on the effective defect model (blue) are compared to the measurement results obtained by the RD42 collaboration indicated in black in the right plot. The two simulation results indicated in red are excluded from the calculation of the radiation constant k_{eDM} since an underestimation of the charge carrier recombination leads to an overestimated CCD value, compare Fig 6.37.

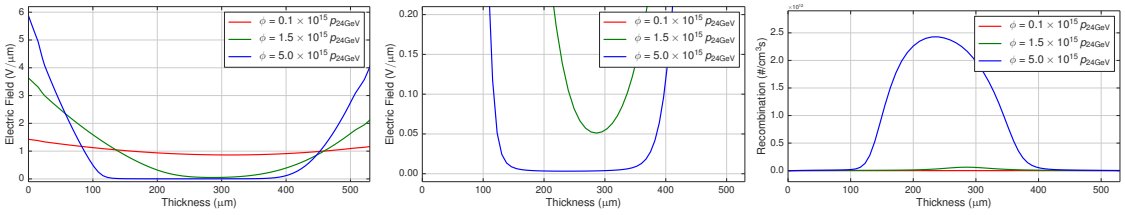

(a) Electrical field **(b)** Electrical field - zoom **(c)** Recombination rate

Figure 6.37: The radiation damage strongly modifies the internal electrical field, see left figure. For an electrical field of $E < 0.02\,\mathrm{V/\mu m}$ the recombination of charge carrier is strongly increased compare middle and right figure. Such low electrical field are not reached for a radiation damage of $\Phi = 1.5 \times 10^{15}\,p_{24\mathrm{GeV}}/\mathrm{cm}^2$ and hence explaining the rather high simulated CCD.

6.4.5.1 Simulation of Radiation Damage for Different Electrical Fields

The effective defect model is used in this section to simulate the charge collection distance as function of radiation damage for diamond sensor operated at different electrical fields. In Fig. 6.38 the simulated CCD of a diamond sensor operated at an electrical field of $E = 1\,\mathrm{V/\mu m}$ is compared to diamond sensors operated at reduced electrical fields of $E = 0.36\,\mathrm{V/\mu m}$ and $E = 0.18\,\mathrm{V/\mu m}$. The simulated CCD is strongly decreased for diamond sensors operated at lower electrical fields. At reduced electrical fields the CCD is already strongly reduced for low radiation damages ($\Phi < 2 \times 10^{15}\,p_{24\mathrm{GeV}}/\mathrm{cm}^2$). After an initially steep decrease the CCD is stabilizing on a plateau and is only slightly further decreased with increased radiation damage. The simulated CCD as function of radiation damage is fitted to the standard radiation model to calculate the radiation constant for each electrical field, listed in Table 6.8. The stabilization of the CCD for increased radiation damage above $\Phi > 2 \times 10^{15}\,p_{24\mathrm{GeV}}/\mathrm{cm}^2$ leads however to a failing of the hyperbolic parameterization. Nevertheless, the calculated radiation constant demonstrates the importance of the electrical fields at which the diamond sensors are operated. A three times reduced electric field from 1 to $0.36\,\mathrm{V/\mu m}$ leads to an increased radiation constant by a factor of ~ 4.7. Furthermore, reducing the electric field by a factor of 5 to an electric field of $E = 0.18\,\mathrm{V/\mu m}$ leads to a ~ 11.3 times increased

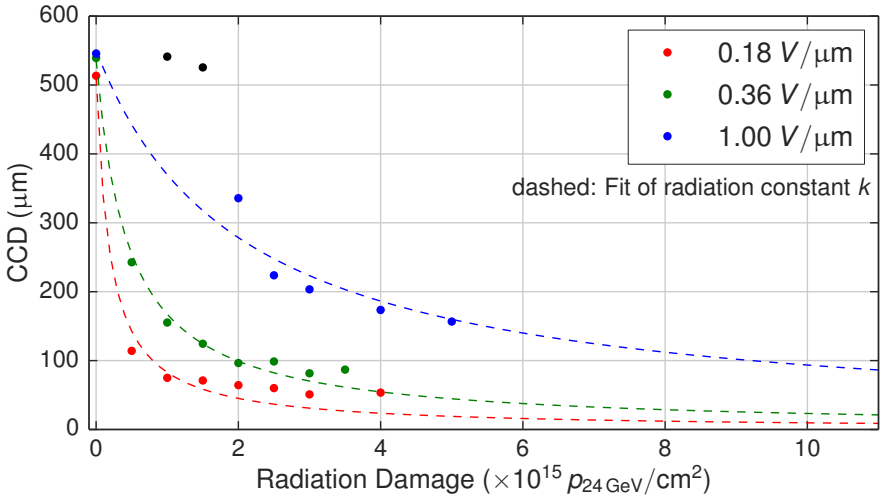

Figure 6.38: Simulation of the CCD as function of radiation damage for a diamond sensor exposed to a ^{90}Sr source. The radiation induced signal degradation was simulated for three different electrical fields at which the diamond detectors are operated: $E = 0.18\text{V}/\mu\text{m}$ in red, $E = 0.36\text{V}/\mu\text{m}$ in green and $E = 1\text{V}/\mu\text{m}$ in blue. Based on the simulated CCD as function of radiation damage, the standard radiation model was fitted to the data, indicated in dashed lines.

Table 6.8: Overview of the calculated radiation constants based on the simulation of the diamond sensor operated at different electrical fields. The diamond was simulated for a particle rate environment created by a ^{90}Sr source. A reduced electrical field at which the diamond sensor is operated leads to a strongly increased radiation constant.

Electrical field (V/µm)	Radiation constant k ($\times 10^{-19}\,\text{cm}^2\mu\text{m}^{-1}$)
RD42	6.5
1.00	8.9 ± 1.1
0.36	41.5 ± 2.6
0.18	101.0 ± 15.7

radiation constant. Hence, the diamond polarization leads to a non-linear increase in the radiation induced signal degradation as function of the electric field at which the diamond is operated.

The simulated CCD at a radiation damage of $\Phi = 2 \times 10^{15}\,p_{24\text{GeV}}$ is reduced by 71% for the sensor operated at $E = 0.36\,\text{V}/\mu\text{m}$ and reduced by 82% for the sensor operated at $E = 0.18\,\text{V}/\mu\text{m}$ compared to the diamond sensor operated at an electrical field of $E = 1\,\text{V}/\mu\text{m}$. This discrepancy in the simulated CCD is caused by the strongly modified electrical field configuration caused by the diamond polarization, shown in Fig. 6.39a. At an external electrical field of $E = 0.18\,\text{V}/\mu\text{m}$ the diamond polarization causes the absence of the internal electrical field in $d_{E<0.1\text{V}/\mu\text{m}} = 395\,\mu\text{m}$ of the diamond bulk which is $\sim 62\%$ of the total diamond thickness. This strongly modified internal electrical field is caused by the creation of the space charge towards the edges, see Fig. 6.39b and leads to a increased recombination rate of the charge carriers for the diamond areas with strongly decreased electrical fields, see Fig. 6.39c. At increased external electrical fields of $E = 0.36\,\text{V}/\mu\text{m}$ and $E = 1\,\text{V}/\mu\text{m}$ the internal electrical field is less suppressed. The absolute charge carrier recombination, calculated by the integration of the recombination rate, results in a $6.6\times$ ($E = 0.18\,\text{V}/\mu\text{m}$)

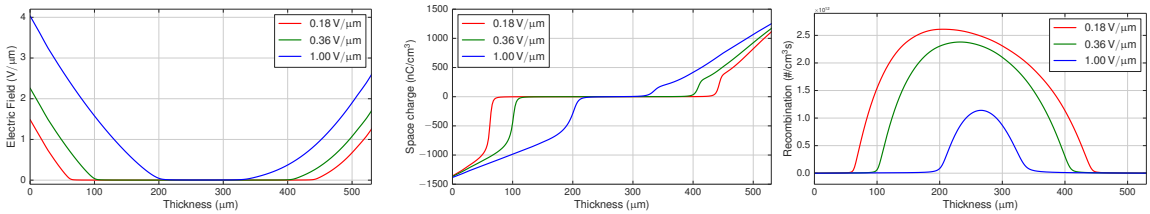

(a) Electrical field **(b)** Space charge **(c)** Normalized recombination

Figure 6.39: Simulation of the electrical field configuration, the space charge distribution and the recombination rate of a radiation damage diamond sensor with $\Phi = 2 \times 10^{15}\, p_{24\mathrm{GeV}}$ for three different external electrical fields of $E = 0.18\,\mathrm{V/\mu m}$ in red, $E = 0.36\,\mathrm{V/\mu m}$ in green and $E = 0.36\,\mathrm{V/\mu m}$ in blue.

and a $4.8\times$ ($E = 0.36\,\mathrm{V/\mu m}$) increased compared to an electrical field of $E = 1.0\,\mathrm{V/\mu m}$.

6.4.5.2 Simulation of Different Particle Rate Environments

In this section a different particle rate environment will be simulated in which the diamond sensor is operated. A ^{90}Sr particle source used in the laboratory to measure the charge collection distance of diamond sensors creates typically a MIP particle rate of $f_{^{90}Sr} = 0.15\,\mathrm{GHz/cm^3}$, compare section 6.4.3.3. The particle rates at the CMS detector are however 10 to 100 times increased depending on the exact detector location. For the BCML1 detector location a MIP particle rate of $f_{\mathrm{BCML1}} = 2.04\,\mathrm{GHz/cm^3}$ and for the BCML2 detector location a MIP particle rate of $f_{\mathrm{BCML2}} = 20.40\,\mathrm{GHz/cm^3}$ is extrapolated. The charge collection distance as function of radiation damage is simulated for a diamond sensor operated at an electrical field of $E = 1\,\mathrm{V/\mu m}$ and compared for the different particle rate environment in Fig. 6.40. The increased particle rate environment leads to a strongly reduced charged collection distance. After an radiation damage, corresponding to a particle fluence of $\Phi = 2 \times 10^{15}\, p_{24\mathrm{GeV}}$, the charge collection distance simulated for the particle rate environment at the BCML1 locations is reduced by 53% compared to the ^{90}Sr particle rate environment. The CCD simulated for the BCML2 particle rate is even further decreased by 62.5% compared to the ^{90}Sr particle

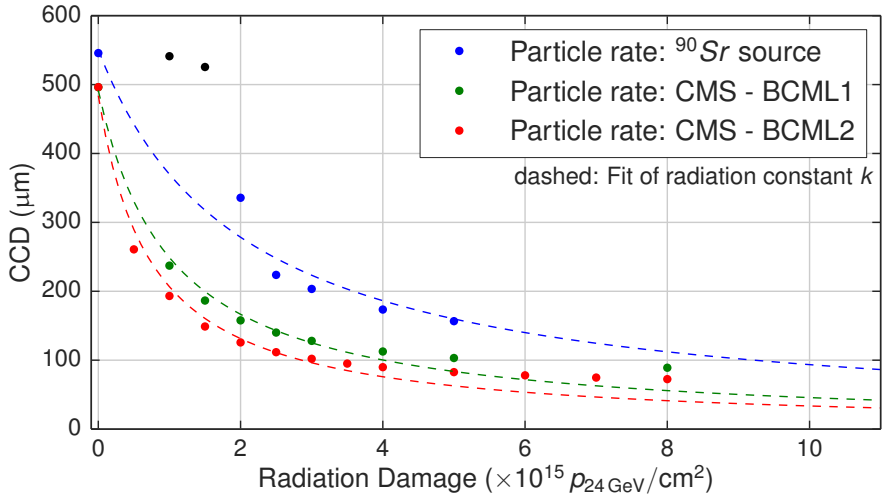

Figure 6.40: Simulation of the CCD as function of radiation damage for a diamond sensor operated at an electrical field of $E = 1\mathrm{V/\mu m}$. The radiation induced signal degradation was simulated for three different particle rate environments: a ^{90}Sr source (blue), the BCML1 (green) and BCML2 (red) sensor location at the CMS detector. Based on the simulated CCD as function of radiation damage, the standard radiation model was fitted to the data, indicated in dashed lines.

Table 6.9: Overview of the calculated radiation constants based on the diamond sensor simulation for three different particle rate environments. The diamond sensor was operated at an electrical field of $E = 1\text{V}/\mu\text{m}$. An increase in the particle rate environment leads to an increased radiation constant.

Location	MIP rate environment (GHz/cm^3)	Radiation constant k ($\times 10^{-19}\,\text{cm}^2\mu\text{m}^{-1}$)
RD42	~ 0.15	6.5
^{90}Sr source	0.15	8.9 ± 1.1
BCML1	2.04	19.8 ± 1.3
BCML2	20.40	27.7 ± 2.1

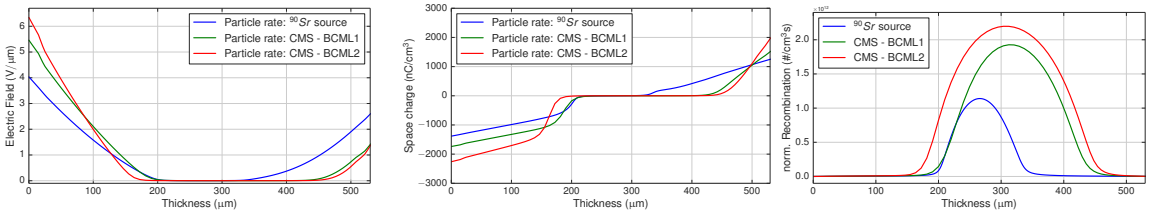

(a) Electrical field **(b)** Space charge **(c)** Normalized recombination

Figure 6.41: Simulation of a diamond sensor operated at an external electrical field of $E = 1\,\text{V}/\mu\text{m}$ for three different particle rate environments: ^{90}Sr source in blue, BCML1 and BCML2 particle rates at the CMS detector in green and red, respectively.

rate environment. The simulation results of the charge collection distance as function of radiation damage can be used to calculate the corresponding radiation constant k for each BCML detector location, see Table 6.9. Based on the effective defect model a $2.2\times$ increased radiation damage constant is calculated for the particle rate environment of the BCML1 location. At the increased particle rate environment of the BCML2 location and even stronger degradation is simulated, resulting in a $3.1\times$ increased radiation damage constant compared to the particle rate environment created by a ^{90}Sr source.

The initial radiation induced signal decrease below a radiation damage of $\Phi < 3.5 \times 10^{15}\,p_{24\text{GeV}}$ can be fitted to the standard radiation model based on a hyperbolic decrease of the CCD as function of radiation damage. For increased radiation damages of $\Phi > 4 \times 10^{15}\,p_{24\text{GeV}}$ the CCD is stabilizing on a flat plateau and the RD42 parameterization is failing. This behavior was observed as well in the parameterization of the radiation damage of the BCML detectors in Run 1 [Gut14a].

The corresponding electrical field configuration for the three different particle rate environments is shown in in Fig. 6.41a for a radiation damage of $\Phi = 2 \times 10^{15}\,p_{24\text{GeV}}$. The increased particle rate environments are leading to an increased build up of space charges towards the edges that is modifying the electrical field configuration, see Fig. 6.41b. For the particle rate environment of the ^{90}Sr source the electrical field is strongly suppressed in about $d_{E<0.1\text{V}/\mu\text{m}} = 163\,\mu\text{m}$ of the diamond bulk. For the increased particle rate corresponding to the BCML1 and BCML2 detector location at the CMS detector the electrical field is suppressed in an even further increased area of $d_{E<0.1\text{V}/\mu\text{m}} = 269\,\mu\text{m}$ and $d_{E<0.1\text{V}/\mu\text{m}} = 299\,\mu\text{m}$, respectively. This severe modification of the electrical field configuration leads to an increased charge carrier recombination, $2.8\times$ and $3.9\times$ increased for the BCML1 and BCML2 detector location compared to the particle rate environment created by a ^{90}Sr source, see Fig. 6.41c.

6.4.5.3 Comparison between Simulated and Measured BCML Detector Signal Degradation

In this last section the simulated BCML detector signal degradation based on the effective defect model is compared to the experimental measurements. The simulated charge collection distance for the increased particle rate is indicated in Fig. 6.42 in blue dashed lines. The increased particle rate environment leads to a strongly reduced charged collection distance. After a radiation damage, corresponding to a particle fluence of $\Phi = 10 \times 10^{14}\, p_{24\mathrm{GeV}}/\mathrm{cm}^2$, the charge collection distance simulated for the particle rate environment at the BCML location is reduced by 53% compared to the ^{90}Sr particle rate environment. Based on these simulation results a three times increased radiation constant of $k_{\mathrm{sim.}} = 27.7 \times 10^{-19}\,\mathrm{cm}^2\mu\mathrm{m}^{-1}$ is calculated, see sec. 6.4.5.2. This radiation constant is now directly compared to the radiation constant measured with the BCML pCVD diamond sensors at the CMS detector (indicated in solid blue). This can be done, since the radiation constant is independent of the diamond material (sCVD or pCVD) used to measure the radiation induced signal degradation [Tri08]. The different diamond material is only reflected in a different initial charge collection distance value, compare sec. 5.1. Hence the experimentally measured radiation constants for the BCML pCVD diamond detector is used to calculate an equivalent charge collection distance of a sCVD diamond detector.

The calculated radiation constant based on the BCML detector degradation of $k_{\mathrm{meas.}} = 56.0 \times 10^{-19}\,\mathrm{cm}^2\mu\mathrm{m}^{-1}$ is still by a factor of two higher than the simulation result, see Table 6.10. This discrepancy can be caused e.g. by an underestimation of the radiation damage, which is based on a FLUKA simulation. Furthermore, the BCML sensors are exposed to a mixed particle field that could contribute to non linear degradation effects of the sensors.

With the dynamic effective trap model presented in this section the radiation induced signal degradation of diamond sensors can be understood. Furthermore the effective trap model can be used to calculate the detector efficiency of the diamond sensors with respect to the radiation damage, the electrical field at which the sensor is operated and with respect to the

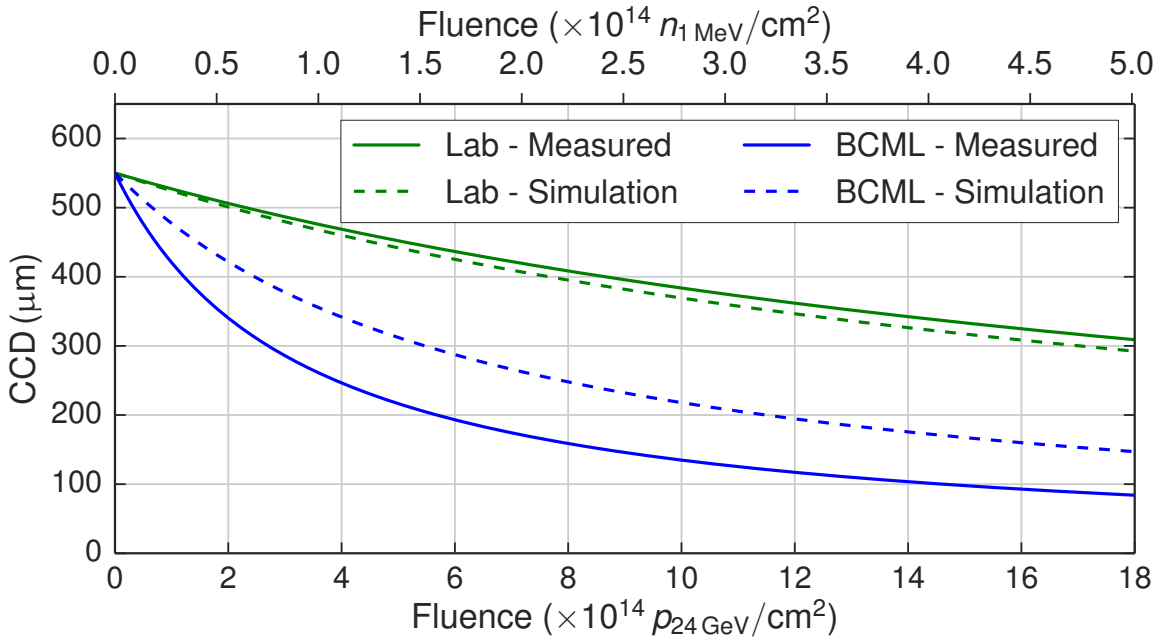

Figure 6.42: Fits of the measured (solid) and simulated (dashed) CCD as function of fluence for an electrical field of $E = 1.0\,\mathrm{V}/\mu\mathrm{m}$ for the laboratory (green) and the BCML (blue) particle rate environment. The data points on which the fits are based rely on the measured and simulated radiation constants k listed in the Tables 5.4 and 6.9 [Kas17].

Table 6.10: Overview of the measured and simulated radiation constants of diamond sensors for different particle rate environments. The diamond sensors were operated at an electrical field of $E = 1.0\,\mathrm{V/\mu m}$.

Particle rate environment	$k_{\mathrm{meas.}}$ ($\times 10^{-19}\,\mathrm{cm}^2/\mu\mathrm{m}$)	$k_{\mathrm{sim.}}$ ($\times 10^{-19}\,\mathrm{cm}^2/\mu\mathrm{m}$)
^{90}Sr	8.2 ± 0.5	8.9 ± 1.1
BCML	56.0 ± 4.1	27.7 ± 0.2

particle rate environment in which the sensor is operated.

Chapter 7

Upgrade Studies to Improve the Radiation Hardness and the Maintainability of the BCML detector

The BCML detector is being operated since the beginning of the LHC operations in 2009 and provided active protection to the CMS tracker from potentially damaging levels of machine induced background radiation. In addition the system provided valuable experiences in the operation of diamond detectors that can be used for future improvements in terms of radiation hardness of the system. Since the first collisions at CMS a total integrated luminosity of about $70\,\mathrm{fb}^{-1}$ was collected, this will be further increased to a total integrated luminosity of $300\,\mathrm{fb}^{-1}$ within the lifetime of LHC. With the upgrade of the LHC to the 'High Luminosity LHC' an increase of the total luminosity to $3000\,\mathrm{fb}^{-1}$ is expected. Hence it's crucial to improve the BCML system in terms of detector radiation hardness and maintainability. New sensor materials with potentially increased radiation hardness are characterized in section 7.1. These new sensor materials, diamond on iridium and sapphire, were compared against conventional sensor material in a test beam, see section 7.2. In the last section 7.3 the upgraded BCML2 detector is discussed, which provides an improved maintainability of the BCML2 detector.

7.1 Improving the Radiation Hardness of the BCML Detectors

An increased performance of the BCML detectors in terms of radiation hardness can be archived by changing the way of the detector operation, e.g. applying an increased bias voltage, or by using new sensor materials. In the following sections two new sensor materials, Diamond on Iridium in section 7.1.1 and Sapphire in section 7.1.2, are discussed for the potential future use in the BCML detector.

The sensor characterization will include the measurement of the signal stability over an extended period of time for different bias voltages, and the measurement of the leakage current as function of bias voltage. These techniques are briefly introduced in the following.

Signal stability measurements
The signal stability over an extended period of time is an important characteristic of the BCML sensors. The occurrence of erratic currents is a known feature for pCVD diamond sensors, see section 4.5.2. However such erratic currents have also been measured with the

sCVD diamond based BCM1F detector resulting in a reduced bias voltage at a reduced charge collection efficiency.

The signal stability of a sensor is measured over an extended period of time (1 hour) at different bias voltages. A ^{90}Sr source is inducing a constant β particle flux that creates a stable signal current. The diamond detector tends to an erratic behavior spontaneously after being operated at a given bias voltage for a particular amount of time. In order to keep the measurements for different bias voltages consistent, the voltage is ramped down to a bias voltage of HV = 0 V after each measurement step for a duration of 10 min.

Leakage current measurements
The leakage current of a sensor is an indicator for its quality. An increased leakage current can be caused e.g. by boron impurities in diamond and hence directly reduce the CCD of the particular sensor. The leakage current is measured over a duration of 60 s at different bias voltage steps. In the scope of the qualification of the BCML sensors the leakage current was measured in 100 V steps within the range of HV = ±1000 V.

7.1.1 Characterization of a Diamond on Iridium Sensor

An alternative to the conventional homoepitaxial growth of sCVD diamonds is the heteroepitaxial CVD diamond growth, see section 3.3.2.3. The diamonds produced with the heteroepitaxial technique are called Diamond on Iridium (DOI), since the most upper substrate layer is iridium. The DOI features the same homogeneity as single crystalline diamond and can be grown in wafer size, like poly crystalline diamond. Therefore it is possible to produces DOI sizes of up to $25 \times 25\,\mathrm{mm}^2$, whereas sCVD diamonds are typically limited to $5 \times 5\,\mathrm{mm}^2$, see section 3.3.2.2.

For the most recent DOI sensors produced by the University of Augsburg a charge collection distance of CCD $\sim$ 400µm was measured, which is already twice as much as a conventional pCVD diamond sensor. A conventional BCML pCVD diamond could therefore be replace by a DOI detector, with just half of its thickness to create the same signal current. The possibility to grow DOI sensors on waver size reduces the price per sensor and makes DOI detector geometries with an increased surface possible. Already today DOI detectors with a surface of $20 \times 20\,\mathrm{mm}^2$ and a thickness of $d = 300\,\mu\mathrm{m}$ are available, which theoretically should create a $\sim 5\times$ increased signal compared to conventional pCVD diamond sensors. At the same time the electrical field could be increased by 60% for the thinner DOI sensor with unmodified BCML hardware. With this increased electrical field the diamond polarization should be reduced that could lead to an increased radiation hard sensors.

This section presents the measurement results obtained with a DOI sensor called 'MFAIX394', which was prepared by the University of Augsburg. The dimensions of the DOI sensor *MFAIX394* are $5 \times 5\,\mathrm{mm}^2$ with a thickness of 500 µm. In section 7.1.1.1 cross polarized pictures of the DOI sensor were taken in order to determine the amount of defects compared to a conventional sCVD diamond. The charge collection efficiency of the DOI sensor was measured using the CCE setup in DESY - Zeuthen, see section 7.1.1.2. The signal current stability for high electrical fields and the leakage current with respect to the bias voltage of the DOI sensor was measured and is discussed in section 7.1.1.4.

7.1.1.1 Cross polarized pictures

Cross polarized pictures, discussed in more detail in section 3.3.5, can be used to determine the crystal quality in terms of its lattice defect density. Lattice defects create tensions in the diamond material leading to birefringence that can be observed using the cross polarized picture technique. Fig. 7.1a shows a cross polarized picture of the DOI sensor. The linear

polarized light is transmitting both polarization filters without a noticeable intensity reduction, hence lots of lattice defects are present in the DOI bulk, rotating the linear polarized light. In comparison to the DOI sensor a cross polarized picture of a high quality sCVD diamond is shown in Fig. 7.1b, measured with the same setup. Almost no light is passing through the sCVD diamond bulk, only at the edges tensions in the lattice are visible. The cross-polarized pictures indicate a strongly increased lattice defect density of this particular DOI sensor compared to the sCVD diamond material. However only the one DOI sensor *MFAIX394* was tested, therefore no general conclusion can be obtained by this result.

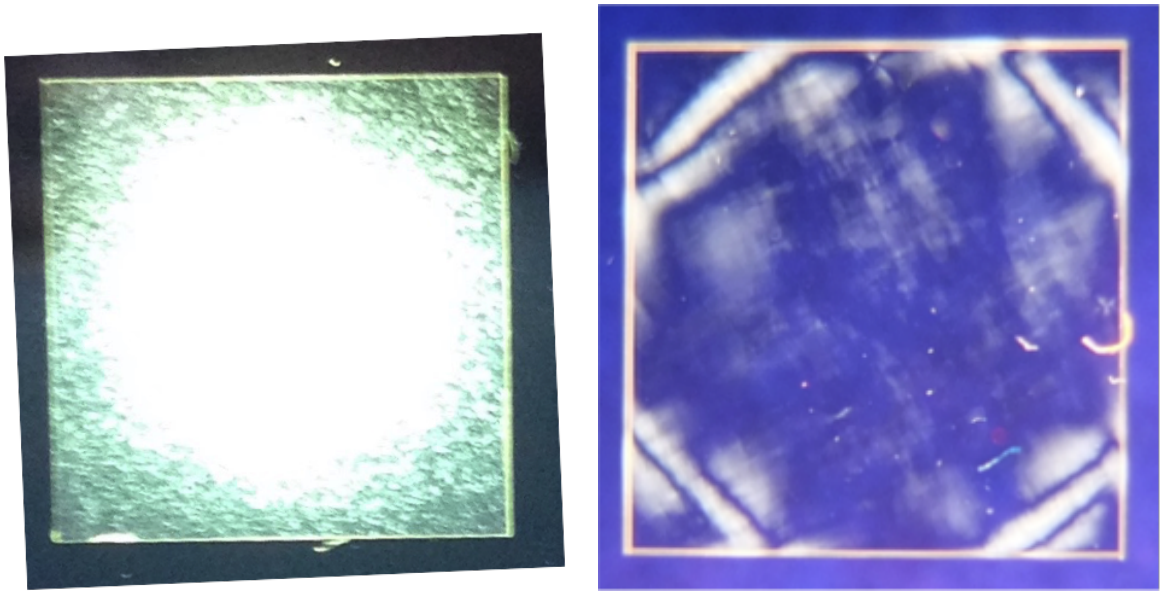

(a) Diamond on Iridium. **(b)** Single crystal CVD diamond.

Figure 7.1: Cross polarized pictures of a DOI and a sCVD sensor. The lattice defect density of the DOI sensor is strongly increased compared to the sCVD diamond sensor.

7.1.1.2 Measurement of the Charge Collection Efficiency

The quality of the DOI sensors could be continuously improved over the last 6 years, resulting in an increase in the measured charge collection efficiency. Table 7.1 summarizes the recent advances in the CCE over the last years. The highest quality DOI sensor reached a CCE for holes of 90% and for electrons of 76% [Kis15].

The charge collection efficiency of the DOI sensor *MFAIX394* was measured using the CCE setup at DESY - Zeuthen, which was introduced in section 6.1.2. The CCE measurement at this setup is based on the signal of a MIP particle and therefore measures the combined charge collection of electron and hole charge carriers. The CCE measurement result is shown in Fig. 7.2 and reaches a maximum charge collection efficiency of 70% at an electrical field of $E = 2\,\mathrm{V/\mu m}$. The CCE behaves symmetrical for both polarities, however never reaches a saturation value. An increased CCE is therefore expected for even higher electrical field. The charge collection efficiency of this DOI sensor however can't be compared to the CCE of high quality sCVD diamonds. These sensors reach a full charge collection of 100% already at low electrical fields of $E \geq 0.2\,\mathrm{V/\mu m}$, see section 6.3.4.

Fig. 7.3 shows the stability of the charge collection efficiency over an extended period of time (30 minutes). The CCE over time was measured for four different electrical fields. At the lowest electrical fields of $E = 0.2\,\mathrm{V/\mu m}$ and $E = 0.4\,\mathrm{V/\mu m}$ the CCE is slightly increasing over time. This is likely caused by the 'pumping' effect (see section 3.3.5), where charge

Table 7.1: Overview of the most recent CCE measurements of the last 6 years, taken from [Kis15]. The CCE results for electron and protons were obtained by a spectroscopic analysis of the energy deposition of an alpha particle, further details can be found in [Cas99]. The CCE result for the DOI sensor MFAIX394 was measured using the DESY-Zeuthen CCE setup, see section 6.1.2. All measurements results are obtained for an electrical field of $E = 1.5\,\mathrm{V/\mu m}$. The last listed CCE values for electron and hole carrier are calculated based on the TCT measurements of an alpha particle at an electrical field of $E = 1.2\,\mathrm{V/\mu m}$.

DOI sensor	Year	$\mathrm{CCE_{electron}}$ (%)	$\mathrm{CCE_{hole}}$ (%)
886-2	2010	18.6 ± 5.2	92.5 ± 2.1
952-1	2011	19.7 ± 42.8	79.4 ± 11.1
955-1	2012	51.2 ± 28.6	77.1 ± 13.2
962	2013	50.7 ± 10.8	87.0 ± 3.1
AIX334	2014	61.0 ± 9.0	84.5 ± 0.84
MFAIX334	2015	$76.0 \pm -$	$90.0 \pm -$
MFAIX394	2016	61.2 ± 0.6	
MFAIX394	2016	$71.8 \pm -$	$77.9 \pm -$

carriers created by the MIP particle source fill up lattice defects. These lattice defects are 'passivated' and do not trap further other charge carriers. This results in an increased mean free path length and hence in an increased CCE value. The CCE measurements over time for the higher electrical fields of $E = 0.2\,\mathrm{V/\mu m}$ and $E = 0.4\,\mathrm{V/\mu m}$ remain constant over time.

7.1.1.3 Electrical field measurements with the TCT Technique

The TCT measurement setup introduced in section 6.1.1 was used to measure the charge carrier drift through the DOI bulk for two different bias voltages of HV = 400 V and HV = 600 V equivalent to an electrical field of $E = 0.8\,\mathrm{V/\mu m}$ and $E = 1.2\,\mathrm{V/\mu m}$, respectively. Previous

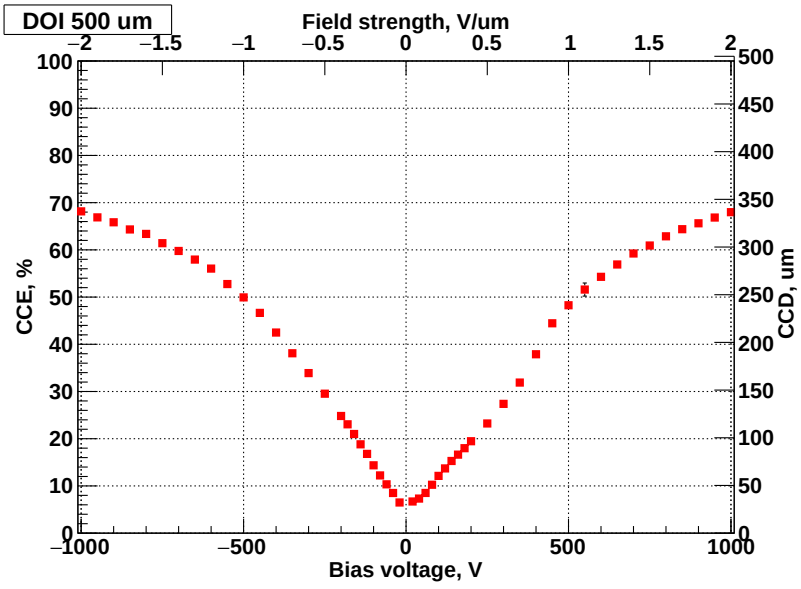

Figure 7.2: CCE measurement of the DOI sensor *MFAIX394* as function of bias voltage.

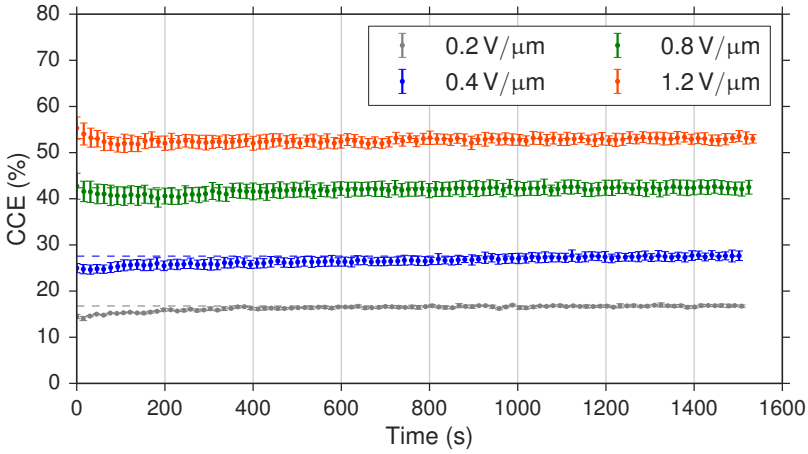

Figure 7.3: CCE measurement over an extended period of time. The CCE of the DOI sensor *MFAIX394* is measured for different electrical fields. The mean CCE value of the last 400 s of the measurement is indicated in dashed lines.

CCE measurements with DOI sensors, listed in Table 7.1, indicated a strong influence of the DOI sensor CCE to priming [Kis15]. The DOI sample was therefore exposed for 12 hours to a ^{90}Sr β particle source prior to the TCT measurements in order to prime the DOI sensor. The TCT pulses were measured over an extended period of time (T_{exp} = 8 hours) to study potential slow polarization effects. The TCT measurement results for both charge carrier are shown in Fig. 7.4 at an electrical field of $E = 0.8\,\mathrm{V/\mu m}$. Based on the long exposure of the DOI sensor to the ^{90}Sr source a passivization of most of the defects is expected that would result in a rectangular TCT pulse shape for a constant electrical field. The TCT pulse of both charge carrier has however a triangular shape, indicating a high charge carrier trapping rate. Furthermore, the TCT pulse of the hole charge carrier drift in Fig. 7.4a shows strong signal oscillations, caused by a very intense initial signal current. This strong initial signal current indicates a initially strong acceleration of the charge carriers due to a strongly modified electrical field. With increased exposure time to the ^{90}Sr source this affect is slightly reduced, indicating a more balanced electrical field configuration. The TCT measurements as function of T_{exp} remain constant and no destabilization of the electrical field configuration is measured.

In Fig. 7.5 the TCT measurement results of the DOI sensors for an increased electrical field of $E = 1.2\,\mathrm{V/\mu m}$ are shown. The TCT measurement results obtained for the increased electrical

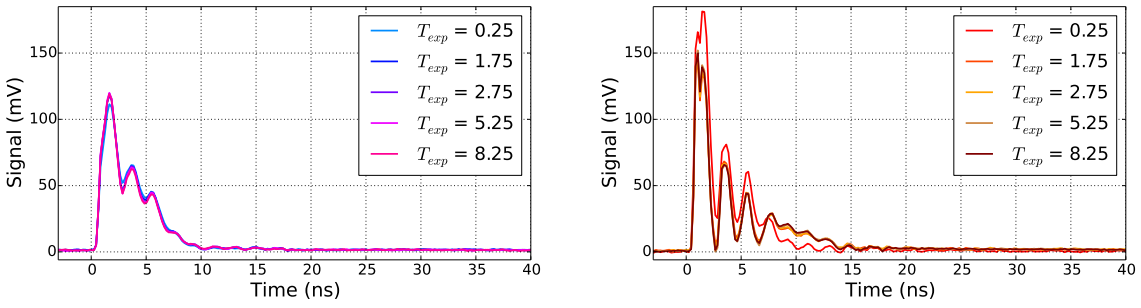

(a) DOI - hole drift.

(b) DOI - electron drift.

Figure 7.4: The TCT measurement of the DOI sensor *MFAIX394* was done at a bias voltage of HV = 400 V, equivalent to an electrical field of $E = 0.8\,\mathrm{V/\mu m}$. Prior to the measurement the DOI sensor was 'pumped' with a ^{90}Sr source for 8 hours. Even after the extensive pumping of the DOI sensors the TCT signal is reduced as function of drift time indicating a high tapping rate.

field confirm the measurement results obtained for an electrical field of $E = 0.8\,\mathrm{V/\mu m}$.

Based on the TCT measurements a charge collection efficiency can be calculated by integrating the entire measured charge $Q_{\mathrm{meas.}}$ and comparing this to the theoretical induced electric charge $Q_{\mathrm{ind.}} = E_{\alpha}/E_{\mathrm{Ion.}}$ by the alpha particle via:

$$\mathrm{CCE}_{\alpha} = \mathrm{Q}_{\mathrm{meas.}}/\mathrm{Q}_{\mathrm{ind.}}, \tag{7.1}$$

with $E_{\alpha} = 4.724\,\mathrm{MeV}$ as deposited energy by the α particle and $E_{\mathrm{Ion.}} = 13\,\mathrm{eV}$ as ionization energy. At an electrical field of $E = 0.8\,\mathrm{V/\mu m}$ a charge collection efficiency of 65.6% and 64.1% for holes and electrons is measured. For the increased electrical field of $E = 1.2\,\mathrm{V/\mu m}$ an increased CCE of 77.9% and 71.8% for holes and electrons is measured, listed as well in Table 7.1.

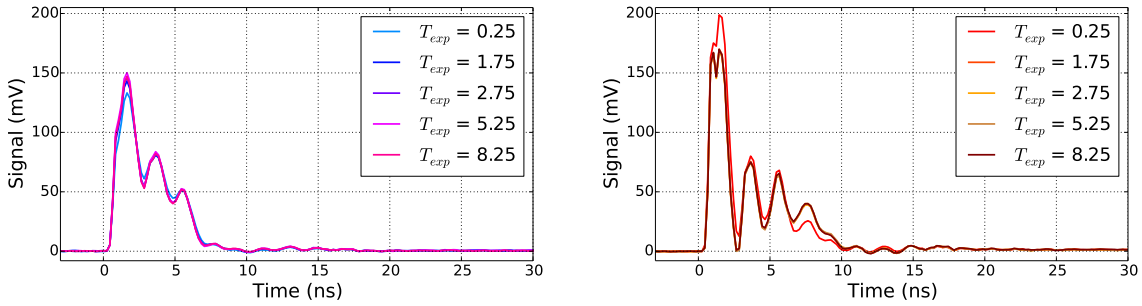

(a) DOI - hole drift.

(b) DOI - electron drift.

Figure 7.5: TCT measurement of the DOI sensor at an electrical field of $E = 1.2\,\mathrm{V/\mu m}$. The measurement results for both charge carrier drifts are comparable to the measurement results obtained at a reduced electrical field of $E = 0.8\,\mathrm{V/\mu m}$.

7.1.1.4 Stability test

On of the most important diamond properties tested during the characterization of the DOI sensor is the signal current stability for high bias voltages. The signal stability problems, manifesting as erratic currents for the BCML2 sensors see section 4.5.2, resulted in reduced operating bias voltages. At lower bias voltages and hence at lower electrical fields the polarization field has an increased impact that leads to the severe signal reduction measured with the BCML2 detectors, see chapter 5. The signal current stability of the DOI sensor was measured by exposing the diamond to an ^{90}Sr source and applying different bias voltages. Figure 7.6 shows the signal current of the DOI sensor at the bias voltages of 200 V, 500 V and 1000 V for both polarities over an extended period of time. For the highest bias voltages of $\pm 1000\,\mathrm{V}$ a slight instability of the signal current for the negative polarity can be seen. An increased bias voltage leads to an increased signal current, which is the result of an unsaturated CCE for bias voltages below $\mathrm{HV} \leq 1000\,\mathrm{V}$, see section 7.1.1.2.

The leakage current with respect to the applied bias voltage is shown in Fig.7.7. The leakage current of the DOI sensor is comparable or even better than the leakage current level of a high quality single crystalline diamond.

7.1.1.5 Conclusion of DOI sensor characterization

The DOI sensor provided by the University of Augsburg is a very promising future sensor material for the BCML detector. The signal stability at high electrical field up to $E = 2.0\,\mathrm{V/\mu m}$ could be the key property of this sensor material to overcome the diamond polarization that is otherwise reducing severely the sensor performance in terms of radiation hardness. The

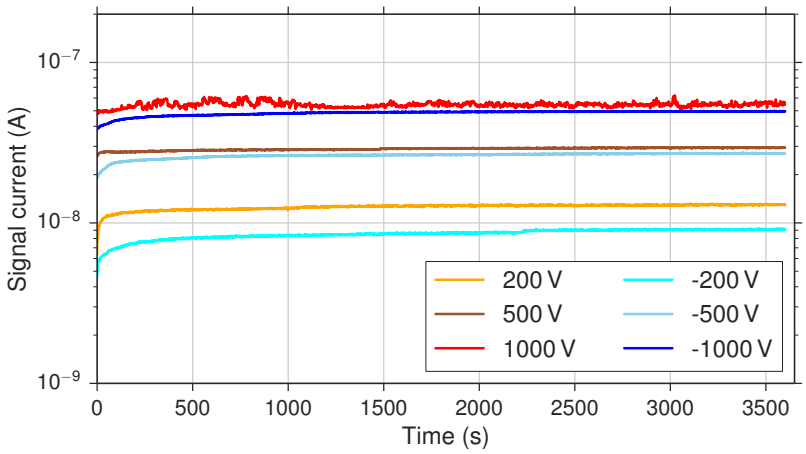

Figure 7.6: Signal current measurements over time for three different bias voltages of 200 V, 500 V and 1000 V for both polarities.

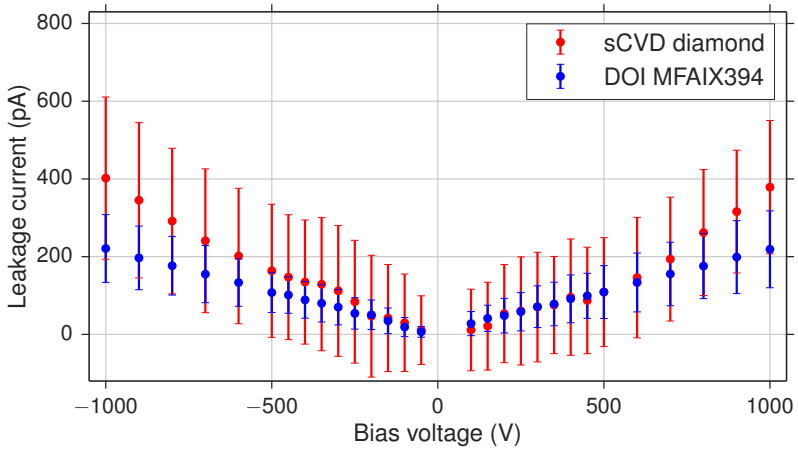

Figure 7.7: Leakage current measurement with respect to the bias voltage. The leakage current measured for the DOI sensor is shown in blue. The measured leakage currents are comparable to the results of a single crystalline diamond (27135475), shown in red.

additional possibility to produce larger sensor sizes of $20 \times 20\,\mathrm{mm}^2$ at reduced sensor thicknesses boosts the possibility of building very radiation hard diamond sensors. The rather low charge collection efficiency of CCE $\sim$ 70% has still room for improvements.

7.1.2 Sapphire detectors

Another promising sensor material in terms of radiation hardness are sapphire based detectors [Sch10], see section 3.2.3. Optical grade single crystal sapphire produced industrially via the Czochralski process is used e.g. for shatter resistant windows or used as display windows for smartphones. Hence sapphire is available at high volume, low cost and in any size. The charge collection efficiency of sapphire reaches up to CCE $\sim$ 10% at an electrical field of $E = 2\,\mathrm{V}/\mu\mathrm{m}$ [Kar15], see Fig. 7.8. This is rather low compared to pCVD diamond sensors with a mean charge collection efficiency of 50%. The reduced CCE of sapphire can however be compensated by the low cost of the material and therefore by increasing the active sensor volume. A high capacitance due to an increased sensor volume is not a problem for the BCML detector; the noise behavior however has to be studied.

In order to test the long-term stability and radiation hardness of sapphire, a sapphire sensor was installed at the BCML2 +Z inner location. The sapphire sensor has a similar geometry

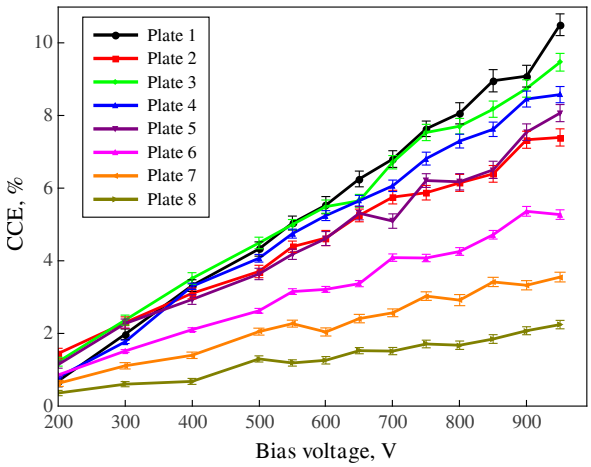

Figure 7.8: Measurement of the mean charge collection efficiency as function of bias voltage for 8 different sapphire samples. Figure taken from [Kar15].

like the BCML2 pCVD diamonds, with a surface of $10\times10\,\mathrm{mm}^2$ and a thickness of $d = 500\,\mu\mathrm{m}$. The sapphire sensor was operated at the BCML2 hardware limit of $\mathrm{HV} = 500\,\mathrm{V}$, equivalent to an electrical field of $E = 1\,\mathrm{V}/\mu\mathrm{m}$. The extrapolated sapphire signal to nominal luminosity during the entire Run 2 is shown in Fig. 7.9. The sapphire signal is 35 times lower compared to the BCML2 pCVD diamond signal ($\mathrm{HV} = 200\,\mathrm{V}$) at the same location. Based on the initial CCE of the BCML2 diamonds of $\mathrm{CCE}_{\mathrm{BCML2}} = 25\%$ in Run 2 (compare section 5.3.2.2) the charge collection efficiency of the sapphire is $\mathrm{CCE}_{\mathrm{Sapphire}} = 1.2\%$ taking to account the reduced charge carrier creation of 22 electron hole pair per µm of sensor thickness for sapphire. The estimated sapphire CCE based on the measurements at the BCML2 location is lower than the expected $\mathrm{CCE}_{\mathrm{Sapphire,lit.}} \sim 2.9\%$ at an electrical field of $E = 1\,\mathrm{V}/\mu\mathrm{m}$ [Kar15]. The CCE of the sapphire sensor can however be improved by applying an increased bias voltage. At the BCML1 location a maximum operating voltage of $\mathrm{HV} = 1000\,\mathrm{V}$ is possible that should result in a CCE value of $\mathrm{CCE}_{\mathrm{Sapphire}} > 2.0\%$.

Beside the absolute detector efficiency the signal stability of the sapphire sensor with increased

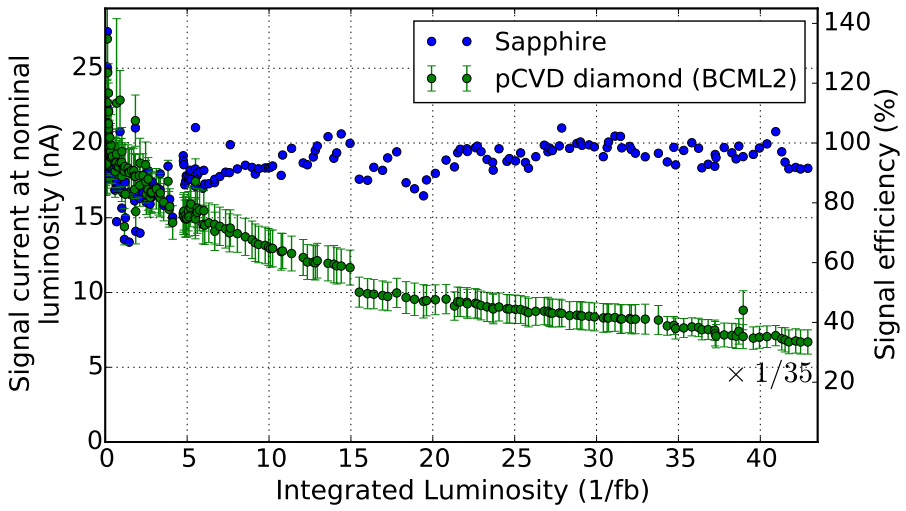

Figure 7.9: Sapphire signal during Run 2. The sapphire detector, which was operated at a bias voltage of 500 V, remained stable throughout the entire Run 2 and didn't show any radiation induced signal degradation. The sapphire signal is 35 times lower compared to the BCML2 pCVD diamond signal (200 V) at the same location. This translates to a sapphire CCE of $\sim 1.2\%$.

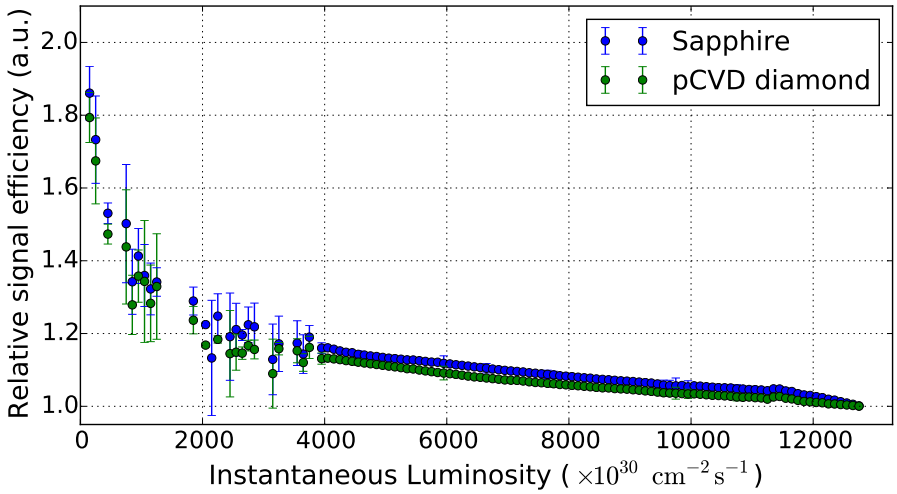

Figure 7.10: Rate dependency of the sapphire signal. The normalized sapphire signal efficiency plotted as function of instantaneous luminosity in blue. The sapphire signal is normalized to the maximum instantaneous luminosity during Fill 5277 of $1.3 \times 10^{34}\,\mathrm{cm}^{-2}\mathrm{s}^{-1}$. The rate dependency of a pCVD diamond installed at the same BCML2 location is shown in green for comparison.

radiation damage can be seen in Fig. 7.9. For a better comparison of the very stable sapphire signal, the BCML2 detector signal (scaled down by a factor of 35) is plotted in green. While the BCML2 detector signal is decreased by almost 60% due to radiation damage, the sapphire sensors remains constant.

In Fig. 7.10 the sapphire signal is normalized to the highest instantaneous luminosity of ($\mathcal{L}_{\mathrm{inst.}} = 1.3 \times 10^{34}\,\mathrm{cm}^{-2}\mathrm{s}^{-1}$) at the beginning of the fill. The normalized sapphire signal is plotted with respect to the instantaneous luminosity and compared to the normalized signal of a pCVD diamonds. For a perfect detector with a linear response to the instantaneous luminosity a constant normalized signal at 1.0 is expected. Both detectors, operated at a bias voltage of $\mathrm{HV} = 500\,\mathrm{V}$ ($E = 1\,\mathrm{V}/\mu\mathrm{m}$), are more efficient for lower rates likely due to rate dependent polarization, see section 5.5. The rate dependency of the two sensor materials is comparable.

The sapphire material is very promising, due to its relative radiation hardness and its cost efficiency. The very low charge collection efficiency can be improved by using higher electrical fields, either achieved by thinner sensors or by higher bias voltages. In addition sapphire sensors can be build as module units, where several sapphire sensors are operated in parallel. A further improvement of the active detector volume can be achieved by increasing the sensor surface from $10 \times 10\,\mathrm{mm}^2$ to $25 \times 25\,\mathrm{mm}^2$. This point will be discussed in more detail in section 7.3, where the next generation of the BCML2 detector hardware will be presented.

7.2 Test Beam with both Prototype Sensors at the Proton Sychroton (PS)

The two sensor materials have been tested at the CERN proton synchrotron (PS) [CER16a]. The main goal of this test beam was the qualification of the prototype sensors in terms of signal stability over extended exposure times to the high energetic ionizing particle bunches. The signal stability was furthermore tested for different electrical field configurations.

The CERN proton sychrotron (PS) has a circumference of 628 m and accelerates protons up to energies of 25 GeV. It severs as the second circular pre-accelerator in the LHC accelerator

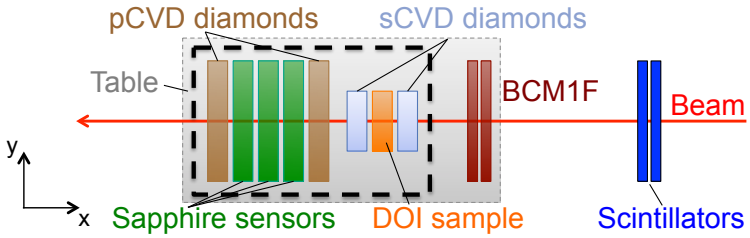

Figure 7.11: Sketch of the BRIL test beam setup. The particle beam entering the experiment area from right to left was traversing two scintillators and two BCM1F detector planes before passing through the BCML prototype sensors. The BCML and the BCM1F sensors were installed on a table, which could be adjusted in the y- and z-axis.

complex and either injects the protons into the next accelerator stage, the SPS, or it guides the protons in the test beam area where several beam lines are available for experiments. The BRIL test beam took place at the T9 beam line [CER16b], which is a secondary particle beam line. The primary protons are collided against a target and the resulting secondary particles are guided in the test area. The T9 beam line serves therefore a variety of particles such as electrons, positrons, muons, pions, kaons and (anti-)protons. The particles of this mixed hadron and electron beam have a momentum of 10 GeV. The beam was delivered uniformly in spills of 0.4 seconds, typically with two spills within 15 s. The particle amount per spill was in the order of 10^6 particles.

7.2.1 Setup and Alignment of Sensors with Respect to the Particle Beam

A schematic drawing of the BRIL beam line setup is shown in Fig. 7.11. The particle beam is entering the experiment area from the right side and is first traversing two scintillators and than passing through two BCM1F detector planes. The BCML sensors, mounted in a support structure, and the BCM1F detectors were mounted longitudinally on a table that could be moved in the z- and y-axis for better alignment to the beam center. The two scintillators, each with an active pad area of $0.5 \times 0.5\,\mathrm{mm}^2$, measured the amount of incoming particles via a coincidence unit. The BCML and BCM1F detector signals were normalized to the count rate of the scintillators to be independent from the spill-to-spill variations.

In total 8 BCML sensors were exposed to the particle beam. Each BCML sensor was mounted on a PCB, shown in Fig. 7.12a. The PCB was connected to the power supply and to the signal current read out system. All 8 BCML sensors were mounted in a support structure shown in Fig. 7.12b. The BCML support structure was installed on the movable table with respect to the location of the BCM1F detector. The signal current of the 8 BCML channel was read out in parallel with the tunnel card, see section 4.1.3.2. The 'USB readout box' was used as substitution for the DAB card readout, used at the CMS experiment. The USB box features all basic function for the tunnel card operation, further details can be found in [Gut14a].

For an optimal position of the BCML and BCM1F detectors the particle beam was scanned in the y- and z-Axis using the BCM1F detector. The results can be seen in Fig. 7.13 showing a Gaussian shaped beam profile. The measured beam width was $\sigma_y = 8.2\,\mathrm{mm}$ and $\sigma_z = 12.1\,\mathrm{mm}$ and therefore wide enough to expose uniformly the entire BCML sensors with a maximum size of $10 \times 10\,\mathrm{mm}^2$.

Raw Data Analysis

The PS accelerator provided spills with a mean duration of 0.4 s to the beam line. Typically two spills arrived within 15 s at the experiment area repeatedly every 40 s, see Fig. 7.14. The signal current was read out at a frequency of 10 Hz to measure the distribution of a single spill,

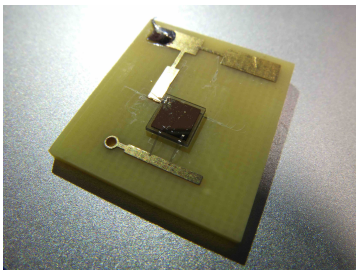

(a) PCB with a diamond sensor glued and wire bonded on.

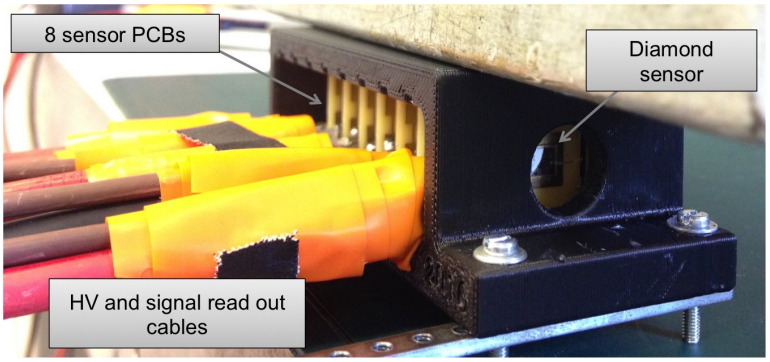

(b) BCML support structure (black) for up to 8 sensors.

Figure 7.12: Support structure for the BCML test sensors. The BCML sensors were mounted on a PCB shown in the left picture. The bottom metallization of the sensor was connected to the pad with conductive glue and the top metallization via wire bonds. All BCML sensors were mounted in a support structure shown in the right picture for better alignment to the particle beam.

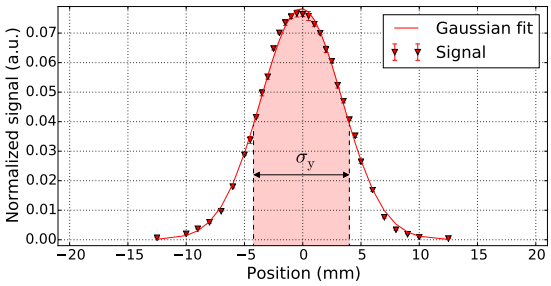

(a) Beam profile in y axis.

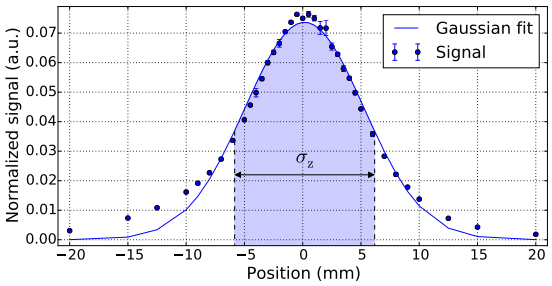

(b) Beam profile in z axis.

Figure 7.13: Measurement of the beam profile in the y- and z-axis.

see Fig. 7.14b. The duration of the spill ($t_{spill} \sim 0.4\,s$) is identical to the flat plateau at the signal maximum, since the tunnel card reads out only the maximum values of the particular running sum. The data analysis is based on running sum 8, equivalent to a signal integration time of 655 ms. The flat plateau of the BCML sensor signal was integrated after the baseline has been removed, like indicated in 7.14b between the red dashed lines, to calculate the total charge created by each spill. The calculated charge was normalized to the count rate of the scintillators in order to remove fluctuations from the spill intensity itself.

7.2.2 BCML sensors tested at this test beam

The BCML test beam was focused on the two prototype sensors, the DOI sensor *MFAIX394* and sapphire as sensor material. The DOI sensor is compared in the following to a single crystalline diamond (27135475 - see section 6.3.1) with identical size of $5\times5\,mm^2$ and thickness of 500 µm. The sapphire sensors will be compared to the performance of pCVD diamonds sensors, as well with an identical size of $10\times10\,mm^2$ and identical thickness of 500 µm. The BCML prototype sensors were both mounted between the sensors to which they are compared to, see Fig. 7.11. The sapphire sensors used in this test beam were bought by *CRYSTAL* [CRY] and were metallized at CERN with an aluminum (99%) - silicon (1%) coating. The silicon was added to improve the hardness of the coating to enable wire boding.

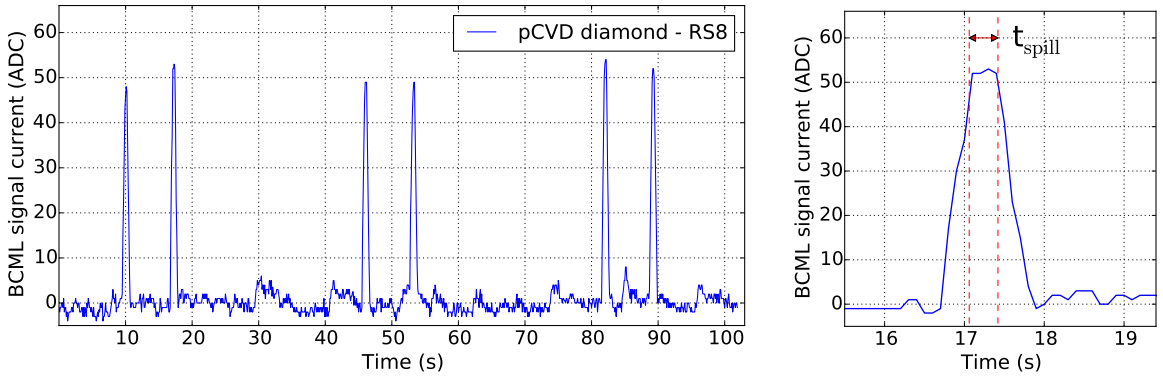

(a) PS spill distribution. **(b)** Single spill structure.

Figure 7.14: The spill structure of the PS test beam measured with a pCVD diamond sensor is shown in the left figure. The right figure shows the distribution of one spill. The charge created in each sensor was used for the data analysis, calculated by integrating the flat plateau of the signal between the two red dashed lines. The spill duration is as expected $t_{spill} \sim 0.4\,s$.

7.2.3 Signal intensity of the DOI and the Sapphire sensors with respect to the applied Bias Voltage

In this section the detector signals of the two prototype sensors were measured with respect to different bias voltages. The signal of the DOI sensor *MFAIX394* compared to the signal of a sCVD diamond for different bias voltages is shown in Fig. 7.15. For very low electrical fields, below a bias voltage of HV $< 200\,V$, the DOI sensor signal is to small to be measured. For a bias voltage of HV $= 600\,V$ the DOI signal current created by the mixed hadron and electron beam is at $\sim 70\%$ of the signal measured by the single crystalline diamond. Based on the CCE measurements done with electron particles, the DOI signal is higher than the expected $\sim 60\%$. The reason for this increased DOI detector signal could be a more effective pumping of the DOI sensor, see section 7.2.5. The DOI sensor was already operated for several days and hence exposed to a high particle flux, before the HV scan was done. Besides that, the DOI sensor was operated the entire time without being exposed to light, which was not absolutely possible for the CCE measurements done at the DESY Zeuthen setup. Photons can force the release of trapped charge carriers and therefore reduce the mean free path length, see section 3.3.5. Finally the relative large standard deviation of the signal measurements reflects the reduced precision of the signal calculation.

The sapphire sensor signal is compared to the pCVD diamond detector for different bias voltages in Fig. 7.16. The signal of the pCVD diamond sensor saturates at a bias voltage of HV $= 500\,V$ at a CCE $\sim 50\%$, whereas the sapphire signal increases linearly with increased bias voltage. The Sapphire 1 detector was behaving stable even up to a bias voltage of HV $= 2500\,V$. At this electrical field of $E = 5.0\,V/\mu m$ the sapphire signal reached 30% of the pCVD diamond signal at an electrical field of $E = 1.0\,V/\mu m$ that is equivalent to an absolute charge collection efficiency of CCE $\sim 24.5\%$. The signal of Sapphire 2 became unstable at bias voltages above HV $= 1100\,V$ and hence couldn't be tested further.

7.2.4 Signal linearity of the DOI and Sapphire sensors with respect to the applied Bias Voltage

In this section the detector linearity for different beam intensities was measured. In order to modify the particle amount per PS spill, collimator located upstream of the test area could be opened and closed. The particle amount per spill could be adjusted in a range of 15000

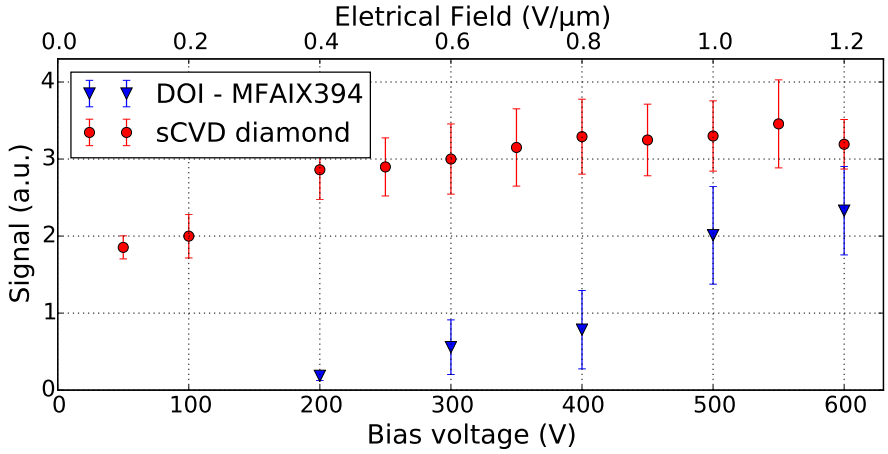

Figure 7.15: The DOI and sCVD diamond detector signals with respect to the applied bias voltage. For each bias voltage the signal was measured for 60 minutes ($\sim$ 220 spill events). The error bars indicate the standard deviation of the signal.

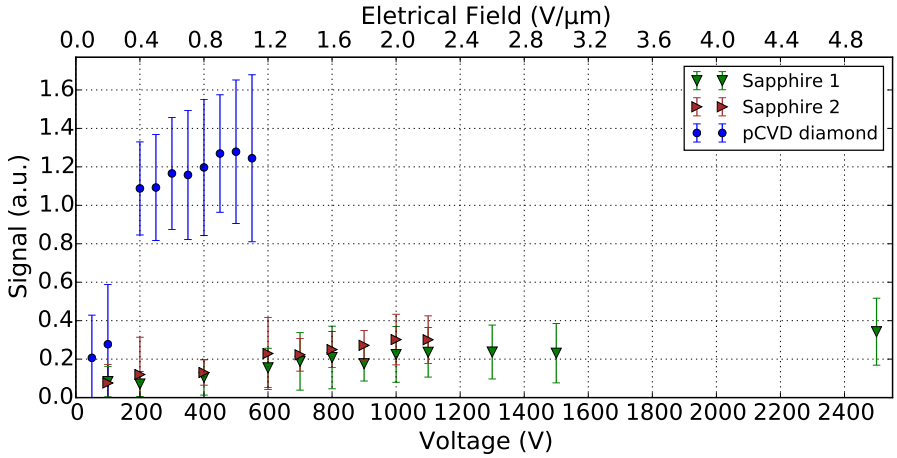

Figure 7.16: HV Scan: The sapphire and pCVD diamond signal for different bias voltages. The pCVD diamond signal is saturating at 500 V. The sapphire signals are linear increasing with the applied bias voltage. Sapphire 1 reached a signal intensity of 30% compared to the saturated pCVD diamond signal at a bias voltage of 2.5 kV.

up to 90000 particles per fill. Besides changing the absolute particle amount per fill, the particle composition was changed as well. With closed collimators an increased amount of muon particle were created.

In Fig. 7.17 and Fig. 7.18 the integrated signal current of the BCML detectors are plotted with respect to the particle flux measured by the coincidence unit of the scintillators. The DOI sensor signal is compared to the sCVD diamond signal and the sapphire sensors are compared to the pCVD diamond sensor. All BCML sensors show a good linear behavior as function of particle flux that is manifested in the low y-offset of the linear regression below $y_{\text{off}} \leq 1.7\,pC$, see Table 7.2. The integrated charge can be used to estimate the MIP particle flux per cm^2 measured by the BCML sensors, using:

$$\text{MIPs}\,(\#) = \frac{\text{Q}_{\text{meas.}}}{\text{A}_{\text{eff}}\,(\text{cm}^2) \times \text{G}_{\text{e-h pairs}}\,(\text{e}/\mu\text{m}) \times \text{CCD}\,(\mu\text{m}) \times \text{q}_{\text{e}}} \tag{7.2}$$

with A_{eff} as active detector surface, $G_{\text{e-h pairs}}$ as average charge created by a MIP particle per µm of sensor thickness (diamond 36 e/h pairs and sapphire 22 e/h pairs), CCD as charge collection distance and q_e as elementary charge. The calculated MIP particle amounts for each detector are summarized in Table 7.2. For a scintillator count of 80000 particles,

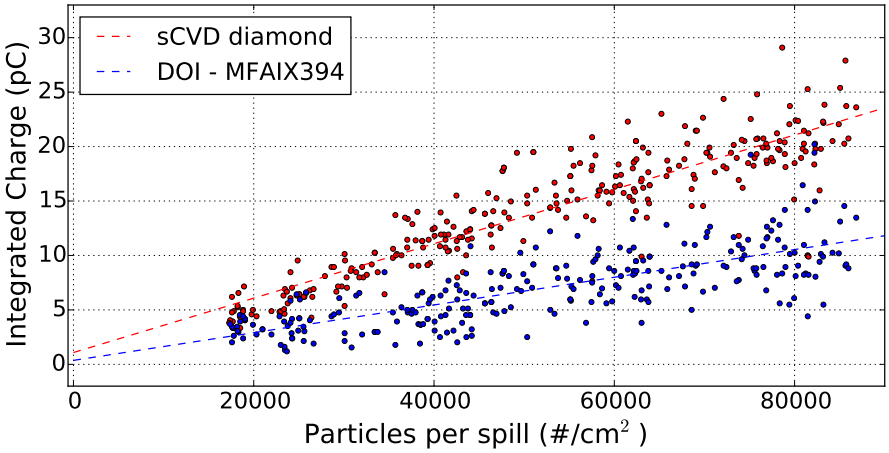

Figure 7.17: Linearity measurement of the DOI detector (blue) and the sCVD diamond (red) for different beam intensities. Both detectors were operated at a bias voltage of HV = 500 V.

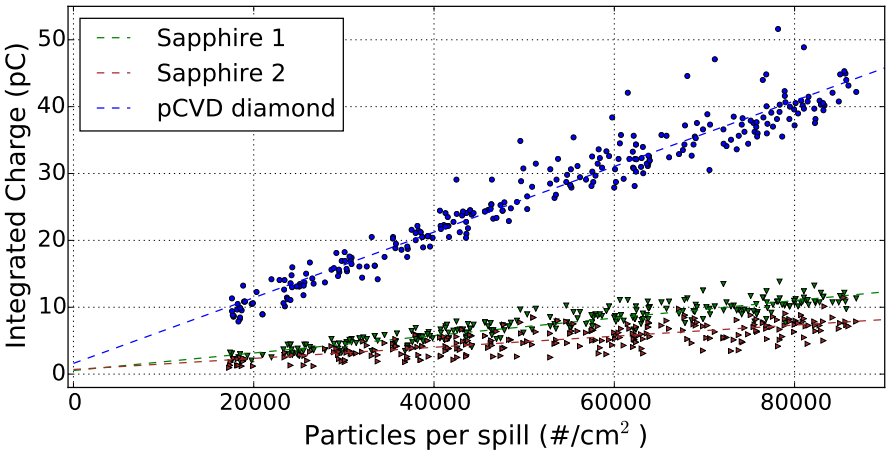

Figure 7.18: Detector linearity measurement for different beam intensities. The sapphire signals (green and brown) are compared to the pCVD diamond signal shown in blue. Sapphire 1 was operated at HV = 2500 V, Sapphire 2 at HV = 1500 V and the pCVD diamond at a bias voltage of HV = 500 V.

the calculated MIP particle amount based on all BCML sensors is $\text{MIP}_{\text{mean}} = 31000 \pm 3500\,\#/\text{cm}^2$. The mean MIP amount calculated based on the BCML sensor measurement is $\sim 60\%$ reduced compared to the scintillator measurements. This could be caused by a wrong alignment of the BCML support structure with respect to the BCM1F detector and therefore result in an operation of the BCML detector slightly off the beam center. The quadrupole magnet were set as well to an infinite focus point, to create an homogeneous particle rate for all BRIL detectors. The different location of the scintillators, located directly at the entrance of the particle beam to the experimental area, and the BCML detectors, located in the middle of the experimental area (about 10 m away from the scintillators) could cause this mismatch in the calculated particle flux. Nevertheless the MIP calculation of each BCML detector is very consistent with the mean value and hence validating the calculated charge collection efficiencies of each sensor type.

7.2.5 Signal stability over extended period of time

In this section the detector signals of the two prototype sensors were measured over an extended period of time. Figure 7.19 shows the DOI signal compared to the sCVD diamond

Table 7.2: Overview of the sensor linearity measurement results. The first column lists the y-intercepts of the linear regression to the BCML detector linearity. This low offset of $y_{\text{off}} < 1.7\,\text{pC}$ shows a good linearity of all tested BCML sensors. The MIP amount measured by the BCML sensors is calculated using Eq. 7.2 for a scintillator count of 80000 particles. The CCD values for each detector are based on the measurement results from the sections: 6.3.1,7.1.1.2 and 7.2.3

Detector	y-intercept (pC)	MIP calculation			
		$Q_{\text{meas.}}$ (pC)	CCD (µm)	$A_{\text{eff.}}$ (cm^2)	$\text{MIP}_{\text{calc.}}$ ($\frac{\#}{\text{cm}^2}$)
sCVD diamond	1.09	21.1	500	0.2	35888
DOI MFAIX394	0.37	10.6	300	0.2	30049
pCVD diamond	1.61	41.0	250	0.925	30156
Sapphire 1	0.54	11.0	100	0.925	33711
Sapphire 2	0.69	7.3	80	0.925	26846

signal over a time duration of 24 hours. The signal of the single crystal diamond, operated at a bias voltage of HV = 500 V, is very constant and no trend is visible. The signal current of the DOI sensor, operated at a bias voltage of HV = 500 V, increased by 25% over time. This is a strong indication for a slow pumping process, which is improving the mean free path of the charge carrier and resulting in an increased charge collection efficiency. The DOI sensor reached after 20 hours of operation a signal that is 35% reduced compared to the sCVD diamond signal. This leads to an absolute charge collection efficiency of the DOI sensor of CCE $\sim$ 65%, by comparing to the sCVD diamond that was operated at full charge collection efficiency.

The long-term stability of the sapphire signal compared to the pCVD diamond signal is shown in Fig. 7.20. Sapphire 1 was operated at a bias voltage of HV = 2500 V, Sapphire 2 at an bias voltage of HV = 1000 V and the pCVD diamond was operated at an bias voltage of HV = 500 V.

The signal of both sapphire sensors remained stable over the entire measurement time of 20 hours. The signal of the pCVD diamond increases by almost 18% after 19 hours of exposure to the particle beam. Similar to the DOI sensor, pumping is the most likely ex-

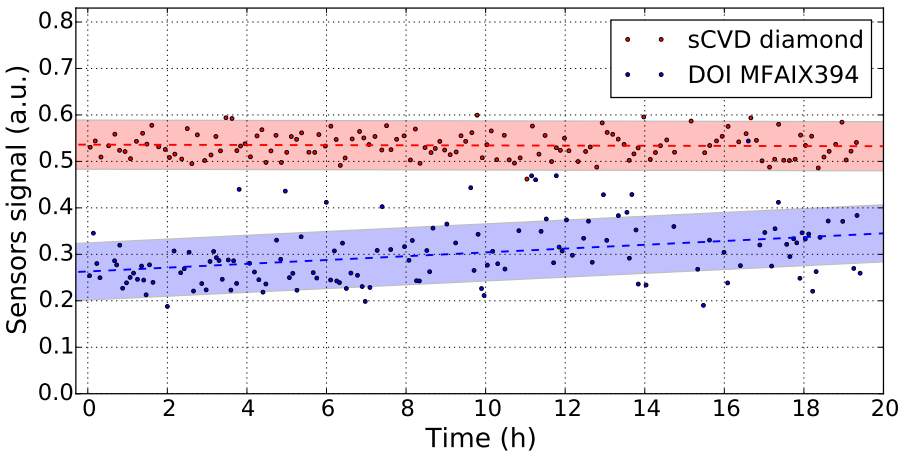

Figure 7.19: Signal stability of the DOI detector (blue) over an extended period of time. The signal stability of the sCVD diamond detector is shown in red for comparison.

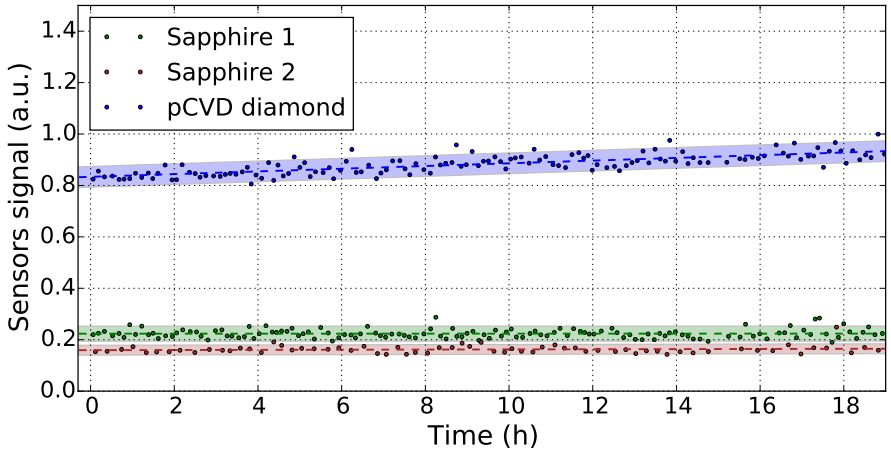

Figure 7.20: Signal stability of the sapphire sensors (green and brown) compared to the pCVD diamond sensor (blue) over an extended period of time.

planation for this signal increase. The Sapphire 1 signal reached 25% and the Sapphire 2 signal reached 20% of the pCVD diamond signal. Assuming a charge collection efficiency of CCE $\sim$ 50% for the pCVD diamond, the charge collection efficiency of the sapphire sensor reached $\mathrm{CCE}_{\mathrm{Sap\,1}} = 20.4\%$ and $\mathrm{CCE}_{\mathrm{Sap\,2}} = 16.3\%$ for a bias voltage of HV = 2500 V and HV = 1000 V that is within the expectations [Kar15].

7.2.6 Conclusion of the test beam measurements

Both prototype sensors showed promising results during the BCML test beam for the future operation at the CMS detector. The signal of the DOI sensor increased by 25% while being exposed to the particle beam and reached an absolute charge collection efficiency of CCE $\sim$ 65%. The highly intense particle rates at the BCML2 detector location (see section 5.2.1) could fully prime the DOI detector and further improve its charge collection efficiency. The high charge collection efficiency compared with the signal stability for high electrical fields, see section 7.1.1.4, is a very promising combination for future radiation hard sensors for the BCML detector.

The sapphire sensors proved its reliability already during Run 1 and showed almost no radiation induced signal degradation. The value of the sapphire sensor is further increased by the possibility to operate the sapphire detectors at electrical field up to $E = 5.0\,\mathrm{V/\mu m}$, at which a charge collection efficiency of up to CCE $\sim$ 20% is reachable. Another very compelling property of the sapphire sensor is the cost efficient availability in addition to the possibility to metallize the sensor 'in house' by a CERN department. The low CCE of sapphire can furthermore be compensated by an increased sensor volume that can be reached by increasing the detector surface and by operating several sapphire sensors planes in parallel as one integrated detector module.

7.3 Upgrade of the BCML2 Hardware Design

The BCML2 detector and its support structure were redesigned for different reasons, which are discussed in section 7.3.1. The new design of the BCML2 hardware and its new features are discussed in section 7.3.2. In the last section 7.3.3 first test measurements with the new BCML2 hardware are presented and the time line for the detector installation is discussed.

7.3.1 Motivation for Upgrading the BCML2 Hardware

The most important reason to upgrade the BCML2 hardware is the CMS Phase 1 upgrade in the Long shutdown 2 (2018), where the beam pipe at the BCML2 location will be replaced. The new beam pipe will have an increased diameter and hence the current BCML2 wheel designed can't be used anymore. Another problem of the current BCML2 design is the low maintainability. The replacement of a broken BCML2 detector forces the uninstallation of the entire BCML2 wheel. This is a very time consuming work and especially critical with respect to the LHC operation in Run 3, where strongly increased radiation levels at the BCML2 region are expected. A simple BCML2 detector design is therefore needed that allows the replacement of a damaged BCML2 sensor with minimal effort, in order to minimize the exposure time to radiation during such an intervention.

7.3.2 Design of the new BCML2 Detector Hardware

The new design of the BCML2 hardware is presented in this section. The new BCML2 hardware consists of three parts, the BCML2 Main PCB, the BCML2 sensor box and a mechanical support structure that provides as well mechanical protection.

7.3.2.1 The BCML2 Main PCB

In Fig. 7.21 the BCML2 wheel used during Run 1 and Run 2 is shown. The diamond sensors, mounted in aluminum boxes, are screwed on the BCML2 wheel structure and are connected via micro coaxial cables to a DSUB-37 connectors, which houses all HV and signal cable connections to each BCML2 diamond detector. The micro coaxial cables are connected via SMA connectors to the sensor boxes and some cables are even soldered directly to the sensors, making a quick replacement impossible. Furthermore, soldering highly irradiated material,

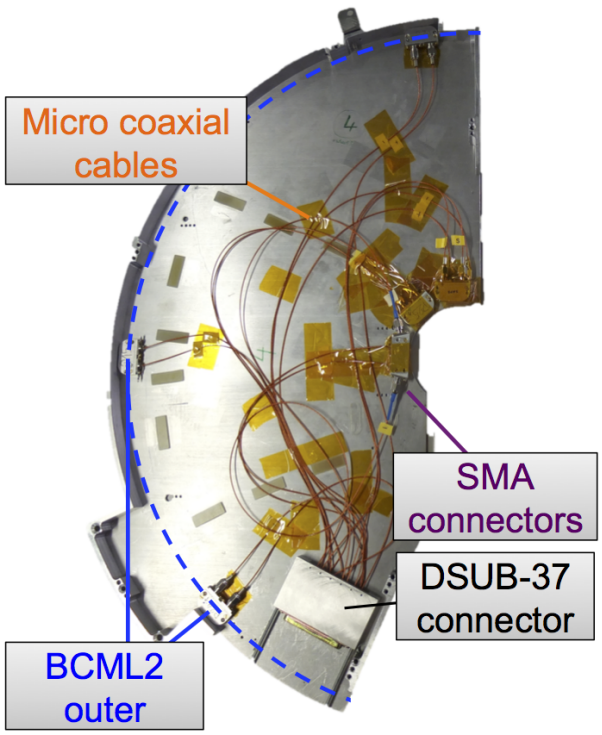

Figure 7.21: The currently used BCML2 wheel is used as support structure for the BCML2 detector modules.

can only be done with special equipment, where aspirating gases can be removed before inhaled. During Run 1 and 2 it turned out that the outer BCML2 diamond sensors are not needed, hence the new BCML2 wheel design can be smaller.

The limitations for the new BCML2 wheel design are the DSUB-37 connector, since the cable connecting the BCML2 diamond detectors to the bias voltage and to the signal read out won't be replaced and the increased beam pipe diameter of $d \sim 7\,\text{cm}$. Based on these requirements a new BCML2 support structure was designed, which is shown in Fig. 7.22. The new design of the BCML2 support structure is now changed to an entire piece of PCB. The BCML2 Main PCB features space for up to 8 BCML2 detectors, located as close as possible to the the beam pipe with increased diameter. The HV, signal and shield cable connections between the DSUB-37 connector and each sensor location are provided by the BCML2 Main PCB internally, removing the need of any cable connection. Depending if the BCML2 Main PCB is mounted right or left handed with respect to the beam pipe, the DSUB connector can be placed for each configuration to the lower side to account for the limited slack of the support cable. The PCB consists in total of 6 layers, whereas the first and the last plane are used as common shield to remove the pick up off high frequent oscillations. The overall dimensions of the BCML2 Main PCB are $270 \times 140 \times 2.4\,\text{mm}^3$. Detailed technical drawing can be found in the appendix, see section A.7.

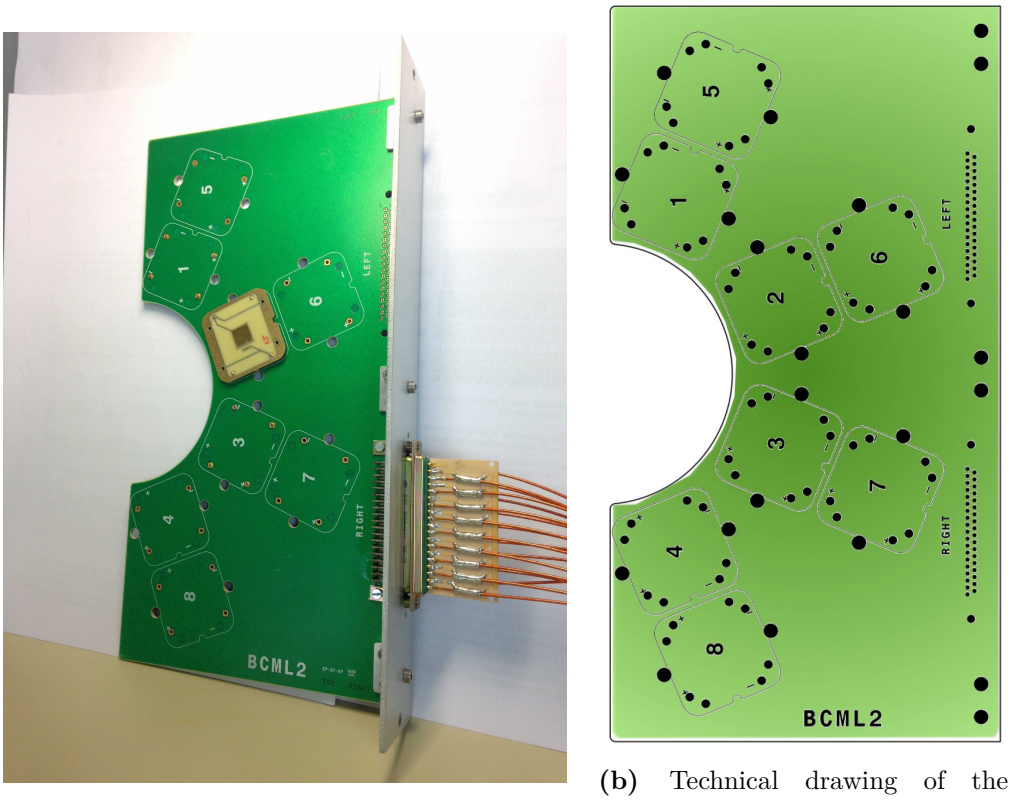

(a) BCML2 Main PCB.

(b) Technical drawing of the BCML2 Main PCB.

Figure 7.22: The new BCML2 Main PCB. The left picture shows the BCML2 Main PCB equipped with a diamond sensor, the DSUB-37 connector and a metal support plate. A technical drawing of the BCML2 Main PCB is shown in the right picture. The HV, signal and shield connections between the sensors and the DSUB-37 connector are provided internally by the PCB.

Figure 7.23: The conventional BCML2 detector housing used during Run 1 and 2.

7.3.2.2 The BCML2 Sensor Box

During Run 1 and 2 the BCML2 diamond sensors were glued in aluminum boxes, where the front and the back metallization was wire bonded to SMA connectors, see Fig. 7.23. This design was fine for the conventional diamond detectors with a maximum size of $10 \times 10\,\mathrm{mm}^2$. With regards to the potential use of new sensor material, like diamond on iridium or sapphire, the sensor housing should support as well other geometries. Additionally the possibility to stack sapphire sensors on top of each other and operate in parallel to increase the signal output would be beneficial. Avoiding in addition a SMA connector type, where the cables have to be screwed to the sensor housing, would improve the handling and reduce the time needed for a replacement of a broken BCML2 sensor.

With the new designed BCML2 sensor box, produced as well entirely as PCB, all of the mentioned goals have been achieved. The BCML2 PCB sensor box consists of a base and a top part, shown in Fig. 7.24. The base part was designed in two variation, to support either large sensor sizes of $25 \times 25\,\mathrm{mm}^2$, or as well small sensor sizes down to $5 \times 5\,\mathrm{mm}^2$. The main difference of the two configurations is the location of the bond pad with respect to the sensor. In order to mount a sensor inside the BCML2 sensor box, the bottom metallization is connected to the ground pad with conductive glue, whereas the top metallization is connected via a bond wires to the bond pad. The base and top plate of the BCML2 sensor box are connected via 4 pins, which are soldered to each plate. In total 8 pins (4 male and 4 female) serve as high voltage supply, signal read out and shield. The closed BCML2 sensor box acts as Faraday cage, since the entire surface of the sensor box is metallized. The sensor box can be connected to the BCML2 Main PCB via the 4 male pins, by just sticking them into the corresponding female pins on the BCML2 Main PCB. The 4 male and 4 female connectors are arranged in such a way that the stacking of the BCML2 sensor boxes is possible. The polarity of the electrical field at which the BCML2 sensor is operated can be changed by mounting

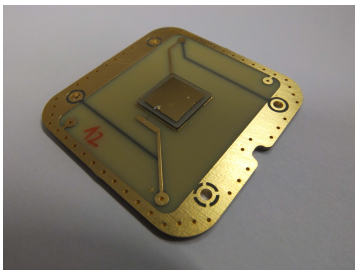

(a) Base plate $10 \times 10\,\mathrm{mm}$.

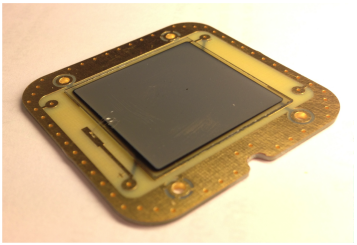

(b) Base plate $25 \times 25\,\mathrm{mm}$.

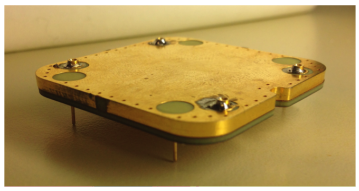

(c) Closed sensor box.

Figure 7.24: The picture on the left shows the small base plate, with a diamond sensor mounted on. The picture in the middle shows the base plate for sensors of larger geometry. The holes with the increase diameter are used for the female pins. The very thin holes located in the surrounding shielding are fully metallized. They act as electrical pillars to create a closed Faraday cage as well in the z-dimension. The picture on the right shows a closed BCML2 sensor box, where the base and top plate are soldered together via the 4 female pins. On the lower side of the picture the male pins are visible, used to connect to the BCML2 Main PCB or onto another BCML2 sensor box.

the BCML2 sensor box rotated by 180°. The total dimension of the BCML2 sensor box is $40 \times 40 \times 4.5\,\mathrm{mm}^3$. Stacking 5 BCML2 sensor boxes on top of each other would therefore result in a total height of 22.5 mm. Such a construction could be stabilized by a mechanical bridge.

7.3.2.3 The BCML2 Mechanical Support Structure

The BCML2 main PCB equipped with the BCML detectors will be installed inside a support structure, which serves as well as mechanical protection. The support structure is designed in such a way that the BCML2 main PCB can be slid into it, as shown in Fig. 7.25. A replacement of the entire BCML2 main PCB or a replacement of a single detector is therefore very simple, and can be accomplished within a few minutes. The only thing that needs to be fixed with screws is the DSUB-37 connector.

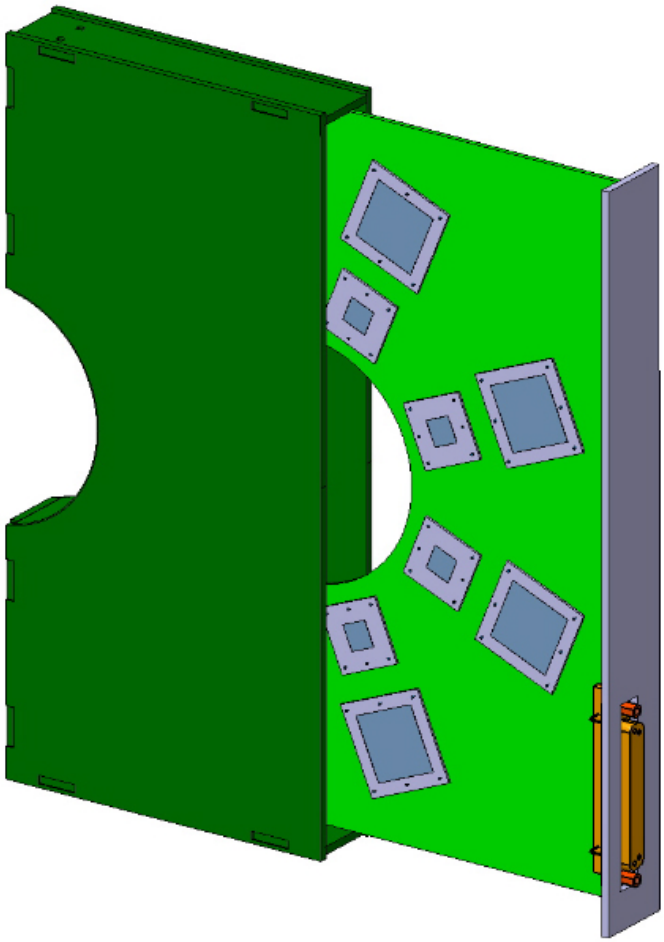

Figure 7.25: The BCML2 support structure serves as well as mechanical protection of the BCML2 detector units.

7.3.3 First test measurements and time line of installation

As a first test of the new BCML2 hardware the signal stability of a diamond sensor was measured over an extended period of time. A ^{90}Sr source was positioned over the diamond sensor to create a constant particle rate. The signal current was measured for 1 hour at three different bias voltages. These measurements are compared in Fig. 7.26 to identical measurements done with the conventional aluminum based BCML2 sensor box. The diamond sensor

behaves for both measurement setups identical and hence demonstrates the functionality of the 4 pin connection between the new BCML2 sensor box and the BCML2 main PCB, see section 7.3.2.2.

The new BCML2 hardware will be installed and fully commissioned during the Year End Technical Stop 2016/17. First beam and therefore the first measurements with the new BCML2 hardware at the CMS experiment are expected for the beginning of May in 2017. The first normal LHC operation with stable proton-proton collisions is expected to happen another 4 weeks later.

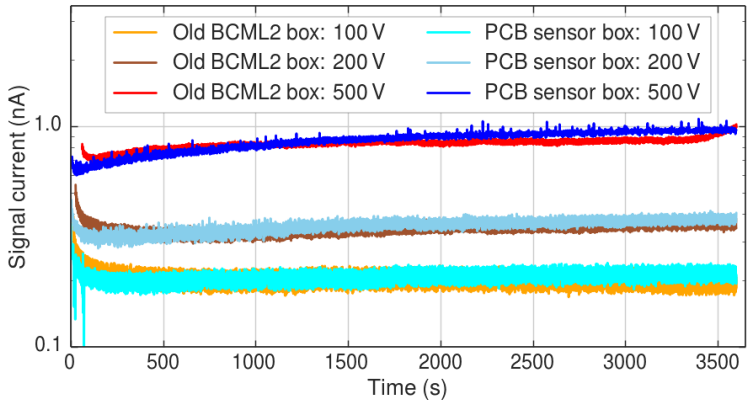

Figure 7.26: First test measurement with new BCML2 hardware. Signal current measurement over an extended period of time with the conventional BCML2 sensor box and the new PCB based sensor housing. The signal current was measured for 3 different bias voltages of HV = 100 V, 200 V and 500 V.

Chapter 8

Summary and outlook

8.1 Summary

The BCML detector was successfully operated during the entire LHC Run 2 since the beginning of 2015 and provided a safe operation of the CMS experiment. The diamond based BCML detector, surrounding the beam pipe at a radius of 5 cm, was operated in an intense particle rate environment and hence suffered radiation damage. The measured radiation damage of the BCML diamond sensors during the operation in Run 2 was a factor 8 worse than expected. Studies of the radiation induced signal degradation indicated a rate dependency of the signal efficiency.

The radiation induced signal reduction of diamond sensors and its rate dependence were extensively studied with a diamond irradiation campaign of high quality sCVD diamond sensors in combination with a dedicated simulation. Based on the optimization of the simulation to the measurement results of the irradiation campaign, an effective diamond defect model was created that describes the charge collection efficiency of the diamond sensor with respect to the radiation damage, to the particle rate environment and to the electrical field at which the detector is operated.

Beside the investigation of the radiation damage to sCVD diamond sensors, new sensor materials with potentially increased signal stabilities as function of radiation damage were studied and were partly already operated at the BCML detector during Run 2.

Operation of the BCML detector during Run 2

- The BCML detector actively protected the CMS tracker against severe radiation damage by once dumping the LHC beam. The beam loss event causing the trigger of the LHC beam dump system was measured as well by the LHC beam loss monitors located close to the CMS detector at a slightly reduced intensity. The beam loss event was caused by an 'Unidentified Falling Object'(UFO) an reached 109% of the predefined beam abort threshold that is equivalent to MIP particle flux of $\Phi = 0.972 \times 10^6\,\mathrm{MIPs/cm^2/40\,\mu m}$. Within the entire Run 2 around ~ 20 other UFO beam loss events were measured at however reduced intensities. An increased intensity of the beam loss events was measured for an increased particle beam intensity.

- During the LHC Run 2 several other beam loss events were measured, caused by different root causes. These beam loss events never reached the intensity of the beam abort threshold, and hence never threatened the CMS tracker. However, these beam loss events were very useful to study the beam loss pattern created at the CMS detector caused by different beam loss scenarios. The artificially increased beam gas pressure

allowed to study the measured beam losses from beam gas interactions created near the CMS detector.

- The beam loss events were also useful to study the BCML detector performance with respect to the beam loss duration. A reduced sensitivity of the BCML1 detector was found for short beam loss events ($t < 3\,\mathrm{ms}$). The reason for the reduced BCML1 detector sensitivity was found to be a wrongly placed decoupling capacitor, which could be repaired and the full sensitivity be restored.

- The BCML hardware was working throughout the entire Run 2 very reliably and prevented only once the injection of a physics LHC fill for about 30 minutes due to a broken CPU card. In the commissioning phase at the beginning of Run 2 the main power supply, supporting the BCML detector system with LV and HV, was working unreliably and was therefore replaced.

Study of the radiation induced signal degradation of diamond detectors with focus on the rate dependent diamond polarization

The severe radiation induced signal degradation of the BCML detector during Run 2 was studied in detail and indicated a particle rate dependent efficiency of the diamond sensors. The radiation induced signal degradation was increased by a factor eight even for the diamond sensors operated at the highest electrical fields of $E = 1.0\,\mathrm{V/\mu m}$ compared to the expected radiation damage measured in a low particle rate environment at the laboratory. The particle rate dependent efficiency of the diamond sensors is caused by a rate dependent build up of space charge in the diamond sensor resulting in a modified internal electrical field structure. This modified electrical field configuration leads to locally reduced electric fields at which the charge carrier recombination is increased, and hence reduce the charge collection efficiency of the diamond sensor. The major work presented in this thesis is a quantitative study of the radiation induced signal degradation of diamond detectors with the focus on the rate dependent polarization:

- The radiation induced signal degradation of diamond detectors was studied in detail with an irradiation campaign of high quality single crystalline diamonds, irradiated stepwise with proton or neutron particles, see chapter 6. Regularly measurements of the electrical field after each irradiation step showed an increased rate dependent build up of space charge in the diamond bulk with respect to the radiation damage. Measurements of the charge collection efficiency demonstrated that this rate dependent build up of space charge results in a reduced charge collection efficiency of the diamond sensor.

- A quantitative understanding of the radiation induced signal degradation of the diamond sensors was gained with a detailed simulation of the TCT and CCE measurements, which takes the radiation damage and trapping with an effective 2 trap model into account. The energy levels and trapping cross sections of the traps were fitted to the data obtained from the irradiation study. A linear correlation between the radiation damage and the effective defect density was found, see Fig. 6.35.

- This effective trap model describes the TCT and CCE measurement results as function of radiation damage and applied external electric field, for all diamond sensors, irradiated with neutrons or proton particles.

- The effective trap model, optimized to laboratory measurements with a ^{90}Sr source, predicts a strongly modified electrical field configuration for high rate environment, like at the CMS detector, resulting in an even further reduced CCE of the diamond sensor

and proofs the theory of the rate dependent signal reduction of radiation damaged diamond sensors.

- The measured detector degradation in the high particle rate environment at the CMS detector with $k_{\text{meas.}} = 56.0 \times 10^{-19}\,\text{cm}^2\mu\text{m}^{-1}$ is still increased compared to the simulation result using the effective defect model, see Fig. 6.42. This discrepancy is most likely caused by an underestimation of the radiation damage, which is based on a FLUKA simulation. Furthermore, the BCML sensors are exposed to a mixed particle field that could contribute to non linear degradation effects of the sensors.

- The effective defect model was used to study the signal degradation with respect to different electrical fields at which the diamond sensors were operated. A non-linear increase in the radiation induced signal degradation as function of the electric field was found, see Table 6.8.

- Using the diamond simulation the absolute electrical field modification caused by the rate dependent diamond polarization could be studied as well as the amount of space charge needed to be trapped to create such strong electrical field modifications. Furthermore, the simulation allows a detailed study of the charge carrier recombination rates causing the severe reduction in the charge collection efficiency.

- The effective diamond defect model is a powerful tool in order to design future diamond sensors and extrapolate the minimum requirements in order to operated the diamond sensors above a specific minimum charge collection efficiency.

Upgrade studies to improve the radiation hardness of future BCML sensors and the redesign of the BCML2 sensor mechanics

Two new sensor materials, Diamond on Iridium and sapphire, were studied for the potential use in the BCML detector.

- Diamond on Iridium was tested and measured extensively with TCT, CCE and test beam measurements. The measured charge collection efficiency of CCE = 61.2% doesn't reach the CCE of sCVD diamond sensors, the DOI sensor could however be operated stable at very high electrical fields that is very crucial in order to prevent diamond polarization.

- A sapphire sensor was operated for two years at the BCML2 detector location and showed almost no radiation induced signal degradation, see Fig. 7.9. The additional creation of lattice defects at the CMS detector is not severely increasing the already high initial defect concentration in the sapphire material and hence explaining the high tolerance against radiation damage. The sapphire signal current is however about 35× smaller compared to pCVD diamonds and has to be increased significantly for the operation at the LHC in 2017. This will be achieved by increasing the sensor volume and by a stacking several sapphire sensors for a parallel signal read out, see next section.

- The BCML2 front end hardware was redesigned and is now based on a PCB that provides internally all connections between the bias voltage cable and the sensor locations. The new BCML2 sensors housings are optimized to be very flat, stackable on top of each other and quick to exchange, see Fig. 7.24.

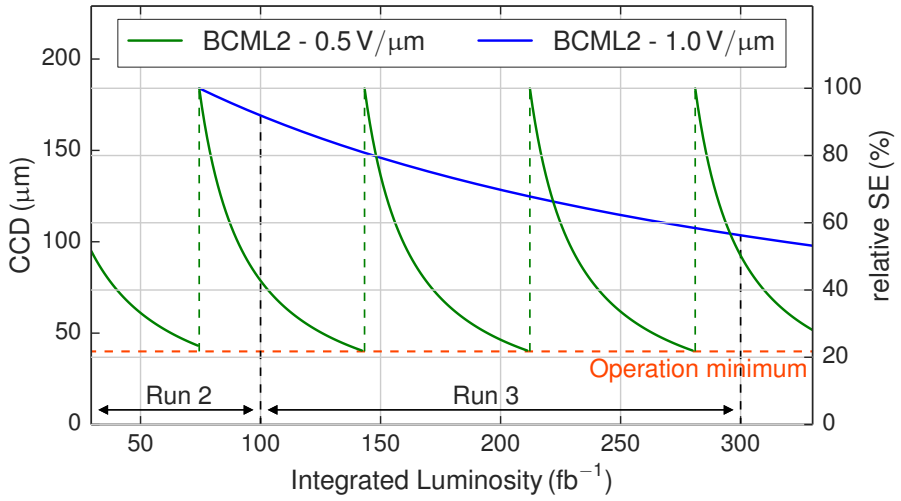

Figure 8.1: Extrapolation of the radiation induced signal degradation of the BCML2 Detector till the end of Run 3. The radiation induced signal degradation based on the BCML2 detector performance during Run 2 at an electrical field of $E = 0.5\,\mathrm{V/\mu m}$ is indicated in green and would force the replacement of the diamond sensors in total of 4 times. Using the effective defect model and simulating the detector performance at an increased electrical field of $E = 1.0\,\mathrm{V/\mu m}$ is indicated in blue and would avoid another need for a replacement of the BCML2 diamond sensors.

8.2 Outlook

During the entire lifetime of the LHC a total integrated luminosity of $\mathcal{L}_{\mathrm{integr.}} = 300\,\mathrm{fb}^{-1}$ is expected to be delivered to the CMS detector. Beyond that, the LHC accelerator will be upgraded to the High Luminosity - LHC (HL-LHC), where a 10 times increased integrated luminosity of $\mathcal{L}_{\mathrm{integr.}} = 3000\,\mathrm{fb}^{-1}$ is expected to be delivered to the CMS experiment. Both of these objectives will be discussed separately, starting with the near term outlook.

Near term outlook

Based on the experiences gained during the BCML detector operations during Run 2 the following points should be upgraded in order to improve the overall performance and maintainability of the BCML detector system:

- The radiation induced signal degradation of the diamond sensors used in the BCML2 detector locations forces a replacement of all diamonds used in the beam abort functionality, since these sensors already passed the minimum required charge collection distance of CCE = 40 µm. Extrapolating the radiation damage of the BCML2 diamond sensors observed during Run 2 for the entire lifetime of the LHC would force another 3 times the replacement of all BCML2 diamond sensors, see Fig 8.1. The BCML2 diamonds were operated during Run 2 at an electrical field of $E = 0.5\,\mathrm{V/\mu m}$ due to erratic currents at increased electric fields. Without the limitation of the electric field due to these erratic currents, higher bias voltage of up to HV = 500 V could be applied to the diamond sensors and hence a reduced signal degradation is expected. Using the effective defect model found in the frame of this PHD thesis, the radiation induced signal degradation in this high particle rate environment can be simulated for an increased electrical field of $E = 1.0\,\mathrm{V/\mu m}$, equivalent to an bias voltage of HV = 500 V, indicated in blue in Fig. 8.1. Base on the simulation result the BCML2 diamond sensors would resist the entire lifetime of the LHC, if the diamond sensors could be operated at an electrical field

of $E = 1.0\,\mathrm{V/\mu m}$. It is therefore crucial to select diamond sensors of highest quality, which allow a stable detector operation at high electrical fields.

- The currently used BCML2 frontend hardware will be replaced in the Extended Year-End Technical Stop (EYETS) 2016/17 by the newly designed BCML2 Main PCB together with the new BCML2 sensors housings. The new BCML2 frontend hardware will enclose the diamond sensors within two separate Faraday cages and likely reduced the noise level even further. The upgraded BCML2 frontend hardware enables furthermore an increase in the total amount of BCML2 channels from 28 up to 32, giving prototype sensors more possibilities to be operated in a very radiation intense environment.

Longer term outlook

An 10 times increased integrated luminosity of the HL-LHC translates directly into a 10 times increased radiation damage to the BCML sensor. At these intense radiation environments a simple increase of the bias voltage to operate the diamond sensor at higher electrical fields is not sufficient to avoid a frequent replacement of the sensors. Hence different approaches have to be analyzed to extend the life time of the currently used diamond sensors. In addition new sensor technologies like 'Diamond on Iridium' (DOI), 3D diamond sensors or sapphire sensors have to be studied in terms of radiation hardness:

- The signal efficiency as function of radiation damage can be strongly increased by using alternating bias voltages. The alternating bias voltage results in a homogeneous distribution of the space charge leading to a constant electrical field and hence to an increased charge collection efficiency as function of radiation damage, see section 6.3.6. The alternating voltage measurements have been done only in low particle rate environment and still have to be tested in high particle rate environments. An increased particle rate environment can perhaps be compensated by an increased switching rate between positive and negative polarity, however remains to be tested.

- The operation of the sapphire sensor during the entire Run 2 at the BCML2 location indicated a very small radiation induced signal reduction. The sapphire signal, about 35× reduced compared to a pCVD diamond sensors, could be increased with:

  - An increased bias voltage. Signal stability measurements of the sapphire sensor during the test beam showed that a bias voltage of $\mathrm{HV} = 2.5\,\mathrm{kV}$ is possible and indicated that a charge collection efficiency of 20% is reachable.
  - Increased sensor volume. Sapphire is grown with the Czochralski method and is therefore cheap and available in different geometries. For the LHC Run 2 in 2017 new sapphire material with a surface of $25 \times 25\,\mathrm{mm}^2$ has been bought and will be installed at the BCML2 location. Even bigger sensor geometries up to the waver dimensions of 4 inches are possible.
  - Operating several sapphire sensors in parallel. The new BCML2 sensor housing (shown in Fig. 7.24) allows the stacking of the BCML2 sensors on top of each other, and hence provides the possibility to increase the sapphire signal by operating them in parallel.
  - A sapphire packet consisting of 5 parallel $25 \times 25\,\mathrm{mm}^2$ sensors is installed for Run2 in 2017 at the BCML2 location and should create a signal comparable to a conventional pCVD diamond sensor.

- Diamond on Iridium has an increased CCE compared to the pCVD diamond sensors and can be operated as well at high electrical fields. The operation of DOI sensors in a high particle rate environments remains to be tested, but the first measurements in

the test beam looked promising. A DOI test sensor will be installed at the BCML2 location for the LHC Run 2 in 2017 as well.

- 3D - Diamond sensors: In contrast to the conventional planar detector layout of diamond sensors, a 3D geometry can be used where electrodes are located inside the diamond bulk. An increased radiation tolerance of such a 3D geometry can be obtained by a reduced distance between the electrodes and therefore a reduced drift length of the charge carriers to reach the electrodes, leading to a reduced trapping probability. In diamond sensors such electrodes in the diamond bulk can be created by using a femtosecond laser pulse to induce a phase transition in the diamond lattice to a combination of diamond-like carbon, amorphous carbon and graphitic material that can be used as electrode [Bac15].
- Besides solid-state detectors, the use of small gaseous ionization detector tubes could be considered since these detectors can be build radiation hard.

Acknowledgments

First and foremost, I want to thank my supervisor Prof. Wim de Boer for his exceptional support throughout the last 3.5 years. Not only for the offer of that interesting study, which resulted in this PhD thesis, but as well for working through and correcting my talks, posters and papers over and over again.
Wim, Thank You a lot!

I am very grateful for Prof. Thomas Müller being my second reviewer and his general support throughout the PhD thesis.

During my time at CERN I had the pleasure to have Anne Dabrowski as my supervisor. Anne, I owe you my deepest gratitude for the support you gave me during the entire time at CERN. It was a pleasure to work with you, knowing that I could always rely on your support in any situation.

My biggest 'Thanks' goes to Moritz Guthoff for supporting me the entire time at CERN. The fruitful discussions with Moritz where not only the foundation for this PhD thesis, but as well resulted in a true friendship.
Moritz, thank you for all your help and support!

I would like to thank my group at CERN, namely the BRIL project for the possibility to work with all of you. It was a great pleasure every single day to see you guys and work through all detector problems, one would never had thought of. Foremost I would like to thank David Stickland, who explained me more than once that we're unfortunately not living in an ideal world, where things tend to go wrong! For the excellent cooperation in the BRIL group I would like to thank: Duccio Abbaneo, Anne Dabrowski, Moritz Guthoff, Olena Karacheban, Andreas Kornmayer, Agnieszka Anna Zagozdzinska, Jessica Lynn Leonard, Sophie Mallows, Gabrielle Hugo, Nicolo Tosi, Grant Riley, Lisa Theresa Gloggler, Stella Orfanelli, Paul Lujan, Arkady Lokhovitskiy and Alan Bell.

As important as the group at CERN was the technical and scientific support from my home institute in Karlsruhe, the IEKP. Many thanks to you, especially in the early days of the PhD thesis to Robert Eber for introducing me to the TCT setup and to Andreas Nürnberg for introducing me to SILVACO TCAD, two very important foundations for this PhD thesis. Furthermore, I want to thank the entire group consisting of: Alexander Dierlamm, Ulrich Husemann, Frank Hartmann, Stefan Heindl, Hans-Jürgen Simonis, Thomas Weiler, Benedikt Freund, Simon Kudella, Stefan Maier, Marius Metzler and Daniel Schell. Beside the scientific staff at the IEKP, I owe a big 'Thank you' to the technicians helping me with the wire bonding of the diamonds, or in particular with the irradiation of the diamond samples! Therefore, Pia Steck, Felix Bögelspacher and Tobias Barvich, thank you for your exceptional support!
I thank all the members of the Institut für Experimentelle Kernphysik for their great support.

Without the support of the DESY Zeuthen group, giving me the possibility to use their CCD setup, this thesis wouldn't have been a success. I owe deep gratitude to Prof. Wolfgang Lohmann for his support. I also thank Olena Karacheban, Wolfgang Lange, Maria Hempel and Martin Stegler for their assistance with the CCD measurements.

From the BLM section of the CERN BE/BI group I thank Christos Zamatzas for the great support in particular with fixing the BLM electronics that suddenly stopped working and prevented a new injection of a physics fill at the LHC. I thank Bernd Dehning and Marcin Bartosik for the interesting discussions about diamond detectors and polarization.

I'm deeply thankful to Eléni Berdermann from the 'Gesellschaft für Schwerionenforschung' for hosting the Christmas workshop 'ADAMAS'. These workshops were always a pleasure to attend with great and enlightening discussions.

A thesis needs a lot of proof reading. For this I especially thank: Moritz Guthoff, Anne Dabrowski and Wim de Boer.

I thank the Wolfgang-Genter-Programme of the Bundesministerium für Bildung und Forschung for the financial support and Michael Hauschild, the coordinator of the program, for his assistance and advice.

Finally, I would like to thank all my friends and family for the moral support during these exciting, but stressful times.

Bibliography

[Aai15] R. Aaij et al., *Observation of J/ψ p Resonances Consistent with Pentaquark States in $\Lambda_b^0 \to J/\psi K^- p$ Decays*, Physical review letters **115**, 7 (2015) 072001.

[Ada96] W. Adam et al., *Development of diamond tracking detectors for high luminosity experiments at the LHC* (1996).

[Ada06] W. Adam et al., *Radiation hard diamond sensors for future tracking applications*, Nuclear Instruments and Methods in Physics Research Section A: Accelerators, Spectrometers, Detectors and Associated Equipment **565**, 1 (2006) 278 – 283.

[Afa14] K. Afanaciev, *Sr-90 tests with high-performance DOI samples*, Talk at ADAMAS workshop at GSI (2014).

[AG01] A. Arauzo-Garcia et al., *LHC Beam Loss Monitors*, Proceedings DIPAC 2001 - ESRF, Grenoble, France (2001).

[Agn92] P. Agnew, *Displacement thresholds in sapphire*, Philosophical Magazine A **65**, 2 (1992) 355–361.

[AID16] AIDA-2020, *Advanced European Infrastructures for Detectors at Accelerators*, http://aida2020.web.cern.ch/ (2016) [Online; accessed 27–October–2016].

[ALI08] ALICE Collaboration, *The ALICE experiment at the CERN LHC*, Journal of Instrumentation **3** (2008) S08002.

[AP11] C. Alabau Pons et al., *IR1 and IR5 aperture at 3.5 TeV* (2011).

[Ass06] R. Assmann et al., *The final collimation system for the LHC*, in *Proceedings of EPAC 2006* (2006).

[ATL08] ATLAS Collaboration, *The ATLAS Experiment at the CERN Large Hadron Collider*, Journal of Instrumentation **3** (2008) S08003.

[ATL12] ATLAS Collaboration, *Observation of a new particle in the search for the Standard Model Higgs boson with the ATLAS detector at the LHC*, Physics Letters B **716**, 1 (2012) 1 – 29.

[Auc14] B. Auchmann et al., *BLM Threshold Strategy (visa-vis UFOs and Quenches)* (2014).

[Bac15] F. Bachmair et al., *A 3D diamond detector for particle tracking*, Nuclear Instruments and Methods in Physics Research Section A: Accelerators, Spectrometers, Detectors and Associated Equipment **786** (2015) 97 – 104.

[Bae11] T. Baer et al., *UFOs in the LHC*, in *4th meeting of the CERN Machine Advisory Committee* (2011).

[Bae12] T. Baer et al., *UFOs in the LHC: Observations, studies and extrapolations*, in *Conf. Proc.*, volume 1205201 (2012), p. THPPP086.

[Bag14] V. Baglin et al., *CERN Vacuum System Activities during the Long Shutdown 1: the LHC Beam Vacuum*, WEPME047, proceedings of IPAC2014, Dresden, Germany (2014).

[Bar04] M. Barbero et al., *Design and test of the CMS pixel readout chip*, Nuclear Instruments and Methods in Physics Research Section A: Accelerators, Spectrometers, Detectors and Associated Equipment **517**, 1 (2004) 349–359.

[Bar11] D. Barney, *CMS slice, CMS Document 5581-v1, https://cms-docdb.cern.ch/cgi-bin/PublicDocDB/ShowDocument?docid=5581* (2011) , [Online; accessed 4–June–2016].

[Bel10] A. J. Bell et al., *Fast beam conditions monitor BCM1F for the CMS experiment*, Nuclear Instruments and Methods in Physics Research Section A: Accelerators, Spectrometers, Detectors and Associated Equipment **614**, 3 (2010) 433 – 438.

[Bel13] A. J. Bell, *Luminosity, beam monitoring and triggering for the CMS experiment and measurement of the total inelastic cross-section atâ ˆš s= 7 TeV*, Ph.D. thesis, University of Geneva (2013).

[Ben14] A. M. Bennett et al., *Development of high-purity optical grade single-crystal CVD diamond for intracavity cooling*, Proc. SPIE **8959** (2014) 89590R–89590R–8.

[Böh14] T. Böhlen et al., *The FLUKA code: developments and challenges for high energy and medical applications*, Nuclear Data Sheets **120** (2014) 211–214.

[Bol06] J. Bol, *Strahlmonitore aus Diamant für primäre Teilchenstrahlen hoher Intensität* (2006).

[Bor94] E. Borchi et al., *Radiation damage in silicon detectors*, La Rivista del Nuovo Cimento (1978-1999) **17**, 11 (1994) 1–63.

[Bou99] D. Boussard et al., *The LHC superconducting cavities*, Particle Accelerator Conference (1999).

[Bru04] M. Bruinsma et al., *CVD diamonds in the BaBar radiation monitoring system*, arXiv preprint physics/0406097 (2004).

[Bru13] R. Bruce et al., *Sources of machine-induced background in the ATLAS and CMS detectors at the CERN Large Hadron Collider*, Nuclear Instruments and Methods in Physics Research Section A: Accelerators, Spectrometers, Detectors and Associated Equipment **729** (2013) 825 – 840.

[Bud98] R. Bud et al., *Instruments of science: an historical encyclopedia*, Taylor & Francis (1998).

[Bur14] E. Burkel et al., *Diamond Formation in Graphene Nanoplatelets, Carbon Nanotubes and Fullerenes Under Spark Plasma Sintering*, Springer Netherlands, Dordrecht (2014), pp. 1–16.

[CAEa] CAEN Power Supply SY1527, http://www.caen.it/csite/CaenProd.jsp?parent=20&idmod=122, [Online; accessed 28–September–2016].

[CAEb] CAEN Power Supply SY4527, http://www.caen.it/csite/CaenProd.jsp?idmod=752&parent=20, [Online; accessed 28–September–2016].

[Can79] C. Canali et al., *Electrical properties and performances of natural diamond nuclear radiation detectors*, Nuclear Instruments and Methods **160** (1979) 73–77.

[Cas99] G. Casse et al., *Scanning of irradiated silicon detectors using alpha particles and low-energy protons*, Nuclear Instruments and Methods in Physics Research Section A: Accelerators, Spectrometers, Detectors and Associated Equipment **434**, 1 (1999) 118–130.

[Cau67] D. Caughey et al., *Carrier mobilities in silicon empirically related to doping and field*, Proceedings of the IEEE **55**, 12 (1967) 2192–2193.

[CDS16] CERN Brochure http://cds.cern.ch/record/1165534/files/CERN–Brochure–2009–003–Eng.pdf, [Online; accessed 1–June–2016].

[CER16a] CERN Accelerators, *The CERN proton sychrotron*, https://espace.cern.ch/be-dep/OP/PS/default.aspx (2016) [Online; accessed 27–October–2016].

[CER16b] CERN Accelerators, *The T9 Beam Line*, http://home.web.cern.ch/sites/home.web.cern.ch/files/file/spotlight_students/information_about_the_t9_beam_line_and_experimental_facilities.pdf (2016) [Online; accessed 27–October–2016].

[Cha12] S. Chatrchyan et al., *Observation of a new boson at a mass of 125 GeV with the CMS experiment at the LHC*, Physics Letters B **716**, 1 (2012) 30–61.

[CMS16] *https://twiki.cern.ch/twiki/bin/view/CMSPublic/LumiPublicResults,* [Online; accessed 3–June–2016].

[CMS06] CMS Collaboration, *CMS physics: Technical design report*, CERN-LHCC-2006-001 (2006).

[CMS07] CMS Collaboration, *CMS Physics Technical Design Report, Volume II: Physics Performance*, Journal of Physics G: Nuclear and Particle Physics **34**, 6995 (2007).

[CMS08] CMS Collaboration, *The CMS experiment at the CERN LHC*, Journal of Instrumentation **3** (2008) S08004.

[CMS12] CMS Collaboration, *Observation of a new boson at a mass of 125 GeV with the CMS experiment at the LHC*, Physics Letters B **716**, 1 (2012) 30 – 61.

[CMS13] CMS collaboration, *The performance of the CMS muon detector in proton-proton collisions at* $\sqrt{s} = 7\,\text{TeV}$ *at the LHC*, Journal of Instrumentation **8**, 11 (2013) P11002.

[Coh66] M. L. Cohen et al., *Band Structures and Pseudopotential Form Factors for Fourteen Semiconductrs of the Diamond and Zinc-blende Structures*, Phsyical Review **141**, 2 (1966) 789–796.

[Cor06] G. Corti et al., *Aspects of machine induced background in the lhc experiments* (2006).

[Cri10] M. Cristinziani et al., *Diamond prototypes for the ATLAS SLHC pixel detector*, Nuclear Instruments and Methods in Physics Research Section A: Accelerators, Spectrometers, Detectors and Associated Equipment **623**, 1 (2010) 174–176.

[CRY] CRYSTAL GmbH, *http://crystal-gmbh.com* , [Online; accessed 31–October–2016].

[Dab11] A. Dabrowski et al., *Proposed modification to CMS BCM2 and BCM1L thresholds for 2012 running*, CMS Technical internal note , 1236236_v1 (2011) 1 – 9.

[Dab16] A. Dabrowski et al., *Upgrade of the CMS instrumentation for luminosity and machine induced background measurements*, Nuclear and Particle Physics Proceedings **273** (2016) 1147–1154.

[Deh09] B. Dehning et al., *First Experience with the LHC Beam Loss Monitoring System*, Particle Accelerator Conference **TH5RFP034** (2009) 3522–3524.

[Die10] A. Dierlamm, *Irradiations in Karlsruhe* (2010).

[DK08] I. Dolenc Kittelmann, *Development of Beam Conditions Monitor for the ATLAS experiment* (2008).

[Dod96] P. E. Dodd, *Device simulation of charge collection and single-event upset*, IEEE Transactions on Nuclear Science **43**, 2 (1996) 561–575.

[Dor98] P. Dore et al., *Infrared properties of chemical-vapor deposition polycrystalline diamond windows*, Appl. Opt. **37**, 24 (1998) 5731–5736.

[Edw05] A. Edwards et al., *Radiation monitoring with CVD diamonds in BABAR*, Nuclear Instruments and Methods in Physics Research Section A: Accelerators, Spectrometers, Detectors and Associated Equipment **552**, 1 (2005) 176–182.

[Eff07] E. Effinger et al., *The LHC beam loss monitoring system's data acquisition card*, 12th Workshop on Electronics For LHC and Future Experiments (2007) 108–112.

[Ele16a] Element6, *The ELEMENT SIX CVD diamond handbook* (2016).

[Ele16] ElementSix, *Synthetic diamond producer*, www.e6.com (2016) [Online; accessed 27–October–2016].

[Eva08] L. Evans et al., *LHC Machine*, Journal of Instrumentation **3**, 08 (2008) S08001.

[Eva09] D. Evans et al., *Diamond–metal contacts: interface barriers and real-time characterization*, Journal of Physics: Condensed Matter **21**, 36 (2009) 364223.

[Fel16] Felix Bachmair on behalf of the RD42 collaboration, *Test beam results of 3D detectors based on scCVD and pCVD diamonds*, 14th vienna conference on instrumentation (2016).

[Fer75] D. K. Ferry, *High-field transport in wide-band-gap semiconductors*, Phys. Rev. B **12** (1975) 2361–2369.

[Fer05] A. Ferrari et al., *FLUKA: A multi-particle transport code (Program version 2005)* (2005).

[FLU] FLUKE, *Fluke VR1710 Voltage Quality Recorder, http://www.fluke.com/fluke/r0en/Electrical-Test-Tools/Power-Quality-Tools/Fluke-VR1710.htm?PID=56202* , [Online; accessed 28–September–2016].

[Fri02] W. Friesenbichler, *Development of the Readout Electronics for the Beam Loss Monitors of the LHC*, Ph.D. thesis, Fachhochschule Wiener Neustadt (2002).

[Fu85] J. Fu et al., *Comparison of 2D memory SEU transport simulation with experiments*, IEEE Transactions on Nuclear Science **32**, 6 (1985) 4145–4149.

[Gsc02] E. Gschwendtner et al., *The beam loss detection system of the LHC ring*, Technical report (2002).

[Gut13] M. Guthoff et al., *Radiation damage in the diamond based beam condition monitors of the CMS experiment at the Large Hadron Collider (LHC) at CERN*, Nuclear Instruments and Methods in Physics Research Section A: Accelerators, Spectrometers, Detectors and Associated Equipment , 0 (2013) –.

[Gut14a] M. Guthoff, *Radiation damage to the diamond based Beam Condition Monitor of the CMS Detector at the LHC*, Ph.D. thesis, Karlsruhe Institute of Technology, IEKP-KA/2014-01 (2014).

[Gut14b] M. Guthoff et al., *Simulation of beam induced lattice defects of diamond detectors using FLUKA*, Nuclear Instruments and Methods in Physics Research Section A: Accelerators, Spectrometers, Detectors and Associated Equipment **735** (2014) 223–228.

[Gut15] M. Guthoff et al., *Performance and perspectives of the diamond based Beam Condition Monitor for beam loss monitoring at CMS*, PoS (2015) 281.

[Gut16] M. Guthoff, *Instrumentation for beam radiation and luminosity measurement in the CMS experiment using novel detector technologies*, Nuclear Instruments and Methods in Physics Research Section A: Accelerators, Spectrometers, Detectors and Associated Equipment (2016) –.

[Hal52] R. N. Hall, *Electron-hole recombination in germanium*, Physical Review **87**, 2 (1952) 387.

[Hem14] M. Hempel et al., *Performance and upgrade of the Fast Beam Condition Monitor at CMS*, Proceedings of IBIC2014, Monterey, CA, USA (2014) 134–138.

[Her03] W. Herr et al., *Concept of luminosity* **361** (2003).

[Her16] P. Hermes et al., *Improved Aperture Measurements at the LHC and Results from their Application in 2015* (2016) 1446–1449.

[HW11] R. Hall-Wilton et al., *Results from a beam test of a prototype PLT diamond pixel telescope*, Nuclear Instruments and Methods in Physics Research Section A: Accelerators, Spectrometers, Detectors and Associated Equipment **636**, 1, Supplement (2011) S130 – S136.

[Iba10] H. Ibach et al., *Solid-state physics: an introduction to principles of materials science*, Advanced texts in physics (Springer, Berlin, 2003). Cerca con Google (2010).

[Ins16] Institute of Experimental Nuclear Pysics at KIT, *Proton Irradiation at KIT - The Cyclotron and the Irradiation Setup*, https://www.ekp.kit.edu/english/264.php (2016) [Online; accessed 27–October–2016].

[Isb02] J. Isberg et al., *High Carrier Mobility in Single-Crystal Plasma-Deposited Diamond*, Science **297**, 5587 (2002) 1670–1672.

[Jea96] J. Jeanneret et al., *Quench levels and transient beam losses in LHC magnets* (1996).

[Jon04] R. Jones, *VME64x Digital Acquisition Board for the LHC Trajectory and Closed Orbit System*, LHC Engineering, LHC-BP-ES-0002, EDMS 410295 v.1.1 (2004).

[Kag09] H. Kagan et al., *Development of Single Crystal Chemical Vapor Deposition Diamonds for Detector Applications*, Technical report, The Ohio State University Research Foundation (United States). Funding organisation: USDOE Office of Energy Research (United States) (2009).

[Kam83] M. Kamo et al., *Diamond synthesis from gas phase in microwave plasma*, Journal of Crystal Growth **62**, 3 (1983) 642 – 644.

[Kar15] O. Karacheban et al., *Investigation of a direction sensitive sapphire detector stack at the 5 GeV electron beam at DESY-II*, Journal of Instrumentation **10**, 08 (2015) P08008.

[Kas15] F. Kassel et al., *Proposed modification to CMS BCML thresholds for Run 2 running*, CMS Technical internal note , 1502426_v1 (2015) 1 – 10.

[Kas16a] F. Kassel et al., *Proposed adjustments of CMS BCML thresholds for 2016*, CMS Technical internal note , 1611082_v1 (2016) 1 – 11.

[Kas16b] F. Kassel et al., *Proposed adjustments of CMS BCML thresholds for the second half of the year 2016*, CMS Technical internal note , 1718878_v1 (2016) 1 – 8.

[Kas16c] F. Kassel et al., *Severe signal loss in diamond beam loss monitors in high particle rate environments by charge trapping in radiation-induced defects*, physica status solidi (a) **213**, 10 (2016) 2641–2649.

[Kas17] F. Kassel et al., *Description of radiation damage in diamond sensors using an effective defect model*, arXiv preprint arXiv:1705.09324 (2017).

[Kis15] M. Kis et al., *TCT characterization of new generation of DoI samples*, ADAMAS workshop - talk (2015).

[Kra12] G. Kramberger et al., *Effects of bias voltage during priming on operation of diamond detectors*, Proceedings of Science - Vertex **13** (2012).

[Kri03] E. S. Krištof, *Fast neutron spectrum in the exposure room of the TRIGA Mark II reactor in Ljubljana*, Proceedings Reviewers (2003) 114.

[Kuz07] E. Kuznetsova, *Design studies and sensor tests for the beam calorimeter of the ILC detector* (2007).

[Lag15] S. Lagomarsino et al., *Radiation hardness of three-dimensional polycrystalline diamond detectors*, Applied Physics Letters **106**, 19 (2015) 193509.

[LHC16] *https://lpc.web.cern.ch/lpc/cgi-bin/filling_schemes.py,* [Online; accessed 1–June–2016].

[LHC08a] LHCb Collaboration, *The LHCb Detector at the LHC*, Journal of Instrumentation **3** (2008) S08005.

[LHC08b] LHCf Collaboration, *The LHCf detector at the CERN Large Hadron Collider*, Journal of Instrumentation **3** (2008) S08006.

[LHC16] LHC-facts.ch, *Beam Loss test*, http://www.lhc-facts.ch/index.php?page=strahlenergie (2016) [Online; accessed 27–October–2016].

[Lin] Linear Technology, *http://www.linear.com/designtools/software/#LTspice* , [Online; accessed 20–August–2016].

[Lin63] J. Lindhard et al., *Integral Equations Governing Radiation Effects.(Notes on atomic collisions, III)*, Kgl. Danske Videnskab., Selskab. Mat. Fys. Medd. **33**, 10 (1963).

[Liu95] H. Liu et al., *Diamond Chemical Vapor Deposition: Nucleation and Early Growth Stages*, Noyes Publications (1995).

[Mar04] P. M. Martineau et al., *Identification of synthetic diamond grown using chemical vapor deposition (CVD)*, Gems & Gemology **40**, 1 (2004) 2–25.

[Mat82] S. Matsumoto et al., *Growth of diamond particles from methane-hydrogen gas*, Journal of Materials Science **17**, 11 (1982) 3106–3112.

[May00] P. W. May, *Diamond thin films: a 21st-century material*, Philosophical Transactions of the Royal Society A **358** (2000) 473–495.

[May13] M. Mayr et al., *Efficiency and mechanism of dislocation density reduction during heteroepitaxial growth of diamond for detector applications*, ADAMAS workshop - talk (2013).

[Mil13] R. Mildren et al., *Optical Engineering of Diamond* (2013).

[Moe13] V. Moens et al., *Comparison of LHC Beam Loss Maps Using the Transverse Damper Blow up and Tune Resonance Crossing Methods* (2013).

[Mol06] M. Moll, *Radiation tolerant semiconductor sensors for tracking detectors*, Nuclear Instruments and Methods in Physics Research Section A: Accelerators, Spectrometers, Detectors and Associated Equipment **565**, 1 (2006) 202 – 211.

[Mue11] M. Mueller, *The Beam Condition Monitor 2 and the Radiation Environment of the CMS Detector at the LHC*, Ph.D. thesis, Karlsruhe Institute of Technology, IEKP-KA/2011-01 (2011).

[Neu11] E. Neu et al., *Single photon emission from silicon-vacancy colour centres in chemical vapour deposition nano-diamonds on iridium*, New Journal of Physics **13**, 2 (2011) 025012.

[Nor75] M. Norgett et al., *A proposed method of calculating displacement dose rates*, Nuclear Engineering and Design **33**, 1 (1975) 50–54.

[Oh99] A. Oh, *CVD Diamant als Material fu Ì^r Teilchendetektoren*, Ph.D. thesis, University Hamburg, Germany (1999).

[Ohl09] M. Ohlerich, *Investigations of the Physics Potential and Detector Development for the ILC*, Ph.D. thesis, University Cottbus (2009).

[Orf15] S. Orfanelli et al., *A novel Beam Halo Monitor for the CMS experiment at the LHC*, Journal of Instrumentation **10** (2015) P11011.

[Pan78] S. T. Pantelides, *The electronic structure of impurities and other point defects in semiconductors*, Reviews of Modern Physics **50**, 4 (1978) 797.

[Pan13] L. S. Pan et al., *Diamond: electronic properties and applications*, Springer Science & Business Media (2013).

[Pap16] G. Papotti et al., *Macroparticle-Induced Losses During 6.5 TeV LHC Operation* (2016) 1481–1484.

[Par16] Particulars, *Advanced Measurement Systems: Particulars Wide Band Current Amplifier*, www.particulars.si (2016) [Online; accessed 08–November–2016].

[Phi58] J. C. Phillips, *Energy-Band Interpolation Scheme Based on a Pseudopotential*, Phys. Rev. **112** (1958) 685–695.

[Pie93] H. O. Pierson, *Handbook of Carbon, Graphite, Diamonds and Fullerenes* (1993) 1 – 419.

[Pie15] T. Pierog et al., *EPOS LHC: Test of collective hadronization with data measured at the CERN Large Hadron Collider*, Physical Review C **92**, 3 (2015) 034906.

[Pom08] M. Pomorski, *Electronic Properties of Single Crystal CVD Diamond and its Suitability for Particle Detection in Hadron Physics Experiments*, Ph.D. thesis, Johann Wolfgang Goethe University in Frankfurt am Main (2008).

[Pom15] M. Pomorski et al., *Characterization of the charge-carrier transport properties of IIa-Tech SC diamond for radiation detection applications*, physica status solidi (a) **212**, 11 (2015) 2553–2558.

[Ram39a] S. Ramo, *Currents Induced by Electron Motion*, Proceedings of the I.R.E. **27 - 9** (1939) 584–585.

[Ram39b] S. Ramo, *Currents induced by electron motion*, Proc. Ire **27**, 9 (1939) 584–585.

[Ros03] L. Rossi, *The LHC superconducting magnets*, Particle Accelerator Conference (2003).

[Row15] S. Rowan et al., *Interactions between macroparticles and high-energy proton beams*, Proc. of IPACâ€™15 (2015).

[Rud15] P. Rudolph, *Handbook of Crystal Growth (Second Edition)* (2015).

[San89] G. S. Sandhu et al., *Reactive ion etching of diamond*, Applied Physics Letters **55**, 5 (1989) 437–438.

[Sas66] W. Saslow et al., *Band Structure and Optical Properties of Diamond*, Phys. Rev. Lett. **16** (1966) 354–356.

[Sch99] M. Schreck et al., *Diamond/Ir/SrTiO3: A material combination for improved heteroepitaxial diamond films*, Applied Physics Letters **74**, 5 (1999) 650–652.

[Sch01] M. Schreck et al., *Diamond nucleation on iridium buffer layers and subsequent textured growth: A route for the realization of single-crystal diamond films*, Applied Physics Letters **78**, 2 (2001) 192–194.

[Sch10] S. Schuwalow, *Radiation hardness studies with relativistic electrons*, Talk at 2nd CARAT Workshop, GSI, Darmstadt (2010).

[Sch14a] R. Schirhagl et al., *Nitrogen-vacancy centers in diamond: nanoscale sensors for physics and biology*, Annual review of physical chemistry **65** (2014) 83–105.

[Sch14b] M. Schreck, *3.11 - Single Crystal Diamond Growth on Iridium*, in V. K. Sarin, editor, *Comprehensive Hard Materials*, Elsevier, Oxford (2014), pp. 269 – 304.

[Sel12] S. Selberherr, *Analysis and simulation of semiconductor devices*, Springer Science & Business Media (2012).

[Sho52] W. Shockley et al., *Statistics of the recombinations of holes and electrons*, Physical review **87**, 5 (1952) 835.

[SIL10] SILVACO Inc., *ATLAS Users Manual - Device Simulation Framework*, https://dynamic.silvaco.com/dynamicweb/jsp/downloads/DownloadManualsAction.do?req=silentmanuals&nm=atlas (2010).

[SIL16] SILVACO Inc., *Atlas - Device Simulation Framework*, http://www.silvaco.com/products/tcad/device_simulation/atlas/atlas_32.pdf (2016) [Online; accessed 27–October–2016].

[Sim71] J. Simmons et al., *Nonequilibrium steady-state statistics and associated effects for insulators and semiconductors containing an arbitrary distribution of traps*, Physical Review B **4**, 2 (1971) 502.

[Spe94] K. Spear, *Synthetic diamond: Emerging CVD Science and Technology*, Wiley Interscience Publication (1994).

[Spi81] B. Spitsyn et al., *Vapor growth of diamond on diamond and other surfaces*, Journal of Crystal Growth **52** (1981) 219 – 226.

[Ste15] M. Stegler, *Characterisation of non-irradiated and irradiated diamond sensors before and after application at LHC*, Ms, BTU Cottbus-Senftenberg, Cottbus (2015), bTU Cottbus-Senftenberg, Masterarbeit, 2015.

[Tal06a] V. Talanov et al., *The study of the machine-induced background and its application at the LHC*, Proceedings of EPAC 2006, Edinburgh, Scotland (2006).

[Tal06b] A. Tallaire et al., *Multiple growth and characterization of thick diamond single crystals using chemical vapour deposition working in pulsed mode*, Journal of Crystal Growth **291**, 2 (2006) 533 – 539.

[Tan74] B. Tanner et al., *Contrast of crystal defects under polarized light*, Philosophical Magazine **29**, 5 (1974) 1081–1094.

[TOT08] TOTEM Collaboration, *The TOTEM Experiment at the CERN Large Hadron Collider*, Journal of Instrumentation **3** (2008) S08007.

[Tre16] Trekinc, *Data sheet of Trak Model 2220*, http://www.trekinc.com/pdf/2220-Sales.pdf (2016) [Online; accessed 08–November–2016].

[Tri08] W. Trischuk et al., *Recent advances in diamond detectors*, arXiv preprint arXiv:0810.3429 (2008).

[Tsu12] J.-W. Tsung et al., *Signal and noise of diamond pixel detectors at high radiation fluences*, Journal of Instrumentation **7**, 09 (2012) P09009.

[Vas00] A. Vasilescu et al., *Notes on the fluence normalisation based on the NIEL scaling hypothesis*, ROSE/TN **2000** (2000).

[Wat04] T. Watanabe et al., *Monte Carlo simulations of electron transport properties of diamond in high electric fields using full band structure*, Jounral of applied physics **95**, 9 (2004) 4866–4874.

[Wika] Wikipedia, *https://commons.wikimedia.org/wiki/File:Carbon_lattice_diamond.png#/media/File:Diamond_structure.gif,* [Online; accessed 28–June–2016].

[Wikb] Wikipedia, *https://en.wikipedia.org/wiki/Crystallographic_defect#/media/File:Defecttypes.png,* [Online; accessed 28–June–2016].

[Wikc] Wikipedia: Sven, *https://commons.wikimedia.org/wiki/File:Sp3-Orbital.svg,* [Online; accessed 28–June–2016].

[Zam06] C. Zamantzas et al., *An FPGA based implementation for real-time processing of the LHC beam loss monitoring system's data*, in *2006 IEEE Nuclear Science Symposium Conference Record*, volume 2, IEEE (2006), pp. 950–954.

[Zie16] J. F. Ziegler, *SRIM - The Stopping and Range of Ions in Matter*, http://www.srim.org (2016) [Online; accessed 27–October–2016].

List of Figures

List of Tables

Appendix A

Appendix

A.1 BCML Detector

A.1.1 Hardware

A.1.1.1 Reduced BCML1 efficiency and LTSpice simulation

The reduced efficiency of the BCML1 detector at CMS was discussed in section 4.1.4.3. Therefore the entire BCML1 electrical readout circuit was tested in the laboratory and as well simulated with the software LTSpice IV. The BCML1 electrical circuit, using a silicon diode as detector and a red LED light as signal source, was tested for different pulse duration of the LED light (10 ms, 3 ms, 1 ms and 500 μs). The BCML1 electrical circuit was set up in two configuration, once with the decoupling filter on the HV line and once with the decoupling filter on the signal return line, see section 4.1.4.3. The results for the different LED pulse durations shown in Fig. A.1 were measured using the tunnel card read out system, used as well at the CMS detector.

Instead of the tunnel card read out system an oscilloscope was used as well to determine the pulse shape of the signal for different signal durations (100 ms, 10 ms and 2 ms), discussed in more detail in section 4.1.4.3. In addition the signal shape was simulated using the software LTSpice IV. The input for the LTSpice IV simulation is shown in fig. A.3. The comparison of the measurements and the simulation for both decoupling filter configuration and as well for different LED pulse durations is shown in Fig. A.2.

A.1.1.2 Schematic drawing of the BCML2 electrical signal circuits.

The electrical signal circuit of the BCML2 detector is schematically shown in Fig. A.4.

A.1.1.3 Tunnel card: Setup of USB read out

In order to use the tunnel card for local measurements a USB box, containing a small FPGA-chip, is used that provides the same readout like the DAB64 readout board. The Tunnel card measrung the current is powered with a 'CMS - type' power supply. This power supply needs to be connected to a low voltage power supply like indicated in Fig. A.5.

A.1.1.4 Technical drawing of the BCML1 sensor boxes

The technical drawings of the BCML1 sensors boxes are shown in Fig. A.6. The diamond sensor is mounted with conductive glue centrally on the sensor PCB and connected on the

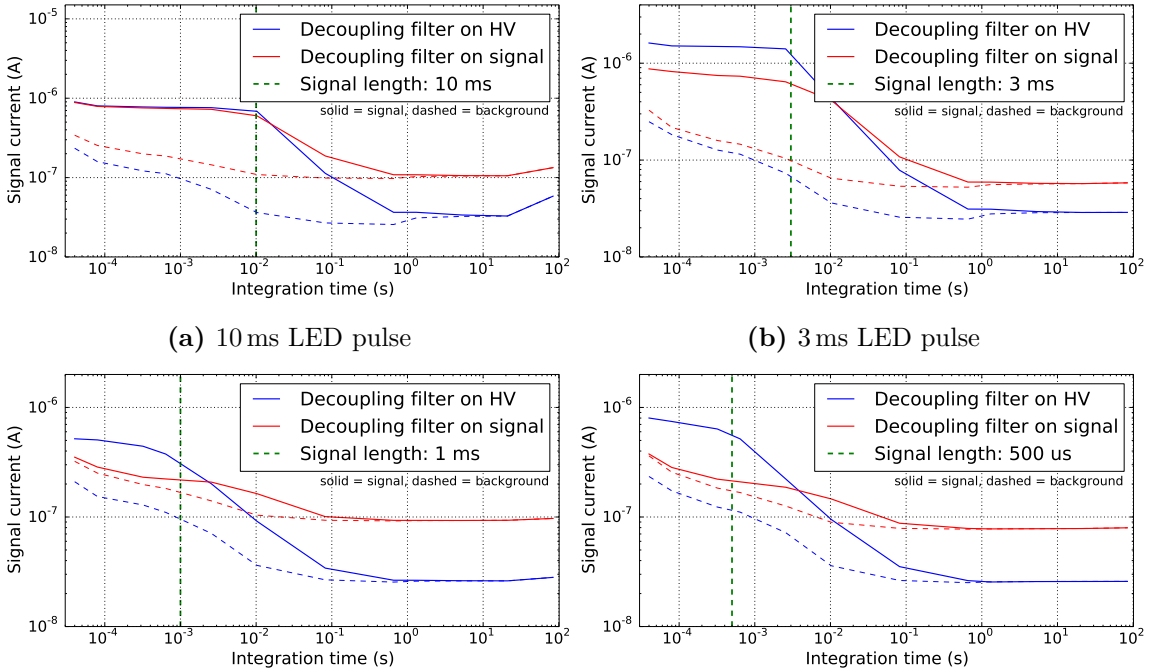

(a) 10 ms LED pulse **(b)** 3 ms LED pulse

(c) 1 ms LED pulse **(d)** 500 µs LED pulse

Figure A.1: Running sum spectra measured with tunnel card for a 10 ms, 3 ms, 1 ms and 500 μs LED pulse.

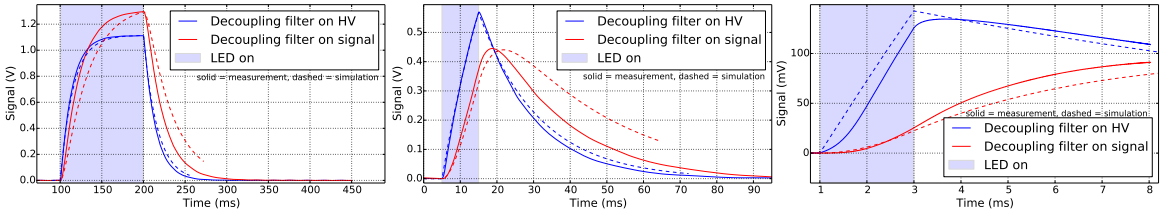

(a) 100 ms LED pulse **(b)** 10 ms LED pulse **(c)** 2 ms LED pulse

Figure A.2: Measurements with an oscilloscope of the LED induced signals for different signal durations: 100 ms, 10 ms and 2 ms. Additionally the signal shape was simulated as indicated in dashed lines.

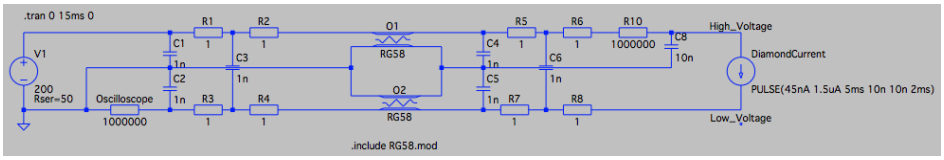

Figure A.3: LTspice simulation of the electrical BCML1 read out circuit.

top side via a wire bond to the HV pad. The diamond sensor is surrounded by two covers of copper acting as Faraday cages.

A.1.1.5 Technical drawings of the BCML2 Main PCB

In Fig. A.7 the PCB design of the new BCML2 Main PCB is shown. The BCML2 Main PCB consits in total of 6 layers, where the bottom and top layer are fully metallzied acting as Faraday cage and connected to the shield. The PCB layers 2-5 are connecting all 8 BCML2 sensor locations with both of the D-SUB37 connectors. Two each BCML2 sensor location a HV, a return line (signal) and a shield is routed.

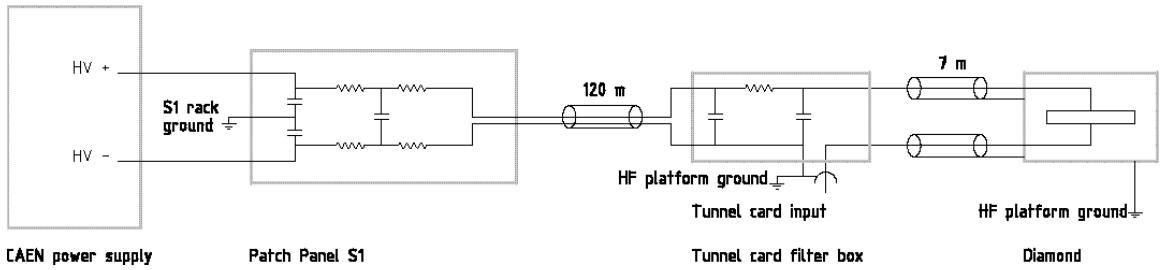

Figure A.4: The high voltage signal from the power supply is filtered twice on the patch panel in the service cavern and close to the BCML2 detector in the experimental cavern. The BCML2 detector is connected to the power supply via a 120 m long coaxial cable. The tunnel card is located close to the detector in the experimental cavern and hence is as well grounded there. The drawing is taken from [Mue11].

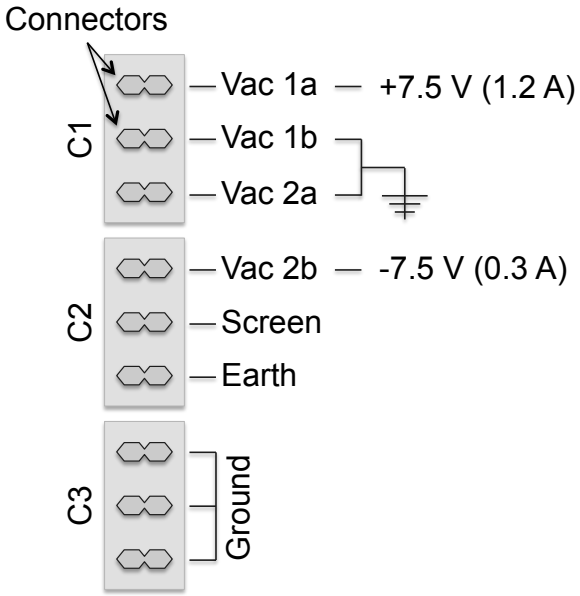

Figure A.5: Drawing of the electrical connection of the power supply for the tunnel card. This power supply is modified and the AC to DC converter was removed, hence just positive and negative DC current with respect to the ground has to be provided. At the 'Earth' and the 'Ground' connectors the power supply should be grounded.

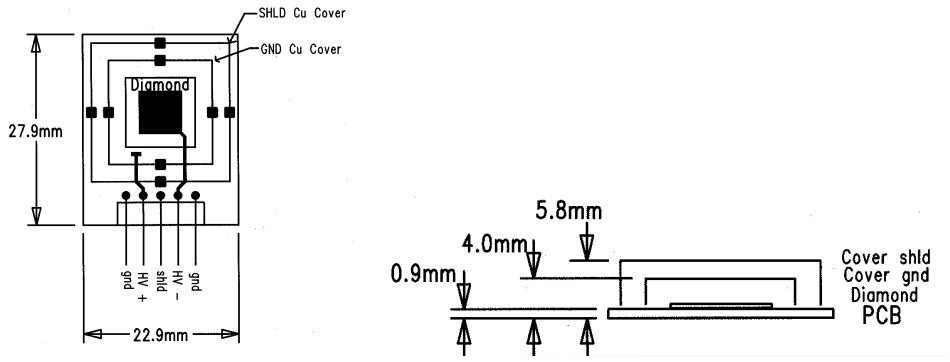

(a) Top view. **(b)** Side view.

Figure A.6: Technical drawing of the BCML1 sensor box.

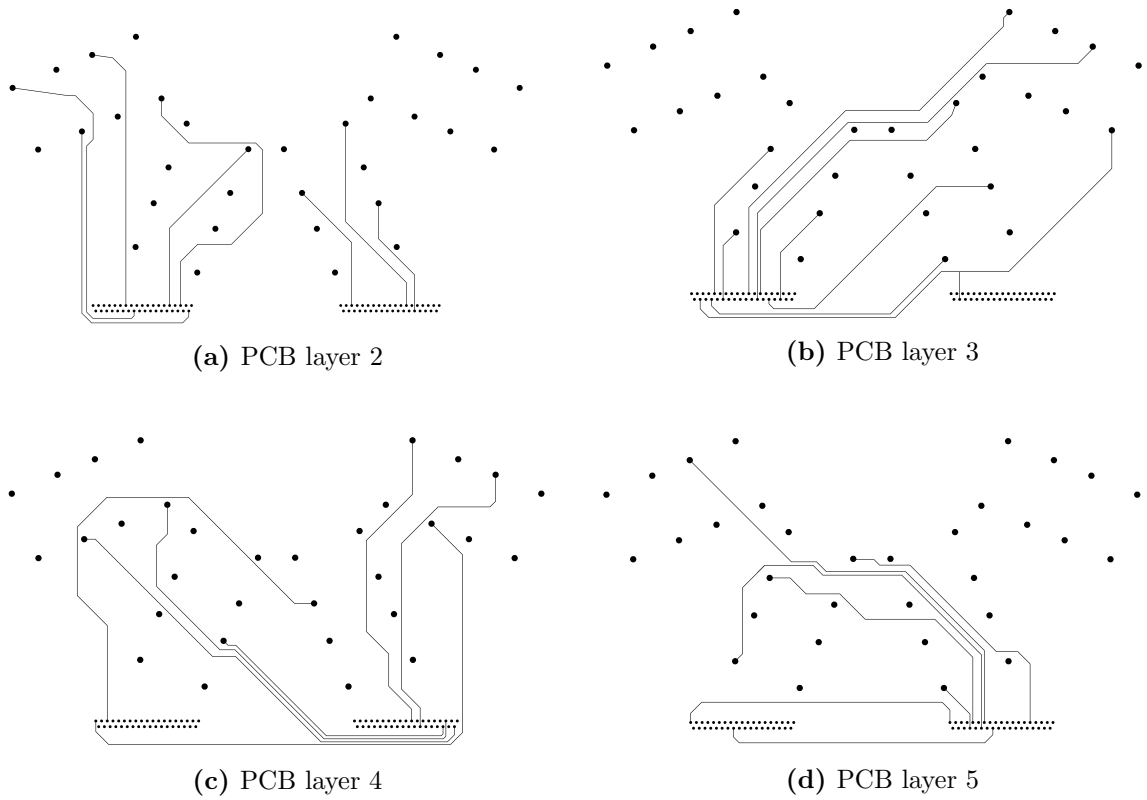

(a) PCB layer 2

(b) PCB layer 3

(c) PCB layer 4

(d) PCB layer 5

Figure A.7: Technical drawing of the BCML2 Main PCB. The routing between BCML2 sensor locations and the two male DSUB-37 connectors is done on the PCB layers 2-5. The PCB layer 1 and 6 are used as shield.

A.1.2 BCML Abort Thresholds

The abort thresholds of the BCML detectors were adjusted with respect to the reduced detectors efficiencies three times during Run 2, see section 4.5.1. The modification of the abort thresholds during Run 2 for running sum 1 are listed in Table A.1 and for running sum 12 are listed in Table A.2, more details can be found in [Kas15, Kas16a, Kas16b].

Table A.1: The BCML1 abort thresholds defined for running sum 1. The default RS1 abort threshold during Run 2 was set to 10 µA resulting in a safety factor of 3000 for an undamaged diamond detector with 100% signal efficiency (SE). In order to maintain the minimum safety factor of 1000, the RS1 abort thresholds for detectors with a lower SE < 33% were accordingly reduced.

Detector location	$SE_{03.15}$	Threshold on 03.15		$SE_{03.16}$	Threshold on 03.16		$SE_{08.16}$	Threshold on 08.16	
	(%)	(ADC)	(µA)	(%)	(ADC)	(µA)	(%)	(ADC)	(µA)
BCML1 -Z far top	100[a]	2050	10	87	2050	10	72[b]	2050	10
BCML1 -Z far bottom[c]	100[a]	2050	10	-	-	-	-	-	-
BCML1 -Z near top	100[a]	2050	10	78	2050	10	78[b]	2050	10
BCML1 -Z near bottom	55[a]	2050	10	83	2050	10	70[b]	2050	10
BCML1 +Z far top	100[a]	2050	10	77	2050	10	60[b]	2050	10
BCML1 +Z far bottom	100[a]	2050	10	55	2050	10	55[b]	2050	10
BCML1 +Z near top[c]	55[a]	2050	10	-	-	-	-	-	-
BCML1 +Z near bottom	100[a]	2050	10	81	2050	10	58[b]	2050	10
BCML2 -Z inner far	55[a]	2050	10	50	2050	10	**24**	**1444**	**7.1**
BCML2 -Z inner up	55[a]	2050	10	50	2050	10	**25**	**1542**	**7.5**
BCML2 -Z inner near	40[a]	2050	10	53	2050	10	**23**	**1413**	**6.9**
BCML2 -Z inner down	40[a]	2050	10	46	2050	10	**22**	**1336**	**6.5**
BCML2 +Z inner far	40[a]	2050	10	50	2050	10	**22**	**1350**	**6.6**
BCML2 +Z inner up	65[a]	2050	10	85	2050	10	**26**	**1568**	**7.7**
BCML2 +Z inner near	40[a]	2050	10	59	2050	10	**23**	**1396**	**6.8**
BCML2 +Z inner down	100[a]	2050	10	52	2050	10	**18**	**1396**	**6.8**

[a] Estimated signal efficiency based on laboratory measurements or performance as previous BCML detectors.
[b] Signal efficiency at 500V.
[c] Channel not working properly and hence was removed from abort functionallity.

A.1.3 Operation

A.1.3.1 Operation of the BCML sensors

In the following Tables A.3 and A.4 all BCML sensors are listed. The initial signal efficiency for the beginning of physics operation at Run 2 (05.2015) was calculated for each sensor. A detailed explanation of the calculation of the signal efficiency can be found in section 4.5.1.

[1] These BCML1 channel were not working properly and were excluded from the beam abort functionality.

Table A.2: The BCML1 abort thresholds defined for running sum 12 is defined as 3 times the expected signal for nominal luminosity. The initial definition for nominal luminosity of $1 \times 10^{34}\,\mathrm{cm}^{-2}\mathrm{s}^{-1}$ was changed to $1.2 \times 10^{34}\,\mathrm{cm}^{-2}\mathrm{s}^{-1}$ for beginning of 2016 and changed to $1.3 \times 10^{34}\,\mathrm{cm}^{-2}\mathrm{s}^{-1}$ at the middle of 2016 due to increased LHC performance.

Detector location	$SE_{03.15}$	Threshold on 03.15		$SE_{03.16}$	Threshold on 03.16		$SE_{08.16}$	Threshold on 08.16	
	(%)	(ADC)	(nA)	(%)	(ADC)	(nA)	(%)	(ADC)	(nA)
BCML1 -Z far top	100[a]	167503725	390	87	178379548	415	72[b]	143096485	333
BCML1 -Z far bottom[c]	100[a]	167503725	390	-	-	-	-	-	-
BCML1 -Z near top	100[a]	167503725	390	78	168277544	392	78[b]	155327501	362
BCML1 -Z near bottom	55[a]	92127049	215	83	189797435	442	70[b]	138593164	323
BCML1 +Z far top	100[a]	167503725	390	77	169496822	395	60[b]	120030624	279
BCML1 +Z far bottom	100[a]	167503725	390	55	142333597	331	55[b]	110386348	257
BCML1 +Z near top[c]	55[a]	92127049	215	-	-	-	-	-	-
BCML1 +Z near bottom	100[a]	167503725	390	81	179155683	417	58[b]	116458503	271
BCML2 -Z inner far	55[a]	740881859	1725	50	714244018	1663	24	418903637	975
BCML2 -Z inner up	55[a]	740881859	1725	50	713781933	1662	25	447271063	1041
BCML2 -Z inner near	40[a]	541165879	1260	53	797313468	1856	23	409755249	954
BCML2 -Z inner down	40[a]	541165879	1260	46	691363112	1610	22	387538700	902
BCML2 +Z inner far	40[a]	541165879	1260	50	714828241	1664	22	391506985	912
BCML2 +Z inner up	65[a]	876173328	2040	85	1224087740	2850	26	454750986	1059
BCML2 +Z inner near	40[a]	541165879	1260	59	836079069	1947	23	404961122	943
BCML2 +Z inner down	100[a]	1352914698	3150	52	731052841	1702	18	323370711	753

[a]Estimated signal efficiency based on laboratory measurements or performance as previous BCML detectors.
[b]Signal efficiency at 500V.
[c]Channel not working properly and hence was removed from abort functionallity.

Table A.3: The BCML1 sensors. The signal efficiency (SE) was calculated for each BCML1 sensor at the maximum stable operating voltage (HV_{max}). All BCML1 sensors are active in the beam abort functionality.

CMS side	Position	Name	DAB channel	$SE_{init.\,Run\,2}$ (%)	HV_{max} (V)
+Z	near top[1]	P37	01	≥ 95	500
	near bottom	CMS12	02	≥ 95	500
	far top	CMS05	03	≥ 95	500
	far bottom	CMS07	04	≥ 95	500
-Z	near top	CMS06	05	≥ 95	500
	near bottom	P36	06	≥ 95	500
	far top	CMS10	07	≥ 95	500
	far bottom[1]	CMS15	08	≥ 95	500

A.1.3.2 Radiation induced signal degradation of the BCML2 outer diamond sensors

A.1.3.3 Beam Loss Maps - Momentum offset

The LHC global beam losses created during the beam loss maps discussed in section 4.4.2.3 is shown in Fig. A.11. The artificially excited beam 1 was colliding with the primary collimator system at Point 7, creating very intense beam loss events further downstream, hence as well at Point 5 at the CMS detector.

A.1.4 Online Monitor of BCML measurements

Fig. A.12 shows a screen short of a browser window with the BCML Web Monitor showing the signal of all BCML1/2 abort channels for RS1 and RS12 in percent of the abort threshold. A BCML channel signal passing the 100% would trigger immediately a LHC beam abort. The web monitor displays in addition the RS9 measurement for all BCML channels, that is a good indication for the absolute signal current.

A.2 Irradiation Campaign

The irradiation steps chosen in the diamond irradiation campaign are listed in the Tables A.5 and A.6 as 24 GeV proton equivalents and equivalents in integrated luminosity for the BCML2 detector locations, respectively.

A.2.1 Irradiation Steps in different equivalent particle fluxes

[2]Used in the Beam Abort funtionality.

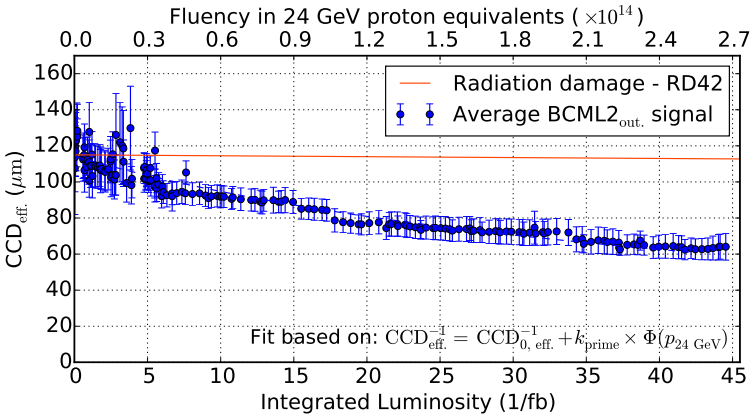

Figure A.8: BCML2 outer diamonds: Radiation induced degradation of effective CCD at a bias voltage of HV = 200 V.

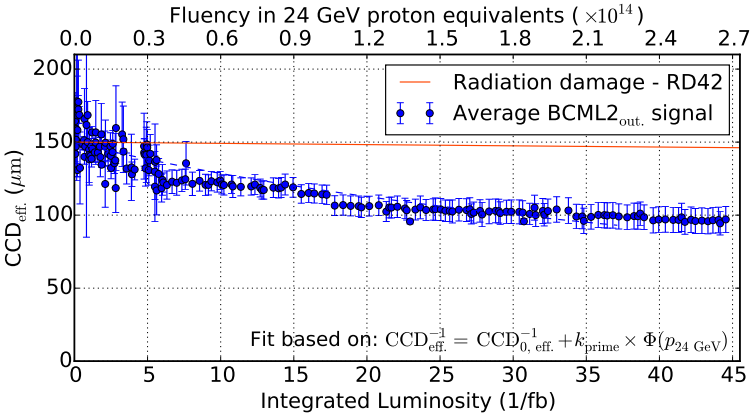

Figure A.9: BCML2 outer diamonds: Radiation induced degradation of effective CCD at a bias voltage of HV = 350 V.

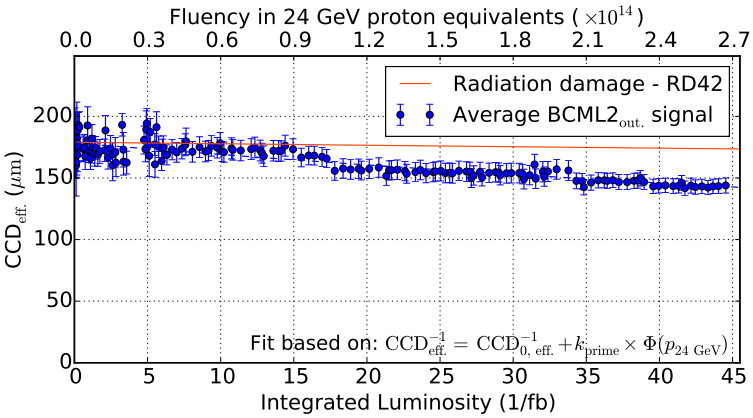

Figure A.10: BCML2 outer diamonds: Radiation induced degradation of effective CCD at a bias voltage of HV = 500 V.

Table A.4: The BCML2 sensors. The signal efficiency (SE) was calculated for each BCML2 sensor at the maximum stable operating voltage (HV_{max}). The BCML2 detectors operated at the same electrical field and mounted at the same location, taking the Φ and the $\pm Z$ symmetry of the CMS detector into account, are assigned to 5 different detector groups: BCML2, $BCML2_{in.\,500}$, $BCML2_{out.\,200}$, $BCML2_{out.\,350}$ and $BCML2_{out.\,500}$

End	Position	Name	DAB #	$SE_{init.\,Run\,2}$ (%)	HV_{max} (V)	Group
	inner top[2]	P47	17	≥ 60	200	BCML2
	inner far[2]	P30	18	≥ 60	200	BCML2
	outer top	P14	19	≥ 75	500	$BCML2_{out.\,500}$
	inner far (B)	P13	20	≥ 60	500	$BCML2_{in.\,500}$
	outer far	P22	21	≥ 70	500	$BCML2_{out.\,500}$
	outer bottom-far	P38	22	≥ 65	500	$BCML2_{out.\,350}$
-Z	-	BLM	24	-	1500	-
	inner near[2]	P29	25	≥ 60	200	BCML2
	inner bottom[2]	P12	26	≥ 50	200	BCML2
	outer near	P18	27	≥ 65	500	$BCML2_{out.\,500}$
	outer top-near	P40	28	≥ 70	500	$BCML2_{out.\,500}$
	outer bottom	P21	29	≥ 75	500	$BCML2_{out.\,500}$
	inner near (B)	P44	30	≥ 60	500	$BCML2_{in.\,500}$
	outer near	P15	33	≥ 45	350	$BCML2_{out.\,350}$
	inner top[2]	P23	34	≥ 95	200	BCML2
	inner near[2]	P39	35	≥ 70	200	BCML2
	inner top-near	P25	36	≥ 50	200	-
	outer top	P20	37	≥ 80	350	$BCML2_{out.\,200}$
	outer bottom-near	P24	38	≥ 40	500	$BCML2_{out.\,200}$
+Z	inner top	SAP_1	39	≥ 95	500	-
	inner near	sCVD_1	40	≥ 95	200	-
	inner far (B)	P16	41	≥ 35	200	-
	inner bottom[2]	CMS11	42	≥ 60	200	BCML2
	outer far	P31	43	≥ 60	200	$BCML2_{out.\,350}$
	inner far[2]	P45	44	≥ 60	200	BCML2
	outer bottom	P28	46	≥ 50	200	$BCML2_{out.\,200}$
	-	BLM	48	-	1500	-

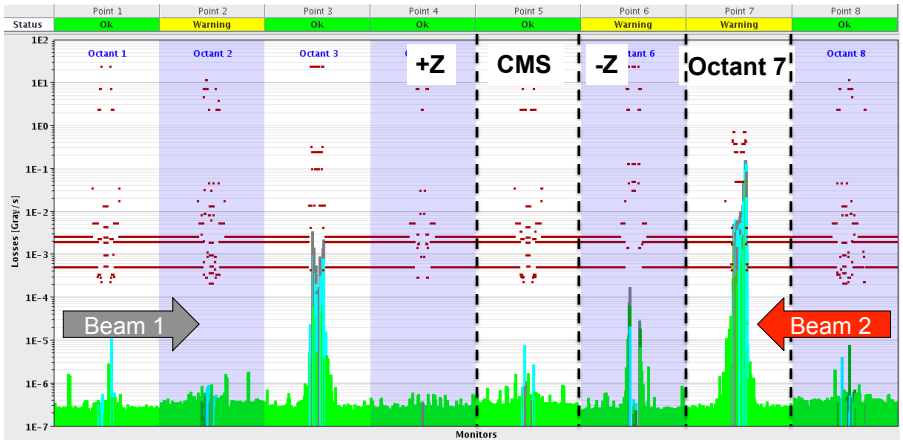

Figure A.11: LHC global measurements of the BLM system detecting the beam loss event of beam 1 scattering at the primary collimator system at Point 7.

Figure A.12: The BCML web monitor displays the abort level in percent for RS1 and RS12. Two LHC fills can be seen with a duration of around 14 hours.

Table A.5: Overview of diamond irradiation steps in 24 GeV proton equivalents. The diamond sample were irradiated up to 7 times to a total irradiation damage of $3.0 \times 10^{14}\, n_{1\,\mathrm{MeV}}$ equivalent to $108.1 \times 10^{13}\, p_{24\,\mathrm{GeV}}$.

Name	Particle type	Total irradiation damage in 24 GeV proton equivalents ($\times 10^{13}$)						
		1^{st}	2^{nd}	3^{rt}	4^{rt}	5^{rt}	6^{rt}	7^{rt}
27135473	$p_{23\,\mathrm{MeV}}$	1.1	2.2	3.2	5.4	16.2	54.1	-
27135474	$p_{23\,\mathrm{MeV}}$	1.1	2.2	3.2	4.3	6.5	17.3	108.1
27135476	$n_{\leq 10\,\mathrm{MeV}}$	0.8	1.6	2.5	5.8	16.8	-	-
24990289	$n_{\leq 10\,\mathrm{MeV}}$	0.8	1.6	2.5	5.8	16.8	-	-

Table A.6: Overview of diamond irradiation steps. The diamond sample were irradiated up to 7 times to a total irradiation damage of $3.0 \times 10^{14}\, n_{1\,\mathrm{MeV}}$ equivalent to $74.0\,\mathrm{fb}^{-1}$ of integrated luminosity for the BCML2 locations.

Name	Particle type	Total Irradiation damage in equivalents of $\mathcal{L}_{\mathrm{int.}}$ (fb^{-1})						
		1^{st}	2^{nd}	3^{rt}	4^{rt}	5^{rt}	6^{rt}	7^{rt}
27135473	$p_{23\,\mathrm{MeV}}$	0.7	1.5	2.2	3.7	11.1	37.0	-
27135474	$p_{23\,\mathrm{MeV}}$	0.7	1.5	2.2	3.0	4.4	11.8	74.0
27135476	$n_{\leq 10\,\mathrm{MeV}}$	0.6	1.1	1.7	4.0	11.5	-	-
24990289	$n_{\leq 10\,\mathrm{MeV}}$	0.6	1.1	1.7	4.0	11.5	-	-

A.2.2 TCT Measurement Results

Diamond sensor #24990892**:** HV $= 100\,\mathrm{V}$ **equivalent to** $E = 0.18\,\mathrm{V/\mu m}$

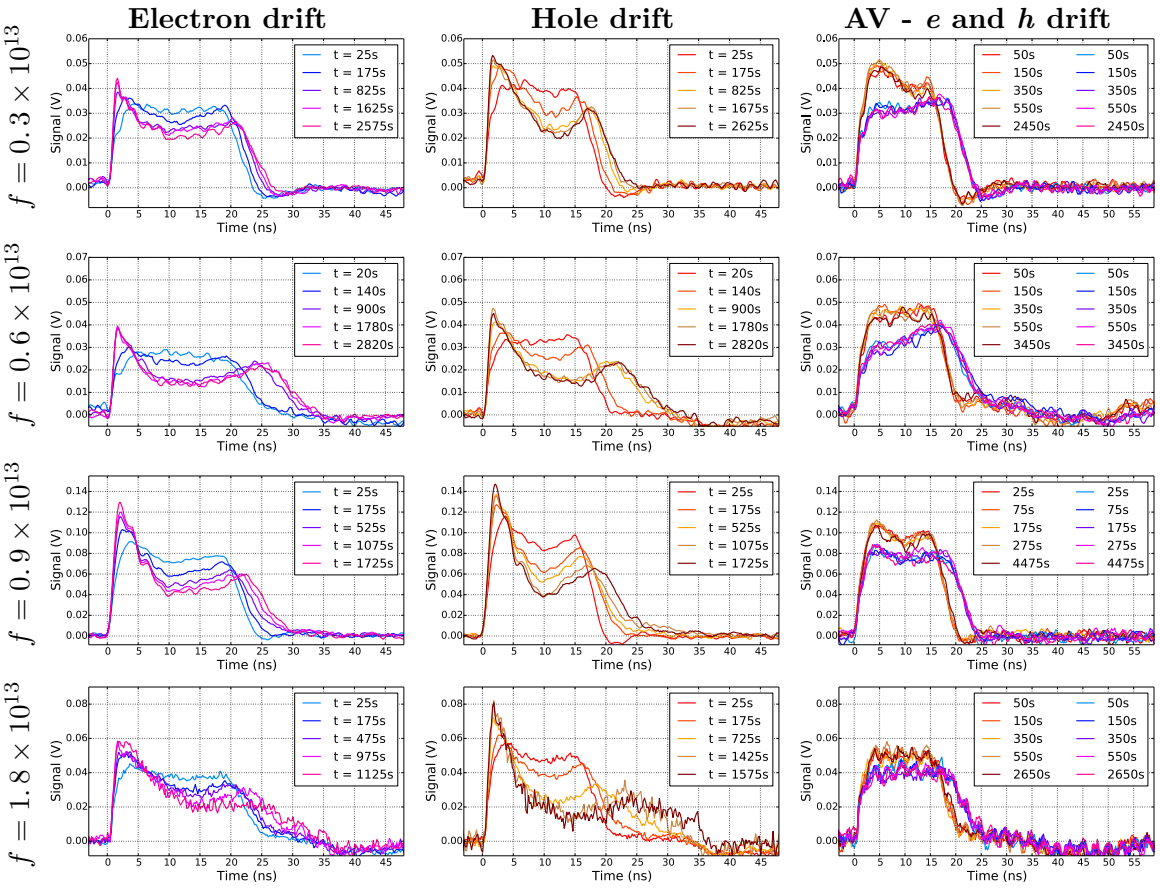

Figure A.13: TCT measurements as function of radiation damage: diamond sensor #24990892 measured at an bias voltage of HV $= 100\,\mathrm{HV}$ equivalent to an electrical field of $E = 0.18\,\mathrm{V/\mu m}$, all fluences given in 1 MeV neutron equivalents.

Diamond sensor #24990892: HV = 200V equivalent to $E = 0.36\,\mathrm{V/\mu m}$

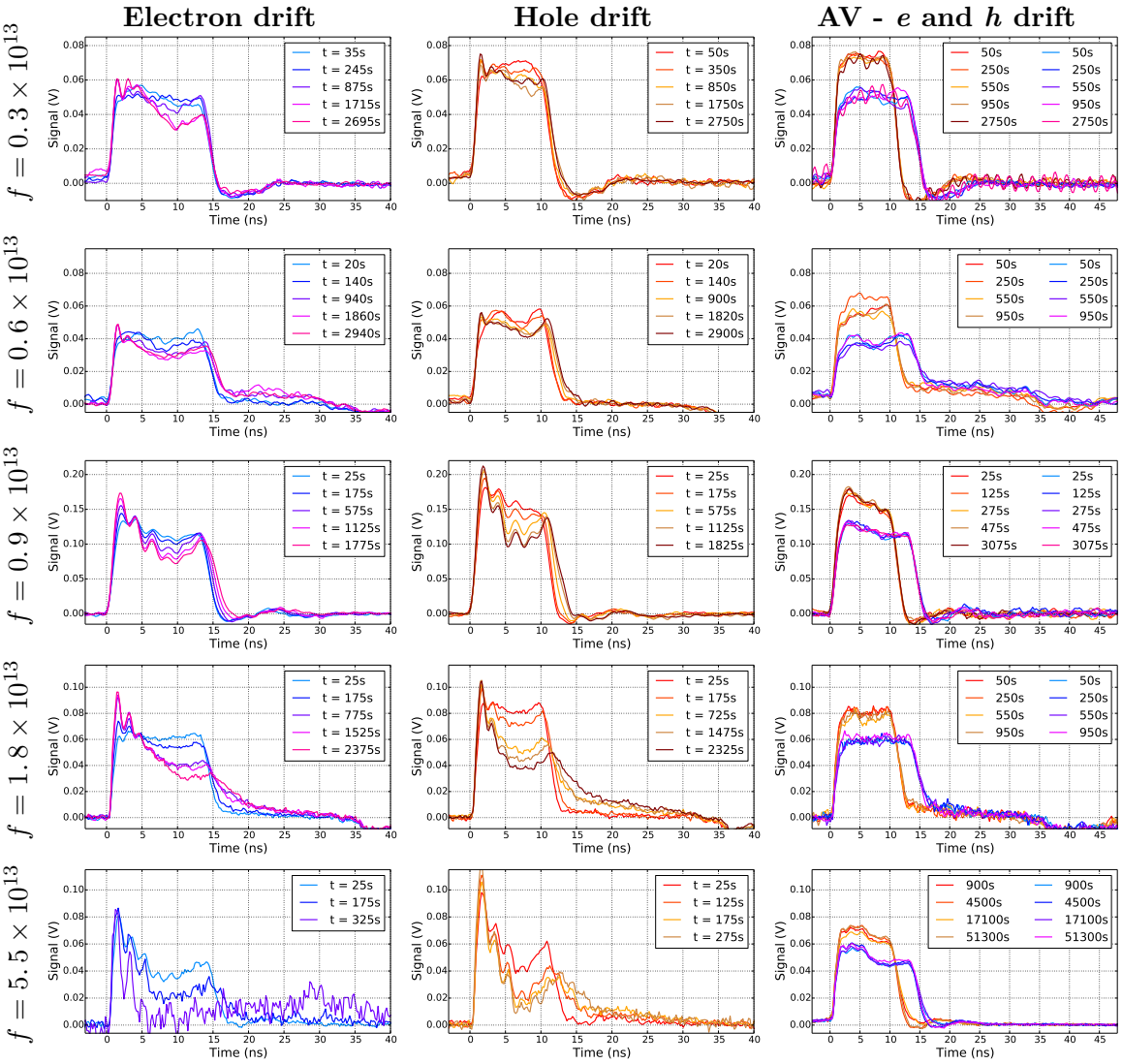

Figure A.14: TCT measurements as function of radiation damage: diamond sensor #24990892 measured at an bias voltage of HV = 200 HV equivalent to an electrical field of $E = 0.36\,\mathrm{V/\mu m}$, all fluences given in 1 MeV neutron equivalents.

Diamond sensor #24990892**:** HV $= 400$V **equivalent to** $E = 0.73\,\mathrm{V/\mu m}$

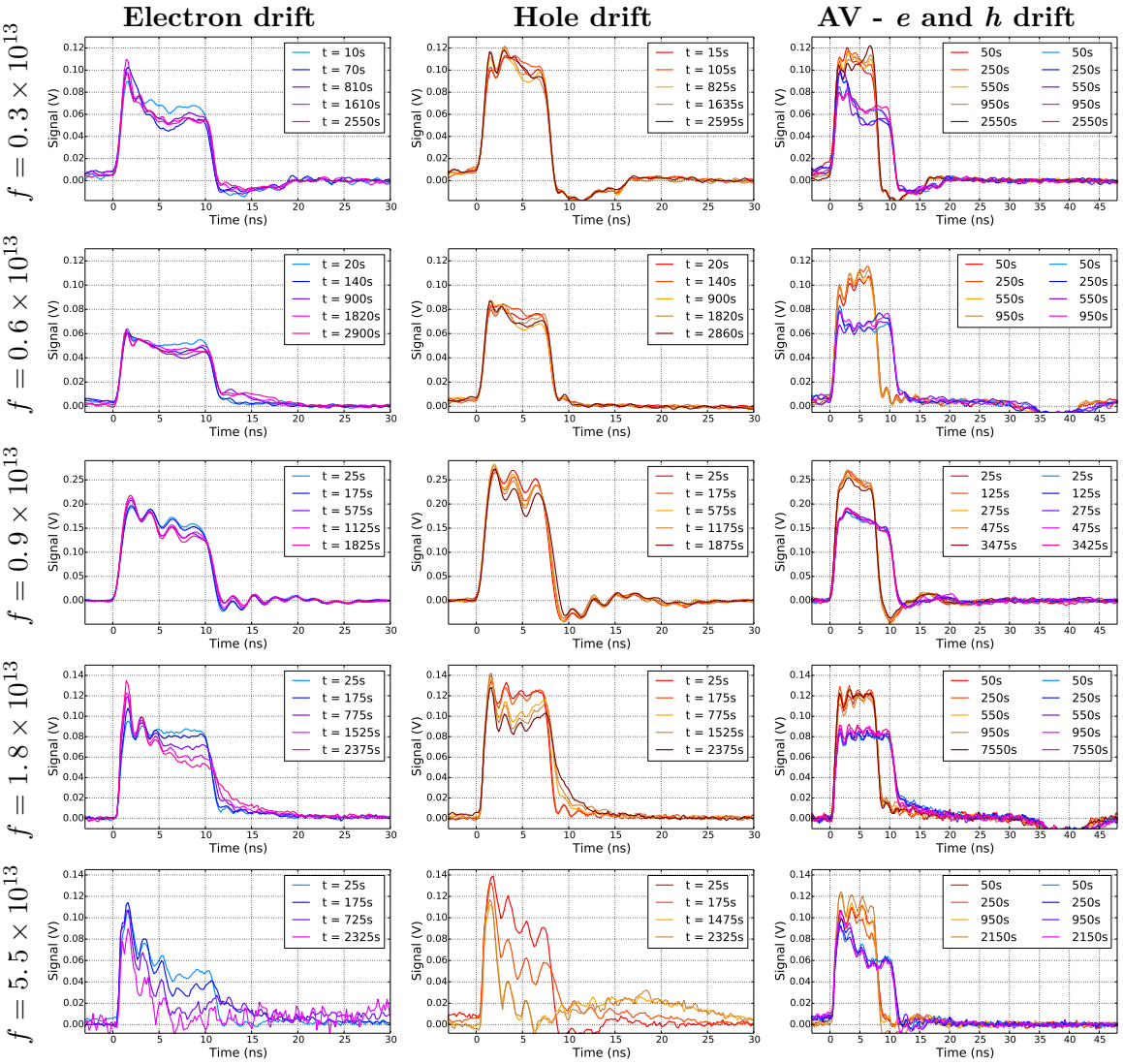

Figure A.15: TCT measurements as function of radiation damage: diamond sensor #24990892 measured at an bias voltage of HV $= 400\,$HV equivalent to an electrical field of $E = 0.73\,\mathrm{V/\mu m}$, all fluences given in 1 MeV neutron equivalents.

Diamond sensor #27135473: HV = 100V equivalent to $E = 0.18\,\mathrm{V/\mu m}$

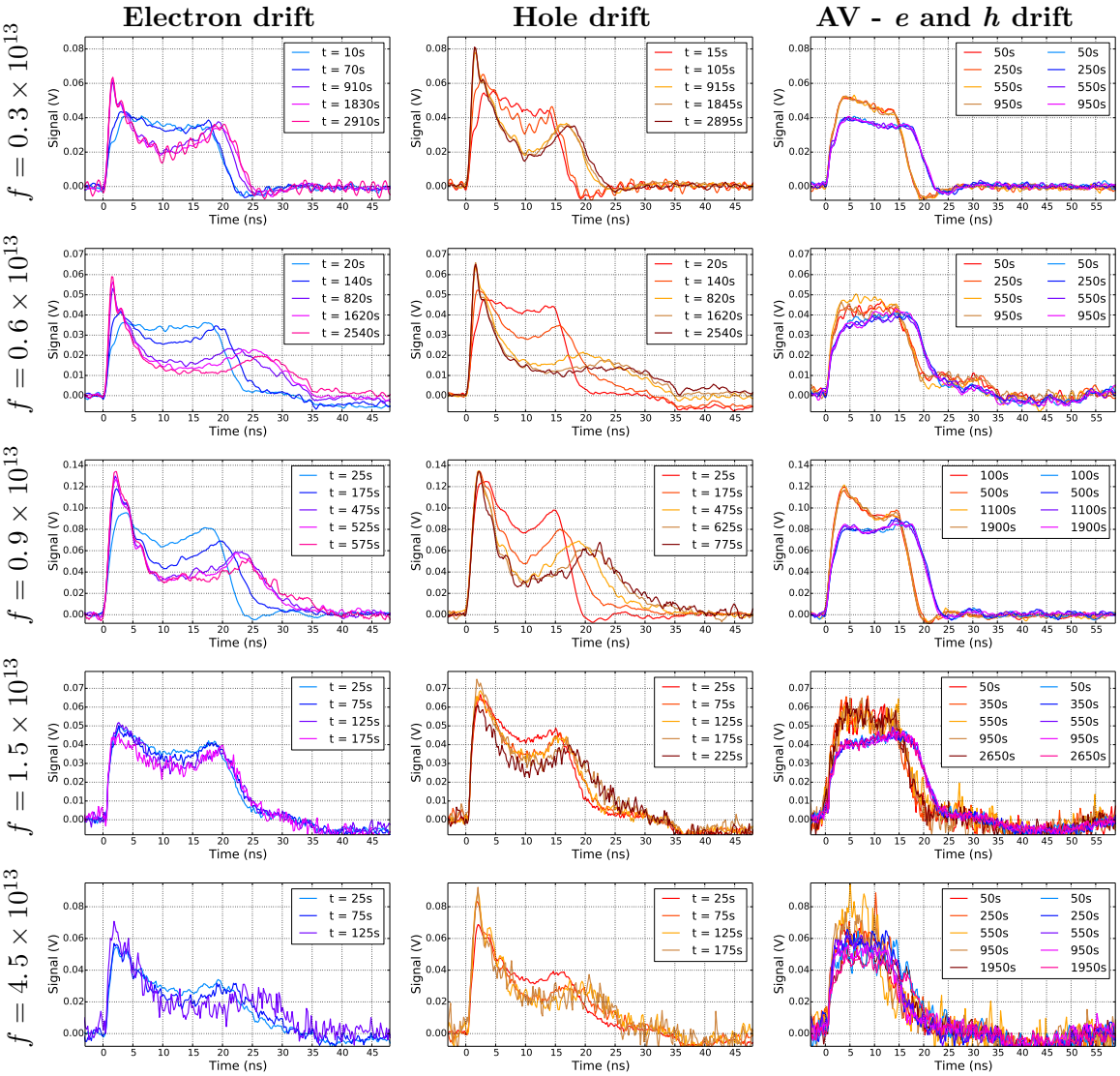

Figure A.16: TCT measurements as function of radiation damage: diamond sensor #27135473 measured at an bias voltage of HV = 100 HV equivalent to an electrical field of $E = 0.18\,\mathrm{V/\mu m}$, all fluences given in 1 MeV neutron equivalents.

Diamond sensor #27135473**:** HV = 200V **equivalent to** $E = 0.36\,\mathrm{V/\mu m}$

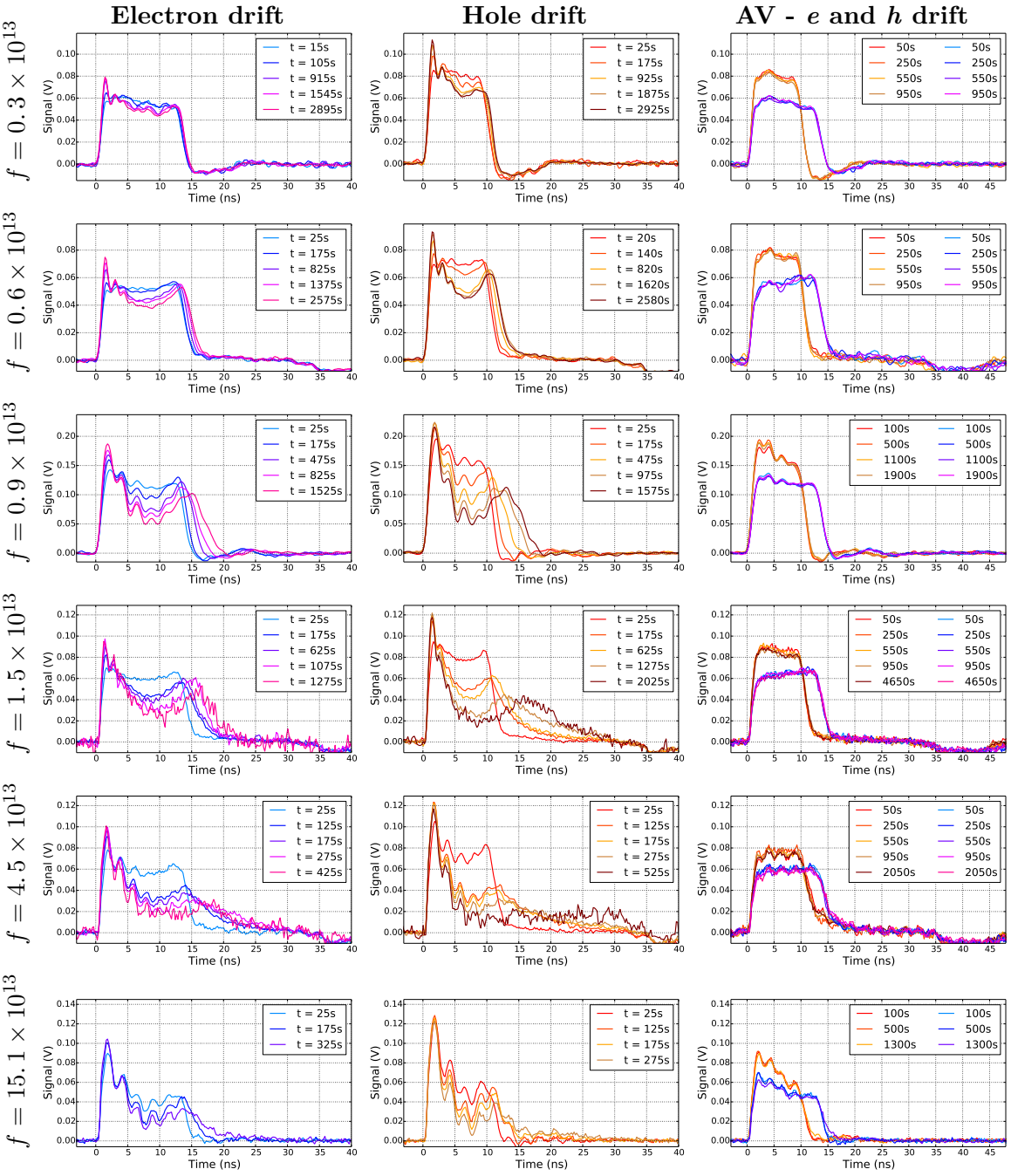

Figure A.17: TCT measurements as function of radiation damage: diamond sensor #27135473 measured at an bias voltage of HV = 200 HV equivalent to an electrical field of $E = 0.36\,\mathrm{V/\mu m}$, all fluences given in 1 MeV neutron equivalents.

Diamond sensor #27135473: HV = 400V equivalent to $E = 0.73\,\mathrm{V/\mu m}$

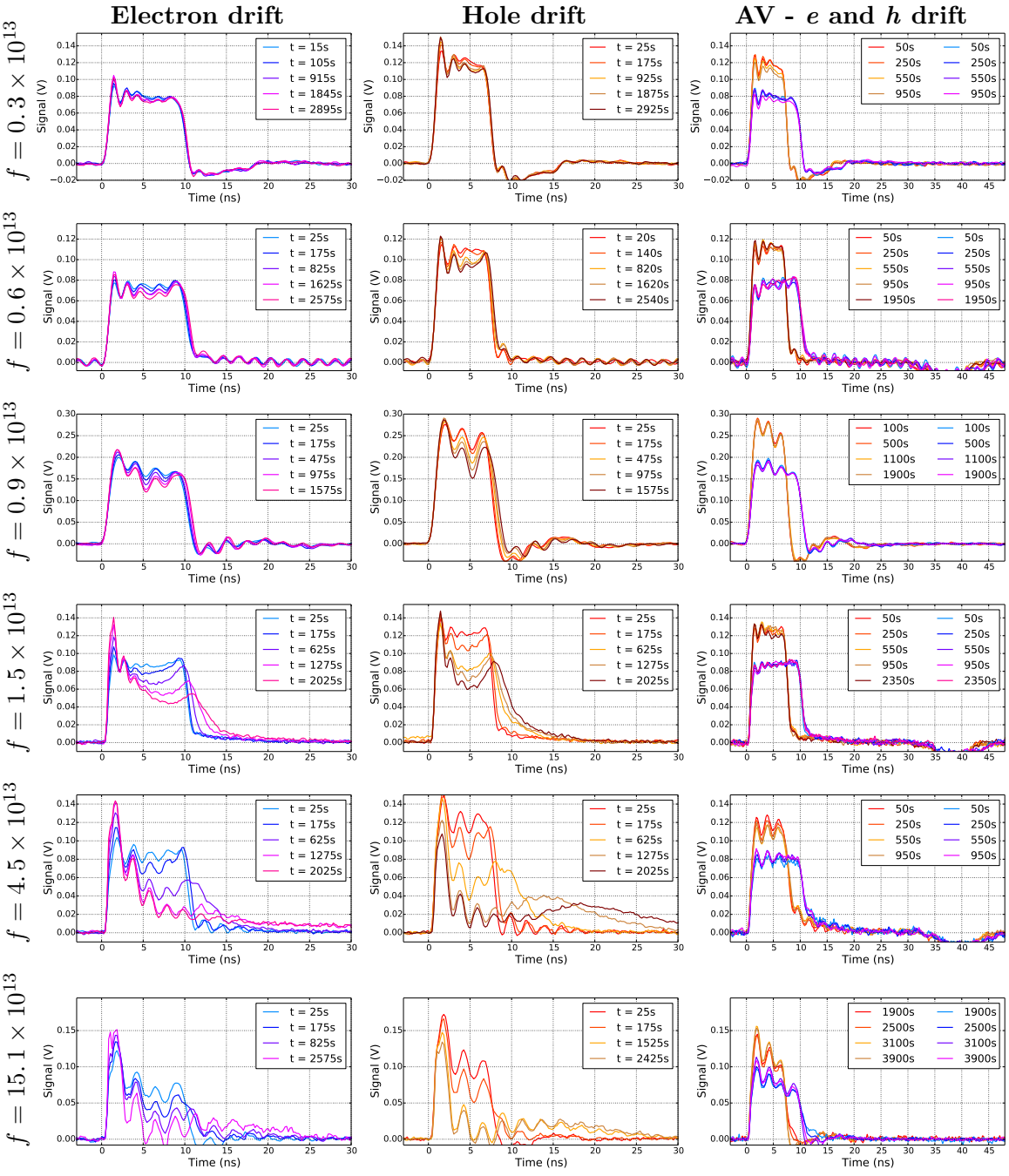

Figure A.18: TCT measurements as function of radiation damage: diamond sensor #27135473 measured at an bias voltage of HV = 400 HV equivalent to an electrical field of $E = 0.73\,\mathrm{V/\mu m}$, all fluences given in 1 MeV neutron equivalents.

Diamond sensor #27135474**:** HV = 100V **equivalent to** $E = 0.18\,\mathrm{V/\mu m}$

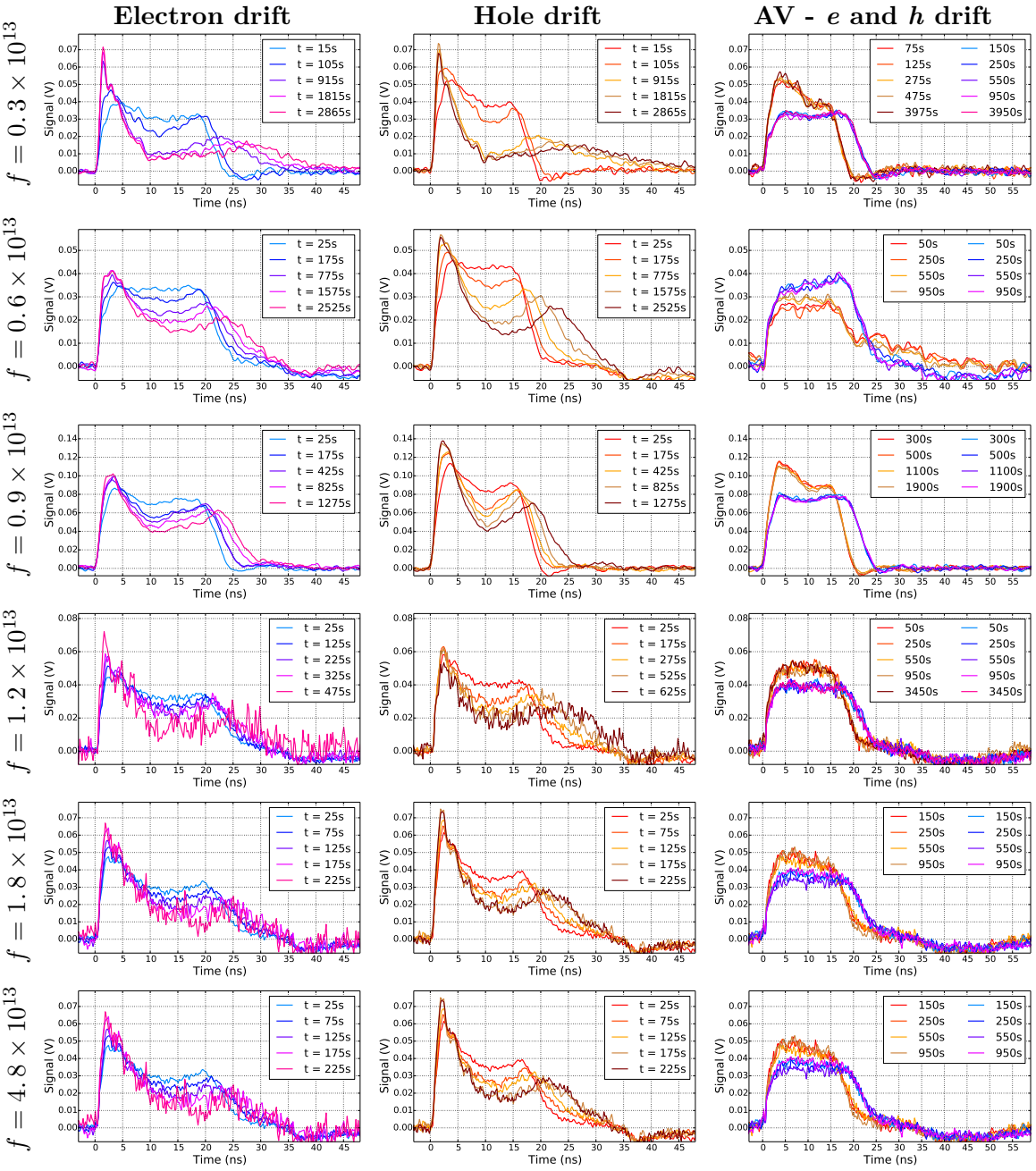

Figure A.19: TCT measurements as function of radiation damage: diamond sensor #27135474 measured at an bias voltage of HV = 100 HV equivalent to an electrical field of $E = 0.18\,\mathrm{V/\mu m}$, all fluences given in 1 MeV neutron equivalents.

Diamond sensor #27135474: HV = 200V equivalent to $E = 0.36\,\mathrm{V/\mu m}$

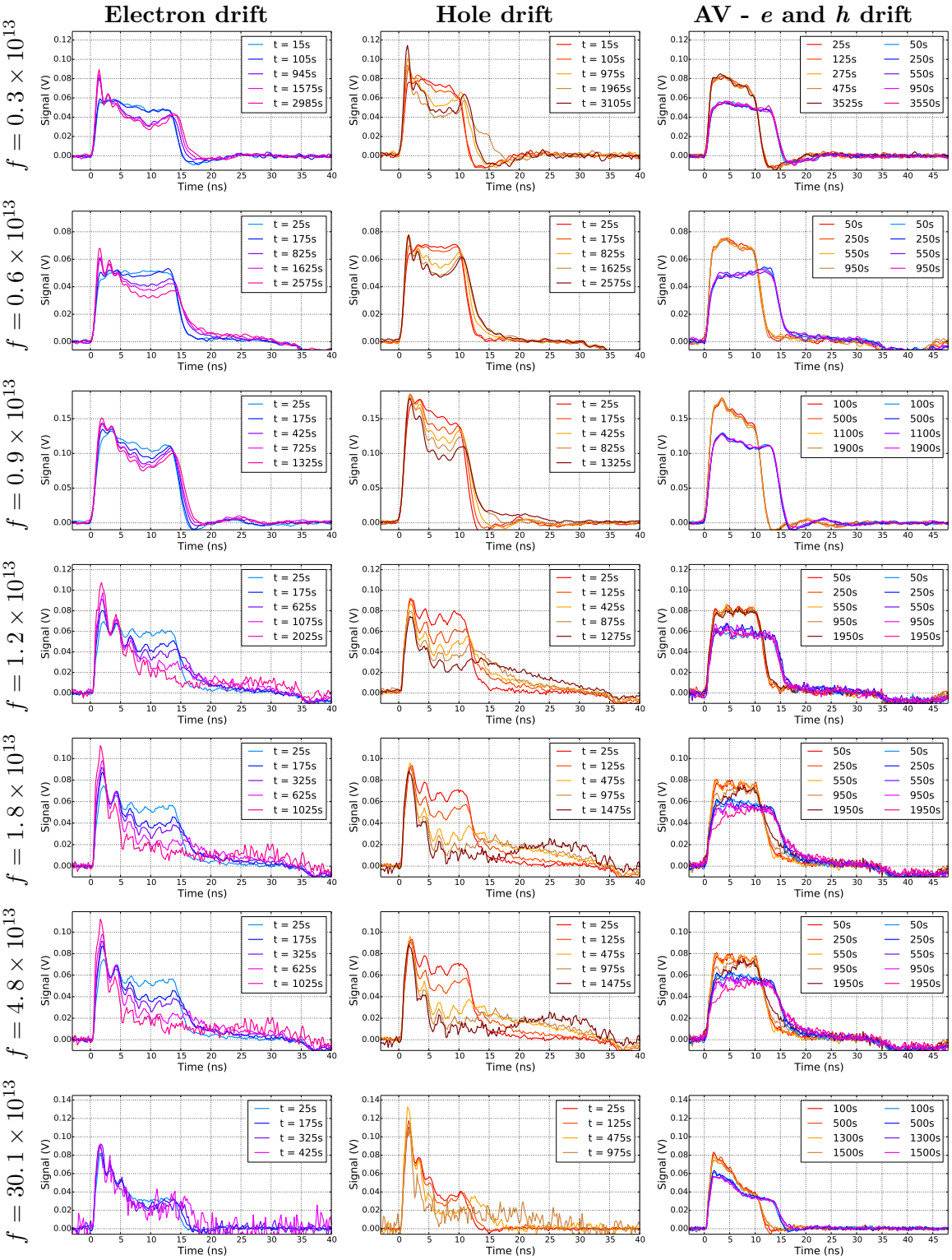

Figure A.20: TCT measurements as function of radiation damage: diamond sensor #27135474 measured at an bias voltage of HV = 200 HV equivalent to an electrical field of $E = 0.36\,\mathrm{V/\mu m}$, all fluences given in 1 MeV neutron equivalents.

Diamond sensor #27135474**:** HV $= 400$V **equivalent to** $E = 0.73\,\mathrm{V/\mu m}$

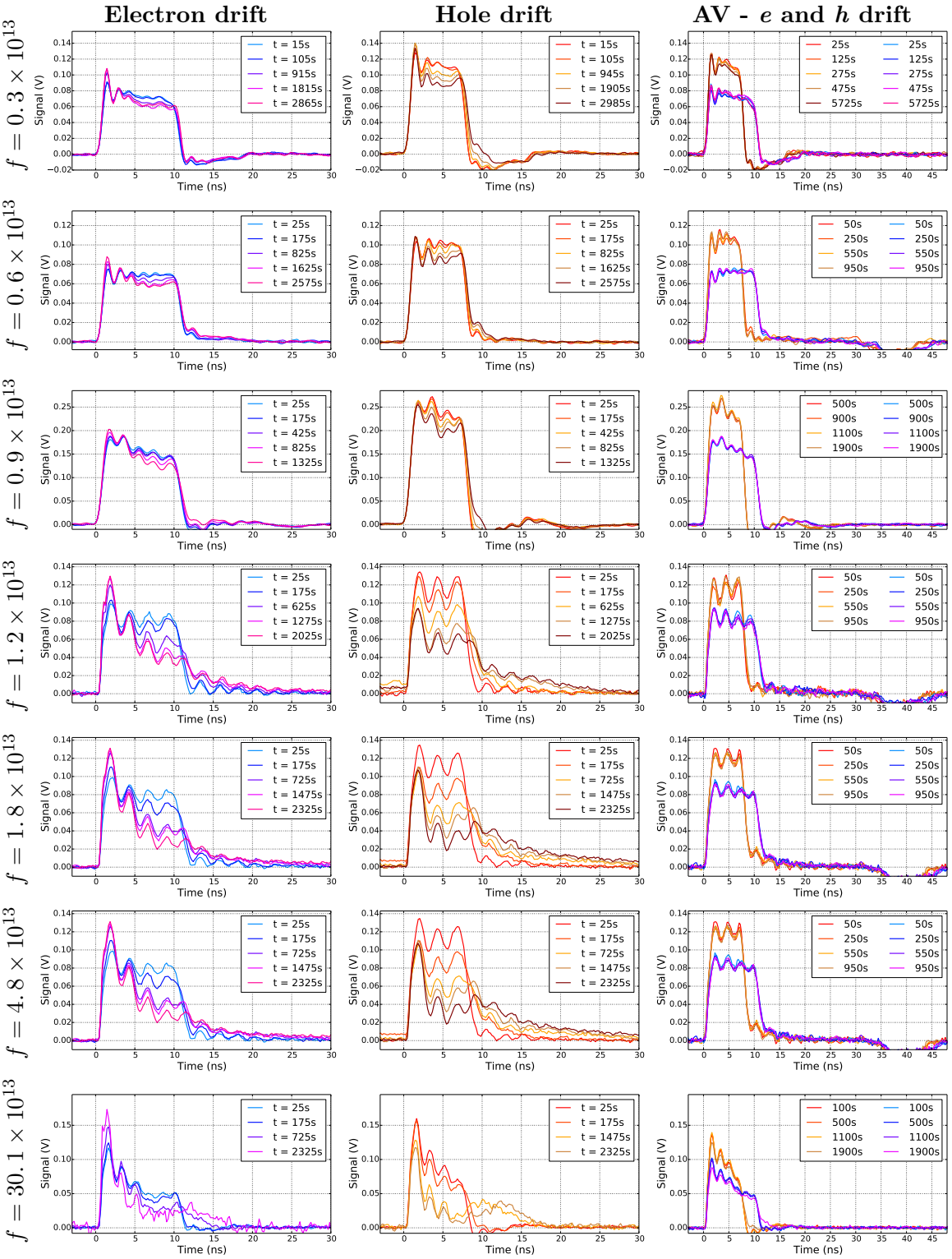

Figure A.21: TCT measurements as function of radiation damage: diamond sensor #27135474 measured at an bias voltage of HV $= 400$ HV equivalent to an electrical field of $E = 0.73\,\mathrm{V/\mu m}$, all fluences given in 1 MeV neutron equivalents.

Diamond sensor #27135476: HV = 98V equivalent to $E = 0.18\,\mathrm{V/\mu m}$

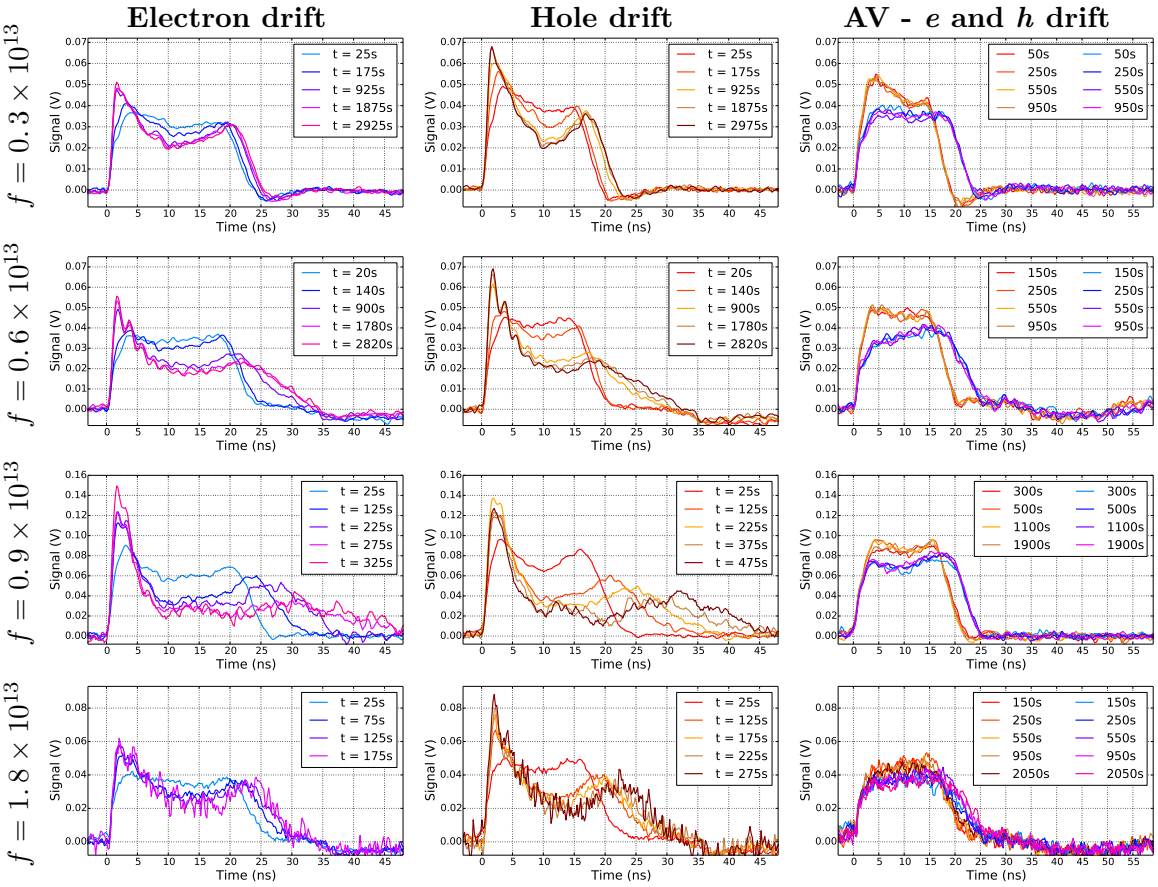

Figure A.22: TCT measurements as function of radiation damage: diamond sensor #27135476 measured at an bias voltage of HV = 98 HV equivalent to an electrical field of $E = 0.18\,\mathrm{V/\mu m}$, all fluences given in 1 MeV neutron equivalents.

Diamond sensor #27135476**:** HV $= 196$V **equivalent to** $E = 0.36\,\mathrm{V/\mu m}$

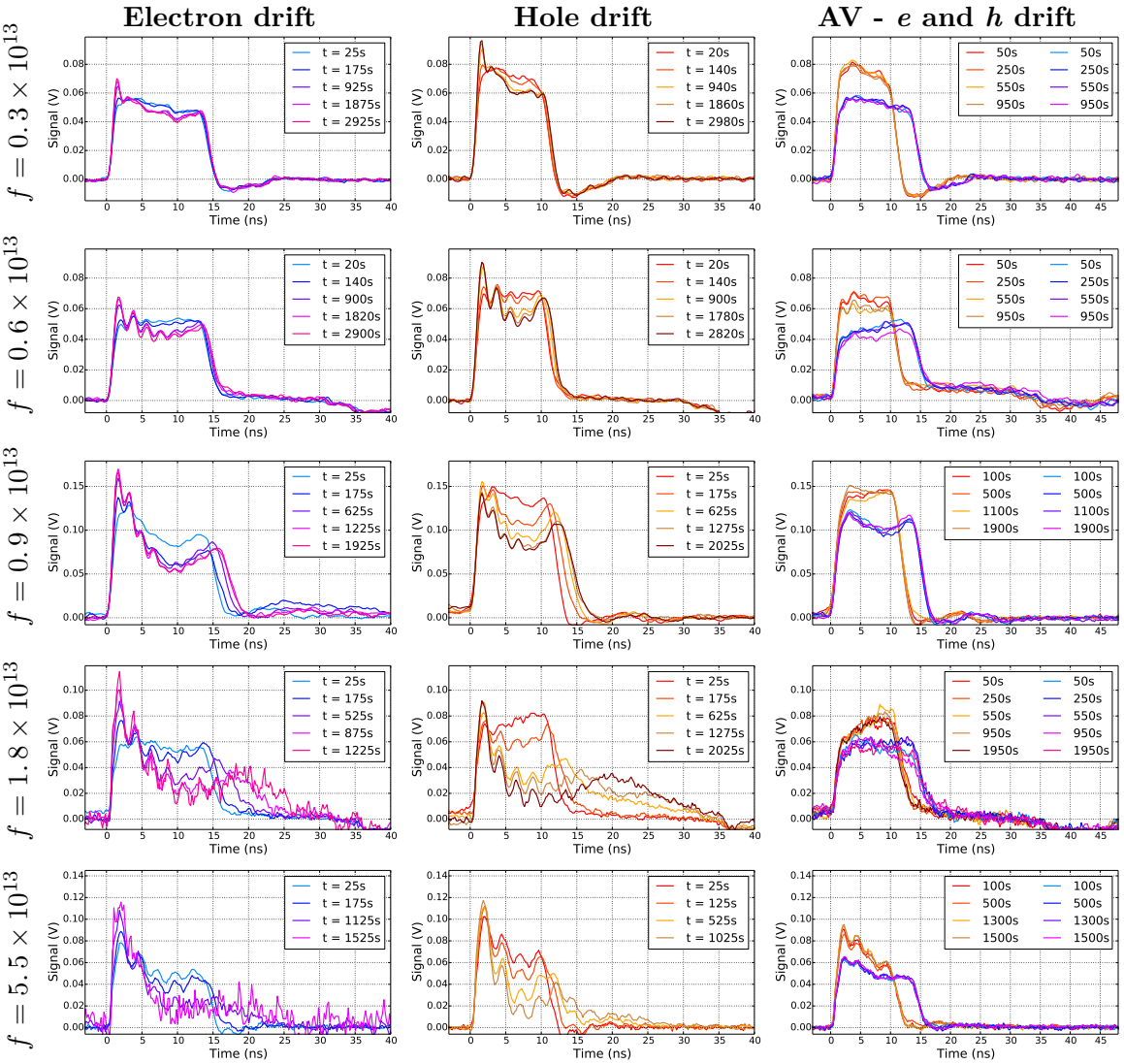

Figure A.23: TCT measurements as function of radiation damage: diamond sensor #27135476 measured at an bias voltage of HV $= 196$ HV equivalent to an electrical field of $E = 0.36\,\mathrm{V/\mu m}$, all fluences given in 1 MeV neutron equivalents.

Diamond sensor #27135476: HV = 383V equivalent to $E = 0.73\,\mathrm{V/\mu m}$

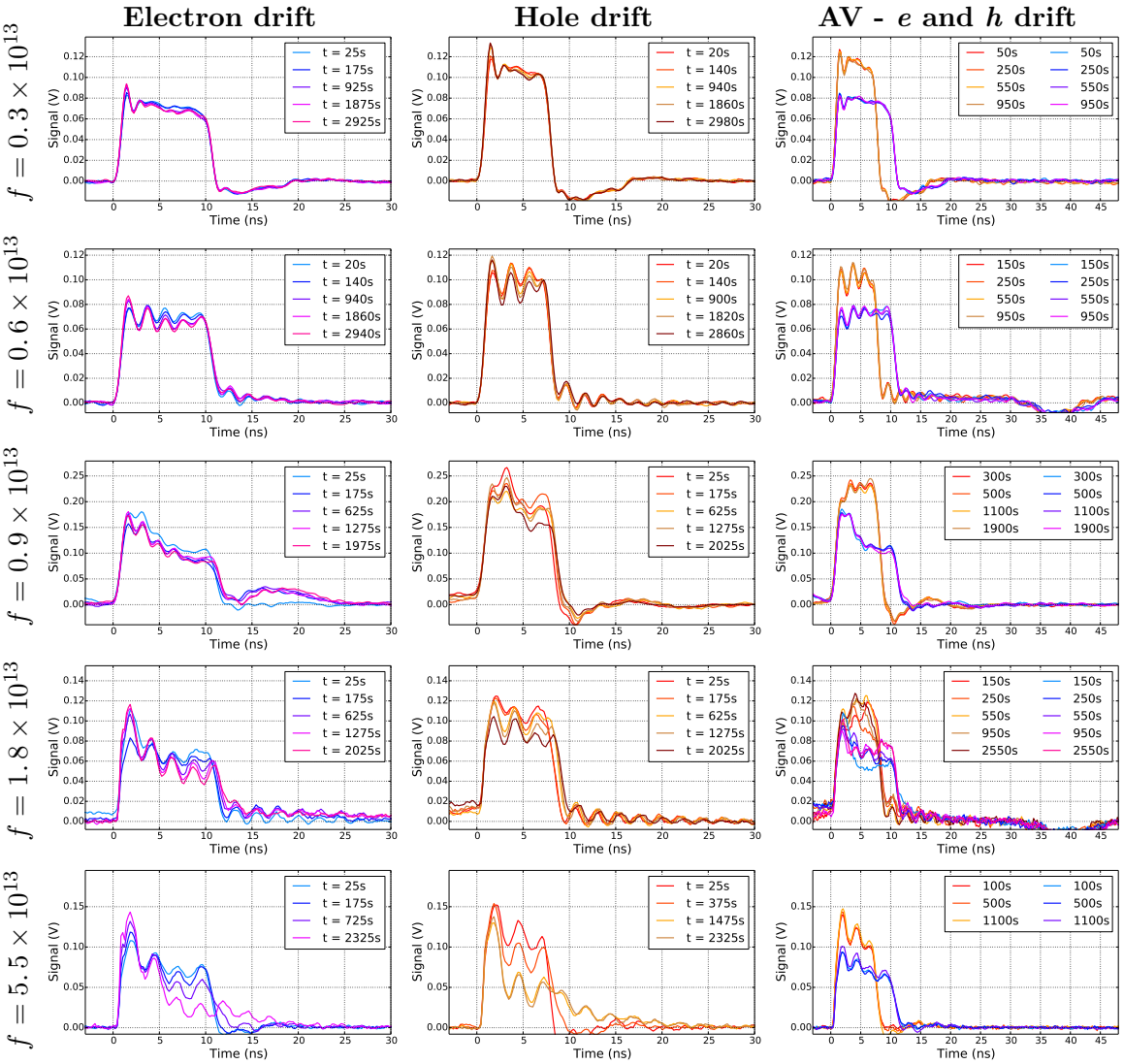

Figure A.24: TCT measurements as function of radiation damage: diamond sensor #27135476 measured at an bias voltage of HV = 383 HV equivalent to an electrical field of $E = 0.73\,\mathrm{V/\mu m}$, all fluences given in 1 MeV neutron equivalents.